

Electrochemical & Photochemical Applications of Multifunctional Metal Phosphonates

International PhD Thesis

Programa de Doctorado
Química y Tecnologías Químicas. Materiales y Nanotecnología
Facultad de Ciencias. Universidad de Málaga


Supervisors
Aurelio Cabeza Díaz
Pascual Olivera Pastor

Inés Ruiz Salcedo
Málaga, 2020



UNIVERSIDAD
DE MÁLAGA

AUTOR: Inés Ruiz Salcedo

 <http://orcid.org/0000-0001-9986-6805>

EDITA: Publicaciones y Divulgación Científica. Universidad de Málaga



Esta obra está bajo una licencia de Creative Commons Reconocimiento-NoComercial-SinObraDerivada 4.0 Internacional:

<http://creativecommons.org/licenses/by-nc-nd/4.0/legalcode>

Cualquier parte de esta obra se puede reproducir sin autorización pero con el reconocimiento y atribución de los autores.

No se puede hacer uso comercial de la obra y no se puede alterar, transformar o hacer obras derivadas.

Esta Tesis Doctoral está depositada en el Repositorio Institucional de la Universidad de Málaga (RIUMA): riuma.uma.es





Tesis Doctoral

Electrochemical and Photochemical Applications of Multifunctional Metal Phosphonates

Inés Ruiz Salcedo

Directores

Dr. Aurelio Cabeza Díaz
Dr. Pascual Olivera Pastor

Química y Tecnologías Químicas. Materiales y Nanotecnología
Departamento de Química Inorgánica, Cristalografía y Mineralogía
Facultad de Ciencias
Universidad de Málaga
Málaga, 2020





UNIVERSIDAD
DE MÁLAGA



UNIVERSIDAD
DE MÁLAGA



Escuela de Doctorado

DECLARACIÓN DE AUTORÍA Y ORIGINALIDAD DE LA TESIS PRESENTADA PARA OBTENER EL TÍTULO DE DOCTOR

D./Dña INÉS RUIZ SALCEDO

Estudiante del programa de doctorado CIENCIAS Y TECNOLOGÍAS QUÍMICAS. MATERIALES Y NANOTECNOLOGÍA de la Universidad de Málaga, autor/a de la tesis, presentada para la obtención del título de doctor por la Universidad de Málaga, titulada: ELECTROCHEMICAL AND PHOTOCHEMICAL APPLICATIONS OF MULTIFUNCTIONAL METAL PHOSPHONATES

Realizada bajo la tutorización de AURELIO CABEZA DÍAZ y dirección de AURELIO CABEZA DÍAZ Y PASCUAL OLIVERA PASTOR (si tuviera varios directores deberá hacer constar el nombre de todos)

DECLARO QUE:

La tesis presentada es una obra original que no infringe los derechos de propiedad intelectual ni los derechos de propiedad industrial u otros, conforme al ordenamiento jurídico vigente (Real Decreto Legislativo 1/1996, de 12 de abril, por el que se aprueba el texto refundido de la Ley de Propiedad Intelectual, regularizando, aclarando y armonizando las disposiciones legales vigentes sobre la materia), modificado por la Ley 2/2019, de 1 de marzo.

Igualmente asumo, ante a la Universidad de Málaga y ante cualquier otra instancia, la responsabilidad que pudiera derivarse en caso de plagio de contenidos en la tesis presentada, conforme al ordenamiento jurídico vigente.

En Málaga, a 21 de MAYO de 2020

Fdo.: INÉS RUIZ SALCEDO



EFQM AENOR



Edificio Pabellón de Gobierno. Campus El Ejido.
29071
Tel.: 952 13 10 28 / 952 13 14 61 / 952 13 71 10
E-mail: doctorado@uma.es

UNIVERSIDAD
DE MÁLAGA





UNIVERSIDAD
DE MÁLAGA

Electrochemical and Photochemical Applications of Multifunctional Metal Phosphonates

Memoria presentada para optar al título de:

**Doctora en Química y Tecnologías Químicas. Materiales y
Nanotecnología
“Mención Internacional”**



Fdo: Inés Ruiz Salcedo

Directores:



Fdo: Dr. Aurelio Cabeza Díaz
Catedrático de la Universidad de
Málaga



Fdo: Dr. Pascual Olivera Pastor
Catedrático de la Universidad de
Málaga

Departamento de Química Inorgánica, Cristalografía y Mineralogía
Facultad de Ciencias
Universidad de Málaga
Málaga, 2020



UNIVERSIDAD
DE MÁLAGA

Dr. Aurelio Cabeza Díaz, Catedrático de Química Inorgánica, y **Dr. Pascual Olivera Pastor**, Catedrático de Química Inorgánica, ambos pertenecientes al Departamento de Química Inorgánica, Cristalografía y Mineralogía de la Facultad de Ciencias de la Universidad de Málaga,

CERTIFICAN:

Que la presente memoria titulada “Electrochemical and Photochemical Applications of Multifunctional Metal Phosphonates”, ha sido realizada bajo nuestra dirección en el Departamento de Química Inorgánica, Cristalografía y Mineralogía de la Facultad de Ciencias de la Universidad de Málaga por la graduada en Química D^a Inés Ruiz Salcedo. Este trabajo reúne, a nuestro juicio, contenido científico suficiente y las condiciones necesarias para optar al grado de Doctora.

Málaga, a 21 de mayo de 2020



Fdo: Dr. Aurelio Cabeza Díaz
Catedrático de la Universidad de
Málaga



Fdo: Dr. Pascual Olivera Pastor
Catedrático de la Universidad de
Málaga



UNIVERSIDAD
DE MÁLAGA

Dr. Pedro Jesús Maireles Torres, Catedrático de la Universidad de Málaga y Director del Departamento de Química Inorgánica, Cristalografía y Mineralogía de la Facultad de Ciencias de la misma universidad,

INFORMA:

Que la presente memoria realizada por D^a Inés Ruiz Salcedo y titulada "Electrochemical and Photochemical Applications of Multifunctional Metal Phosphonates", ha sido realizada bajo la dirección del Catedrático Dr. Aurelio Cabeza Díaz y del Catedrático Pascual Olivera Pastor en el Departamento de Química Inorgánica, Cristalografía y Mineralogía de la Facultad de Ciencias de la Universidad de Málaga. Este trabajo constituye la Memoria de Tesis Doctoral de la interesada, cuya presentación autorizo.

Málaga, a 21 de mayo de 2020

 UNIVERSIDAD
DE MÁLAGA
FACULTAD DE CIENCIAS
DPTO. QUÍMICA INORGÁNICA
CRISTALOGRAFÍA Y MINERALOGÍA



Fdo: Dr. Pedro Jesús Maireles Torres
Catedrático de la Universidad de Málaga



UNIVERSIDAD
DE MÁLAGA

AGRADECIMIENTOS

Llegados a este punto, me gustaría dedicar unas palabras de agradecimiento a todas las personas que me han acompañado durante este camino.

En primer lugar, me gustaría agradecer a mis directores, los catedráticos Aurelio Cabeza Díaz y Pascual Olivera Pastor, por la oportunidad brindada. Ya que, si ellos no hubieran contado conmigo, nada de esto habría sido posible. Os agradezco de corazón todo el tiempo dedicado, el apoyo y la confianza que habéis depositado en mí.

Por supuesto, agradecer a todos los miembros del departamento de Química Inorgánica, Cristalografía y Mineralogía. En especial a ellos, “los becarios”, que empezaron siendo compañeros y han terminado siendo amigos. A Rosario y Montse, “las niñas fosfonatos”, por ayudarme desde el minuto uno y por todos los buenos ratos. A mis niñas bailongas, Mari y Sandra, ¡qué gran descubrimiento! A Jowilí, (aunque todos saben que es por regalarme a mí Paquillo Pichín), a Rocío y nuestro amor-odio, a Ana, que por fin entiende mis bromas y no se enfada (o me las perdona con ositos Lulú), a Ale y Jesús por alegrar el despacho desde el primer momento que lo pisaron, a Adri (aunque siempre reniegue de nosotras), a Javi y a su caos, a Shiva y su vocación contagiosa, a Inma, por regalarnos el momentazo de la caja (¡no te enfades Inmi!), a Lucía y nuestras aventuras en Inglaterra, a Isa al cuadrado... En definitiva, ¡a todos!

Otra de las cosas buenas que ha tenido mi paso por la universidad ha sido conocer a Samara y Sergio, con los que he compartido carrera, vocación y amistad. Si estamos Samara y yo juntas, la mala suerte está asegurada, pero ¿y qué más da? Siempre podemos echar mano de nuestro ingrediente secreto...

También quiero agradecer a mis amigas de siempre: Bea, Manuela, María, Noelia, Mara, Carmen, ... ¡Gracias!

Por último, agradecer a toda mi familia por su apoyo incondicional. En especial a mis padres, porque sí he llegado hoy hasta aquí es indudablemente gracias a ellos (quizás también tendría que hacer una mención especial a los “cuadernillos Rubio”). A mi hermanísima, que aun siendo la única que tengo es mi preferida, y a Rafa, por acompañarme siempre.

Se cierra una etapa, pero se abren otras que espero que sean igual de buenas o mejores.

A mis padres y mi hermana



UNIVERSIDAD
DE MÁLAGA

Resumen	1
I. Introducción	3
II. Objetivos	6
III. Resultados & Discusión	6
III.1. Hidroxifosfonoacetatos de Metales de Transición	7
III.2. Sulfofosfonatos Metálicos	9
III.3. Trifosfonatos Lantánidos	12
III.4. Tetrafosfonatos de Metales Alcalinos y Alcalinotérreos	15
Chapter 1. Introduction	19
1.1. Coordination Polymers	21
1.2. Metal-Organic Frameworks	22
1.3. Metal Phosphonates	23
1.3.1. Multifunctional Metal Phosphonates	26
1.4. Applications	28
1.4.1. Photocatalysis	28
1.4.2. Proton Conductivity	31
1.4.3. Luminescent Sensors	39
1.4.4. Gas Adsorption and Separation	41
1.4.5. Drug Storage and Delivery	42
1.5. References	44
Chapter 2. Objectives	57
Chapter 3. Instrumental Techniques	61
3.1. C, H, N and S Elemental Analysis	63
3.1.1. Basic Principles	63
3.1.2. Instrumentation	63
3.2. Thermogravimetric and Differential Thermal Analysis (TG-DTA)	64
3.2.1. Basic Principles	64
3.2.2. Instrumentation	65
3.3. Inductively Coupled Plasma - Mass Spectrometry (ICP-MS)	65

INDEX

3.3.1. Basic Principles	65
3.3.2. Instrumentation	66
3.4. X-Ray Diffraction	66
3.4.1. Basic Principles	66
3.4.2. Single Crystal X-Ray Diffraction (SCXRD)	69
3.4.3. X-Ray Powder Diffraction (XRPD)	69
3.4.3.1. Indexing and Space Group Determination	69
3.4.3.2. Structural Resolution	70
3.4.3.3. Rietveld Refinement	71
3.4.3.4. Synchrotron X-Ray Powder Diffraction	73
3.4.4. Pair Distribution Function	73
3.4.5. Instrumentation	75
3.5. X-Ray Photoelectron Spectroscopy (XPS)	78
3.5.1. Basic Principles	78
3.5.2. Instrumentation	78
3.6. Scanning Electron Microscopy (SEM)	79
3.6.1. Basic Principles	79
3.6.2. Instrumentation	79
3.7. Fourier Transform Infrared Spectroscopy (FT-IR)	80
3.7.1. Basic Principles	80
3.7.2. Instrumentation	80
3.8. Solid State Nuclear Magnetic Resonance (Solid-state NMR)	80
3.8.1. Basic Principles	80
3.8.2. Instrumentation	82
3.9. Particle Size Distribution	83
3.9.1. Basic Principles	83
3.9.2. Instrumentation	84
3.10. Microwave-assisted Synthesis	85
3.10.1. Basic Principles	85
3.10.2. Instrumentation	86
3.11. Photoreactor	86
3.11.1. Instrument	86

3.12. Total Organic Carbon (TOC)	87
3.12.1. Basic Principles	87
3.12.2. Instrumentation	88
3.13. Impedance Spectroscopy	88
3.13.1. Basic Principles	88
3.13.2. Instrumentation	90
3.14. Photoluminescence Spectroscopy	92
3.14.1. Basic Principles	92
3.14.2. Instrumentation	93
3.15. References	93
Chapter 4. Transition Metals Hydroxyphosphonoacetates	97
4.1. Synthesis	104
4.1.1. Synthesis of $\text{Fe}[\text{HO}_3\text{PCH}(\text{OH})\text{CO}_2] \cdot 2.5\text{H}_2\text{O}$ (Fe-HPAA)	105
4.1.2. Synthesis of $\text{Zn}[\text{HO}_3\text{PCH}(\text{OH})\text{CO}_2] \cdot 2.5\text{H}_2\text{O}$ (Zn-HPAA)	105
4.1.3. Synthesis of $\text{Fe}_x\text{M}_{1-x}[\text{HO}_3\text{PCH}(\text{OH})\text{CO}_2] \cdot 2.5\text{H}_2\text{O}$ ($\text{Fe}_x\text{M}_{1-x}$ -HPAA)	106
4.2. Characterisation	106
4.2.1. Elemental, Thermogravimetric and Inductively Coupled Plasma Mass Spectrometry Analysis	106
4.2.2. Structural Characterisation	107
4.3. Post-Synthesis Modification	110
4.3.1. Ammonia Adsorption	110
4.4. Proton Conductivity	120
4.5. Photocatalytic Properties	125
4.6. Conclusions	132
4.7. References	133
Chapter 5. Metal Sulfophosphonates	139
5.1. Synthesis	146
5.1.1. Synthesis of Divalent Transition Metal Sulfophosphonates	146
5.1.2. Synthesis of Lanthanide Sulfophosphonates	150
5.2. Characterisation	151
5.2.1. Elemental Analysis and Thermal Stability	151



INDEX

5.2.2. Structural Characterisation	154
5.3. Proton Conductivity	163
5.4. Preparation and Characterisation of Composite Membranes	168
5.5. Conclusions	174
5.6. References	175
Chapter 6. Lanthanide Metals Triphosphonates	181
6.1. Synthesis	187
6.1.1. Series Ln-I	188
6.1.2. Series Ln-II	188
6.2. Characterisation	189
6.2.1. Elemental and Inductively Coupled Plasma Analysis	189
6.2.2. Structural Characterisation and Thermal/Chemical Stability	190
6.3. Proton Conductivity	209
6.4. Preparation and Characterisation of Composite Membranes	213
6.5. Luminescent Properties	219
6.6. Conclusions	222
6.7. References	223
Chapter 7. Alkali & Alkaline Earth Metals Tetrakisphosphonates	227
7.1 Synthesis	233
7.1.1. Synthesis of Alkali Metal Tetrakisphosphonates	233
7.1.2. Synthesis of Magnesium Tetrakisphosphonates	235
7.2. Characterisation	236
7.2.1. Elemental and Thermogravimetric Analysis	236
7.2.2. Structural Characterisation	238
7.2.3. Gas Adsorption Characterisation	253
7.3. Post-Synthesis Modification	255
7.4. Proton Conductivity	257
7.5. Conclusions	263
7.6. References	264

Chapter 8. Conclusions & Future Prospects	269
Capítulo 8. Conclusiones & Perspectivas Futuras	275
Appendices	283
Appendix I. Abbreviations	285
Appendix II. CHNS Elemental Analysis	289
Appendix III. Final Rietveld Plots	295
Appendix IV. Nyquist Plots	303
Appendix V. Articles	313
Appendix VI. Other Articles	367
Appendix VII. Copyright Permission	371



UNIVERSIDAD
DE MÁLAGA

Resumen



UNIVERSIDAD
DE MÁLAGA

I. Introducción

Los polímeros de coordinación (CPs) están formados por la unión de iones metálicos con ligandos mediante enlaces de coordinación, dando lugar a redes infinitas que se extienden en una, dos o tres dimensiones. El estudio de estos materiales, tanto en química como en ciencia de los materiales, ha experimentado un crecimiento exponencial debido a sus interesantes topologías y su diversidad estructural, así como sus potenciales aplicaciones en una gran variedad de campos (almacenamiento y separación de gases, luminiscencia, catálisis, conductividad, magnetismo, etc.). Además, debido a la alta cristalinidad que suelen exhibir estos materiales, se pueden establecer correlaciones entre sus propiedades y su estructura. Esto nos permite diseñar CPs para aplicaciones concretas gracias a la selección adecuada tanto del ligando orgánico como del ion metálico, así como de las condiciones de síntesis apropiadas.

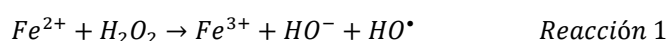
Los materiales con ensamblaje metal-orgánico (MOFs, del inglés *Metal-Organic Frameworks*) constituyen una subclase de los polímeros de coordinación, los cuales, en la mayoría de los casos, exhiben porosidad permanente. Estos materiales presentan características muy atractivas, como son un gran área superficial, gran estabilidad química, alta cristalinidad, posibilidad de ajustar el tamaño de poros y una gran versatilidad funcional, que los hacen también buenos candidatos para muy diversas aplicaciones. Después del desarrollo de MOFs empleando carboxilatos como ligandos, su preparación empleando otro tipo de grupos funcionales como pueden ser sulfonatos, fosfonatos, hidroxilos, etc. ha recibido una gran atención. En esta tesis doctoral, los fosfonatos metálicos (MPs) han sido el tema de estudio, los cuales constituyen una importante clase dentro de los CPs. En estos materiales, el ligando orgánico posee al menos un grupo fosfónico. Los enlaces M-O-P (siendo M un ion metálico) poseen una mayor estabilidad, tanto térmica como química, a la del enlace análogo en los carboxilatos metálicos (M-O-C), lo que los hace muy interesantes para el diseño de nuevos CPs. Además, el grupo fosfónico del ácido correspondiente muestra una gran versatilidad de modos de coordinación a los iones metálicos, ya que puede presentar distintos estados de protonación ($R-PO_3H_2$, $R-PO_3H$ y $R-PO_3^{2-}$, siendo R un grupo orgánico) y distintas conectividades. Esto hace que la química de los fosfonatos metálicos sea menos predecible y se puedan obtener distintas estructuras dependiendo de las condiciones de síntesis. Además, el número de posibles modos de coordinación y la disposición estructural de los ligandos puede aumentar al incorporar grupos funcionales adicionales, tales como carboxilatos,

RESUMEN

aminos, hidroxilos, sulfonatos, etc. Éstos deben ser seleccionados dependiendo de la estructura y las propiedades que se deseen en el compuesto final. Sin embargo, la adición de otros grupos funcionales hace aún menos predecible su modo de coordinación y, por ende, la estructura obtenida.

Es evidente que muchas de las aplicaciones de los fosfonatos metálicos deben estar basadas en sus características estructurales, pero, además, tratándose de sólidos metal-orgánicos, ciertas aplicaciones pueden derivar de las propiedades específicas, tanto del tipo de ion metálico como del ligando, o de ambos sinérgicamente. Una posible aplicación de los fosfonatos metálicos, de gran interés medioambiental, está relacionada con el tratamiento de aguas contaminadas, fundamentado en la combinación, en un mismo material, de un ion metálico con propiedades catalíticas y un ligando químicamente resistente en presencia de agentes fuertemente reactivos.

Los procesos avanzados de oxidación (AOPs, del inglés *Advanced Oxidation Processes*) y, dentro de estos, los procesos Fenton, constituyen una metodología apropiada para eliminar contaminantes orgánicos de aguas residuales gracias a la producción *in situ* de radicales hidroxilos que actúan como agentes oxidantes. El proceso Fenton se puede resumir en las siguientes reacciones:



Si se irradia con luz UV o visible (Proceso foto-Fenton), se puede aumentar la eficiencia de este proceso de oxidación gracias a la rápida regeneración de Fe^{2+} mediante foto-reducción de los iones Fe^{3+} , por ejemplo:



La eficiencia de estos procesos depende de diferentes parámetros, siendo el pH el más importante, debido a que determina la disponibilidad de las especies catalíticamente activas. El uso de catalizadores heterogéneos, donde el metal activo se encuentra estabilizado en su estructura, puede favorecer su aplicación en un amplio intervalo de pH. En este sentido, los MOFs han sido estudiados como

catalizadores Fenton debido a sus excelentes características (estructuras bien definidas y gran volumen de poros y de área específica).

Por otro lado, la necesidad de obtener nuevas fuentes de energías limpias, así como de reducir el empleo de combustibles fósiles, hacen que las pilas de combustible de membranas de intercambio protónico (PEMFCs, del inglés *Proton-exchange Membrane Fuel Cells*) sean una alternativa factible. Estas pilas de combustible producen energía eléctrica a partir de hidrógeno y oxígeno, los cuales son inyectados en el ánodo y el cátodo respectivamente. Ambos electrodos se encuentran separados por una membrana de electrolito polimérico, la cual permite el paso de los cationes, pero no el de los electrones. La membrana de electrolito polimérico más empleada es el Nafion®, la cual presenta altos valores de conductividad protónica, que oscilan entre 10^{-2} y 10^{-1} S·cm⁻¹ (a 60-80 °C y 98% RH), y bajos valores de energía de activación (< 0.5 eV), los cuales son típicos de un mecanismo de transporte protónico tipo Grotthuss. Sin embargo, también presenta algunas desventajas, como su alto coste y la disminución de la conductividad protónica a altas temperaturas y bajas humedades relativa, que hacen que sea necesario el desarrollo de nuevos electrolitos más baratos y con un mejor rendimiento, pudiendo operar en un mayor rango de temperaturas.

Los MOFs en general, y los fosfonatos metálicos en particular, son candidatos apropiados como conductores protónicos debido a sus propiedades inherentes. Además, la alta cristalinidad que suelen presentar estos materiales hacen que sea posible establecer una relación entre su estructura y sus propiedades. Los conductores protónicos se pueden clasificar en dos:

- (i) Conductores protónicos modulados por agua, los cuales operan a baja temperatura (20-80 °C) y dependen de los enlaces de hidrógeno creados mediante interacciones con moléculas de agua.
- (ii) Conductores protónicos anhidros, los cuales suelen operar en un rango de temperatura de 100 a 250 °C y sus conductividades dependen de la presencia de especies o sustituyentes del ligando con afinidad protónica.

Con respecto a los conductores protónicos modulados por agua, éstos pueden presentar dos mecanismos distintos de conducción:

- (i) Mecanismo Grotthuss, transporte protónico a través de una red extensa de enlaces de hidrógeno. Se caracteriza por su bajo valor de energía de activación (< 0.5 eV).

RESUMEN

- (ii) Mecanismo vehicular, implica la difusión de portadores de protones para la conducción. Ya que este mecanismo implica el movimiento de iones más grandes, la contribución de energía que requiere es mayor (> 0.5 eV).

Los CPs proporcionan también oportunidades para desarrollar nuevos materiales con ciertas propiedades ópticas. Los materiales luminiscentes son de gran interés debido a sus potenciales aplicaciones. En los CPs, esta propiedad puede ser debido al ligando orgánico, al ion metálico o a ambos. Los compuestos de elementos lantánidos han recibido mucha atención por sus propiedades luminiscentes, basadas principalmente en las transiciones electrónicas f-f, las cuales dan lugar a emisiones con un alto grado de pureza y con grandes tiempos de emisión. Entre los iones lantánidos, el europio y el terbio son los más estudiados debido a sus excelentes propiedades luminiscentes en la parte visible del espectro.

Los MOFs son también candidatos prometedores para el almacenamiento y la separación de gases debido a sus grandes áreas superficiales, así como a la posibilidad de ajustar el tamaño de sus poros. Debido a la dificultad de obtener fosfonatos metálicos microporosos, éstos no son tan empleados como los MOFs en este tipo de aplicaciones. Sin embargo, la mayoría presentan canales que pueden interactuar con adsorbatos específicos, convirtiéndolos en posibles candidatos para esta aplicación.

II. Objetivos

El objetivo principal de esta tesis doctoral se centra en la síntesis de nuevos polímeros de coordinación basados en fosfonatos multifuncionales y el estudio de sus propiedades de conductividad protónica, así como el comportamiento fotocatalítico y las propiedades luminiscentes de algunos de ellos. Además, se pretende establecer correlaciones entre estructura y propiedades, con el fin de determinar los rasgos estructurales esenciales que influyen decisivamente en sus características.

III. Resultados & Discusión

A continuación, se resumen los principales resultados obtenidos en esta investigación. Se dividen en cuatro secciones según el ligando empleado, desde un ácido multifuncional monofosfónico hasta uno tetrafosfónico.

III.1. Hidroxifosfonoacetatos de Metales de Transición

A partir de una nueva síntesis alternativa y simplificada de la ya publicada en la literatura, se han obtenido derivados de Fe(II) y Zn del ácido *R,S* 2-hidroxifosfonoacético, HPAA: $\text{Fe}[\text{HO}_3\text{PCH}(\text{OH})\text{CO}_2]\cdot 2.5\text{H}_2\text{O}$ (**Fe-HPAA**) y $\text{Zn}[\text{HO}_3\text{PCH}(\text{OH})\text{CO}_2]\cdot 2.5\text{H}_2\text{O}$ (**Zn-HPAA**). Ambos sólidos fueron ampliamente caracterizados empleando diversas técnicas, tales como DRX, análisis elemental CHN y ATD-TG, con el fin de confirmar la validez del nuevo método de síntesis. Este nuevo procedimiento de síntesis a reflujo en presencia de hierro metálico permitió reducir coste y tiempo de reacción (de 96 a 24h) y eliminar reactivos innecesarios (NaF y ácido acético). Además, también se sintetizaron las correspondientes disoluciones sólidas bimetálicas, $\text{Fe}_x\text{M}_{1-x}[\text{HO}_3\text{PCH}(\text{OH})\text{CO}_2]\cdot 2.5\text{H}_2\text{O}$ (**Fe_xM_{1-x}-HPAA**, M= Mn^{2+} , Co^{2+} o Zn^{2+}) para estudiar la influencia de otros metales de transición divalentes en sus propiedades fotocatalíticas y de conductividad protónica.

La estructura laminar de los sólidos **Fe_xM_{1-x}-HPAA** fue confirmada mediante afinamiento de Rietveld. La sustitución parcial de Fe^{2+} por Zn^{2+} dio lugar a una sutil reducción en el volumen de celda debido al menor tamaño del Zn^{2+} .

La presencia tanto de grupos ácidos como de moléculas de agua hace que estos sólidos sean buenos candidatos como conductores protónicos. Las medidas de impedancia se llevaron a cabo en un amplio rango de temperatura (80-25 °C) y 95% RH, confirmando la baja/moderada conductividad protónica de los mismos ($1.1\cdot 10^{-5}$ S·cm⁻¹ para **Fe-HPAA**, $4.7\cdot 10^{-5}$ S·cm⁻¹ para **Fe_{0.71}Zn_{0.29}-HPAA** y $9.8\cdot 10^{-6}$ S·cm⁻¹ para **Fe_{0.41}Zn_{0.59}-HPAA** a 80 °C y 95% RH). Con el fin de aumentar las propiedades de conductividad protónica de estos sólidos laminares, se llevaron a cabo modificaciones post-síntesis mediante la exposición a vapores de amoníaco (disolución acuosa de NH_3 al 14%) durante distintos tiempos (1, 5, 12, 24, 36, 42, 48 y 72h). El objetivo fue generar redes de enlaces de hidrógeno con la participación de las moléculas huéspedes de NH_3 y H_2O (**Fe-NH₃-xh** y **Fe_xZn_{1-x}-NH₃-xh**). La adsorción de amoníaco condujo a una fracción amorfa, la cual fue cuantificada mediante el método de Rietveld, empleando TiO_2 (33% w/w) como estándar interno. Esta fracción amorfa aumentó con cantidades crecientes de amoníaco adsorbido. Los compuestos **Fe-NH₃-xh** (x= 0, 36, 48 y 72h) se analizaron mediante la función de distribución de pares (*Pair Distribution Function*, PDF) con el fin de comprobar si la fracción amorfa seguía manteniendo el orden local que presenta la fase cristalina. Por una parte, la adsorción de 1.75 moles de NH_3 por fórmula en la muestra **Fe-NH₃-72h** resultó en una

RESUMEN

amorfización total de la muestra, con pérdida del orden atómico a distancias mayores de 5 Å. Por otro lado, la fase cristalina presente en los sólidos **Fe-NH₃-36h** y **Fe-NH₃-48h** se corresponde con una fracción microcristalina del sólido sin reaccionar. Esto se pudo comprobar debido a que los parámetros de celda permanecieron prácticamente inalterados en la región de 10 a 50 Å. Sin embargo, las distancias P-O, Fe-O y Fe-P (1.55, 2.14 y 3.29 Å respectivamente) fueron bastante similares para todas las muestras. Esto nos indica que el entorno local del hierro se preservó tras la exposición a amoníaco. Tanto las curvas de ATD-TG, en las que se observa un comportamiento térmico similar, como la obtención del mismo producto (Fe₂P₂O₇) al pirolizar las muestras **Fe-NH₃-0h** y **Fe-NH₃-72h** a 700 °C en atmósfera de N₂, son evidencias adicionales de que la integridad del fosfonato de Fe(II) se mantiene. En relación con las medidas de impedancia tanto de **Fe-NH₃-xh** como de las muestras **Fe_xZn_{1-x}-NH₃-xh**, se observó un aumento gradual de casi dos órdenes de magnitud de la conductividad protónica al aumentar el contenido de amoníaco (Tabla 1). Cabe resaltar que las muestras con el mismo contenido en moléculas de NH₃ y H₂O, como **Fe-NH₃-72h** y **Fe_{0.71}Zn_{0.29}-NH₃-5h**, presentan una conductividad protónica equivalente. Por tanto, estas especies huéspedes son determinantes para la conductividad protónica del material, que se puede atribuir a la formación de trayectorias de transferencia protónica más eficientes. Los valores de energía de activación para todas estas muestras, determinados a partir del gráfico de Arrhenius, son indicativos de un mecanismo de transferencia de protones tipo Grotthuss.

Tabla 1. Valores de conductividad protónica a 80 °C y 95% RH, de energía de activación y contenido en H₂O/NH₃.

Compuesto	x (h)	σ (S·cm ⁻¹)	Ea (eV)	Contenido de H ₂ O/NH ₃ (mol/formula)
Fe-NH₃-xh	0	1.1·10 ⁻⁵	0.36	2.5/0
	72	1.8·10 ⁻³	0.45	3/1.2
Fe_{0.71}Zn_{0.29}-NH₃-xh	0	4.7·10 ⁻⁵	0.41	2.5/0
	5	1.3·10 ⁻³	0.43	3/1.1
Fe_{0.41}Zn_{0.59}-NH₃-xh	0	9.8·10 ⁻⁶	0.44	3/0
	1	1.5·10 ⁻⁴	0.57	2.5/0.75

Por otro lado, se investigaron también las propiedades fotocatalíticas del **Fe-HPAA** y de las disoluciones sólidas **Fe_xM_{1-x}-HPAA** para la degradación de fenol, 4-clorofenol y azul de metileno (MB), contaminantes recalcitrantes muy comunes en aguas residuales. En una publicación previa se demostró que el ligando en el compuesto **Fe-HPAA** es resistente en las condiciones de reacción.

Los ensayos fotocatalíticos se llevaron a cabo bajo radiación UV-A y/o visible en un reactor fotocatalítico Luzchem CCP-4V. El primer paso fue el pretratamiento del catalizador con el fin de mejorar su eficiencia. Por esta razón, al catalizador se irradió usando 6 lámparas (8 W) UV-A junto con una pequeña cantidad de H₂O₂ (50 mg·L⁻¹) durante 30 minutos. Posteriormente, el ensayo se llevó a cabo bajo radiación visible (14 lámparas) o UV-A (6 lámparas), para los ensayos con fenol y 4-clorofenol, a un pH inicial de 4.0 y adicionando 500 mg·L⁻¹ de H₂O₂. Cuando el contaminante fue MB, el procedimiento fue el mismo exceptuando que no se realizó pretratamiento y se empleó radiación UV-A (14 lámparas). La fotodegradación de los contaminantes se siguió mediante la medida del Carbono Orgánico Total (TOC), la valoración iodométrica del consumo de H₂O₂ y la determinación de la cantidad disuelta de iones metálicos y fósforo lixiviado, por ICP-MS.

Al comparar las fuentes de luz empleadas, para la fotodegradación del fenol y del 4-clorofenol, se observó que con luz UV-A se lograban porcentajes de eliminación más altos en tiempos cortos de reacción (~68% en 30 min y 87% en 50 min para el fenol y 4-clorofenol respectivamente). Sin embargo, a mayores tiempos de reacción, los porcentajes de eliminación tienden a ser equivalentes en ambas condiciones (~89% en 180 min y 93% en 240 min para el fenol y 4-clorofenol respectivamente). Para la degradación del fenol bajo radiación visible, las disoluciones sólidas (**Fe_{0.8}Mn_{0.2}**, **Fe_{0.78}Co_{0.22}** o **Fe_{0.71}Zn_{0.29}-HPAA**), mostraron un comportamiento equivalente al del **Fe-HPAA**. En ausencia de luz, no se apreció degradación del fenol, confirmando la actividad foto-Fenton de los catalizadores. Para la fotodegradación del MB, el **Fe-HPAA** mostró los mejores resultados bajo radiación UV-A (~75% en 30 min), mientras que al utilizar **Fe_{0.71}Zn_{0.29}-HPAA** esta reacción fue más lenta inicialmente, pero se alcanzaron porcentajes similares de eliminación al cabo de 180 minutos.

Estos resultados se han publicado en Salcedo et al., 2020 (Anexo V, artículo #1).

III.2. Sulfofosfonatos Metálicos

El ácido 2-[bis(fosfonometil)amino]-etanosulfónico, H₂SP, es el ácido sulfofosfónico que se ha empleado para la síntesis de sulfofosfonatos de metales de

RESUMEN

transición divalentes (Mn, Zn) y sulfosfonatos lantánidos. Este ácido es altamente higroscópico y por ello se emplearon, en su lugar, las sales triamónica, $(\text{NH}_4)_3\text{H}_2\text{SP}$, y pentasódica, Na_5SP . Como metodologías de síntesis, se eligieron procesos hidro-/solvotermiales y síntesis asistida por microondas. Para las reacciones hidro- y solvotermiales, se usó un procedimiento de síntesis en paralelo (“high-throughput”) con objeto de optimizar las condiciones de preparación. Para el zinc, se estudiaron dos relaciones molares $\text{Zn}^{2+}:(\text{NH}_4)_3\text{H}_2\text{SP}$ (1:2 y 1.4:1) así como diferentes mezclas de disolventes: etanol/ H_2O (1:5 y 2:5 v/v) o isopropanol/ H_2O (1:5 y 2:5 v/v). La optimización de estos parámetros permitió aislar dos derivados cristalinos: $\text{Zn}_2[(\text{O}_3\text{PCH}_2)_2\text{-NH-(CH}_2)_2\text{-SO}_3]\text{Zn}_{0.4}[(\text{O}_3\text{PCH}_2\text{-NH-CH}_3)]_{0.4}(\text{NH}_3)_2\cdot 4\text{H}_2\text{O}$ (***m-Zn₂HSP***) y $\text{Zn}_2[(\text{O}_3\text{PCH}_2)_2\text{-NH-(CH}_2)_2\text{-SO}_3]\cdot 7\text{H}_2\text{O}$ (***h-Zn₂HSP***). El derivado de manganeso, $\text{Mn}_2[(\text{O}_3\text{PCH}_2)_2\text{-NH-(CH}_2)_2\text{-SO}_3]\cdot 3\text{H}_2\text{O}$ (***o-Mn₂HSP***), se obtuvo por ambos métodos de síntesis, empleando una relación Mn^{2+} :ligando 1.4:1 y un intervalo de pH entre 2.5 y 4.5. La síntesis por microondas permitió reducir los tiempos de reacción de 96 a 1h. En cuanto a los derivados lantánidos, se estudiaron diversos parámetros como la relación molar $\text{Ln}^{3+}:(\text{NH}_4)_3\text{H}_2\text{SP}$ o $\text{Ln}^{3+}:\text{Na}_5\text{SP}$ (1:1, 1:2, 2:1 y 1.5:1), el pH inicial (de 0.5 a 4.0), la temperatura (140 y 160 °C) y los disolventes empleados (H_2O o mezcla $\text{H}_2\text{O}:\text{EtOH}$, 3:1, 1:1 y 1:3). Finalmente, se obtuvieron dos fases cristalinas, con fórmula $\text{Ln}[\text{H}(\text{O}_3\text{PCH}_2)_2\text{-NH-(CH}_2)_2\text{-SO}_3]\cdot 2\text{H}_2\text{O}$ (***m-LaH₂SP*** o ***o-LnH₂SP***, Ln= Pr, Nd, Sm, Eu, Gd y Tb), a 140 °C usando una relación molar $\text{Ln}^{3+}:(\text{NH}_4)_3\text{H}_2\text{SP}$ o Na_5SP 2:1, pH < 2.0 y H_2O como disolvente. El sólido ***o-EuH₂SP*** también se obtuvo por síntesis asistida por microondas.

Las estructuras cristalinas de los sólidos ***o-Mn₂HSP***, ***m-LaH₂SP***, ***o-PrH₂SP*** y ***o-SmH₂SP*** se resolvieron mediante metodología *ab initio* a partir de datos de difracción de rayos-X de polvo, tomados en la línea BLO4-MSPD del sincrotrón ALBA (Barcelona). La estructura cristalina del ***o-SmH₂SP*** se utilizó como modelo inicial para los afinamientos de Rietveld de los restantes compuestos ***o-LnH₂SP***. En cambio, para los derivados de zinc, ***m-Zn₂HSP*** y ***h-Zn₂HSP***, los cuales se indexan en el sistema monoclinico y hexagonal respectivamente, no se ha podido resolver sus estructuras.

o-Mn₂HSP y ***o-LnH₂SP*** son compuestos laminares que cristalizan en el sistema cristalino ortorrómbico. En ambos casos, el grupo sulfonato queda libre de unión al ion metálico y se encuentra orientado hacia el espacio interlaminar. Por otra parte, ***m-LaH₂SP*** cristaliza en el sistema monoclinico. En este caso, el sólido también presenta un entramado laminar, pero con el grupo sulfonato coordinado al ion lantánido.

Con el fin de evaluar el efecto de la conectividad del ligando y la contribución de los restantes grupos ácidos en la conductividad protónica de estos materiales, se han llevado a cabo medidas de impedancia en un amplio rango de temperatura (25-80 °C) y humedad relativa (70, 75, 85, 90 y 95%). Los valores de conductividad más altos corresponden a los derivados de zinc ($\sim 10^{-2}$ S·cm⁻¹ a 80 °C y 95% RH). La diferencia entre la conductividad protónica de los derivados de Zn y ***o*-Mn₂HSP** ($7.3 \cdot 10^{-4}$ a 80 °C y 95% RH) podría deberse al mayor contenido en agua de los primeros, lo que puede favorecer a la formación de redes de enlaces de hidrógeno más eficientes para el transporte protónico.

Entre los derivados lantánidos, la mayor conductividad protónica corresponde al derivado de samario ($\sim 10^{-3}$ S·cm⁻¹ a 80 °C y 95% RH). El compuesto de manganeso, que también se caracteriza por presentar el grupo sulfónico libre, muestra un valor similar, lo que lleva a pensar que este grupo, -SO₃(H), tiene un papel relevante en la formación de trayectorias de transferencia de protones eficientes, por su capacidad para establecer extensas redes de enlace de hidrógeno. Las diferencias encontradas en los valores de conductividad protónica entre ***o*-SmH₂SP** y ***m*-LaH₂SP** ($1.2 \cdot 10^{-4}$ S·cm⁻¹ a 80 °C y 95% RH) se pueden, en principio, explicar del mismo modo. Sin embargo, el hecho de que la conductividad protónica de los restantes ***o*-LnH₂SP** sea similar a la exhibida por el ***m*-LaH₂SP** indica que esta propiedad es una combinación de varios factores y no depende exclusivamente de la estructura cristalina. Los valores de energía de activación encontrados en estos materiales fueron típicos de un mecanismo tipo Grotthuss.

Entre los derivados lantánidos, se seleccionó el ***o*-SmH₂SP** para la preparación de membranas mixtas derivadas de Nafion, empleado como matriz polimérica debido a sus buenas propiedades como conductor protónico. Se prepararon membranas mixtas conteniendo un 3 y 5% en peso de ***o*-SmH₂SP** (**Nafion/SmH₂SP-X**, siendo X el porcentaje de ***o*-SmH₂SP** incorporado). Los estudios preliminares de preparación y caracterización de las membranas mixtas se llevaron a cabo en colaboración con el Instituto de Ciencias y Tecnología de Polímeros, ICTP-CSIC (Madrid). Mediante difracción de rayos-X se pudo demostrar que el compuesto ***o*-SmH₂SP** se incorporó en la matriz polimérica. Además, mediante SEM-EDS se pudo comprobar que la distribución de partículas submicrométricas de ***o*-SmH₂SP** dentro de la matriz de Nafion era uniforme, aunque también se observaron la formación de agregados de partícula, especialmente en el caso de **Nafion/SmH₂SP-5**. Las medidas de adsorción

RESUMEN

de agua pusieron de manifiesto una menor capacidad de adsorción con respecto a la membrana de Nafion al aumentar la carga de **o-SmH₂SP**.

Para determinar su rendimiento en condiciones de operación usuales para las pilas de combustible (PEMFCs) se realizaron ensamblajes membrana-electrodo (*Membrane Electrode Assemblies*, MEAs) con las membranas preparadas. En cuanto a la conductividad protónica, en un intervalo de temperatura de 70 a 90 °C y 100% RH, se observaron cambios significativos en comparación con el comportamiento de la membrana de Nafion sin modificar, ya que en ésta decae la conductividad en el rango de temperatura de 70 a 90 °C, mientras que en las membranas compuestas **Nafion/SmH₂SP-X** no se observó este comportamiento ($2.76 \cdot 10^{-2}$ y $2.61 \cdot 10^{-2}$ S·cm⁻¹ a 90 °C para **Nafion/SmH₂SP-3** y **Nafion/SmH₂SP-5**, respectivamente). Esto se puede explicar por la presencia de partículas hidrofílicas del sulfofosfonato lantánido, el cual mantiene el grado de hidratación de las membranas en un mayor intervalo de temperatura.

Al comprobar su comportamiento en sistemas PEMFCs a 80 °C, 100% RH y presión atmosférica, se observó que ambas membranas mixtas, **Nafion/SmH₂SP-3** y **Nafion/SmH₂SP-5**, funcionaban adecuadamente. Cabe destacar que la incorporación del 3% de **o-SmH₂SP** en la matriz de Nafion mejora el comportamiento electroquímico de la membrana de Nafion pura, alcanzando una densidad de corriente máxima de 3300 mA·cm⁻² y una densidad de potencia máxima de 946 mW·cm⁻² (2900 mA·cm⁻² y 923 mW·cm⁻², respectivamente, para la membrana de Nafion pura). Este comportamiento puede explicarse debido a la mejor dispersión del **o-SmH₂SP** en la matriz de Nafion, lo que también resulta en una mayor adsorción de agua con respecto a la membrana **Nafion/SmH₂SP-5**. Por lo tanto, estas membranas mixtas son buenas candidatas para su empleo como electrolitos en PEMFCs. Sin embargo, sería necesario realizar un trabajo adicional para mejorar algunas de sus características.

Algunos de estos resultados ya han sido publicados en Bazaga-García et al., 2019 (Anexo V, artículo #2), mientras que otros están pendientes de publicación.

III.3. Trifosfonatos Lantánidos

Se han sintetizado dos series polimórficas de derivados de lantánidos del ácido comercial aminotris(metilenfosfónico), H₆NMP, en las que se incorpora también sulfato con diversas funciones estructurales. Mediante cristalización controlada a 25 °C se aislaron los sólidos: {Ln₂[HN(CH₂)₃(PO₃H)₃]₂(H₂O)₄}(HSO₄)₂·nH₂O (Ln= Pr, Nd, Sm, Eu, Gd, Tb, Er, Yb; n= 4-5), **Ln-I**, y Ln[HN(CH₂)₃(PO₃H₂)(PO₃H)₂]SO₄·2H₂O (Ln= Pr, Nd, Eu,

Gd, Tb), **Ln-II**. Estas dos familias se prepararon acorde a las relaciones molares $\text{Ln}^{3+}:\text{H}_6\text{NMP}:\text{H}_2\text{SO}_4:\text{H}_2\text{O}$ empleadas: desde 1:5:19.3:3715 hasta 1:5:135:3715 para los derivados de la Serie **Ln-I**, y 1:5:193:3715 para los derivados de la Serie **Ln-II**.

Las estructuras cristalinas de los sólidos **Nd-I**, **Sm-I** y **Tb-I** se han resuelto mediante difracción de rayos-X de monocristal, mientras que la de los restantes compuestos de la Serie **Ln-I** se obtuvieron mediante afinamiento de Rietveld a partir de datos de difracción de polvo de laboratorio. Estos sólidos laminares cristalizan en el grupo espacial $P 2_1/c$ y su estructura cristalina es equivalente a la que exhibe el sólido $[\text{Ln}(\text{H}_4\text{NMP})(\text{H}_2\text{O})_2]\text{Cl}\cdot 2\text{H}_2\text{O}$. En este caso, es el ion hidrogenosulfato el que, como lo hacía el ion cloruro, actúa de compensador de la carga positiva de las láminas formadas por poliedros LnO_8 aislados y enlazados a través de los grupos fosfónicos del ligando. El ion hidrogenosulfato se sitúa en el espacio interlamina, interactuando mediante enlaces de hidrógeno con las moléculas de agua, tanto de coordinación como de cristalización, y con los átomos de oxígeno de los grupos fosfonatos. Estas interacciones crean redes de enlaces de hidrógeno que se extienden unidireccionalmente y que los hacen excelentes candidatos como conductores protónicos. Sin embargo, los sólidos de la Serie **Ln-I** experimentan cambios estructurales irreversibles al aumentar la temperatura de 25 a 80 °C a alta humedad relativa (95% RH), acompañados por la pérdida parcial de hidrogenosulfato, y dando lugar a los sólidos de composición $\{\text{Ln}_2[\text{HN}(\text{CH}_2)_3(\text{PO}_3\text{H})_3]_2(\text{H}_2\text{O})_3\}(\text{SO}_4)\cdot n\text{H}_2\text{O}$ (**SD-Ln-I**, Ln= Pr, Nd, Eu, Gd y Tb; n= 4-5). De acuerdo con los resultados de análisis elemental y difracción de rayos-X, la composición de estos derivados, **SD-Ln-I**, concuerda con la publicada para el derivado de lantano, $[\text{La}_2(\text{H}_4\text{NMP})_2(\text{H}_2\text{O})_m(\text{SO}_4)]\cdot n\text{H}_2\text{O}$ (n=1,2, 6 u 8; m= 2 o 3). Por tanto, la disolución parcial del sólido en estas condiciones no implica un cambio en la carga ni en la conectividad del ligando, sino simplemente una conversión del ion HSO_4^- a ion SO_4^{2-} . Por el contrario, para el derivado de Yb se observó la pérdida total de sulfato, tal y como se observó para el compuesto isorecticular $[\text{Ln}(\text{H}_4\text{NMP})(\text{H}_2\text{O})_2]\text{Cl}\cdot 2\text{H}_2\text{O}$. Además, la deshidratación de los compuestos de la Serie **Ln-I** a 230 °C durante 2h permitió obtener una nueva fase cristalina anhidra: $\text{Ln}_2[\text{HN}(\text{CH}_2)_3(\text{PO}_3\text{H})_3]_2(\text{HSO}_4)_2$ (**Ln-I-230**). La resolución estructural de la fase anhidra permitió comprobar que el ion hidrogenosulfato se coordina, mediante uno de sus átomos de oxígeno, al lantánido tras el proceso de deshidratación. Cabe destacar que este proceso permite estabilizar la cantidad inicial de sulfato presente en la estructura.

RESUMEN

Por otro lado, la estructura cristalina de los derivados de la Serie **Ln-II**, fue resuelta empleando métodos directos a partir de datos de difracción de polvo. Estos sólidos bidimensionales cristalizan en el grupo espacial triclinico $P\bar{1}$. Sus láminas están formadas por dímeros de Ln_2O_{14} que comparten aristas, interconectados por iones sulfatos que actúan como puente. Su estabilidad térmica fue estudiada mediante termodifracción de rayos-X, así como mediante análisis termogravimétrico. Estos compuestos son estables hasta 140 °C, a partir de la cual empiezan a amorfizarse por deshidratación. A diferencia de los sólidos de la Serie **Ln-I**, estos compuestos se mantienen estables a 80 °C y 95% RH.

La conductividad protónica de los compuestos **SD-Ln-I**, **Ln-I-230** y **Ln-II** fue estudiada a distintas humedades (75 y 95% RH) debido a la presencia en sus estructuras de redes de enlaces de hidrógeno. Todos los sólidos mostraron excelentes propiedades como conductores protónicos, con valores comprendidos entre $1.1 \cdot 10^{-3}$ y $3.6 \cdot 10^{-2} \text{ S} \cdot \text{cm}^{-1}$ a 80 °C y 95% RH. Estos valores son muy similares a los exhibidos por Nafion® y mayores al encontrado para el compuesto isorecticular $[\text{Gd}(\text{H}_4\text{NMP})(\text{H}_2\text{O})_2]\text{Cl} \cdot 2\text{H}_2\text{O}$ ($3 \cdot 10^{-4} \text{ S} \cdot \text{cm}^{-1}$ a 80 °C y 95% RH). Este resultado es compatible con la mayor capacidad de los iones sulfatos para establecer interacciones de enlaces de hidrógeno con las especies disponibles. Los valores de energía de activación de estos compuestos indican que el mecanismo de transporte protónico es tipo Grotthuss.

En vista de las excelentes propiedades de conductividad protónica de todos estos sólidos, se llevó a cabo un estudio preliminar de la preparación y caracterización de membranas mixtas para su uso en PEMFCs. Para ello, se seleccionaron los sólidos **Eu-I-230**, **SD-Eu-I** y **Tb-II** como muestras representativas de ambas series, utilizando una carga del 3 % en peso y Nafion como matriz polimérica (**Nafion/Eu-I-230**, **Nafion/SD-Eu-I** y **Nafion/Tb-II**). Estas membranas mixtas mostraron un comportamiento muy similar al de la membrana de Nafion pura, produciéndose un pequeño decaimiento en la conductividad protónica a 90 °C debido a la pérdida del grado de hidratación óptimo de la membrana. Además, también se evaluaron como membranas de intercambio protónico en PEMFCs a distintas temperaturas (70, 80 y 90 °C) y 100% RH. Tanto **Nafion/Eu-I-230** como **Nafion/SD-Eu-I** y **Nafion/Tb-II** mejoraron las propiedades electroquímicas de la membrana de Nafion a 70 °C, mientras que a 80 y 90 °C se observaron características similares para las membranas de **Nafion/Eu-I-230**, **Nafion/SD-Eu-I** y de Nafion puro. Por otro lado, **Nafion/Tb-II** mostró los mejores resultados de densidad de corriente (3800 mA·cm

²) y potencia (1007 mW·cm⁻²) en todo el intervalo de temperatura, siendo estos valores superiores a los obtenidos para la membrana de Nafion. Actualmente se están realizando estudios adicionales para estas membranas mixtas.

Finalmente, se prepararon disoluciones sólidas bimetálicas de la Serie **Ln-I** (**Eu_{1.6}Tb_{0.4}-I** and **Tb_{1.6}Eu_{0.4}-I**) con el fin de estudiar sus propiedades luminiscentes. Para estos sólidos, la emisión es debida exclusivamente a los iones lantánidos, ya que ni el H₆NMP ni el HSO₄⁻ o SO₄²⁻ son responsables de la emisión de luz.

Todos estos resultados expuestos en esta sección están pendientes de publicación.

III.4. Tetrafosfonatos de Metales Alcalinos y Alcalinotérreos

Se han aislado derivados alcalinos (Li⁺, Na⁺, K⁺, Rb⁺ y Cs⁺) y de magnesio del ácido tetrafosfónico hexametilendiamina-N,N,N',N'-tetrakis(metilenfosfónico), HDTMP. Los derivados alcalinos se prepararon por cristalización a temperatura ambiente, empleando etanol como codisolvente para facilitar la cristalización en la capa H₂O/EtOH. La fórmula general de estos compuestos es:

Li₂(HO₃PCH₂)₂NH(CH₂)₆NH(CH₂PO₃H)₂·4H₂O, (Li-HDTMP-4W),
 Na₂(HO₃PCH₂)₂NH(CH₂)₆NH(CH₂PO₃H)₂·6H₂O (Na-HDTMP),
 K₂(HO₃PCH₂)₂NH(CH₂)₆NH(CH₂PO₃H)₂·8H₂O (K-HDTMP),
 Rb(H₂O₃PCH₂)₂NH(CH₂)₆NH(CH₂PO₃H)₂(H₂O)₂·2H₂O (Rb-HDTMP) y
 Cs(H₂O₃PCH₂)₂NH(CH₂)₆NH(CH₂PO₃H)₂(H₂O)₂·2H₂O (Cs-HDTMP). Además, una nueva fase cristalina anhidra se obtuvo al calentar el derivado de litio, Li-HDTMP-4W, a 200 °C durante 2h, Li-HDTMP-0W.

Las condiciones óptimas de síntesis de los derivados de magnesio se establecieron siguiendo una metodología de síntesis en paralelo o "*high-throughput*". Tras la optimización de los diferentes parámetros de síntesis se aislaron dos fases cristalinas: {Mg[(HO₃PCH₂)₂NH(CH₂)₆NH(CH₂PO₃H)₂·H₂O]_n} (Mg-HDTMP-1) y {Mg[(HO₃PCH₂)₂NH(CH₂)₆NH(CH₂PO₃H)₂]_n} (Mg-HDTMP-2). Además, una tercera fase anhidra fue obtenida al calentar el Mg-HDTMP-1 a 180 °C, Mg-HDTMP-1deh. El sólido Mg-HDTMP-1 solo fue obtenido mediante reacción hidrotermal a 140 °C durante 7 días, utilizando una relación molar Mg:HDTMP 1:2 y un pH de 1. Por otro lado, el compuesto Mg-HDTMP-2 se obtuvo tanto por reacción hidrotermal (relación molar Mg:HDTMP 1:2.8, 180 °C, 5 días) como por reacción solvotermal (mezcla DMF/H₂O 2:1 v/v, relación molar Mg:HDTMP 1:4, 130 °C, 3 días) a un pH óptimo de 2.1. Con el fin de reducir los tiempos de reacción, el mismo procedimiento se llevó a cabo

RESUMEN

mediante síntesis asistida por microondas, lo que permitió la preparación de ambos sólidos en 30 minutos y condujo además a un aumento de los rendimientos de la reacción.

La estructura cristalina de los derivados alcalinos se resolvió mediante difracción de rayos-X de monocristal, excepto en el caso del **Li-HDTMP-0W**, cuya estructura cristalina fue resuelta mediante datos de difracción de rayos-X de polvo tomados con radiación sincrotrón. Estos compuestos muestran una gran diversidad estructural, la cual depende del tamaño del catión, obteniéndose entramados desde monodimensionales (Li^+ y Na^+), pasando por laminares (K^+), hasta sólidos laminares pilareados (Rb^+ y Cs^+). Destacar que la deshidratación del compuesto de litio, **Li-HDTMP-0W**, conlleva un aumento en la dimensionalidad del sólido (2D) siendo éste un proceso reversible para dar nuevamente el sólido **Li-HDTMP-4W** bajo condiciones ambiente o bien, de manera más rápida, a 80 °C y 95% RH.

La estructura cristalina de los derivados de magnesio **Mg-HDTMP-1** y **Mg-HDTMP-2** se resolvió mediante metodología *ab initio* utilizando datos de difracción de polvo de laboratorio, mientras que la estructura del **Mg-HDTMP-1deh** fue resuelta empleando la estructura $\text{Mg-ODTMP}\cdot 2\text{H}_2\text{O}\cdot (\text{DMF})_{0.5}$ previamente publicada como modelo de partida, debido a sus similitudes en los parámetros de la celda unidad y grupo espacial. Todos los derivados de magnesio presentan estructuras laminares pilareadas.

Las propiedades texturales de los sólidos **Mg-HDTMP-1** y **Mg-HDTMP-2** fueron analizadas mediante isothermas de adsorción de N_2 y CO_2 las cuales evidenciaron bajas áreas superficiales con una capacidad de adsorción de CO_2 de 0.105 y 0.05 $\text{mmol}\cdot\text{g}^{-1}$ respectivamente. Por otro lado, el sólido **Mg-HDTMP-1deh** se comportó como un sólido sensible a moléculas huésped tras la adsorción de CO_2 a alta presión (10.5 bar).

También se han evaluado las propiedades como conductores protónicos de los tetrafosfonatos alcalinos y de magnesio no higroscópicos (**Li-HDTMP-4W**, **Mg-HDTMP-1** y **Mg-HDTMP-2**) debido a la presencia en sus estructuras cristalinas de redes de enlaces de hidrógeno. Para estos compuestos también se determinaron sus propiedades de conductividad tras ser expuestos a vapores de amoníaco (disolución acuosa de NH_3 14%) con el fin de correlacionar sus propiedades de conductividad protónica con los cambios estructurales producidos tras la adsorción. Sin embargo, todas las muestras que contenían amoníaco resultaron ser altamente higroscópicas a alta humedad relativa. Los sólidos **Li-HDTMP-4W** y **Mg-HDTMP-1** exhibieron de

moderados a bajos valores de conductividad protónica ($7.6 \cdot 10^{-4} \text{ S} \cdot \text{cm}^{-1}$ y $1.6 \cdot 10^{-5} \text{ S} \cdot \text{cm}^{-1}$ a $80 \text{ }^\circ\text{C}$ y $95\% \text{ RH}$, respectivamente), los cuales aumentaron en casi un orden de magnitud tras el proceso reversible de deshidratación/rehidratación ($4.4 \cdot 10^{-3} \text{ S} \cdot \text{cm}^{-1}$ y $6.6 \cdot 10^{-5} \text{ S} \cdot \text{cm}^{-1}$ a $80 \text{ }^\circ\text{C}$ y $95\% \text{ RH}$, respectivamente). La caracterización completa de estos sólidos tras la medida de impedancia (ATD, tamaño medio de partícula y ^1H -MAS-NMR de sólidos) sugirió que el incremento observado en la conductividad protónica podría atribuirse a pequeños cambios en las redes de enlaces de hidrógeno formados tras la rehidratación.

Todos estos resultados están publicados en Salcedo et al., 2018 (Anexo V, artículo #3) y Colodrero et al., 2018 (Anexo V, artículo #4).



UNIVERSIDAD
DE MÁLAGA

Chapter 1

Introduction



UNIVERSIDAD
DE MÁLAGA

1.1. Coordination Polymers

Coordination polymers (CPs) have become an active topic in chemistry and materials science due to the extensive variety of their applications. CPs are built up from metal ions linked by ligands into an infinite array leading to one-, two- and three-dimensional networks (Batten et al., 2013; Figure 1.1). This infinite network is defined by coordination bonds, which are highly specific and directional as well as stronger enough to provide robust materials (Batten, Neville & Turner, 2008). Although CPs consist essentially of metals and ligands, they can also include other auxiliary components, such as guest molecules or counterions (Kitagawa et al., 2004).

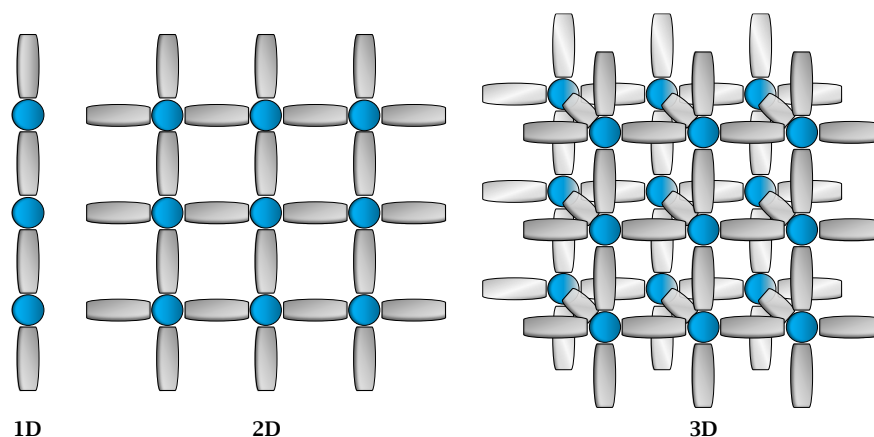


Figure 1.1. Example of 1D, 2D and 3D coordination polymers.

Crystal engineering of CPs involves a careful selection of organic ligands and metal ions as well as suitable synthetic conditions to obtain desirable structures for certain applications (Moorthy & Vittal, 2006). Depending on the metal ion employed and its valence, it will give rise to different geometries (linear, trigonal-planar, tetrahedral, square-planar, etc.) (Morsali & Hashemedi, 2017). Transition metals have been widely employed due to the more predictable nature of their coordination geometries, with coordination numbers up to seven, or in the case of lanthanide ions, up to ten, leading to polyhedral geometries and obtaining interesting topologies (Batten et al., 2008; Kitagawa, Kitaura & Noro, 2004). Furthermore, lanthanide ions exhibit inherent interesting properties such as luminescence (Firmino et al., 2017a; Liu et al., 2020) and unsaturated ion centres can be generated by the removal of coordinated solvent molecules, making them suitable for chemical adsorption,

CHAPTER 1

heterogeneous catalysis and sensors (Pan et al., 2003; Kitagawa, Kitaura & Noro, 2004). On the other hand, it is also important the selection of the organic ligands, which can have particular functional groups and coordination sites, since changes in flexibility, length and symmetry can lead in a wide range of diverse architectures for different functions (Morsali & Hashemedi, 2017). Different conformations of the ligands can lead to a variety of symmetries and connection modes, which can be determined by the synthetic conditions. For that reason, changes on pH values, temperature, pressure, solvents, etc. can lead to a variety of structures for a given set of metal ions and organic ligands (Hong & Chen, 2009; Kerr et al., 2019). In addition, the ligand that is forming part of the CP can respond to external stimuli such as pressure, temperature or guest molecules to change their conformations, triggering the structure transformation and dynamic behaviours of the CPs (Li et al., 2018).

The great attention on CPs is due to their intriguing topologies and diverse structures as well as their potential applications in gas storage/separation (Li et al., 2019a), luminescent materials (Firmino et al., 2017a; Li et al., 2020; Liu et al., 2020), catalysis (Gu et al., 2019; Sang et al., 2020), magnetics (Feng et al., 2019a; Liang et al., 2019), conductivity (Shigematsu, Yamada & Kitagawa, 2011), etc. In addition, structure-properties relationship can be studied, allowing to design the CPs for desired applications.

1.2. Metal-Organic Frameworks

Metal-organic frameworks (MOFs), also known as porous coordination polymers (PCPs), are infinitely extending networks built up by coordination assembly between metal ions or clusters and organic ligands, exhibiting potential voids. MOFs are a subclass of coordination polymers, on the basis of compounds exhibiting porosity (Batten et al., 2013).

MOFs can exhibit robust structures with homogeneous porosity or, conversely, flexible and dynamic behaviour to external stimuli. The main dynamic behaviours in MOFs are (Schneemann et al., 2014): (i) breathing and swelling phase transitions, which involve changes in unit cell volume, (ii) subnetwork displacement and (iii) ligands rotation. The modularity of synthetic components in MOFs provides the scope to optimize for the desired dynamic behaviour (Peh, Karmakar & Zhao, 2019).

MOFs have attractive characteristics, such as large surface area, good chemical stability, tuneable pore sizes, high crystallinity and versatile functionality, making them potential candidates for a wide variety of applications, such as gas storage and

selective separation (Li et al., 2019b), catalysis (Corma, García & Lladrés i Xamena, 2010; Puthiaraj & Ahn, 2020), fluorescence sensing (Chen et al., 2020), drug delivery (Orellana-Tavra et al., 2020) and conductors (Deng et al., 2020).

Upon the development of stable frameworks based on carboxylate ligands (Xie et al., 2020), the study of MOFs preparation using ligands based on other donor groups, such as sulfonates, phosphonates, hydroxyl etc., has received great attention (Natarajan & Mahata, 2009).

1.3. Metal Phosphonates

Metal phosphonates (MPs) constitute an important class within CPs. They are made of a metal ion and an organic ligand that possess a phosphonic group. The phosphonic acid group is a pentavalent, tetrahedral P atom connected via a double bond with one O atom (P=O) and via single bonds with two OH groups. The P atom is also connected via single bond to a C atom (P-C) from an aliphatic or aromatic organic group (R), which may have other functional groups such as amino, hydroxyl, carboxylate, sulfonate, etc. (Brunet, Colón & Clearfield, 2015; Figure 1.2).

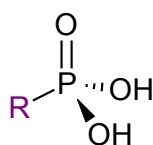
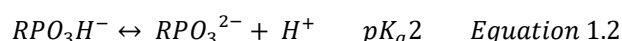
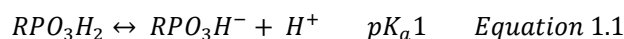


Figure 1.2. A representation of phosphonic acids.

The synthesis of phosphonic acid ligands is carried out by well-established reactions, such as the Michaelis-Arbuzov reaction or the Mannich reaction (Zon, Garczarek & Bialek, 2012; Firmino et al., 2018). This phosphonic acid moiety shows versatile coordination modes due to it has three oxygen atoms that can bind up to metal ions as well as different states of protonation that influences its coordinative properties. In solution, phosphonic acids can dissociate releasing one or two protons. The pK_a values also depend on the backbone of the phosphonic acid molecule and the presence of other functional groups. However, the first proton exhibits very high acidity ($pK_{a1} < pK_{a2}$). This allows synthesising a variety of potential novel phosphonate-containing structures, by simply varying the pH (Brunet, Colón & Clearfield, 2015).

CHAPTER 1



M-O-P bonds exhibit high thermal and chemical stability, making phosphonic groups very interesting for design new CPs. Water stability of metal phosphonates depends on the metal ion valence, increasing with higher valences.

The first metal phosphonates were reported by Alberti and co-workers in 1978 (Alberti et al., 1978): (1) zirconium phenylphosphonate, $Zr(C_6H_5PO_3)_2$, and (2) zirconium hydroxymethylphosphonate, $Zr(HOCH_2PO_3)_2$. These zirconium phosphonates exhibited comparable layered structure to α -zirconium bis(monohydrogen orthophosphate) monohydrate, with the organic moieties pointed to the interlayer space instead of the hydroxyl groups (Figure 1.3). In the following years, the initial MPs were based on monophosphonates and diphosphonates employing zirconium or other tetravalent metals (Alberti et al., 1996; Dines et al., 1982; Dines & Griffith, 1983a and b; Vivani, Constantino & Taddei, 2012). However, it soon spread to other metals and ligands. Johnson et al. (1984 and 1989) and Huan et al. (1992) studied the synthesis and intercalation chemistry of vanadyl organophosphonates. These solids exhibited useful sorptive and catalytic properties. Bujoli and coworkers studied the synthesis, characterisation and magnetism properties of divalent metals phosphonates (Le Bideau et al., 1994 and 1995; Bujoli, Palvadeau & Rouxel, 1990; Bujoli et al., 1993; Drumel et al., 1995). In addition, progress in solving structures from XRPD data helped to the development of this field due to the difficulty of obtaining suitable single crystals.

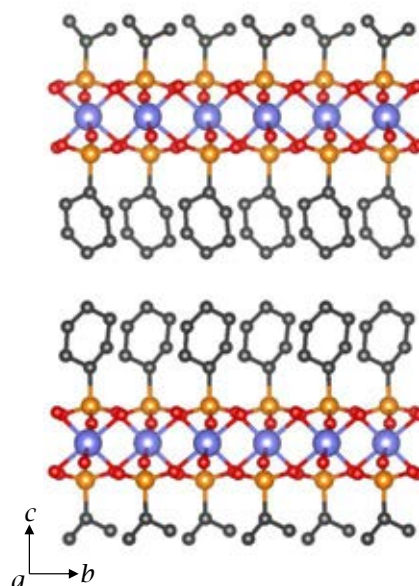


Figure 1.3. View of the 2D packing along *a*-axis for zirconium phenylphosphonate (Poojari et al., 1993).

Synthesis of metal phosphonates can be carried out via several different routes that do not necessarily give products with the same structure. This increases the variety of structures that can be obtained, making them very versatile. A rich diversity of architectures and topologies can be obtained, from 0D molecular to 3D open frameworks, being the most common 2D layered structures (Clearfield & Demadis, 2012). Generally, the synthesis is carried out by hydro- or solvothermal reactions. In order to screen the reaction parameters, high-throughput methodology is one of the most efficiency methodology, allowing the optimization of the synthesis conditions in a short period of time (Colodrero et al., 2010). Pioneering work by Stock & Bein (2004) demonstrated that applying systematic procedures of synthesis, through a high-throughput methodology, in which parameters such as temperature, pH, time, solvent, etc. can be evaluated; is a convenient way of obtaining a variety of structures and compositions, as exemplified for the case of cadmium derivatives of the phosphonocarboxylic acid $(\text{H}_2\text{O}_3\text{PCH}_2)_2\text{NCH}_2\text{C}_6\text{H}_4\text{COOH}$, H_3L (Bauer & Stock, 2007).

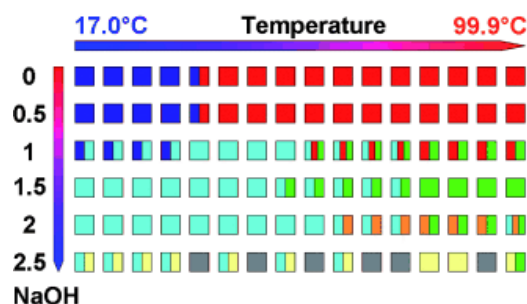


Figure 1.4. HT investigation of the influence of temperature and pH value on product formation in the system $\text{CdCl}_2/\text{H}_3\text{L}/\text{NaOH}$. Reproduced from Ref. Bauer & Stock (2007) with permission from Wiley Online Library. Copyright (2007).

1.3.1. Multifunctional Metal Phosphonates

The number of possible modes of coordination and structural arrangements of ligands can be increased by the incorporation of additional functional groups, such as carboxylate, amine, hydroxyl, sulfonate, etc., although it makes their coordination less predictable. They should be selected depending on the desirable structures and properties of the final compound (Garczarek, Janczak & Zoń, 2013).

Carboxyphosphonic ligands are heterofunctional ligands that generate a great interest due to the possibility of combine properties of both functional groups. Regarding to synthetic methodologies, hydrothermal reaction is one of the most used, although other methodologies such as solvothermal, ionothermal or RT synthesis among other have been also reported in the literature. Due to the different acidity of these functional groups, by varying the pH of the synthesis, a wide variety in coordination modes can result. Generally, synthesis at low pHs favours protonation of the carboxylic groups, while at higher pHs, more oxygen atoms from both, carboxylate and phosphonate groups are available to bind to metal ions. These synthesis aspects, as well as the diverse resulting topologies and main applications of metal carboxyphosphonates, have been reviewed (Cabeza & Aranda, 2012).

Regarding to aminophosphonates, the amino functional group of the aminophosphonic ligands can provide them with additional coordination modes due to their zwitterionic character. Depending on the synthesis conditions, the amino group can be protonated or coordinated to metal ions (Cardiano et al., 2017).

Lin & Zhou (2020) reported the hydrothermal reaction of divalent metal salts with 4-[(phosphonomethylamino)methyl]benzoic acid (H_3L), leading to four metal aminocarboxyphosphonates: $\text{Ni}(\text{HL})(\text{H}_2\text{O})_2$ (**1**), $\text{Cd}(\text{HL})$ (**2**), $\text{CdCl}(\text{H}_2\text{L})$ (**3**) and

$\text{Pb}_{1.5}\text{Cl}_2(\text{H}_2\text{L})$ (4). Different modes of the ligand coordination were observed. For 2D layered (1), the ligand is coordinated to the metal ion through the phosphonate group and the amino group, while the carboxylate group is protonated and pointed to the interlayer region. For the 2D layered (4) solid, the ligand is only coordinated to the lead ion through the oxygen from the phosphonate group. For 3D pillared-layered frameworks (2) and (3), the ligand is coordinated to the metal ion through the phosphonate and carboxylate groups.

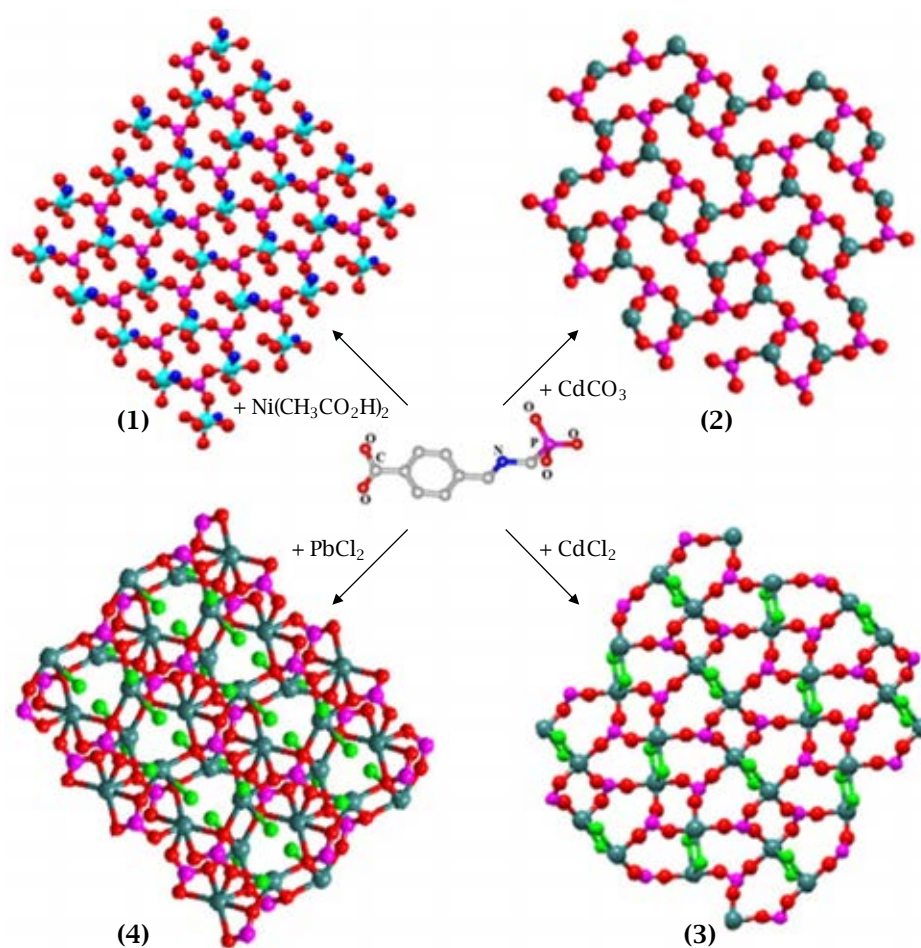


Figure 1.5. Structure of solid (1), (2), (3) and (4). Adapted from Ref. Lin & Zhou (2020) with permission from Elsevier. Copyright (2020).

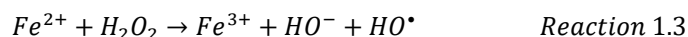
1.4. Applications

As previously mentioned, these materials have several potential applications. Some of them have been reviewed in books, such as “Metal Phosphonates Chemistry: From Synthesis to Applications” (Clearfield & Demadis, 2012) and “Tailored Organic-Inorganic Materials” (Brunet, Colón & Clearfield, 2015), as well as in reviews (Shearan et al., 2019).

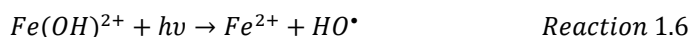
1.4.1. Photocatalysis

Water is one of the most important natural resources. However, large amounts of organic pollutants are released daily into water from different industries, such as pharmaceuticals, pesticides, textile, and paper among other industries. Most of these pollutants are recalcitrant organic contaminants, which means they are highly stable to sunlight irradiation as well as microbial attack.

Advanced oxidation processes (AOPs) refer to a group of treatments intended to remove organic pollutants from wastewater. They are based on the in-situ production of hydroxyl radicals as the main oxidizing agent (Cheng et al., 2016). Within AOPs, Fenton and photo-Fenton processes have become some of the most important water treatments, since the Fenton’s reagent, an aqueous solution of hydrogen peroxide and ferrous ions, was proposed by H. J. H. Fenton in 1894 to oxidize organic compounds in acidic medium (Brillas, Sirés & Oturan, 2009). The Fenton and photo-Fenton processes have been successfully applied for degradation of many pollutants (Clarizia et al., 2017) and can be outlined with the following reactions:



The efficiency in producing the oxidant HO^{\bullet} species can be enhanced by irradiation with UV or visible light (photo-Fenton process), due to rapid regeneration of Fe^{2+} through photo-reduction of Fe^{3+} ions, such as:



The efficiency of Fenton and photo-Fenton processes is affected by different parameters such as the pH, temperature, concentration of catalyst, hydrogen peroxide and pollutant, etc., being the pH value the most crucial parameter. Hydroxide precipitation occurs when it does not operate over the appropriate pH (pH= 2.8-3.5) (Katsumata et al., 2005). However, it can be solved by the use of heterogeneous catalyst, where the iron (or other transition metals) is stabilised on/in the structure of the catalyst, reducing the hydroxide precipitation over a wider pH range (Bazaga-García et al., 2012; Shi et al., 2017; Wu et al., 2020).

MOFs have been employed as Fenton-like catalysts due to their excellent features, such as their well-defined structure, large pore volume and high specific area (Cheng et al., 2018). These MOFs include single and multiple transition metals, such as iron, cobalt or copper among other. Some of them are summarized in Table 1.1.

Gao et al. (2017a) reported the employment of MIL-88B-Fe as heterogeneous Fenton-like catalyst for phenol degradation. The catalytic activity test was carried out at RT over a pH range from 4 to 6. The catalytic activity of MIL-88B-Fe was compared with three homogeneous catalysts, Fe_2O_3 , $\alpha\text{-FeOOH}$ and Fe_3O_4 , and two other heterogeneous iron-based MOFs, MIL-53-Fe and MIL-101-Fe. In all cases, MIL-88B-Fe displayed higher catalytic activity (44% TOC removal in 30 min) mainly attributed to the abundance of active sites, the flexible structure and the enhanced Fe(III)/Fe(II) redox properties.

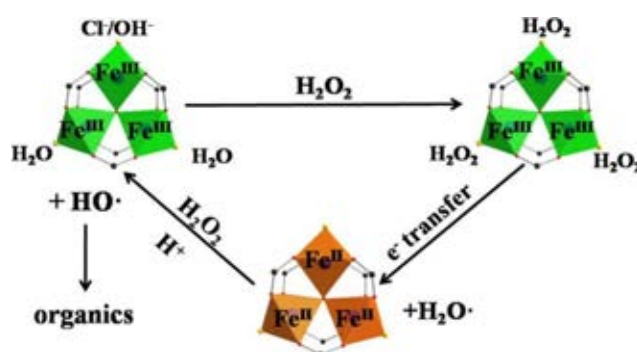


Figure 1.6. Schematic diagram of the reaction mechanism of H_2O_2 activation by MIL-88B-Fe. Reproduced from Ref. Gao et al. (2017a) with permission from Elsevier. Copyright (2017).

Recently, Cheng et al. (2018) have reviewed a wide series of MOFs for highly efficient heterogeneous Fenton-like catalysis.

Table 1.1. Summary of MOFs employed as Fenton-like catalyst.

Catalyst	Pollutant	Irrad.	Conditions	Removal	References
Fe ₃ O ₄ -PAC (0.1 g·L ⁻¹)	Tetracycline (20 mg·L ⁻¹)	UV-C	[H ₂ O ₂]= 5 mM pH= 3 T= 25 °C	99% (44% TOC) in 60 min	Kakavandi et al., 2016
MIL-101 (0.1 g·L ⁻¹)	Tetracycline hydrochloride (50 mg·L ⁻¹)	Vis	H ₂ O ₂ = 10 mL·L ⁻¹ pH= 4.1 T= 14 °C	80% in 20 min	Wu et al., 2020
Fe ₃ O ₄ -MWCNT (0.6 g·L ⁻¹)	Norfloxacin (0.5 mg·L ⁻¹)	Vis	[H ₂ O ₂]= 98 mM pH= 2-7 T= 25 °C	90% in 120 min	Shi et al., 2017
MIL-53(Fe) (0.1 g·L ⁻¹)	Clofibric acid (CA) Carbamazepine (CBZ) (40 mg·L ⁻¹)	Vis	[H ₂ O ₂]= 20 mM pH= 3	98% CA and 90% CBZ in 240 min	Gao et al., 2017b
Pd@MIL-100 (Fe) (0.125 g·L ⁻¹)	Theophylline (20 mg·L ⁻¹)	Vis	[H ₂ O ₂]= 9.75 mM pH= 4	95% in 120 min	Liang et al., 2015
MIL-88B-Fe (0.1 g·L ⁻¹)	Phenol (50 mg·L ⁻¹)	-	[H ₂ O ₂]= 15 mM [Fe ²⁺]= 2 mg·L ⁻¹ pH= 4-6 RT	90% (44% TOC) in 30 min	Gao et al., 2017a
Fe-bpydc (0.01 g·L ⁻¹)	Phenol (0.25 mM)	-	[H ₂ O ₂]= 1.5 mM pH= 5.3	> 90% in 120 min	Li et al., 2016
PCN-250(Fe ₂ Mn) (0.5 g·L ⁻¹)	MB (15 mg·L ⁻¹)	Vis	[H ₂ O ₂]= 6 mM T= 25 °C	100% in 300 min	Kirchon et al., 2020
Fe ₃ O ₄ /C/Cu (0.5 g·L ⁻¹)	MB (100 mg·L ⁻¹)	Vis	[H ₂ O ₂]= 163.7mM T= 35 °C	100% in 60 min	Li et al., 2017a
MIL-88A-1 or MIL-88A-2 (0.2 g·L ⁻¹)	Rhodamine B (10 mg·L ⁻¹)	Vis	[H ₂ O ₂]= 2 mM	95% (MIL-88A-1) and 100% (MIL-88A-2) in 80 min	Fu et al., 2020
Fel-Co PBA (0.012 g·L ⁻¹)	Rhodamine B (12 mg·L ⁻¹)	UVA	[H ₂ O ₂]= 4 mM pH= 4.8 T= 35 °C	93% in 30 min	Li et al., 2015
Fe-Cr-MIL-101 (0.3 g·L ⁻¹)	RR195 Dye (100 mg·L ⁻¹)	UVA	[H ₂ O ₂]= 136 mg·L ⁻¹ pH= 5.5 RT	98% in 100 min	Vu et al., 2014
Fe ³⁺ -CA/MIL-101 (0.1 g·L ⁻¹)	X-3B dye (100 mg·L ⁻¹)	Vis	[H ₂ O ₂]= 1.96 mM pH= 6	90% in 80 min	Qin et al., 2015

1.4.2. Proton Conductivity

Due to the necessity of obtaining new sources of clean energy, fuel cells (FCs) have been highly developed in the recent years. FCs are electrochemical devices that convert chemical energy from a chemical reaction into electrical energy in a clean and sustainable way. Generally, FCs use hydrogen as fuel and oxygen as oxidising agent. Among different FCs, proton exchange membrane fuel cells (PEMFCs) can be a feasible alternative to reduce fossil fuel dependence due to their characteristics, such as their high power density, clean pollutant free operation, compactness, low weight and volume, low operating temperatures, etc. PEMFCs operates injecting hydrogen-rich as combustible by the anode and oxygen by the cathode. Both electrodes are separated by an electrolyte, which is a polymer electrolyte membrane that allows positively ionic conduction and blocks electrons. This membrane must be properly humidified because proton conductivity is highly dependent on the water content. For this reason, input gases are previously humidified. On the anode side, catalytic oxidation of hydrogen occurs, dissociating the hydrogen into protons and electrons. These electrons are led to the cathode via an external circuit, where they reduce oxygen. On the surface of the cathode, the oxygen molecules and protons combine to produce water, which is a product together with heat. The electrical potential difference, originated by both catalytic oxidation and reduction reactions between electrodes, produces electricity (Figure 1.7). These electrodes are normally made of a porous carbon compound coated with a catalyst such as platinum or palladium, to improve the efficiency of electrochemical reactions, being one of the most expensive components of FCs. The basic chemical reactions in a PEMFC are:



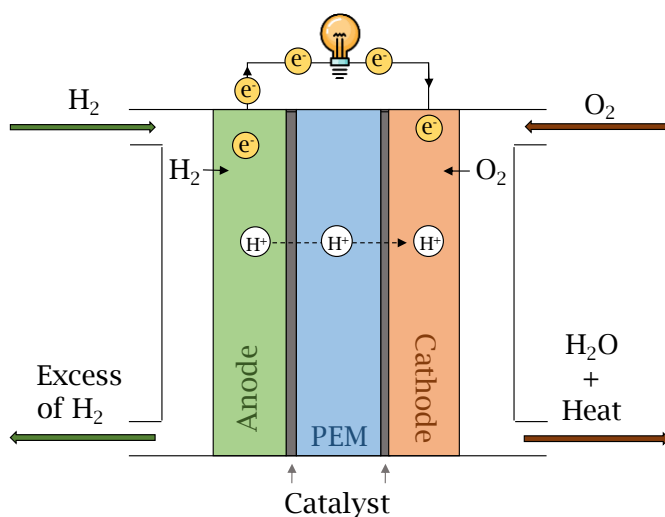


Figure 1.7. Fuel Cell.

Membrane-electrode assembly (MEA) is the name of the combination of electrodes and polymeric electrolyte membrane. There are two different approaches to its construction: (i) the catalyst is deposited on a porous substrate and then placed at both sides of the membrane or (ii) the catalyst is deposited directly on the membrane.

Due to proton conduction is a key factor in these FCs, PEM enhancement is an important research field. Nafion is the most common electrolyte employed in PEMFCs among other such as polybenzimidazole and sulfonated polyether ether ketones. Commercial Nafion membranes, developed by DuPont (Gierke, Munn & Wilson, 1981), exhibit proton conductivity values ranging from 10^{-2} to 10^{-1} S·cm⁻¹ at 98% RH and moderate temperature range (60-80 °C), with low activation energies (< 0.5 eV). However, it declines at higher temperatures and lower RH values. In addition, the cost of Nafion membrane is high. These disadvantages limit their large-scale use in many technologies. Therefore, to overcome this limitation, it is desirable to develop cheaper and better performing electrolytes that operate over a wide temperature range. The electrolyte material of a PEMFC must meet some conditions (Meng et al., 2017):

- (i) High inherent proton conductivity and low electronic conductivity.
- (ii) High chemical, thermal and mechanical stability under operating conditions.

(iii) Long lifetime under operating conditions.

(iv) Low cost.

Proton-conducting membranes based on inorganic or composite materials have been explored (Liang et al., 2013; Bai et al., 2020).

MOFs are potential candidates for proton conduction due to their porosity, which allows guest molecules to lodge within them, as well as the versatility of their organic ligands and structures. In addition, the crystallinity of these materials allows establishing structure-properties relationship. Therefore, MOFs are candidates as electrolytes in PEMFCs. They have to offer some requirements such as robustness, display high proton conductivity values and relatively good thermal and chemical stability (Bao, Shimizu & Zheng, 2019).

Proton conduction, as the other ionic conductivities, can be expressed by the following equation (Deng et al., 2020):

$$\sigma = \frac{n(Ze)^2 D}{kT} e^{-\frac{E_a}{kT}} \quad \text{Equation 1.7}$$

where n is the carrier concentration, D is the self-diffusion coefficient, Ze is the charge of the conducting carrier (for protons is 1), E_a is the activation energy of ion transport, T is the temperature and k is the Boltzmann constant. The mobility (η) is proportional to the self-diffusion coefficient:

$$\eta = \frac{ZeD}{kT} \quad \text{Equation 1.8}$$

There are two important factors to improve proton conductivity: (i) increasing proton carrier concentration and (ii) increasing the proton carrier mobility. The proton carrier concentration depends on the overall acidity of the proton sources and it can be enhanced by the introduction of acidic guest molecules (H_3O^+ , NH_4^+ , inorganic acids, etc.), proton-related substitute groups in ligands ($-\text{COOH}$, $-\text{PO}_3\text{H}$, $-\text{SO}_3\text{H}$, $-\text{OH}$, etc.) as well as coordination water molecules, which could partially dissociate due to the Lewis acidity of metal ions (Bao, Shimizu & Zheng, 2019; Deng et al., 2020). On the other hand, the mobility of the proton can be increased by the formation of a continuous H-bond network containing protic sites.

CHAPTER 1

Proton conductive MOFs can be classified in two categories (Yamada et al., 2013): (i) water-assisted proton conductors, which operate at low temperatures (20-80 °C) and depend on the H-bond created by the interactions with water and (ii) anhydrous proton conductors, which usually operate from 100 to 250 °C (medium temperatures) and their conductivities are due to the presence of protophilic guests or ligand substituents. Regarding to water-assisted proton conductors, two different conduction mechanisms can be exhibited:

- (i) Grotthuss mechanism involves a proton being transported by hopping through an infinite H-bond network. The H-bond is cut off during proton transfer, while the neighbouring proton acceptor rearranges and forms an uninterrupted proton migration orbit. This mechanism can be identified by its low activation energy value ($E_a < 0.5$ eV), which is sufficient to break the energy of the H-bond (2-3 kcal/mol; ~ 0.11 eV) (Agmon, 1995).
- (ii) Vehicle mechanism implies the diffusion of proton carriers for conduction. As this mechanism involves the migration of larger ions, it requires a relatively larger energy contribution ($E_a > 0.5$ eV) (Kreuer et al., 1982).

Due to the crystalline nature of MOFs, it is possible to employ diffraction techniques to visualize the H-bond network and suggest possible proton transportation pathways in them. However, it is not an easy task because solvent molecules are sometimes highly disordered and it is difficult to identify the orientation of the proton carriers (Li et al., 2017b).

There are two main design strategies to obtain expected high proton conductor MOFs (Deng et al., 2020):

- (i) Intrinsic conductive performance of the MOF. Enhancing proton conduction by introducing protophilic substitute groups, such as $-\text{NH}_2$, $-\text{SO}_3\text{H}$, $-\text{COOH}$, $-\text{OH}$, $-\text{SH}$, etc., in ligands or coordinated solvents on metal centres, which promoting the formation of extended H-bond networks.
- (ii) Introducing protophilic guest molecules in pores, such as H_2O , imidazole, pyridine, etc., to obtain a continuous H-bond network pathway.

Xing et al., 2019 reported a new gadolinium-based MOF, $\{\text{H}[(\text{N}(\text{CH}_3)_2)_2][\text{Gd}_3(\text{NIPA})_6]\} \cdot 3\text{H}_2\text{O}$, synthesised by solvothermal reaction between Gd^{3+} and the 5-nitroisophthalic acid in a tetramethylammonium-containing solution of

DMF. Its crystal structure was claimed to be composed of a 3D anionic framework $[\text{Gd}_3(\text{NIPA})_6]_n^{3n-}$ with acid groups and tetramethylammonium cations acting as counterions within the pores, where also are placed the water molecules. This MOF exhibited excellent water stability at 75 °C for 2h. In addition, excellent single-crystal proton conductivity values were found for this material ($7.17 \cdot 10^{-2} \text{ S} \cdot \text{cm}^{-1}$ at 75 °C and 98% RH). This was explained as being due to the presence of protonated species and water molecules placed within the infinite 3D pore channels, which can form complex hydrogen bonded networks facilitating proton-conducting processes. Furthermore, the crossed infinite channels with hydrophilic frameworks are suitable for water absorption at high RH.

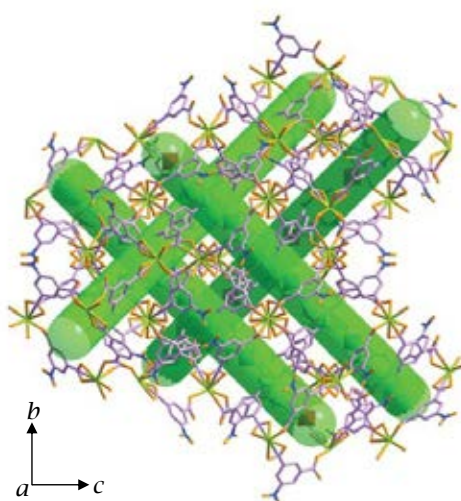


Figure 1.8. The 1D channels in $\{\text{H}[(\text{N}(\text{CH}_3)_4)_2][\text{Gd}_3(\text{NIPA})_6]\} \cdot 3\text{H}_2\text{O}$ showing four different orientations. Reproduced from Ref. Xing et al. (2019) with permission from The Royal Society of Chemistry. Copyright (2019).

Wahiduzzaman et al., (2019) studied the incorporation of highly acidic hydrogensulfate species into the inorganic building unit of the titanium-based MOF MIP-177-LT. For that reason, MIP-177-LT powder sample was dispersed in a 6M H_2SO_4 aqueous solution with continuous stirring at RT for 24 h, generating the product named as MIP-177- $\text{SO}_4\text{H-LT}$. This hydrogensulfate decorated titanium carboxylate ($2.6 \cdot 10^{-2} \text{ S} \cdot \text{cm}^{-1}$) displayed proton conductivity values higher than the pristine MIP-177-LT ($4.3 \cdot 10^{-6} \text{ S} \cdot \text{cm}^{-1}$) at 25 °C and 95% RH. *ab initio* molecular dynamics simulations were employed to elucidate the proton transfer mechanism, which revealed that it

CHAPTER 1

was initiated by a proton transfer from the acidic hydrogensulfate groups toward neighbouring guest water molecules followed by a proton shuttle over longer distances, through the extended H-bond network.

Regarding to metal carboxyphosphonates, Ramaswamy et al., (2015) reported the synthesis and proton conductivity properties of PCMOF10, which is a magnesium derivative of the 2,5-dicarboxy-1,4-benzenediphosphonic acid. PCMOF10 displayed a high water stability as well as swelling resistance upon hydration. High proton conductivity values were observed ($3.6 \cdot 10^{-2} \text{ S} \cdot \text{cm}^{-1}$ at 70 °C and 95% RH) thanks to the extended H-bond network that involves lattice and coordinated water molecules and phosphonate and carboxylate groups.

Representative proton conductive MOFs, as well as metal phosphonates are summarized in the following table (Table 1.2.):

Table 1.2. Characteristics of selected proton conductor metal phosphonates and MOFs.

	Dimensionality	σ (S·cm ⁻¹)	Ea (eV)	T (°C)	RH (%)	References
METAL PHOSPHONATES						
Metal carboxyphosphonates						
Li-HPA: [Li ₃ (HPA)(H ₂ O) ₄] _n ·H ₂ O	1D	1.1·10 ⁻⁴	0.84	24	98	Bazaga-García et al., 2015
Na-HPA: Na ₂ (HHPA)(H ₂ O) ₄	3D	5.6·10 ⁻³	0.39	24	98	Bazaga-García et al., 2014
Ca-PPhtA-I	3D	1.3·10 ⁻³	0.23	24	98	Colodrero et al., 2012a
Ca-PPhtA-NH ₃	3D	6.6·10 ⁻³	0.40	24	98	Ramaswamy et al., 2015
LaHPA-I: La ₃ (H _{0.75} HPA) ₄ ·16H ₂ O	3D	5.6·10 ⁻⁶	0.20	21	98	Wei et al., 2017
GdHPA-II: Gd ₃ (H _{0.75} HPA) ₄ ·16H ₂ O	3D	3.2·10 ⁻⁴	0.23	21	98	Grohol et al., 1996
PCMOF10	2D	3.6·10 ⁻²	0.21	70	95	
(Me ₂ NH ₂)[Eu(L)]	2D	3.8·10 ⁻³	0.74	100	98	
[UO ₂ (Hppa) ₂ (H ₂ O)] ₂ ·8H ₂ O	1D	3.3·10 ⁻³	0.36	25	85	
Metal aminophosphonates						
Mg(H ₆ ODTMP)·6H ₂ O	3D	1.6·10 ⁻³	0.31	19	100	Colodrero et al., 2012b
La(H ₅ DTMP)·7H ₂ O	3D	8.0·10 ⁻³	0.25	24	98	Colodrero et al., 2012c
[La ₂ (H ₃ NMP) ₂ (H ₂ O) ₄] _n ·4.5H ₂ O	1D	2.0·10 ⁻³	0.27	80	95	Bazaga-García et al., 2016
[Gd(H ₄ NMP)(H ₂ O) ₂] _n ·2H ₂ O	2D	3.0·10 ⁻⁴	0.49	80	95	

Table 1.2. Characteristics of selected proton conductor metal phosphonates and MOFs (Continuation).

	Dimensionality	σ (S·cm ⁻¹)	Ea (eV)	T (°C)	RH (%)	References
Metal sulfophosphonates						
Zr(HPO ₄) _{0.7} (HO ₃ SC ₆ H ₄ PO ₃) _{1.3} ·2H ₂ O	2D	6.3·10 ⁻²	0.15	100	90	Zima et al., 2010
PCMOF2 _{1/2}	3D	2.1·10 ⁻²	0.21	85	90	Kim et al., 2013
Metal polyphosphonates						
PCMOF-5: La(H ₅ L ⁹)(H ₂ O) ₄	3D	2.5·10 ⁻³	0.16	60	98	Taylor, Dawson & Shimizu, 2013
MOFs						
Fe(C ₂ O ₄)(H ₂ O) ₂	1D	1.3·10 ⁻³	0.40	25	98	Yamada, Sadakiyo & Kitagawa, 2009
[Co(bpy)(H ₂ O) ₄](btec) _{0.5} ·H ₂ O	1D	4.2·10 ⁻²	0.29	80	98	Elahi et al., 2018
[Tb ₄ (TTHA) ₂ (H ₂ O) ₄]·7H ₂ O	2D	2.5·10 ⁻²	0.68	60	98	Feng et al., 2019b
Zn ₃ (bpdcc) ₂ (pdc)(DMF)·6DMF	2D	1·10 ⁻²	0.45	60	97	Meng et al., 2018
MIL-100-Fe-Cl	3D	1.6·10 ⁻³	-	RT	99.9	Mao et al., 2014
{H[(N(CH ₃) ₂)] ₂][Gd ₃ (NIPA) ₆]} ₃ ·H ₂ O	3D	7.2·10 ⁻²	0.13	75	98	Xin et al., 2019
[(Me ₂ NH) ₃ (SO ₄) ₂] ₂ [Zn ₂ (ox) ₄]	3D	4.2·10 ⁻²	-	25	98	Nagarkar et al., 2014
(H ₃ O)[Y ₂ (H ₃ brp)(H ₄ brp)]·H ₂ O	3D	2.6·10 ⁻²	0.40	94	98	Firmino et al., 2017b
[Cu ^I Cu ^{II} ₄ L _{4n}]-NH ₃	3D	1.1·10 ⁻²	0.39	100	98	Liu et al., 2018
MIP-202(Zr)	3D	1.1·10 ⁻²	0.22	90	95	Wang et al., 2018

1.4.3. Luminescent Sensors

Luminescence is the response by light emission of having absorbed some energy. Luminescent response can be classified depending on the type of energy used to excite the material: (i) photoluminescence, when the material is excited by the adsorption of photons or light; (ii) electroluminescence, when the excitation is carried out through electrical energy and (iii) cathodoluminescence, when the material is excited by a beam of electrons or cathode rays (Hix, 2012).

Nowadays, luminescent materials have attracted attention due to their applicability in solid-state lighting, luminescence-based sensors and organic light emitting diodes (OLEDs) (Kaur et al., 2019). For this purpose, they have to satisfy three basic requirements: (i) respond to external stimuli; (ii) be insensitive towards possible undesired luminescent quenching, which could be induced by testing environment and (iii) exhibit chemical and physical stability (Zhang et al., 2018). Generally, these materials are inorganic, although organic-inorganic hybrid materials such as MOFs and metal phosphonates provide new opportunities for developing new luminescent materials. These last are excellent candidates for this application, where the luminescence can arise from either organic linkers or metal ions (Hix, 2012).

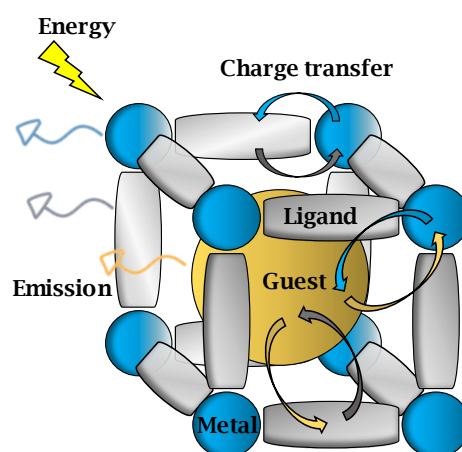


Figure 1.9. Representation of emission possibilities modes in MOFs, wherein metal ions or clusters (blue circles) are linked by organic ligands (grey cylinders) with a guest molecule in the formed void (yellow circle).

CHAPTER 1

Among these materials, Ln³⁺-based compounds have been widely studied due to their properties, based mainly on f-f electronic transitions, which lead to high colour purity distinctive emissions as well as long emission lifetimes. Europium and terbium are the most studied due to their strong luminescence in the visible part of the spectrum.

Hou et al. (2020) reported the hydrothermal synthesis of four 2D lanthanide derivatives from the 5-methyl-1,3-phenylenebis(methylene)bisphosphonic acid, Ln(HL)(H₂O)₂ (Ln= Nd **1**, Eu **2**, Tb **3** and Er **4**). Luminescence properties were investigated for compounds **2** and **3** at RT. When compound **2** was excited at 246 nm, it emitted at 596.8, 624.6, 654.8 and 705.6 nm. These bands correspond to the ⁵D₀→⁷F_n Eu³⁺ transitions. In addition, one ligand-centred emission was found at 471.6 nm. For compound **3**, upon excitation at 354 nm, it emitted strong emission bands at 492.2, 549.0, 589.6 and 625.2 nm, which are typical of the Tb³⁺ ion (⁵D₀→⁷F_n transitions). A ligand-centered emission band was also observed in the range of 400–475 nm. Due to the strong emission of compound **3**, its sensing abilities toward metal ions and anions were investigated, showing interesting sensing ability towards Fe³⁺ and Cr₂O₇²⁻ ions. In both cases, the luminescence was quenched in the presence of these ions, probably due to their competition for energy absorption which prohibits the energy transfer from the phosphonate ligand to the terbium ion and leads to the reduction of emission intensity (Figure 1.10).

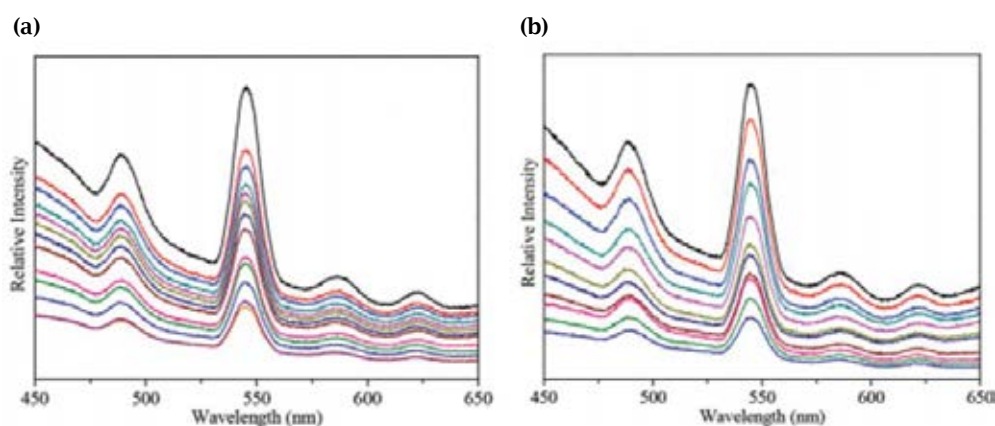


Figure 1.10. Emission spectra in the presence of different volumes of 10⁻³M (a) Fe³⁺ and (b) Cr₂O₇²⁻ solutions: from 0 (black) to 500 μL (violet). Adapted from Ref. Hou et al. (2020) with permission from The Royal Society of Chemistry. Copyright (2020).

1.4.4. Gas Adsorption and Separation

Gas separation from a mixture can be achieved based on selective adsorption. Generally, porous solid materials such as zeolites, activated carbons, etc. are employed for this application. Looking for most efficient adsorbents, MOFs are promising candidates due to their large surface areas as well as their tuneable porous size and properties (Li, Kuppler and Zhou, 2009). Despite the difficulty of obtaining microporous MPs, most of them exhibit channel-like pores, which could interact with the specific adsorbate species, making them potential candidates for gas adsorption and separation applications, as well as are MOFs (Shearan et al., 2019). Furthermore, MPs would offer a much greater likelihood of forming polar pores (Horike et al., 2006) that is translated to distinctive selectivity (Shimizu, Vaidhyanathan & Taylor, 2009).

The principal properties of an adsorbent are its adsorption capacity and selectivity. This depends on its nature, the presence of effective functional group as well as a high surface area. However, the equilibrium pressure and temperature also play a major role.

Gas separation can be carried out via selective adsorption due to the different affinities of the adsorbent to adsorb the diffused guest molecule. There are four mechanisms (Ghanbari, Abnisa & Daud, 2020):

- (i) Sieving effect or steric separation. The selective gas adsorption depends on the size and/or shape of the adsorbate molecules.
- (ii) Thermodynamic equilibrium effect. When all the components of the gas mixture can pass inside the adsorbent, the interaction between the surface of the adsorbent and the adsorbate plays an important role in the selective adsorption. The strength of the interaction between adsorbate and adsorbent is due to their properties (i.e. polarizability, the permanent dipole moment, etc.).
- (iii) Kinetic effect. This mechanism depends on the different diffusion rates, making that certain components enter the pores and become adsorbed faster than other components.
- (iv) Quantum sieving effect. It is due to the differences in diffusion speeds between the different guest molecules and the compatibility of the pore diameter with the de Broglie wavelength of these molecules.

However, typically gas adsorption is carried out through more than one mechanism (Keller & Staudt, 2005; Yang, 2003).

Recently, Zhang et al. (2020) reported a 3D Zr-MOF, UPC-50, based on 3,3',5,5'-tetra(4-carboxyphenyl)bimesityl. UPC-50 exhibits 2D channels ($10.6 \times 16.4 \text{ \AA}$) as well as high hydrothermal and chemical stabilities that make it a potential candidate for gas adsorption and separation, showing high adsorption capacity for propylene ($252.67 \text{ cm}^3 \cdot \text{g}^{-1}$ at 273K and 1 bar) and excellent selectivity for the separation of propylene from methane in a 50:50 mixture (78.28 at 273K and 1 bar). In addition, H_2 adsorption was also tested at 77K, showing a maximum adsorption capacity of $131.1 \text{ cm}^3 \cdot \text{g}^{-1}$ comparable with other reported MOFs such as IRMOF-9, IRMOF-2 and ZIF-8 (Rowsell & Yaghi, 2006; Park et al., 2006).

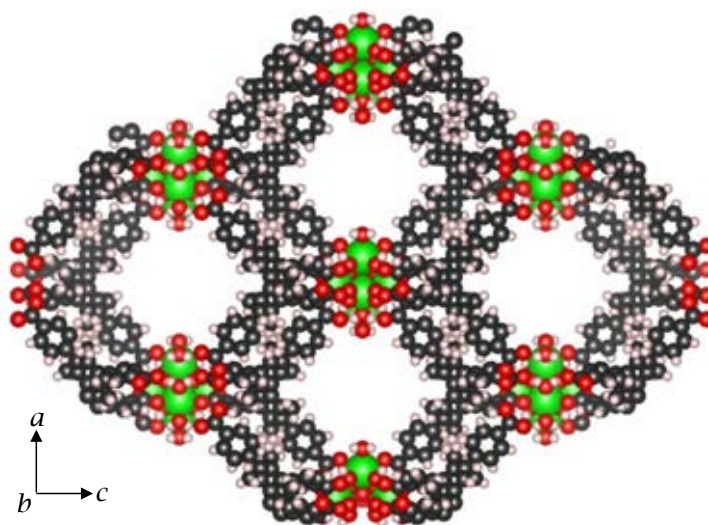


Figure 1.11. Structure of UPC-50 view along the *b*-axis.

1.4.5. Drug Storage and Delivery

It is important to develop controllable drug delivery system to reduce side effects as well as enhance therapeutic efficacy. The drug loading method can be classified in three types of strategies: encapsulation, direct assembly or post-synthesis strategies (Figure 1.12). Then, they are released at a specific rate to a specific site (Wang, Zheng & Xie, 2018). MOFs are potential candidates due to (i) their porous structures and large surface areas, (ii) their tuneable cavities for strong guest-host interactions, (iii) their relatively high thermal and chemical stabilities, (iv) the different synthetic methodologies to obtain them and (v) the possibility to modify their surfaces. The employment of MOFs and MPs for drug delivery implies that they

should be nontoxic, biocompatible and stable in physiologic conditions. Mg, Ca, Sr, Ba, Zn, Fe, Ti and Zr are commonly employed as metal ions due to their low toxicity (Shearan et al., 2019; Gulcay & Erucar, 2020).

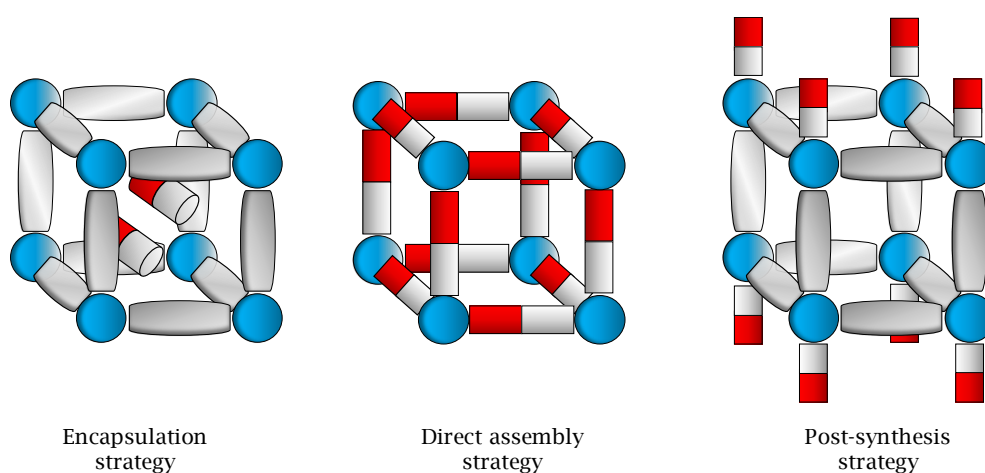


Figure 1.12. Three types of drug loading method: encapsulation, direct assembly and post-synthesis strategies.

Li et al. (2019c) studied the drug loading and delivering of ketoprofen in a Sr-based MOF, namely Sr/PTA-MOF, for treating osteoarthritis. A high amount of ketoprofen (36 %) was encapsulated in the pores of Sr/PTA-MOF. The drug releasing showed two behaviours: a quick release at the first 8 hours (80 % of drug) and a slow and controlled release after these eight hours (90% of drug released after 24 h). In addition, cytotoxic experiments revealed that Sr/PTA-MOF has no poisonous effect on osteoarthritis chondrocytes.

Recently, Pham et al. (2020) reported the employment of two iron-based MOFs, MIL-53 and MIL-88B, for in vitro drug loading and delivering of a model drug such as ibuprofen. Both MOFs are based on terephthalic acid and iron ions, but their crystal structures are different. MIL-53 exhibits 1D channel while MIL-88B has a 3D cage structure. MIL-53 (37.0 wt %) exhibited a higher loading capacity than MIL-88B (19.5 wt %) by encapsulation, while MIL-88B showed a slower controlled drug release. Cytotoxicity studies revealed that MIL-88B is biodegradable and non-cytotoxic.

1.5. References

A

- Agmon, N. The Grotthuss mechanism. *Chem. Phys. Let.*, **1995**, 244(5-6), 456-462.
- Alberti, G.; Costantino, U.; Allulli, S.; Tomassini, N. Crystalline Zr(R-PO₃)₂ and Zr (R-OPO₃)₂ compounds (R= organic radical): A new class of materials having layered structure of the zirconium phosphate type. *J. Inorg. Nucl. Chem.*, **1978**, 40(6), 1113-1117.
- Alberti, G.; Casciola, M.; Costantino, U.; Vivani, R. Layered and pillared metal(IV) phosphates and phosphonates. *Adv. Mater.*, **1996**, 8, 291-303.

B

- Bai, Z.; Liu, S.; Cheng, G.; Wu, G.; Liu, Y. High proton conductivity of MOFs-polymer composite membranes by phosphoric acid impregnation. *Micropor. Mesopor. Mat.*, **2020**, 292, 109763.
- Bao, S. S.; Shimizu, G. K.; Zheng, L. M. Proton conductive metal phosphonate frameworks. *Coord. Chem. Rev.*, **2019**, 378, 577-594.
- Batten, S. R.; Neville, S. M.; Turner, D. R. Coordination polymers: design, analysis and application. *RSC Publishing*, **2008**.
- Batten, S. R.; Champness, N. R.; Chen, X. M.; Garcia-Martinez, J.; Kitagawa, S.; Öhrström, L.; O'Keeffe, M.; Suh, M. P.; Reedijk, J. Terminology of metal-organic frameworks and coordination polymers (IUPAC Recommendations 2013). *Pure Appl. Chem.*, **2013**, 85(8), 1715-1724.
- Bauer, S.; Stock, N. Implementation of a Temperature-Gradient Reactor System for High-Throughput Investigation of Phosphonate-Based Inorganic–Organic Hybrid Compounds. *Angew. Chem. International Edition*, **2007**, 46(36), 6857-6860.
- Bazaga-Garcia, M.; Cabeza, A.; Olivera-Pastor, P.; Santacruz, I.; Colodrero, R. M.; Aranda, M. A. Photodegradation of Phenol over a Hybrid Organo-Inorganic Material: Iron (II) Hydroxyphosphonoacetate. *J. Phys. Chem. C*, **2012**, 116(27), 14526-14533.
- Bazaga-García, M.; Colodrero, R. M.; Papadaki, M.; Garczarek, P.; Zoń, J.; Olivera-Pastor, P.; Losilla, E. R.; León-Reina, L.; Aranda, M. A. G.; Choquesillo-Lazarte, D.; Demadis, K. D.; Cabeza, A. Guest molecule-responsive functional calcium phosphonate frameworks for tuned proton conductivity. *J. Am. Chem. Soc.*, **2014**, 136(15), 5731-5739.

- Bazaga-García, M.; Papadaki, M.; Colodrero, R. M.; Olivera-Pastor, P.; Losilla, E. R.; Nieto-Ortega, B.; Aranda, M. A. G.; Choquesillo-Lazarte, D.; Cabeza, A.; Demadis, K. D. Tuning Proton Conductivity in Alkali Metal Phosphonocarboxylates by Cation Size-Induced and Water-Facilitated Proton Transfer Pathways. *Chem. Mater.*, **2015**, 27(2), 424-435.
- Bazaga-García, M.; Angeli, G. K.; Papathanasiou, K. E.; Salcedo, I. R.; Olivera-Pastor, P.; Losilla, E. R.; Choquesillo-Lazarte, D.; Hix, G. B.; Cabeza, A.; Demadis, K. D. Luminescent and Proton Conducting Lanthanide Coordination Networks Based on a Zwitterionic Tripodal Triphosphonate. *Inorg. Chem.*, **2016**, 55(15), 7414-7424.
- Brillas, E; Sirés, I.; Oturan, M. A. Electro-Fenton Process and Related Electrochemical Technologies Based on Fenton's Reaction Chemistry. *Chem. Rev.*, **2009**, 109, 12, 6570-6631.
- Brunet, E.; Colón, J. L.; Clearfield, A. Tailored organic-inorganic materials. *John Wiley & Sons*, **2015**.
- Bujoli, B.; Palvadeau, P.; Rouxel, J. Synthesis of New Lamellar Iron (III) Phosphonates. *Chem. Mater.*, **1990**, 2(5), 582-589.
- Bujoli, B.; Pena, O.; Palvadeau, P.; Le Bideau, J.; Payen, C.; Rouxel, J. Synthesis, Structure, and Magnetic Properties of a New Lamellar Iron Phosphonate, $\text{Fe}^{\text{II}}(\text{C}_2\text{H}_3\text{PO}_3)\cdot\text{H}_2\text{O}$. *Chem. Mater.*, **1993**, 5(4), 583-587.

C

- Cabeza, A.; Aranda, M. A. G. Metal Carboxyphosphonates in Metal Phosphonates Chemistry. From synthesis to Applications. *RSC: Cambridge*, 2012, Ch. 4, p. 107-132.
- Cardiano, P.; Cigala, R. M.; Cordaro, M.; De Stefano, C.; Milea, D.; Sammartano, S. On the complexation of metal cations with "pure" diethylenetriamine-N, N, N', N'', N''-pentakis (methylenephosphonic) acid. *New J. Chem.*, **2017**, 41(10), 4065-4075.
- Chen, L.; Liu, D.; Peng, J.; Du, Q.; He, H. Ratiometric fluorescence sensing of metal-organic frameworks: Tactics and perspectives. *Coord. Chem. Rev.*, **2020**, 404, 213113.
- Cheng, M.; Zeng, G.; Huang, D.; Lai, C.; Xu, P.; Zhang, C.; Liu, Y. Hydroxyl radicals based advanced oxidation processes (AOPs) for remediation of soils contaminated with organic compounds: a review. *Chem. Eng. J.*, **2016**, 284, 582-598.

CHAPTER 1

- Cheng, M.; Lai, C.; Liu, Y.; Zeng, G.; Huang, D.; Zhang, C.; Qin, L.; Hu, L.; Zhou, C.; Xiong, W. Metal-organic frameworks for highly efficient heterogeneous Fenton-like catalysis. *Coord. Chem. Rev.*, **2018**, 368, 80-92.
- Clarizia, L.; Russo, D.; Di Somma I.; Marotta, R.; Andreatti, R. Homogeneous photo-Fenton processes at near neutral pH: a review. *Appl. Catal. B: Environ.*, **2017**, 209, 358-371.
- Clearfield, A.; Demadis, K.D. Metal Phosphonate Chemistry. From synthesis to applications. *RSC: Cambridge*, **2012**.
- Colodrero, R. M. P.; Olivera-Pastor, P.; Cabeza, A.; Papadaki, M.; Demadis, K. D.; Aranda, M. A. Structural mapping and framework interconversions in 1D, 2D, and 3D divalent metal R, S-hydroxyphosphonoacetate hybrids. *Inorg. Chem.*, **2010**, 49(2), 761-768.
- Colodrero, R. M. P.; Papathanasiou, K. E.; Stavgianoudaki, N.; Olivera-Pastor, P.; Losilla, E. R.; Aranda, M. A. G.; León-Reina, L.; Sanz, J.; Sobrados, I.; Choquesillo-Lazarte, D.; García-Ruiz, J. M.; Atienzar, P.; Rey, F.; Demadis, K. D.; Cabeza, A. Multifunctional Luminescent and Proton-Conducting Lanthanide Carboxyphosphonate Open-Framework Hybrids Exhibiting Crystalline-to-Amorphous-to-Crystalline Transformations. *Chem. Mater.*, **2012a**, 24(19), 3780-3792.
- Colodrero, R. M. P.; Olivera-Pastor, P.; Losilla, E. R.; Hernández-Alonso, D.; Aranda, M. A. G.; León-Reina, L.; Rius, J.; Demadis, K. D.; Moreau, B.; Villemin, D.; Palomino, M.; Rey, F.; Cabeza, A. High Proton Conductivity in a Flexible, Cross-Linked, Ultramicroporous Magnesium Tetrakisphosphonate Hybrid Framework. *Inorg. Chem.*, **2012b**, 51(14), 7689-7698.
- Colodrero, R. M. P.; Olivera-Pastor, P.; Losilla, E. R.; Aranda, M. A. G.; León-Reina, L.; Papadaki, M.; McKinlay, A. C.; Morris, R. E.; Demadis, K. D.; Cabeza, A. Multifunctional lanthanum tetrakisphosphonates: Flexible, ultramicroporous and proton-conducting hybrid frameworks. *Dalton Trans.*, **2012c**, 41(14), 4045-4051.
- Corma, A.; García, H.; Lladrés i Xamena, F. X. Engineering metal organic frameworks for heterogeneous catalysis. *Chem. Rev.*, **2010**, 110(8), 4606-4655.
- D**
- Deng, X.; Hu, J. Y.; Luo, J.; Liao, W. M.; He, J. Conductive Metal-Organic Frameworks: Mechanisms, Design Strategies and Recent Advances. *Top. Curr. Chem.*, **2020**, 378(2), 1-50.

- Dines, M. B.; Digiacomo, P. M.; Callahan, K. P.; Griffith, P. C.; Lane, R. H.; Cooksey, R. E. Derivatized layered M (IV) phosphonates. *ACS Symp. Ser.*, **1982**, 192, 223-240.
- Dines, M. B.; Griffith, P. C. Synthesis and characterization of layered tetravalent metal terphenyl mono-and bis-phosphonates. *Polyhedron*, **1983a**, 2(7), 607-611.
- Dines, M. B.; Griffith, P. C. The mixed-component layered tetravalent metal phosphonate system $\text{Th}(\text{O}_3\text{PPh})_x(\text{O}_3\text{PC}_6\text{H}_4\text{Ph})_{2-x}$. *Inorg. Chem.*, **1983b**, 22(3), 567-569.
- Drumel, S.; Janvier, P.; Barboux, P.; Bujoli-Doeuff, M.; Bujoli, B. Synthesis, Structure and Reactivity of Some Functionalized Zinc and Copper(II) Phosphonates. *Inorg. Chem.*, **1995**, 34(1), 148-156.
- E**
- Elahi, S. M.; Chand, S.; Deng, W. H.; Pal, A.; Das, M. C. Polycarboxylate-Templated Coordination Polymers: Role of Templates for Superprotonic Conductivities of up to $10^{-1} \text{ S cm}^{-1}$. *Angew. Chem.*, **2018**, 57(22), 6662-6666.
- F**
- Feng, X.; Shang, Y.; Zhang, H.; Li, R.; Wang, W.; Zhang, D.; Wang, L.; Li, Z. Enhanced luminescence and tunable magnetic properties of lanthanide coordination polymers based on fluorine substitution and phenanthroline ligand. *RSC adv.*, **2019a**, 9(29), 16328-16338.
- Feng, L.; Wang, H. S.; Xu, H. L.; Huang, W. T.; Zeng, T. Y.; Cheng, Q. R.; Pan, Z. Q.; Zhou, H. A water stable layered Tb(III) polycarboxylate with high proton conductivity over $10^{-2} \text{ S}\cdot\text{cm}^{-1}$ in a wide temperature range. *Chem. Commun.*, **2019b**, 55(12), 1762-1765.
- Firmino, A. D.; Mendes, R. F.; Ananias, D.; Vilela, S. M.; Carlos, L. D.; Tomé, J. P. C.; Rocha, J.; Paz, F. A. A. Microwave Synthesis of a photoluminescent Metal-Organic Framework based on a rigid tetraphosphonate linker. *Inorganica Chim. Acta*, **2017a**, 455, 584-594.
- Firmino, A. D.; Mendes, R. F.; Antunes, M. M.; Barbosa, P. C.; Vilela, S. M.; Valente, A. A.; Figueiredo, F. M. L.; Tomé, J. P. C.; Paz, F. A. A. Robust Multifunctional Yttrium-Based Metal-Organic Frameworks with Breathing Effect. *Inorg. Chem.*, **2017b**, 56(3), 1193-1208.
- Firmino, A. D.; Figueira, F.; Tomé, J. P.; Paz, F. A. A.; Rocha, J. Metal-Organic Frameworks assembled from tetraphosphonic ligands and lanthanides. *Coord. Chem. Rev.*, **2018**, 355, 133-149.

CHAPTER 1

Fu, H.; Song, X. X.; Wu, L.; Zhao, C.; Wang, P.; Wang, C. C. Room-temperature preparation of MIL-88A as a heterogeneous photo-Fenton catalyst for degradation of rhodamine B and bisphenol a under visible light. *Mater. Res. Bull.*, **2020**, 125, 110806.

G

Gao, C.; Chen, S.; Quan, X.; Yu, H.; Zhang, Y. Enhanced Fenton-like catalysis by iron-based metal organic frameworks for degradation of organic pollutants. *J. Catal.*, **2017a**, 356, 125-132.

Gao, Y.; Yu, G.; Liu, K.; Deng, S.; Wang, B.; Huang, J.; Wang, Y. Integrated adsorption and visible-light photodegradation of aqueous clofibric acid and carbamazepine by a Fe-based metal-organic framework. *Chem. Eng. J.*, **2017**, 330, 157-165.

Garczarek, P.; Janczak, J.; Zoń, J. New multifunctional phosphonic acid for metal phosphonate synthesis. *J. Mol. Struct.*, **2013**, 1036, 505-509.

Ghanbari, T.; Abnisa, F.; Daud, W. M. A. W. A review on production of metal organic frameworks (MOF) for CO₂ adsorption. *Sci. Total Environ.*, **2020**, 707, 135090.

Gierke, T. D.; Munn, G. E.; Wilson, F. The morphology in nafion perfluorinated membrane products, as determined by wide-and small-angle x-ray studies. *J. Polym. Sci. Pol. Phys.*, **1981**, 19(11), 1687-1704.

Grohol, D.; Subramanian, M. A.; Poojary, D. M.; Clearfield, A. Synthesis, Crystal Structures, and Proton Conductivity of Two Linear-Chain Uranyl Phenylphosphonates. *Inorg. Chem.*, **1996**, 35(18), 5264-5271.

Gu, J.; Wen, M.; Cai, Y.; Shi, Z.; Nesterov, D. S.; Kirillova, M. V.; Kirillov, A. M. Cobalt(II) Coordination Polymers Assembled from Unexplored Pyridine-Carboxylic Acids: Structural Diversity and Catalytic Oxidation of Alcohols. *Inorg. Chem.*, **2019**, 58(9), 5875-5885.

Gulcay, E.; Erucar, I. Metal-organic frameworks for biomedical applications in Two-Dimensional Nanostructures for Biomedical Technology. *Elsevier*, **2020**, Ch. 6, p. 173-210.

H

Hix, G. B. Luminescent Metal Phosphonate Materials in Metal Phosphonate Chemistry. From Synthesis to Applications. *RSC: Cambridge*, **2012**, Ch. 16. p.525-550.

Hong, M. C.; Chen, L. Design and construction of coordination polymers. *John Wiley & Sons*, **2009**.

- Horike, S.; Matsuda, R.; Tanaka, D.; Mizuno, M.; Endo, K.; Kitagawa, S. Immobilization of Sodium Ions on the Pore Surface of a Porous Coordination Polymer. *J. Am. Chem. Soc.*, **2006**, 128(13), 4222-4223.
- Hou, X.; Yan, C. C.; Xu, X.; Liang, A. Q.; Song, Z. W.; Tang, S. F. Two-dimensional layered lanthanide diphosphonates: synthesis, structures and sensing properties toward Fe^{3+} and $\text{Cr}_2\text{O}_7^{2-}$. *Dalton Trans.*, **2020**, 49, 3809-3815.
- Huan, G.; Jacobson, A. J.; Johnson, J. W.; Goshorn, D. P. Hydrothermal Synthesis and Characterization of Two Vanadium Organophosphonates: $\text{VO}(\text{C}_6\text{H}_5\text{PO}_3)_y(\text{CH}_3\text{PO}_3)_z \cdot 1.5\text{H}_2\text{O}$, $y = 0.50$ and 0.75 . *Chem. Mater.*, **1992**, 4(3), 661-665.

J

- Johnson, J. W.; Jacobson, A. J.; Brody, J. F.; Lewandowski, J. T. Layered compounds with alternating organic and inorganic layers: vanadyl organophosphonates. *Inorg. Chem.*, **1984**, 23(24), 3842-3844.
- Johnson, J. W.; Jacobson, A. J.; Butler, W. M.; Rosenthal, S. E.; Brody, J. F.; Lewandowski, J. T. Molecular recognition of alcohols by layered compounds with alternating organic and inorganic layers. *J. Am. Chem. Soc.*, **1989**, 111(1), 381-383.

K

- Kakavandi, B.; Takdastan, A.; Jaafarzadeh, N.; Azizi, M.; Mirzaei, A.; Azari, A. Application of $\text{Fe}_3\text{O}_4@\text{C}$ catalyzing heterogeneous UV-Fenton system for tetracycline removal with a focus on optimization by a response surface method. *J. Photoch. Photobio. A*, **2016**, 314, 178-188.
- Katsumata, H.; Kaneco, S.; Suzuki, T.; Ohta, K.; Yobiko, Y. Degradation of linuron in aqueous solution by the photo-Fenton reaction. *Chem. Eng. J.*, **2005**, 108(3), 269-276.
- Kaur, H.; Sundriyal, S.; Pachauri, V.; Ingebrandt, S.; Kim, K. H.; Sharma, A. L.; Deep, A. Luminescent metal-organic frameworks and their composites: Potential future materials for organic light emitting displays. *Coord. Chem. Rev.*, **2019**, 401, 213077.
- Keller, J. U.; Staudt, R. Gas adsorption equilibria: experimental methods and adsorptive isotherms. *Springer Science & Business Media*, **2005**.
- Kerr, A. T.; Ridenour, J. A.; Noring, A. A.; Cahill, C. L. Two uranyl-copper (II) bimetallic coordination polymers containing trans-3, 3 (pyridyl) acrylic acid: Structural variance through synthetic subtleties. *Inorganica Chim. Acta*, **2019**, 494, 204-210.

CHAPTER 1

- Kim, S.; Dawson, K. W.; Gelfand, B. S.; Taylor, J. M.; Shimizu, G. K. H. Enhancing Proton Conduction in a Metal-Organic Framework by Isomorphous Ligand Replacement. *J. Am. Chem. Soc.*, **2013**, 135, 963-966.
- Kirchon, A.; Zhang, P.; Li, J.; Joseph, E. A.; Chen, W.; Zhou, H. C. Effect of Isomorphous Metal Substitution on the Fenton and Photo-Fenton Degradation of Methylene Blue Using Fe-Based Metal-Organic Frameworks. *ACS Appl. Mater. Interfaces*, **2020**, 12(8), 9292-9299
- Kitagawa, S.; Kitaura, R.; Noro, S. I. Functional Porous Coordination Polymers. *Angew. Chem.*, **2004**, 43(18), 2334-2375.
- Kreuer, K. D.; Rabenau, A.; Weppner, W. Vehicle Mechanism, a New Model for the Interpretation of the Conductivity of Fast Proton Conductors. *Angew. Chem.*, **1982**, 21(3), 208-209.

L

- Le Bideau, J.; Payen, C.; Palvadeau, P.; Bujoli, B. Preparation, Structure, and Magnetic Properties of Copper (II) Phosphonates. β -Cu^{II}(CH₃PO₃), an Original Three-Dimensional Structure with a Channel-Type Arrangement. *Inorg. Chem.*, **1994**, 33(22), 4885-4890.
- Le Bideau, J.; Payen, C.; Bujoli, B.; Palvadeau, P.; Rouxel, J. A new family of 2D antiferromagnets: the layered phosphonates M^{II}(RPO₃)·H₂O; M= Mn, Fe, Co, Ni; R= alkyl, phenyl. *J. Magn. Magn. Mater.*, **1995**, 140, 1719-1720.
- Li, J. R.; Kuppler, R. J.; Zhou, H. C. Selective gas adsorption and separation in metal-organic frameworks. *Chem. Soc. Rev.*, **2009**, 38(5), 1477-1504.
- Li, X.; Liu, J.; Rykov, A. I.; Han, H.; Jin, C.; Liu, X.; Wang, J. Excellent photo-Fenton catalysts of Fe-Co Prussian blue analogues and their reaction mechanism study. *Appl. Catal. B: Environ.*, **2015**, 179, 196-205.
- Li, Y.; Liu, H.; Li, W. J.; Zhao, F. Y.; Ruan, W. J. A nanoscale Fe(II) metal-organic framework with a bipyridinedicarboxylate ligand as a high performance heterogeneous Fenton catalyst. *RSC Adv.*, **2016**, 6(8), 6756-6760.
- Li, A. L.; Gao, Q.; Xu, J.; Bu, X. H. Proton-conductive metal-organic frameworks: Recent advances and perspectives. *Coord. Chem. Rev.*, **2017a**, 344, 54-82.
- Li, K.; Zhao, Y.; Janik, M. J.; Song, C.; Guo, X. Facile preparation of magnetic mesoporous Fe₃O₄/C/Cu composites as high performance Fenton-like catalysts. *Appl. Surf. Sci.*, **2017b**, 396, 1383-1392.

- Li, N.; Feng, R.; Zhu, J.; Chang, Z.; Bu, X. H. Conformation versatility of ligands in coordination polymers: From structural diversity to properties and applications. *Coord. Chem. Rev.*, **2018**, 375, 558-586.
- Li, G. B.; Song, B. Q.; Wang, S. Q.; Pei, L. M.; Liu, S. G.; Song, J. L.; Yang, Q. Y. Selective Adsorption of Water, Methanol, and Ethanol by Naphthalene Diimide-Based Coordination Polymers with Constructed Open Cu²⁺ Metal Sites and Separation of Ethanol/Acetonitrile. *ACS Omega*, **2019a**, 4(1), 1995-2000.
- Li, H.; Li, L.; Lin, R. B.; Zhou, W.; Zhang, Z.; Xiang, S.; Chen, B. Porous metal-organic frameworks for gas storage and separation: Status and challenges. *Energy Chem.*, **2019b**, 1(1), 100006.
- Li, Z.; Peng, Y.; Xia, X.; Cao, Z.; Deng, Y.; Tang, B. Sr/PTA Metal Organic Framework as A Drug Delivery System for Osteoarthritis Treatment. *Sci Rep.*, **2019c**, 9, 17570.
- Li, J. F.; Du, P.; Liu, Y. Y.; Xu, G. H.; Ma, J. F. Three thiacalix[4]arene-based Cu(I) coordination polymers: catalytic activities for azide-alkyne cycloaddition reactions and luminescence properties. *Dalton Trans.*, **2020**, 49, 3715-3722.
- Liang, X.; Zhang, F.; Feng, W.; Zou, X.; Zhao, C.; Na, H.; Liu, C.; Sun, F.; Zhu, G. From metal-organic framework (MOF) to MOF-polymer composite membrane: enhancement of low-humidity proton conductivity. *Chem. Sci.*, **2013**, 4(3), 983-992.
- Liang, R.; Luo, S.; Jing, F.; Shen, L.; Qin, N.; Wu, L. A simple strategy for fabrication of Pd@MIL-100(Fe) nanocomposite as a visible-light-driven photocatalyst for the treatment of pharmaceuticals and personal care products (PPCPs). *Appl. Catal. B: Environ.*, **2015**, 176, 240-248.
- Liang, J.; Zhang, J.; Liang, J.; Zhai, L.; Wu, H.; Niu, X.; Hu, T. Five new coordination polymers with a Y-shaped N-heterocyclic carboxylic acid: structural diversity, bifunctional luminescence sensing and magnetic properties. *Cryst. Eng. Comm.*, **2019**, 21(38), 5767-5778.
- Lin, Y. P.; Zhou, T. Syntheses, crystal structures, and characterizations of a series of divalent metal carboxylate-phosphonates. *J. Solid State Chem.*, **2020**, 287, 121343.
- Liu, R.; Zhao, L.; Yu, S.; Liang, X.; Li, Z.; Li, G. Enhancing Proton Conductivity of a 3D Metal-Organic Framework by Attaching Guest NH₃ Molecules. *Inorg. Chem.*, **2018**, 57(18), 11560-11568.

CHAPTER 1

Liu, J. Q.; Luo, Z. D.; Pan, Y.; Singh, A. K.; Trivedi, M.; Kumar, A. Recent developments in luminescent coordination polymers: Designing strategies, sensing application and theoretical evidences. *Coord. Chem. Rev.*, **2020**, 406, 213145.

M

Mao, C.; Kudla, R. A.; Zuo, F.; Zhao, X.; Mueller, L. J.; Bu, X.; Feng, P. Anion Stripping as a General Method to Create Cationic Porous Framework with Mobile Anions. *J. Am. Chem. Soc.*, **2014**, 136(21), 7579-7582.

Meng, X.; Wang, H. N.; Song, S. Y.; Zhang, H. J. Proton-conducting crystalline porous materials. *Chem. Soc. Rev.*, **2017**, 46(2), 464-480.

Meng, X.; Wei, M. J.; Wang, H. N.; Zang, H. Y.; Zhou, Z. Y. Multifunctional luminescent Zn(II)-based metal-organic framework for high proton-conductivity and detection of Cr³⁺ ions in the presence of mixed metal ions. *Dalton Trans.*, **2018**, 47(5), 1383-1387.

Moorthy, J. N.; Vittal, J. J. Coordination polymers. *J. Mol. Struct.*, **2006**, 796.

Morsali, A.; Hashemi, L. Main Group Metal Coordination Polymers. *John Wiley & Sons, Inc.*, **2017**.

N

Nagarkar, S. S.; Unni, S. M.; Sharma, A.; Kurungot, S.; Ghosh, S. K. Two-in-One: Inherent Anhydrous and Water-Assisted High Proton Conduction in a 3D Metal-Organic Framework. *Angew. Chem.*, **2014**, 53(10), 2638-2642.

Natarajan, S.; Mahata, P. Non-carboxylate based metal-organic frameworks (MOFs) and related aspects. *Curr. Opin. Solid State Mater. Sci.*, **2009**, 13(3-4), 46-53.

O

Orellana-Tavra, C.; Köppen, M.; Li, A.; Stock, N.; Fairen-Jimenez, D. Biocompatible, crystalline and amorphous bismuth-based metal-organic frameworks for drug delivery. *ACS Appl. Mater. Interfaces*, **2020**, 12(5), 5633-5641.

P

Pan, L.; Adams, K. M.; Hernandez, H. E.; Wang, X.; Zheng, C.; Hattori, Y.; Kaneko, K. Porous Lanthanide-Organic Frameworks: Synthesis, Characterization, and Unprecedented Gas Adsorption Properties. *J. Am. Chem. Soc.*, **2003**, 125(10), 3062-3067.

Park, K. S.; Ni, Z.; Côté, A. P.; Choi, J. Y.; Huang, R.; Uribe-Romo, F. J.; Chae, H. K.; O'Keeffe, M.; Yaghi, O. M. Exceptional chemical and thermal stability of

zeolitic imidazolate frameworks. *Proc. Natl. Acad. Sci.*, **2006**, 103(27), 10186-10191.

Peh, S. B.; Karmakar, A.; Zhao, D. Multiscale Design of Flexible Metal–Organic Frameworks. *Trends in Chemistry*, **2019**, 2(3), 199-213.

Pham, H.; Ramos, K.; Sua, A.; Acuna, J.; Slowinska, K.; Nguyen, T.; Bui, A.; Weber, M. D. R.; Tian, F. Tuning Crystal Structures of Iron-Based Metal–Organic Frameworks for Drug Delivery Applications. *ACS Omega*, **2020**, 5(7), 3418-3427.

Poojary, M. D.; Hu, H. L.; Campbell, F. L.; Clearfield, A. Determination of crystal structures from limited powder data sets: crystal structure of zirconium phenylphosphonate. *Acta Crystallogr. B*, **1993**, 49(6), 996-1001.

Puthiaraj, P.; Ahn, W. S. Metal–Organic Frameworks as Catalysts in Catalyst Immobilization: Methods and Applications, *Wiley Online Library*, **2020**, Ch. 5, 159-185.

Q

Qin, L.; Li, Z.; Xu, Z.; Guo, X.; Zhang, G. Organic-acid-directed assembly of iron-carbon oxides nanoparticles on coordinatively unsaturated metal sites of MIL-101 for green photochemical oxidation. *Appl. Catal. B: Environ.*, **2015**, 179, 500-508.

R

Ramaswamy, P.; Wong, N. E.; Gelfand, B. S.; Shimizu, G. K. A water stable magnesium MOF that conducts protons over 10^{-2} S·cm⁻¹. *J. Am. Chem. Soc.*, **2015**, 137(24), 7640-7643.

Rowsell, J. L. C.; Yaghi, O. M. Effects of Functionalization, Catenation, and Variation of the Metal Oxide and Organic Linking Units on the Low-Pressure Hydrogen Adsorption Properties of Metal–Organic Frameworks. *J. Am. Chem. Soc.*, **2006**, 128(4), 1304-1315.

S

Sang, X.; Hu, X.; Tao, R.; Zhang, Y.; Zhu, H.; Wang, D. A Zirconium Indazole Carboxylate Coordination Polymer as an Efficient Catalyst for Dehydrogenation-Cyclization and Oxidative Coupling Reactions. *ChemPlusChem*, **2020**, 85(1), 123-129.

Schneemann, A.; Bon, V.; Schwedler, I.; Senkowska, I.; Kaskel, S.; Fischer, R. A. Flexible metal-organic frameworks. *Chem. Soc. Rev.*, **2014**, 43(16), 6062-6096.

CHAPTER 1

- Shearan, S. J.; Stock, N.; Emmerling, F.; Demel, J.; Wright, P. A.; Demadis, K. D.; Vassaki, M.; Constantino, F.; Vivani, R.; Sallard, S.; Salcedo, I. R. (2019). New Directions in Metal Phosphonate and Phosphinate Chemistry. *Crystals*, **2019**, 9(5), 270.
- Shi, T.; Peng, J.; Chen, J.; Sun, C.; He, H. Heterogeneous Photo-Fenton Degradation of Norfloxacin with Fe₃O₄-Multiwalled Carbon Nanotubes in Aqueous Solution. *Catal. Lett.*, **2017**, 147(6), 1598-1607.
- Shigematsu, A.; Yamada, T.; Kitagawa, H. Wide control of proton conductivity in porous coordination polymers. *J. Am. Chem. Soc.*, **2011**, 133(7), 2034-2036.
- Shimizu, G. K. H.; Vaidhyanathan, R.; Taylor, J. M. Phosphonate and sulfonate metal organic frameworks. *Chem. Soc. Rev.*, **2009**, 38, 1430-1449
- Stock, N.; Bein, T. High-Throughput Synthesis of Phosphonate-Based Inorganic-Organic Hybrid Compounds under Hydrothermal Conditions. *Angew. Chem.*, **2004**, 43(6), 749-752.

T

- Taylor, J. M.; Dawson, K. W.; Shimizu, G. K. A Water-Stable Metal-Organic Framework with Highly Acidic Pores for Proton-Conducting Applications. *J. Am. Chem. Soc.*, **2013**, 135(4), 1193-1196.

V

- Vivani, R.; Costantino, F.; Taddei, M. Zirconium Phosphonates. In Metal Phosphonate Chemistry. *RSC: Cambridge*, **2012**; Ch.2, p. 45-86.
- Vu, T. A.; Le, G. H.; Dao, C. D.; Dang, L. Q.; Nguyen, K. T.; Dang, P. T.; Tran, H. T. K.; Duong, Q. T.; Nguyen, T. V.; Lee, G. D. Isomorphous substitution of Cr by Fe in MIL-101 framework and its application as a novel heterogeneous photo-Fenton catalyst for reactive dye degradation. *RSC Adv.*, **2014**, 4(78), 41185-41194.

W

- Wahiduzzaman, M.; Wang, S.; Schnee, J.; Vimont, A.; Ortiz, V.; Yot, P. G.; Retoux, R.; Daturi, M.; Lee, J. S.; Chang, J. S.; Serre, C.; Maurin, G.; Devautour-Vinot, S. A High Proton Conductive Hydrogen-Sulfate Decorated Titanium Carboxylate Metal-Organic Framework. *ACS Sustainable Chem. Eng.*, **2019**, 7(6), 5776-5783.
- Wang, L.; Zheng, M.; Xie, Z. Nanoscale metal-organic frameworks for drug delivery: a conventional platform with new promise. *J. Mater. Chem. B*, **2018**, 6(5), 707-717.

Wei, Y. S.; Hu, X. P.; Han, Z.; Dong, X. Y.; Zang, S. Q.; Mak, T. C. Unique Proton Dynamics in an Efficient MOF-Based Proton Conductor. *J. Am. Chem. Soc.*, **2017**, 139(9), 3505-3512.

Wu, Q.; Yang, H.; Kang, L.; Gao, Z.; Ren, F. Fe-based metal-organic frameworks as Fenton-like catalysts for highly efficient degradation of tetracycline hydrochloride over a wide pH range: Acceleration of Fe (II)/Fe (III) cycle under visible light irradiation. *Appl. Catal. B: Environ.*, **2020**, 263, 118282.

X

Xie, X. X.; Yang, Y. C.; Dou, B. H.; Li, Z. F.; Li, G. Proton conductive carboxylate-based metal-organic frameworks. *Coordi. Chem. Rev.*, **2020**, 403, 213100.

Xing, X. S.; Fu, Z. H.; Zhang, N. N.; Yu, X. Q.; Wang, M. S.; Guo, G. C. High proton conduction in an excellent water-stable gadolinium metal-organic framework. *Chemical communications*, **2019**, 55(9), 1241-1244.

Y

Yamada, T.; Sadakiyo, M.; Kitagawa, H. High Proton Conductivity of One-Dimensional Ferrous Oxalate Dihydrate. *J. Am. Chem. Soc.*, **2009**, 131(9), 3144-3145.

Yamada, T.; Otsubo, K.; Makiura, R.; Kitagawa, H. Designer coordination polymers: dimensional crossover architectures and proton conduction. *Chem. Soc. Rev.*, **2013**, 42(16), 6655-6669.

Z

Zhang, Y.; Yuan, S.; Day, G.; Wang, X.; Yang, X.; Zhou, H. C. Luminescent sensors based on metal-organic frameworks. *Coord. Chem. Rev.*, **2018**, 354, 28-45.

Zhang, X.; Wang, X.; Fan, W.; Wang, Y.; Wang, X.; Zhang, K.; Sun, D. A multifunctional Zr-MOF for the rapid removal of $\text{Cr}_2\text{O}_7^{2-}$, efficient gas adsorption/separation, and catalytic performance. *Mater. Chem. Front.*, **2020**, 4, 1150-1157

Zima, V.; Svoboda, J.; Melánová, K.; Beneš, L.; Casciola, M.; Sganappa, M.; Brus, J.; Trchová, M. Synthesis and characterization of new zirconium 4-sulfophenylphosphonates. *Solid State Ion.*, **2010**, 181(15-16), 705-713.

Zon, J.; Garczarek, P.; Bialek, M. Synthesis of Phosphonic Acids and Their Ester as Possible Substrates for Reticular Chemistry in Metal Phosphonate Chemistry: From Synthesis to Applications. *RSC: Cambridge*, **2012**, Ch. 6, p.170-191.



UNIVERSIDAD
DE MÁLAGA

Chapter 2

Objectives





UNIVERSIDAD
DE MÁLAGA

The main objective of this research is obtaining new multifunctional phosphonate-based coordination polymers and studying their proton conductivity properties, as well as the photocatalytic behaviour and photoluminescence properties of some of them, in order to establish useful structure-properties relationships. In doing so, the following partial goals have been devised:

- Synthesis of new crystalline Fe(II)- and bimetallic Fe(II)-based 2-hydroxyphosphonoacetates, transition metal- and lanthanide-sulfophosphonates, sulfate-containing lanthanide aminotrismethylenephosphonates and, finally, alkali metal- and alkaline-earth metal- hexamethylenediamine tetramethylenephosphonates. For this task, optimal synthesis conditions have to be determined by using systematic synthetic methodologies.
- Solving the crystal structures of the metal phosphonates by single crystal, where possible, or from laboratory X-ray powder diffraction data. In special cases, synchrotron X-ray powder diffraction can be also a choice. To provide information about local bonding environments of amorphous solids, total scattering data analysed by the Pair Distribution Function (PDF) methodology are foreseeably.
- Full characterisation of the solids, in addition to the acquired structural information, by using a number of chemical-physical techniques, among them TG-DTA, ICP-MS, XPS, FT-IR and SEM.
- Study of the photocatalytic activity of Fe(II)-based 2-hydroxyphosphonoacetates as heterogeneous Photo-Fenton catalysts in processes of degradation/mineralization of recalcitrant water pollutants, such as phenol, 4-chlorophenol and methylene blue, under visible and UV-A light.
- Study of photoluminescence properties focused on lanthanide phosphonates, in particular, solid solutions containing Eu^{3+} and Tb^{3+} as dopants, because they present characteristic emission lines in the range of the visible spectrum.

CHAPTER 2

- Studies on proton conductivity of the as-synthesized and post synthesis-modified solids focusing on correlations between properties and structural features and/or changes in composition. From the impedance measurements, proton transfer mechanisms, Grotthuss-type or vehicular, will be determined.
- Preparation and characterization of Nafion[®]-based composite membranes employing different loads of selected metal phosphonates as fillers, in order to investigate their performance in MEAs, under the operation conditions of PEMFCs.

Chapter 3

Instrumental Techniques





UNIVERSIDAD
DE MÁLAGA

3.1. C, H, N and S Elemental Analysis

3.1.1. Basic Principles

CHNS elemental analysis provides the determination of carbon, hydrogen, nitrogen and sulphur in a wide range of materials (organic and inorganic; solids, liquids, volatile and viscous samples).

CHNS elemental analyser requires a combustion process, where carbon is converted to CO_2 , hydrogen to H_2O , nitrogen to N_2 or nitrogen oxides and sulphur to SO_2 . If other elements are present in the sample, they will also be converted to combustion products. However, a wide number of absorbents are employed to remove these additional products. Furthermore, catalysts are present in the combustion tube in order to aid conversion. Combustion products are carried by a gas flow, such as helium, and pass through a heated high purity copper, which converts any nitrogen oxides to N_2 and removes any oxygen not consumed in the initial combustion. Detection process can be carried out in different ways, for instance employing a chromatographic column, infra-red, thermal conductivity cells, etc. Elements quantification requires calibration for each one, employing high purity standards such as acetanilide and benzoic acid (Thompson, 2008).

This technique is used together with the TG-DTA to determine the stoichiometry of the sample.

3.1.2. Instrumentation

CHNS elemental analysis were carried out on an TruSpec Micro CHN/CHNS/O and TruSpec Macro CHN/CHNS at SCAI (University of Málaga). This analyser heated over 1300 °C to achieve a total combustion of the sample under an oxygen atmosphere.

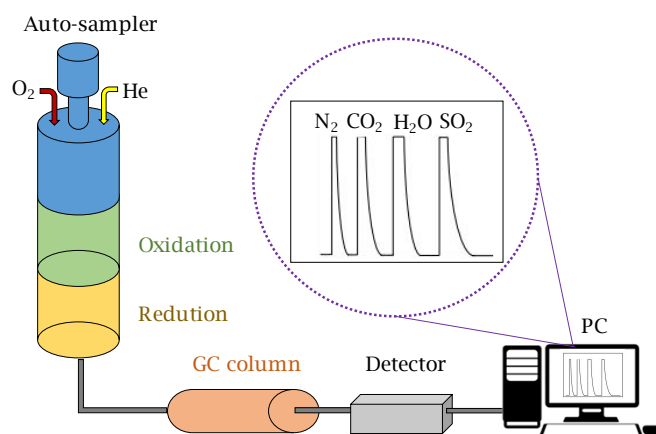


Figure 3.1. Schematic operation of a general CHNS analyser.

3.2. Thermogravimetric and Differential Thermal Analysis (TG-DTA)

3.2.1. Basic Principles

Thermogravimetric (TG) and differential thermal analysis (DTA) is a measuring technique, which study the response of a material to being heated in comparison with a reference sample such as Al₂O₃, which remains stable in the experimental conditions. TG analysis measures the weight change while DTA allows to know if the sample absorbs or releases energy as a function of the temperature in a particular experimental condition. Both techniques together allow us to correlate the observed weight losses to the released or absorbed energy, identifying the type of process that takes place:

- (i) Exothermic process, due to reactions or process that release energy in the form of heat from the system to its surroundings, such as oxidations, combustions, etc.
- (ii) Endothermic process, reactions or process that absorb energy in the form of heat from its environment, such as dehydration, changes of the state, etc.

This technique is commonly used to characterise the decomposition product as well as the thermal stability of the sample in a temperature range (Young & Weller, 2017e).

3.2.2. Instrumentation

TG-DTA were recorded on an SDT-Q600 thermal analyser from TA instruments at University of Málaga. This analyser provides simultaneous measurement of TG and DTA curves from RT to 1500 °C. Furthermore, it features with horizontal dual beam and two different gas inlets (air and N₂). It can be computer controlled through Q Series software. Measurements were carried out on samples in open platinum pans (100 µL) from RT to 900-1000 °C with a heating rate of 10 °C·min⁻¹ and under air or N₂ flow (100 mL·min⁻¹). The reference material employed was calcined Al₂O₃.

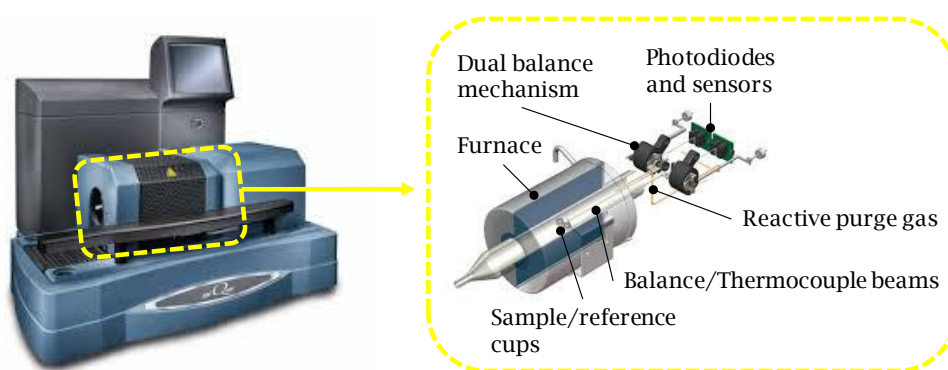


Figure 3.2. SDT-Q600 thermal analyser.

3.3. Inductively Coupled Plasma - Mass Spectrometry (ICP-MS)

3.3.1. Basic Principles

ICP-MS offers the possibility to detect a wide range of elements at low concentrations (ppm and ppt). Liquid sample is inserted with a peristaltic pump into a nebulizer, where the sample is converted into an aerosol with Ar gas. The aerosol is injected into the plasma torch. The plasma is generated by the interaction between an electromagnetic field, which is produced by radiofrequency (RF) energy passing through a Cu coil, and an Ar gas flowing through a torch. Plasma is an electrically neutral gas formed by cations and free electrons, having enough energy to ionize elements present in a sample. Plasma formation is initiated by the collision of accelerated electrons with the ionized gas (Ar). These collisions produce additional electrons, which sustain the plasma (inductive coupling). The ions produced in the plasma are conducted into the mass spectrometer under vacuum by the sampler and skinner cone (interface region). Optic lens direct the ion beam as well as stop photons and neutral species to reach the detector (Taylor, 2001; Thomas, 2013).

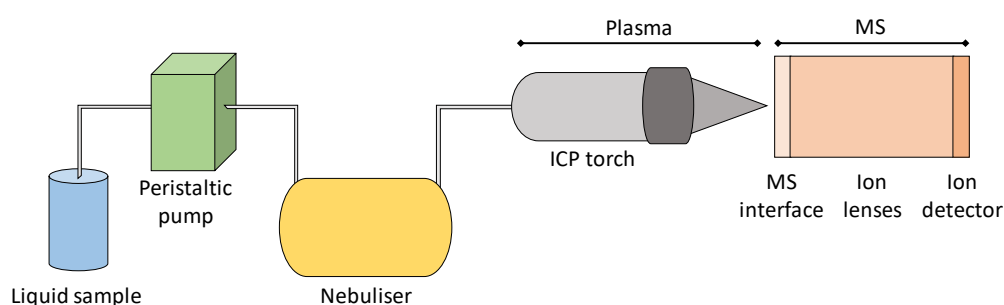


Figure 3.3. Schematic of ICP-MS.

3.3.2. Instrumentation

Samples were previously prepared as following. A quantity of the sample (50 mg) was digested in a $\text{HNO}_3:\text{H}_2\text{O}$ 1:1 solution (10 mL) under vigorous magnetic stirring. The solution was levelled with DI water in a 25 mL flask. ICP-MS analysis were carried out on a NexION 300X from Perkin-Elmer (Figure 3.4) at SCAI (University of Málaga). This instrument operates in three different modes: standard, collision and reaction, allowing us to choose the most appropriate technique for specific samples or application. Furthermore, it is equipped with a triple cone interface and a quadrupole ion deflector.



Figure 3.4. NexION 300X ICP-MS.

3.4. X-Ray Diffraction

3.4.1. Basic Principles

X-ray diffraction (XRD) is a non-destructive technique, which provides a complete structural description of crystalline samples. Although this method is

generally applicable to crystalline compounds, some structural information can be obtained from amorphous samples.

X-rays are electromagnetic waves in the wavelength range from 0.01 to 10 nm. When X-rays with a wavelength λ and an intensity I_0 interact with matter, they become attenuated (μ), absorbed (τ), scattered (σ) and undergo the so-called “pair-building” (π). Diffraction occurs when X-rays are scattered by a material. Regarding to scattering process, two main interactions can be distinguished: coherent (Thomson scattering, where X-rays are scattered elastically without change their energy values) and incoherent scatter (Compton scattering and fluorescence).

X-rays are commonly generate by (i) deflecting high-energy electrons by electromagnetic fields, typically used in synchrotrons, or (ii) bombarding an anode with a focused electron beam. Electrons are emitted by a hot filament (cathode) and accelerated by the high voltage difference between the anode and the cathode. The kinetic energy of electrons is converted into heat (99%) and X-ray radiation (1%). An atom consists of a nucleus surrounded by electrons grouped in shells. If an atom is irradiating with X-ray photons or electrons with appropriate energy, it can remove an electron, producing a void in a shell. Restoring the original configuration of the atom is carried out by transferring an electron from an outer shell, emitting the energy excess as an X-ray photon. The emitted radiation is characteristic for an atom due to each one has its specific energy levels.

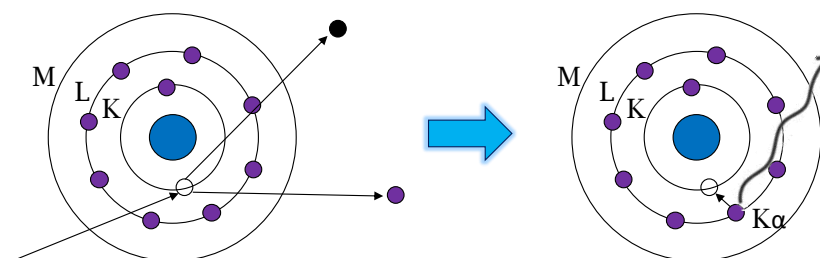


Figure 3.5. Production of characteristic radiation.

When a monochromatic X-ray beam with a wavelength of λ falls on a regular arrangement of atoms with an angle θ , it undergoes constructive interference leading to diffraction (Bragg's Law). This wavelength, λ , is comparable to the inter-atomic spacing of a crystal.

$$2d\sin\theta = n\lambda \quad \text{Equation 3.1}$$

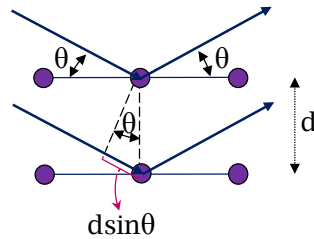


Figure 3.6. Bragg's Law.

Lattice planes are defined by Miller indices (h , k and l). The separation of these planes depends on dimensionality and symmetry of the unit cell, which is the smallest unit that has the full symmetry of the crystal and can build it up by translational displacements. The unit cell is defined by its lattice parameters: the length of the cell edges (a , b and c) and the angles between them (α , β and γ). There are seven crystal systems as a result of the relationship between the lattice parameters in three dimensions.

Table 3.1. The crystal systems.

System	Lattice parameters
Cubic	$a = b = c, \alpha = \beta = \gamma = 90^\circ$
Tetragonal	$a = b \neq c, \alpha = \beta = \gamma = 90^\circ$
Hexagonal	$a = b \neq c, \alpha = \beta = 90^\circ, \gamma = 120^\circ$
Trigonal	$a = b = c, \alpha = \beta = \gamma \neq 90^\circ$
Orthorhombic	$a \neq b \neq c, \alpha = \beta = \gamma = 90^\circ$
Monoclinic	$a \neq b \neq c, \alpha = \gamma = 90^\circ \neq \beta$
Triclinic	$a \neq b \neq c, \alpha \neq \beta \neq \gamma$

The intensity of the reflections is principally influenced by the structure factor (F_{hkl}), the amount of material and the absorption in the material while the shape of the diffraction peaks can be influenced by instrument and sample related effects.

The structure factor, F_{hkl} , is the sum of all the scattering of an X-ray beam by all the electrons in the crystal. The expression for the structure factor is:

$$F_{hkl} = \sum_j f_j e^{2\pi i(hx+ky+lz)} \quad \text{Equation 3.2}$$

where f_i is the scattering factor for an atom j located at (x, y, z) position.

Each scattered X-ray is defined by its amplitude, $|F_{hkl}|$, and the phase of the diffracted wave, φ_{hkl} .

$$F_{hkl} = |F_{hkl}|e^{i\varphi_{hkl}} \quad \text{Equation 3.3}$$

The intensity of a reflection, I_{hkl} , is proportional to the structure factor squared, being C_{hkl} a calculable constant dependent on the sample absorption and instrumental factors:

$$I_{hkl} = C_{hkl}F_{hkl}^2 \quad \text{Equation 3.4}$$

It is not possible to obtain directly the crystal structure from a diffraction experiment because the phases cannot be measured. However, it can be obtained indirectly from a set of amplitude values, $|F_{hkl}|$.

There are two main X-ray diffraction techniques, single crystal X-ray diffraction and X-ray powder diffraction (Ermrich & Opper, 2011; Young & Weller, 2017a).

3.4.2. Single Cristal X-Ray Diffraction (SCXRD)

In SCXRD, the sample is a single crystal, which is rotated around various axes in order to find a large number of different reflections. The crystal structure can be determined from the angular positions and the intensity of these reflections. There are different programs to obtain the structure solution from single crystal X-ray diffraction data such as SHELXL (Sheldrick, 2017) or Olex2 (Dolomanov et al., 2009).

3.4.3. X-Ray Powder Diffraction (XRPD)

Samples in a polycrystalline or powdered form contain a large number of small crystallites that adopt randomly a full range of possible orientations, being necessary to vary the incidence and diffraction angles. This technique can be used for different applications such as qualitative and quantitative phase identification, particle size determination, structural resolution, etc. (Young & Weller, 2017a).

3.4.3.1. Indexing and Space Group Determination

Indexing is the process of assigning Miller indices to each reflection to obtain the lattice parameters of the sample. It can be carried out using different programs such as DICVOL06 (Boultif & Louer, 2004), TREOR (Werner, Eriksson & Westdahl,

1985) or ITO (Visser, 1969). These programs propose possible unit cells based on at least 20 or 30 reflections. The best solution is one that presents a complete indexing of all reflections, a high figure of merit and the lowest volume of the unit cell. Once the lattice parameters are determined, the space group is obtained by looking for systematic extinctions. A high-quality powder diffraction data is necessary to obtain a correct indexing of the diffraction pattern.

3.4.3.2. Structural Resolution

Structural resolution from powder diffraction data is more difficult than from single crystal data. However, it is not always possible to obtain single crystals, so high-quality diffraction data are necessary for a successful structure solution.

As phases cannot be measured, a method of determining or assigning phases is needed. The most common are:

- (i) **The Patterson synthesis.** It is an appropriate method for structures containing a low number of heavy atoms (higher scattering powers). The Patterson function can be calculated from experimental data:

$$P_{xyz} = \frac{1}{V} \sum_{hkl} |F_{hkl}|^2 e^{-2\pi i(hx+ky+lz)} \quad \text{Equation 3.5}$$

A map of vectors between pairs of atoms can be obtained plotting P_{xyz} values (Patterson map). Heights of the peaks in the Patterson map are proportional to the scattering factors. The strongest peaks in the map correspond to the few vectors between heavy atoms. When heavy atoms are located from the Patterson map, their amplitudes and phases of the reflections can be calculated. Fourier electron density difference map can be employed to determine the rest of the structure.

- (ii) **Direct methods.** It is an appropriate method for compounds where the majority of the scattering atoms have similar atomic numbers. It consists of assigning phases to the strongest reflections observed in the diffraction pattern. The amplitudes combined with the correct phases must correspond to a positive electron density at each point in the unit cell. The structure can be deduced from the electron density map. In addition, Fourier electron density difference map can be employed to determine the rest of the structure.

(iii) Simulated annealing methods or direct space methods. These methods involves the generation of a random sequence of trial structures starting from an appropriate 3D model and moving it until a good match between the calculated and the observed pattern is found. The chemical knowledges of the molecules (bond distances, bond angles and ring conformation, etc.) are used to reduce the number of parameters to be varied during the procedure. It can be carried out using EXPO2014 program (Altomare et al., 2013).

3.4.3.3. Rietveld Refinement

Rietveld refinement is employed when the crystallographic structure of the material is known. It consists in minimize the difference between an experimental and a calculated diffraction pattern, employing an approximated structural model and parameters that allow to distribute the intensities of the different reflections in the diffraction pattern. Initial parameters has to be as close as possible to the final parameters. This method employs the entire diffraction pattern instead of the integrated intensities of the diffraction peaks, allowing to solve the overlap peak problem and to extract the maximum information from the diffraction pattern.

It is based on a least-squares refinement of a crystal structure that is employed as a starting model. The function to minimize is:

$$S_y = \sum_i w_i |y_i(o) - y_i(c)|^2 \quad \text{Equation 3.6}$$

where $y_i(o)$ and $y_i(c)$ are the observed and the calculated intensities of the i -th point respectively, and w_i is the weight assigned to each point.

Two types of data are necessary to obtain the calculated intensities, (i) atomic parameters such as atomic positions, atomic displacement parameters and site occupancies, and (ii) global parameters such as scale factors of each phase for crystalline compounds mixtures, background parameters, zero shift, profile function, unit cell parameters, preferred orientation, extinction and absorption parameters. Both types of parameters are optimised during the refinement process until the best fit is obtained.

CHAPTER 3

The calculated intensity, $y_i(c)$, for each point, $2\theta_i$, is obtained as the sum of all the background contribution, $b(2\theta_i)$, and reflections (k) contributions with intensity at that point of the diffraction pattern:

$$y_i(c) = b(2\theta_i) + S_\alpha \sum_k m_k |F_k|^2 h(2\theta_i - 2\theta_k) Lp(2\theta_i) P_k \quad \text{Equation 3.7}$$

where S_α is the scale factor of the α phase, k represents the Miller indices for one reflection, m_k is the multiplicity of the k reflection, $h(2\theta_i - 2\theta_k)$ is the function that describes the shape of the peaks, $Lp(2\theta_i)$ contains the Lorentz and polarization correction factors, P_k corrects absorption, extinction and preferred orientation effects and F_k is the structure factor.

Equation 3.7 can be extended to a sample that contains m crystalline phases:

$$y_i(c) = y_b(2\theta_i) + \sum_{i=1}^m S_i \sum_k m_k |F_k|^2 h(2\theta_i - 2\theta_k) Lp(2\theta_i) P_k \quad \text{Equation 3.8}$$

In Rietveld refinement, it is important to use high-quality diffraction data. There are three influencing factors of data quality: (i) the crystallinity of the sample, (ii) measurement conditions and (iii) the radiation employed (preferably monochromatic radiation, $K_{\alpha 1}$). Furthermore, soft constraints, such as angles or bond distances, can be added to increase the number of observations for the refinement. Soft constraints can be used when part of the geometry is known.

The quality of the refinement can be seen by different disagreement factors. Weight profile R-factor (R_{WP}) is the most common, employing all the diffraction pattern points:

$$R_{WP}(\%) = 100 \sqrt{\frac{\sum_{i=1}^n w_i [y_i(o) - y_i(c)]^2}{\sum_{i=1}^n w_i y_i(o)^2}} \quad \text{Equation 3.9}$$

Profile R-factor (R_p) also evaluate all the diffraction pattern points:

$$R_p(\%) = 100 \cdot \frac{\sum_{i=1}^n |y_i(o) - y_i(c)|}{\sum_{i=1}^n y_i(o)} \quad \text{Equation 3.10}$$

There is another set of disagreement factor values similar to those used for single crystal diffraction. In this case, it is calculated by the difference between the observed and calculated structure factors:

$$R_F(\%) = 100 \cdot \frac{\sum_{hkl} |F_{hkl}(o) - F_{hkl}(c)|}{\sum_{hkl} F_{hkl}(o)} \quad \text{Equation 3.11}$$

R-Bragg value (R_i) is obtained when the structure factors are changed by the intensities:

$$R_I(\%) = 100 \cdot \frac{\sum_{hkl} |I_{hkl}(o) - I_{hkl}(c)|}{\sum_{hkl} I_{hkl}(o)} \quad \text{Equation 3.12}$$

The observed R_{wf} should match the expected R_{exp} factor:

$$R_{exp}(\%) = 100 \sqrt{\frac{N - P + C}{\sum_{i=1}^n w_i y_i(o)^2}} \quad \text{Equation 3.13}$$

where N is the number of independent observations, P is the number of refinement parameters and C is the number of equation that restrict the refinement (Cabeza et al., 2014).

3.4.3.4. Synchrotron X-Ray Powder Diffraction

Synchrotron radiation is produced when relativistic electrons are accelerated in a circular orbit by the action of a magnetic field. Synchrotron sources generate more intense X-ray beams than laboratory diffractometers and over a wide range of energies, allowing to select a monochromatic wavelength using a monochromator. In addition, data collection is faster (Hulbert & Williams, 2000).

3.4.4. Pair Distribution Function

Amorphous compounds have only a short-range order of the atoms, which leads to very broad humps in the diffraction pattern instead of clear diffraction peaks. Pair Distribution Function (PDF) analysis is a powerful technique that allows studying amorphous as well as crystalline materials, providing information about distances between neighbouring atoms. The difference between conventional XRPD and PDF

CHAPTER 3

experiments is that the latter uses a wide-angular range over X-rays are detected and considers both diffuse and Bragg scattering. For that reason, PDF experiments are also called total scattering experiments.

PDF, $G(r)$, is the truncated Fourier transform of the total scattering structure function:

$$G(r) = \frac{2}{\pi} \int_{Q_{min}}^{Q_{max}} F(Q) \sin(Qr) dQ \quad \text{Equation 3.14}$$

The variable Q , which is used to measure location in reciprocal space, is the magnitude of the scattering momentum:

$$Q = \frac{4\pi \sin\theta}{\lambda} \quad \text{Equation 3.15}$$

where θ is half the scattering angle and λ is the X-ray wavelength. This magnitude should be as high as possible ($Q_{max} \sim 24\text{-}30 \text{ \AA}^{-1}$) while in standard XRD measurements Q_{max} is normally around 5 \AA^{-1} . However, Q_{max} is normally reduced below the experimental maximum to eliminate noisy data from the high- Q region of the PDF. PDF data can be collected from laboratory diffractometers, but Q_{max} tends to be limited and measurement times are long.

PDF data can be analysed directly, comparing experimentally determined PDF from samples under study and from known control samples, or through modelling, following the equation 3.16 to fit the PDF generated from a structure model to an experimental PDF. PDF data show the probability of finding atoms separated by distance- r and it is related to the atom pair density in the material.

$$G(r) = 4\pi r [\rho(r) - \rho_0] \quad \text{Equation 3.16}$$

$$\rho(r) = \frac{1}{4\pi r^2 N} \sum_i \sum_{j \neq i} \frac{b_i b_j}{\langle b \rangle^2} \delta(r - r_{ij}) \quad \text{Equation 3.17}$$

where ρ_0 is the atomic number density, $\rho(r)$ is the atomic pair density, b_i is the scattering factor of atom i , $\langle b \rangle$ is the average scattering factor and r_{ij} is the distance between atoms i and j (Billinge, 2019).

PDF fitting is carried out by adjusting structure model parameters, such as lattice parameters, atom position, atomic displacement parameters, to minimize the agreement between the theoretical and an experimental PDF. It can be fitted using PDFgui software (Farrow et al., 2007). The standard data reduction can be obtained by PDFgetX3 (Juhàs et al., 2013).

3.4.5. Instrumentation

SCXRD data were collected at RT on a Bruker SMART APEX II diffractometer using graphite-monochromated Mo $K\alpha$ radiation ($\lambda = 0.71073 \text{ \AA}$) at IACT-CSIC (Granada, Spain) or on a Rigaku AFC-12 goniometer with a conventional sealed Mo X-ray tube ($\lambda = 0.770 \text{ \AA}$) and a Saturn 724+ CCD detector at University of Southampton (United Kingdom). Structures were solved by employing SHELXTL direct methods and refined by full-matrix least squares on F2, using the APEX2 software package (Bruker, 2014). All non-H atoms were refined with independent anisotropic displacement parameters, while H atoms were placed at calculated positions and refined using a riding model, except for the water, phosphonic acid and hydrogensulfate O–H hydrogens. These H atoms were located from the Fourier difference density maps and refined using a riding model with O–H distance restraints.

Three different diffractometers have been employed to collect PXRD data: Empyrean and X'Pert PRO MPD from PANalytical and D8 ADVANCE from Bruker. Empyrean PANalytical diffractometer (Cu $K\alpha_{1,2}$) is equipped with a PIXcel 1D detector in a Bragg-Brentano configuration. X'Pert PRO MPD diffractometer allows to collect data in Bragg-Brentano reflection configuration using a X'Celerator detector and equipped with a Ge (111) primary monochromator (Cu $K\alpha_1$). D8 ADVANCE diffractometer is equipped with a Johansson Ge (111) primary monochromator (Mo $K\alpha_1$, $\lambda = 0.7093 \text{ \AA}$). Data were collected in transmission geometry (θ/θ).

Some of the crystal structures were solved following an *ab initio* methodology. The program DAJUST (Vallcorba et al., 2012) was used to extract the integrated intensities. The structure determination was carried out by direct methods employing the program XLENS (Rius, 2011) or EXPO2014 (Altomare et al., 2013). Missing atoms were localized by difference Fourier maps. Finally, structural model were optimized by the Rietveld method (Rietveld, 1969) using the program GSAS

CHAPTER 3

(Larson & von Dreele, 2000) and the graphical interface EXPEGUI (Toby, 2001). Soft constraints were used to maintain chemically reasonable geometries (Table 3.2). Other crystal structures were solved by Rietveld refinement using a crystal structure as starting model.

Table 3.2. Soft constraints employed for the Rietveld refinements.

Geometry	Bond (-) or angle (···)	Distance (Å)
PO₃C tetrahedron	P-O	1.53(1)
	P-C	1.80(1)
	O···O	2.55(2)
	O···C	2.73(2)
N(CH₂)₃ Amine group	N-C	1.50(1)
	C···C	2.45(2)
	N···P	2.68(2)
Alkyl chain	C-C	1.50(1)
	C _{chain} ···C _{chain}	2.50(2)
C₁OH-C₂OO group	C ₁ -C ₂	1.50(1)
	C ₂ -O _{carb}	1.23(1)
	C ₁ -OH	1.40(1)
	C ₂ ···OH	2.40(2)
	P···OH	2.68(2)
	O _{carb} ···O _{carb}	2.21(2)
	C ₁ ···O _{carb}	2.36(2)
SO₃C tetrahedron	S-O	1.46(1)
	S-C _{chain}	1.78(1)
	O···O	2.45(2)
	O···C	2.58(2)
	SO₄ tetrahedron	S-O
O···O		2.45(2)

Thermodiffraction studies were carried out employing an Anton Paar TTK450 or HTK1200N camera under static air. Data were collected at different temperature intervals, in general from RT up to 270 °C. It was used a heating rate of 5 °C·min⁻¹ and a delay time between 5 and 15 minutes to ensure thermal stabilisation. Data acquisition range was 4-70° (2θ) with a step size of 0.017° and an equivalent counting

time of 230 s per step. Crystallographic studies at different temperature and relative humidity values were carried out using an Anton Paar MHC-trans chamber. Data were collected at different temperature intervals, from RT up to 80 °C and 95% RH. A heating rate of 1 °C·min⁻¹ and a delay time of 10 minutes was employed to ensure that any transformation took place. Crystallite sizes were calculated from Williamson-Hall plot. HighScore Plus v4.6a (PANalytical B.V.) software and LaB₆ as standard were used to determinate the instrumental resolution function.

Synchrotron X-ray diffraction data were collected on beamline ID15A at ESRF (Grenoble, France) as well as beamline BL04-MSPD at ALBA synchrotron (Barcelona, Spain). At ID15A beamline, the beam was monochromated with a double bent Laue monochromator ($\lambda = 0.18972$ Å). Data were collected in transmission geometry using a Pilatus3 X CdTe 2 M hybrid proton counting detector with a pixel size of 172x172 μm^2 . Five patterns were collected (acquisition time of 8 s per pattern) over the angular range of 0.95-13.5°. On the other hand, at ALBA synchrotron, the wavelength was selected with a double-crystal Si (111) monochromator and determined from Si (NIST 640d) standard ($a = 5.43123$ Å) measurements. The detector system was the MYTHEN, which allows fast collection of good resolution patterns over an angular range of 1.2-40° (2 θ). In both cases borosilicate glass capillaries (0.7 mm of diameter) was rotated during data collection. In addition, in situ synchrotron powder diffraction data were collected under different pressures of CO₂ (up to 10 bar) and temperatures (from RT up to 200 °C) using the ICP-ITQ-ICIQ-ALBA capillary flow cell. This cell allows to perform high pressure (up to 15 bar) and high temperature (up to 750 °C) experiments with a flow gas.

For PDF analysis, XRPD data were collected on beamline BL04-MSPD at ALBA synchrotron (Barcelona, Spain). Data were collected in transmission (Debye-Scherrer mode) using a wavelength of 0.4124(1)Å (30 keV) selected with a double-crystal Si (111) monochromator and determined from a Si standard (NIST 640d) measurement. A MYTHEN detector was employed. Five patterns for each sample were collected (adquisition time of 37 minutes per each pattern) and added to minimize the signal-to-noise ratio. Samples were placed into glass capillaries (0.7 mm of diameter), which rotated during data adquisition to improve diffracting particle statistics. PDF experimental data were obtained using PDFgetX3 with $Q_{\text{max}} = 24$ Å⁻¹ and fitted using PDFgui software. Global optimized parameters were: scale factor, unit cell parameters, atomic displacement parameters (ADPs) and atomic positions (in some selected cases). In addition, delta-2 parameter (low-r correlated motion peak

sharpening factor) was refined for the low- r region fits. Measuring a similar data set for crystalline nickel, instrumental parameters were obtained ($Q_{\text{broad}} = 0.00273 \text{ \AA}^{-1}$ and $Q_{\text{damp}} = 0.00738 \text{ \AA}^{-1}$). The standard data reduction obtained by PDFgetX3 does not include the standard deviations of G , so result errors cannot be reported.

3.5. X-Ray Photoelectron Spectroscopy (XPS)

3.5.1. Basic Principles

XPS surface analysis instruments employ soft X-rays to excite and, therefore, provide information on core electron energy levels. Normally, a magnesium or aluminium anode is employed in laboratory XPS as source for the X-rays. This anode is bombarded by a high-energy electron beam, producing soft X-ray radiation. The X-ray photons produced are directed onto the sample, causing ionisations from core orbitals in the elements present. As the ionisation energies are characteristic of each element and its oxidation state, this technique provides information about which elements are present as well as their oxidation states. It is usually employed to determine chemical composition and environment from the surface of the sample (Young & Weller, 2017d).

3.5.2. Instrumentation

XPS analysis were performed on a Physical Electronics ESCA 5701 spectrometer at SCAI (University of Málaga). This instrument is equipped with a multichannel detector and a hemispheric analyser. The X-ray source employed was Mg $K\alpha$ ($h\nu = 1253.6 \text{ eV}$) or Al $K\alpha$ ($h\nu = 1486 \text{ eV}$), operating at 300 W (15kV, 20 mA) with an angle of 45° and a step energy of 29.35 eV. The pressure of the analytic chamber was $8 \cdot 10^{-7} \text{ Pa}$.

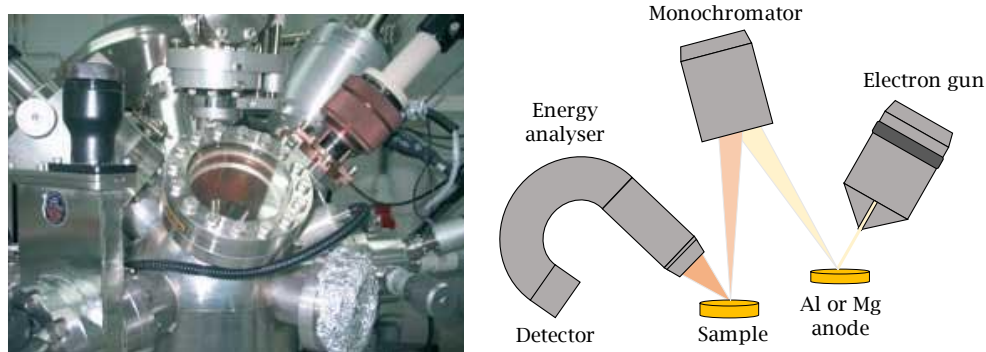


Figure 3.7. Physical Electronics ESCA 5701 XPS instrument.

3.6. Scanning Electron Microscopy (SEM)

3.6.1. Basic Principles

SEM measurements provide information about morphology and chemical composition of materials. Scanning electron microscope (SEM) operates like a conventional optical microscope but employing electrons instead of photons. A tungsten filament (W) or lanthanum hexaboride (LaB₆) cathode is employed to create an electron beam, which is accelerated using a potential between 0.2 and 50 keV. This electron beam is focused to a 0.4-5 mm spot using electric fields and it can penetrate 100 nm - 5 μm into the surface, depending on different parameters such as the energy of the electron beam and the density and atomic mass of the sample. The electron beam scans over the surface of the sample, interacting by three main processes: (i) reflection of high-energy electrons by elastic scattering, (ii) emission of secondary electrons by inelastic scattering and (iii) production of X-rays. Each of these interactions can be studied with different detectors. The X-rays produced by the interaction with the electron beam can be studied by energy dispersive analysis of X-rays (EDX) or energy dispersive spectroscopy (EDS), giving information about chemical composition of the sample surface. An image of the sample can be obtained by imaging the backscattered electrons (Leng, 2009; Young & Weller, 2017d).

3.6.2. Instrumentation

SEM and EDS measurements were carried out on a Helios Nanolab 650 (FEI Company) equipped with an Oxford EDX detector at SCBI (University of Málaga). Samples were placed on the sample support using a conductive double coated carbon tape as adhesive and metallised using Ir.

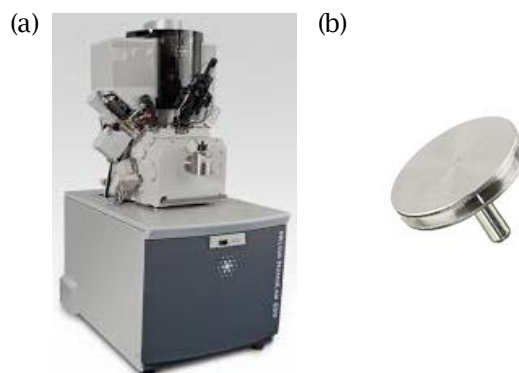


Figure 3.8. (a) Helios Nanolab 650 microscope and (b) SEM pin stub.

3.7. Fourier Transform Infrared Spectroscopy (FT-IR)

3.7.1. Basic Principles

In FT-IR spectroscopy, the sample is exposed to IR radiation ($100\text{-}4000\text{ cm}^{-1}$), involving vibrational motion of atoms in molecules. Some of this radiation is absorbed by the sample and some of it transmitted. The IR beam passes to the detector and FT-IR spectrum is obtained by Fourier transformation (Young & Weller, 2017c).

This technique is widely employed to characterise organic and inorganic compounds due to vibrational frequencies are characteristic of each functional group presents in the sample.

3.7.2. Instrument

FT-IR spectra were recorded on a Vertex 70 spectrophotometer (Bruker) equipped with a Golden Gate Single Reflection Diamond ATR System. Measurements were carried out at SCAI (University of Málaga). Spectra acquisition was carried out in a spectral range from 4000 to 500 cm^{-1} , with a resolution of 4 cm^{-1} and 64 accumulations per sample.



Figure 3.9. Vertex 70 spectrophotometer.

3.8. Solid State Nuclear Magnetic Resonance (Solid-state NMR)

3.8.1. Basic Principles

NMR spectroscopy provides information about the different environments of many common atom types, their numbers and ultimately their structure. It is useful to characterise organic and inorganic compounds containing hydrogen, carbon, fluorine, phosphorous, silicon and boron as well as many transition metal nuclei,

together with diffraction techniques. Compounds can be studied in solution or as pure liquids as well as solids. Furthermore, it is normally a non-destructive technique.

Fundamental particles such as electrons, protons and neutrons, have different spin quantum numbers. A charge associated with the spin gives rise to a magnetic moment, which is related with the spin by the gyromagnetic ratio (γ). As nuclei are made up of a combination of protons and neutrons and the magnetic moment depends on the number of protons and neutrons, the nuclear magnetic moment is an intrinsic property of a particular nucleus. Only nuclei with non-zero spin ($I \geq \frac{1}{2}$) can be studied by RMN spectroscopy (Table 3.3).

Table 3.3. Nuclear spin quantum numbers obtained from odd and even combinations of protons and neutrons.

Number of neutrons (n)	Number of protons (p)	Spin (I)	Example
Even	Even	0	^{12}C : n= 6, p= 6, I= 0
Even	Odd	1/2, 3/2, 5/2, etc.	^{13}C : n= 7, p= 6, I= 1/2
Odd	Even	1/2, 3/2, 5/2, etc.	^{23}Na : n= 12, p= 11, I= 3/2
Odd	Odd	1, 2, 3, etc.	^{10}B : n= 5, p= 5, I= 3

When a nucleus of spin I is situated in an external magnetic field, it can take up $2I+1$ orientations (m_I), which have associated different energy (Figure 3.10). It is the energy separation (ΔE) between these energy levels (m_I) what the NMR technique exploits:

$$\Delta E = \hbar\gamma B_0 \quad \text{Equation 3.18}$$

where \hbar is Planck's constant and B_0 is the magnetic induction (T).

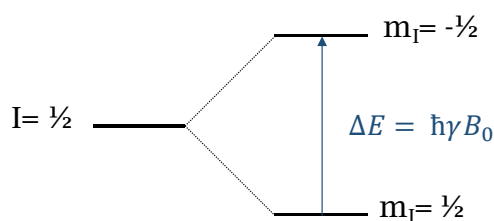


Figure 3.10. Splitting diagram for $I = \frac{1}{2}$.

When a radiofrequency with the same energy than the energy separation of two energy levels (Larmor frequency) is applied to a nucleus subjected to a magnetic field, this nucleus absorbs part of this energy and is excited to the highest energy level. When the radiofrequency is turned off, the nucleus returns to its basal energy state by emitting radiation, which is measured by this technique as voltage as a function of time (Free Induction Decay, FID). A plot of amplitude versus frequency is obtained by Fourier transformation (FT).

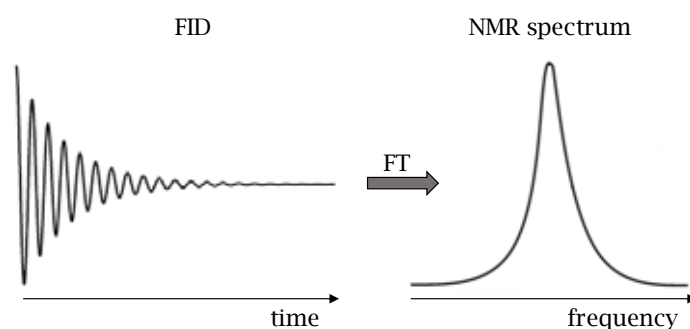


Figure 3.11. Schematic representation of Fourier transformation of a FID plot.

When samples are solids, signals suffer from broadening due to various interactions while in liquids samples the atomic motion is faster than the interaction frequency, avoiding these interactions and the widening of the signals. Some of these interactions can be avoided by spinning the sample very quickly at an angle of 54.74° to the axis of the applied magnetic field (magic angle spinning, MAS).

Normally, when there is a compound, which possess more than one nucleus with a magnetic moment, more than one spectrum would be collected because resonances for different nuclei occur at different frequencies (MacKenzie & Smith, 2002; Young & Weller, 2017b).

3.8.2. Instrumentation

^1H -MAS-NMR spectra were performed on a Bruker Ascend-600 spectrometer at SCAI (University of Málaga). This spectrometer is equipped with a 2.5 mm MAS probe, which operates at ^1H -NMR frequency of 600.09 MHz. ^1H -MAS-NMR spectra were recorded at a spinning rate of 30 kHz with a pulse width of 2 μs , dwell time of 6.50 μs and a delay of 3 s. An external reference as adamantane was using to reference ^1H

chemical shift. DMFIT program was employed to carry out the ^1H -MAS-NMR spectra deconvolution.



Figure 3.12. Bruker Ascend-600 spectrometer.

3.9. Particle Size Distribution

3.9.1. Basic Principles

Particle size distribution is measured by Dynamic Light Scattering (DLS). Particles are illuminated with a laser, scattering the light in all directions. A screen held close to the particles will be illuminated by the scattered light, showing a speckle pattern. The bright areas of the speckle pattern are due to constructive interferences while dark areas are due to destructive interferences. However, particles suspended in a liquid are constantly moving due to the random collision with the molecules of the liquid (Brownian motion). Small particles move quicker than large particles. Stokes-Einstein equation defines the relationship between the particle size and its speed. As particles are moving, the intensity in the scattered light appears to fluctuate. Particle size analysers measure the rate of the intensity fluctuation using a digital correlator, which measures the similarity degree between two signals over a period of time. The size distribution can be extracted from the correlation function (Malvern, 2013).

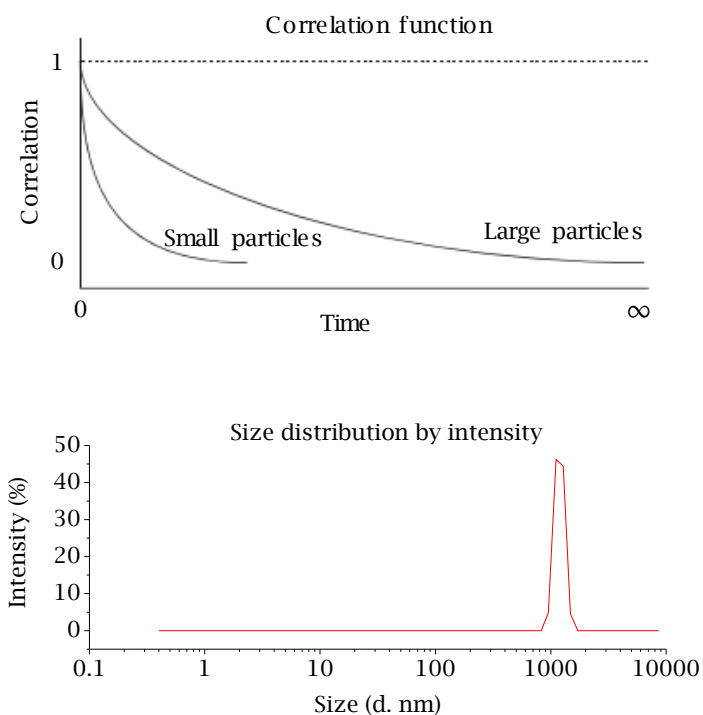


Figure 3.13. (Top) Correlation function and (bottom) size distribution graph.

3.9.2. Instrumentation

Particle suspensions were prepared with a concentration of 1 mg/mL in MilliQ water and homogenized by sonication (1 min in a water bath). Particle size measurements were carried out on a Zetasizer Nano ZS (Malvern) at SCAI (University of Málaga). The size was determined by Dynamic Light Scattering (light source of 632.8 nm) and multiple scattering was minimized by measuring backscattered light at 173° . Results were averaged and presented in intensity. Samples were measured in 1 cm pathlength disposable polystyrene cuvettes.



Figure 3.14. Zetasizer Nano ZS for particle size analysis.

3.10. Microwave-assisted Synthesis.

3.10.1. Basic Principles

Microwave irradiation is electromagnetic radiation in the frequency range from 0.3 to 300 GHz ($\lambda = 1$ mm to 1 m), operating those employed for chemical synthesis at 2.45 GHz ($\lambda = 12.25$ cm).

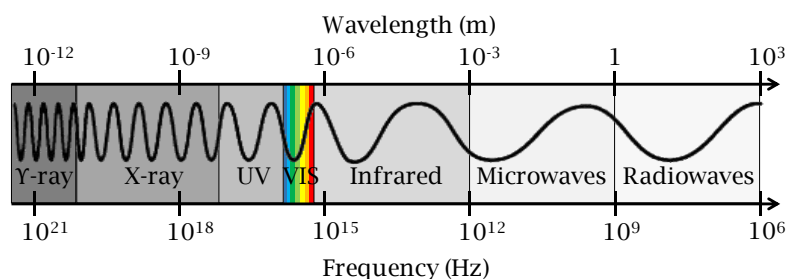


Figure 3.15. Electromagnetic spectrum.

Microwave radiation is too low to cleave molecular bonds and induce chemical reaction such as ultraviolet or visible light (photochemistry). However, this radiation can efficiently heat materials by dielectric heating effects. Dielectric heating can be produced by two major mechanisms:

- (i) Dipolar polarization: the substance must be a dipole to generate heat. The dipoles align to the microwave field, which is oscillating, rotating, rubbing and finally producing heat energy.
- (ii) Ionic conduction: ions oscillate with the microwave field, causing collisions between these ions and molecules or atoms and producing heat energy.

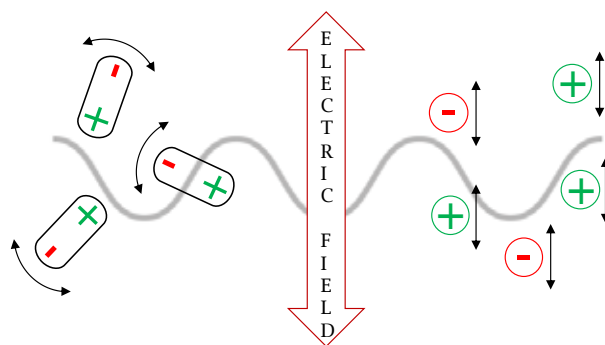


Figure 3.16. Schematic illustration of (left) dipolar polarization and (right) ionic conduction.

Some advantages of the microwave against conventional heating are that (i) microwaves pass through the vessel (microwave transparent material), minimizing wall effects, (ii) provide of a direct “in-core” heating instead of a connective process and (iii) allow faster heating (Kremsner & Stadler, 2018).

3.10.2. Instrumentation

Microwave-assisted synthesis were carried out on a Monowave 300 from Anton-Paar reactor. It is equipped with magnetic stirrer, pressure sensors and IR sensors for reaction temperature control. The maximum temperature, pressure and magnetic stirrer that can reach is 300 °C, 30 bar and 1200 rpm respectively. Borosilicate glass vials with a total volume of 10 or 30 mL were employed.



Figure 3.17. (Left) Anton-Paar Monowave 300 reactor and (right) borosilicate glass vials.

3.11. Photoreactor

3.11.1. Instrument

A Luzchem CCP-4V photoreactor was employed to carry out the photocatalytic test at University of Málaga. This photoreactor is equipped with 14 lamps, a power sensor and magnetic stirring. It can be computer controlled through CCP-4V software.

Catalyst pre-treatment was carried out under six UV-A lamps (Hitachi FL8BL-B, 8W) while 14 visible lamps (Prilux, 8W) were employed during the photocatalytic test. However, photocatalytic test for MB removal was carried out without pre-treatment and employing 14 UV-A lamps.

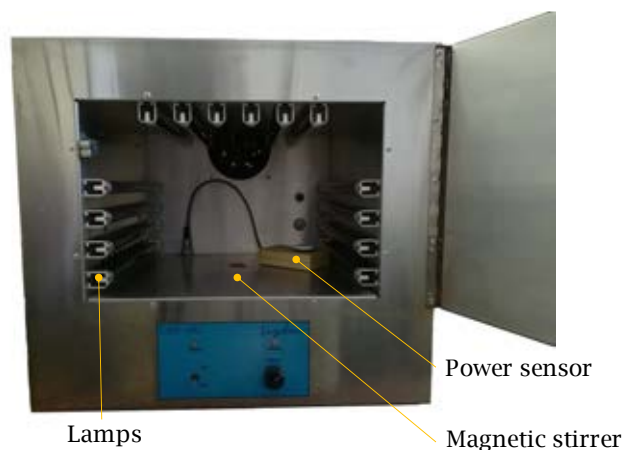


Figure 3.18. Luzchem CCP-4V photoreactor.

3.12. Total Organic Carbon (TOC)

3.12.1. Basic Principles

Total organic carbon (TOC) is the amount of organic carbon present in a sample. TOC analysis discriminates between the inorganic carbon (IC), which is present such as dissolved CO_2 , carbonate and bicarbonate, and the organic carbon (CO_2 generated from the oxidation of organic molecules). TOC is an indirect measure that results from subtracting the measured IC from the measured total carbon (TC):

$$TOC = TC - IC \quad \text{Equation 3.19}$$

First step of TC measurement involves the catalytic oxidation by combustion. Samples are injected (100 μL) into a furnace ($T = 680\text{ }^\circ\text{C}$) with a platinum catalyst in the presence of oxygen. In this step, all carbon content is converted to CO_2 and swept into a non-dispersive infrared analyser (NDIR) by a carrier gas (synthetic air).

On the other hand, IC measurement involves the conversion of inorganic carbon to CO_2 under acidic conditions (H_3PO_4). This acidic condition does not allow the organic carbon oxidation.

TOC measurements are usually employed to determine the organic pollution degree in water.

3.12.2. Instrumentation

TOC measurements were carried out on a Shimadzu TOC-V-CHS equipped with an auto-sampler (ASI-5000A) at Analytical Chemistry Department (University of Málaga).



Figure 3.19. Shimadzu TOC-V-CHS.

3.13. Impedance Spectroscopy

3.13.1. Basic Principles

Electrochemical impedance spectroscopy studies the system response to the application of a current flow, providing information about the interface, its structure and the reactions taking place there in a non-destructive way. The measurement of the complex impedance is carried out at different frequencies or in a certain frequency range. Different behaviours in the impedance spectra allow differentiating different phenomena concerning electrolyte and electrodes.

Electrical resistance (R) is the ability of a circuit element to resist the electrical current flow, which is defined in Ohm's Law as the ratio between input voltage (V) and output current (I).

$$R (\Omega) = \frac{V}{I} \quad \text{Equation 3.20}$$

However, only ideal resistors follow Ohm's Law. Assuming an ideal behaviour of the sample, its resistance when an external voltage is applied also can be defined as:

$$R (\Omega) = \rho \frac{d}{A} \quad \text{Equation 3.21}$$

where the characteristic electrical resistivity of the material is ρ ($\Omega \cdot \text{cm}$), the electrodes area is A (cm^2) and d (cm) is the distance between both electrodes. The conductivity (σ) is the inverse of the resistivity:

$$\sigma (S \cdot \text{cm}^{-1}) = \frac{1}{\rho} \quad \text{Equation 3.22}$$

If two electrodes are separated by a dielectric medium, the current flow is rejected. The ideal element is called capacitor and the capacitance is defined as:

$$C (F) = \frac{\epsilon_0 \epsilon A}{d} \quad \text{Equation 3.23}$$

where ϵ_0 is the constant electrical permittivity of a vacuum ($8.85 \cdot 10^{-14} \text{ F} \cdot \text{cm}^{-1}$) and ϵ is the relative permittivity, which represents the characteristic ability of the sample to store electrical energy.

Typically, an electrochemical impedance measurement is carried out by exciting the system with an AC voltage signal V with small amplitude V_A applied at frequency f . The voltage signal expressed as a function of time:

$$V(t) = V_A \sin(2\pi f t) = V_A \sin(\omega t) \quad \text{Equation 3.24}$$

In a linear system, the current response to a sinusoidal voltage input is shifted in phase (ϕ) and has a different amplitude (I_A):

$$I(t) = I_A \sin(\omega t + \phi) \quad \text{Equation 3.25}$$

The complex impedance of the system as an analogous expression to Ohm's Law:

$$Z^* = \frac{V(t)}{I(t)} = \frac{V_A \sin(\omega t)}{I_A \sin(\omega t + \phi)} = Z_A \frac{\sin(\omega t)}{\sin(\omega t + \phi)} \quad \text{Equation 3.26}$$

It is possible to express the impedance as a complex function by using Euler's relationship (Equation 3.27):

$$\exp(j\phi) = \cos\phi + j\sin\phi \quad \text{Equation 3.27}$$

$$V(t) = V_A e^{j\omega t} \quad \text{Equation 3.28}$$

$$I(t) = I_A e^{j\omega t - j\phi} \quad \text{Equation 3.29}$$

$$Z^* = \frac{V}{I} = Z_A e^{j\phi} = Z_A (\cos\phi + j\sin\phi) = Z_{REAL} + jZ_{IM} \quad \text{Equation 3.30}$$

Complex impedance of a material or system provides more information than only resistance, capacitance or inductance, because it considers at the same time both the real and the imaginary part.

Complex impedance data are normally represented by a Nyquist or Bode plots. While Nyquist plot is a representation of the imaginary and the real part of the complex impedance, Bode plot represents the phase angle and the logarithm of the impedance magnitude as a function of the logarithm of frequency (Lasia, 2002; Lvovich, 2012; Macdonald, 2006).

3.13.2. Instrumentation

Two different impedance analyser were employed to collect impedance data of the powered polycrystalline samples as cylindrical pellets, AUTOLAB PGSTAT302N and HP4284A, over a frequency range from 10^6 to 0.1 Hz with an applied voltage of 0.35 or 0.5V. All measurements were electronically controlled by NOVA software or winDETA package of programs.

Cylindrical pellets of ~5mm diameter and ~0.9-1.1 mm thickness were obtained by pressing ~30-40 mg of sample at 250 MPa for 1 minute. Pellets were placed between porous C electrodes (Sigracet, GDL 10 BB, no Pt) inside a temperature and humidity controlled chamber (Espec SH-222) (Figure 3.20). Water content equilibration of the samples was carried out by preheating from 25 to 80 °C at 95% RH (0.2 °C/min). AC impedance data were collected over upon cooling normally using a stabilization time of 5h at different temperature intervals (80, 70, 60, 50, 40, 30 and 25 °C) and at different relative humidity. For measurements at high relative humidity (>75%), water condensation was avoided by reducing it first to 75% before decreasing the temperature (Figure 3.21).



Figure 3.20 Sample preparation.

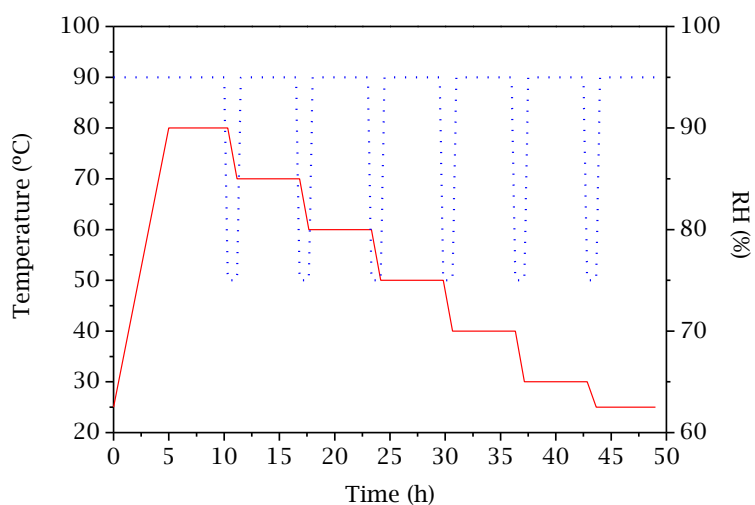


Figure 3.21. Temperature (red) and relative humidity (blue) conditions in an impedance measurement from 80 to 25 °C at 95% RH.

The total pellet resistance (R_T) was obtained from the intercept of the spike and/or the arc (low-frequency end) on the Z' axis.

On the other hand, in situ through-plane proton conductivity of the membranes was determined on Membrane Electrode Assemblies (MEAs) in collaboration with the Institute of Science and Technology of Polymers, ICTP-CSIC (Madrid). The catalyst layer ink for both anode and cathode consisted of Pt/C (40% Pt on Vulcan XC-72, E-TEX) with a Pt load of 1 mg Pt·cm⁻², 30% Nafion (1100 EW) and 2:1 isopropanol/water mixture as dispersion media. After sonicating for 3h, the catalyst ink was sprayed

onto a nonwoven carbon paper gas diffusion layer with a microporous layer (MPL) and 5% PTFE treated (Sigracet 39 BC GDL) using an automatic spraying system EFD. An experimental 5 cm² single cell (ElectroChem Inc.) was used as cell hardware for all the electrochemical measurements. Electrochemical impedance data were collected at 70, 80 and 90 °C and 100% RH using a potentiostat AUTOLAB PGSTAT30 equipped with a FRA module over the frequency range from 10⁵ to 10 Hz and a DC bias potential of 0.45V. The amplitude of the sinusoidal signal was 10 mV. The cell was continuously supplied (200 mL·min⁻¹) with humidified hydrogen (SHE, anode). Equation 3.31 was employed to obtain the through-plane proton conductivity (σ_{TP}), where L is the membrane thickness, R is the resistance and S is the active area of the MEA (5 cm²).

$$\sigma_{TP}(S \cdot cm^{-1}) = \frac{L (cm)}{R (\Omega) \cdot S (cm^2)} \quad \text{Equation 3.31}$$

The resistance was determined from the intersection on the real axis in the Nyquist plots. In order to ensure good data reproducibility, each sample was measured at least five times after it had reached a constant value.

3.14. Photoluminescence Spectroscopy

3.14.1. Basic Principles

Photoluminescence process consists in the absorption and subsequent emission of photons by a sample. When a sample absorbs photons, an electron from the electronic basal state (S_0) is promoted to vibrational levels ($v = 0, 1, 2 \dots$) from the first (S_1) or higher electronic excited states ($S_2, S_3 \dots$). Firstly, the excited electron relaxes to the lowest vibrational level ($v = 0$) of the excited state by vibrational relaxation (VR) and then to the first electronic excited state (S_1) by internal conversion (IC). Further deactivation can occur radiatively by emitting a photon or non-radiatively through one of these three processes: (i) IC quenching to the S_0 , (ii) collisional quenching to the S_0 and (iii) inter-system crossing (ISC) to a triplet excited state (T_1). From T_1 , the electron can either emit a photon (phosphorescence) or deactivate through IC to S_1 . When the electron emits a photon from a singlet state, the process is called fluorescence. Photoluminescence implies both fluorescence and phosphorescence (Baer & Theyuthasan, 2010).

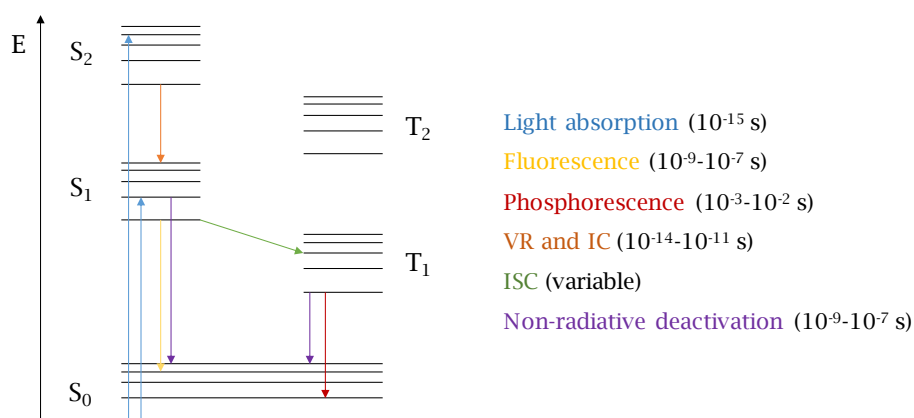


Figure 3.22. Jablonski diagram.

3.14.2. Instrumentation

Photoluminescence spectra of powder samples were carried out on an Axio Imager.A2m microscope (Carl Zeiss) connected to a QE Pro spectrometer (Ocean Optics) via a fibre optic waveguide. The system was used in fluorescence mode employing a HBO 100 mercury lamp. Photoluminescence measurements were carried out at The International Research Center of Nanophotonics and Metamaterials (St. Petersburg, Russia).

3.15. References

A

Altomare, A.; Cuocci, C.; Giacobazzo, C.; Moliterni, A.; Rizzi, R.; Corriero, N; Falcicchio, A. EXPO2013: a kit of tools for phasing crystal structures from powder data. *J. Appl. Cryst.*, **2013**, 46, 1231-1235.

B

Baer, D. R.; Thevuthasan, S. Characterization of thin films and coatings in Handbook of Deposition Technologies for Films and Coatings. *William Andrew Publishing*, **2010**, Ch. 16, p. 749-864.

Billinge, S. J. The rise of the X-ray atomic pair distribution function method: a series of fortunate events. *Phil. Trans. R. Soc. A*, **2019**, 377(2147), 20180413.

Boultif, A; Louer, D. Powder pattern indexing with the dichotomy method. *J. Appl. Cryst.*, **2004**, 37, 724-731.

Bruker. APEX2 v2014.9-0, *Bruker AXS Inc.*, Madison, WI, **2014**

CHAPTER 3

C

Cabeza, A.; de la Torre, A. G.; León-Reina, L.; Aranda, M. A. G. Fundamentos del método de Rietveld in El método de Rietveld. *Ciències Experimentals*, **2014**, Ch. 4, p. 117-166.

D

Dolomanov, O. V.; Bourhis, L. J.; Gildea, R. J.; Howard, J. A.; Puschmann, H. OLEX2: a complete structure solution, refinement and analysis program. *J. Appl. Cryst.*, **2009**, 42(2), 339-341.

E

Ermrich, M.; Opper, D. XRD for the analyst. Getting acquainted with the principles. *Panalytical GmbH*, **2011**.

F

Farrow, C. L.; Juhás, P.; Liu, J.; Bryndin, D.; Božin, E. S.; Bloch, J.; Proffen, T.; Billinge, S. J. PDFfit2 and PDFgui: computer programs for studying nanostructure in crystals. *J. Phys: Condens. Mat.*, **2007**, 19(33), 335219.

H

Hulbert, S. L.; Williams, G. P. Synchrotron Radiation Sources in Vacuum Ultraviolet Spectroscopy I. *London: Academic Press*, **2000**, Ch. 1, p. 1-25.

J

Juhàs, P.; Davis, T.; Farrow, C.L.; Billinge, S.J. PDFgetX3: a rapid and highly automatable program for processing powder diffraction data into total scattering pair distribution functions. *J. Appl. Crystallogr.*, **2013**, 46(2), 560-566.

K

Kremsner, J. M.; Stadler, A. A Chemist's Guide to Microwave Synthesis. Basics, Equipment & Application Examples. *Anton Paar GmbH*, **2018**.

L

Larson, A. C.; von Dreele, R. B. General structure analysis system (GSAS). Los Alamos National Laboratory Report LAUR, 2004, 86-748.

Lasia, A. Electrochemical Impedance Spectroscopy and its Applications. *Modern Aspects of Electrochemistry*, **2002**, 32, 143-248.

Leng, Y. Materials characterization: introduction to microscopic and spectroscopic methods. *John Wiley & Sons*, **2009**.

Lvovich, V. F. Impedance Spectroscopy: Applications to Electrochemical and Dielectric Phenomena. *John Wiley & Sons*, 2012.

M

Macdonald, D. D. Reflections on the history of electrochemical impedance spectroscopy. *Electrochim. Acta*, 2006, 51(8-9), 1376-1388.

MacKenzie, K. J., & Smith, M. E. Multinuclear solid-state nuclear magnetic resonance of inorganic materials. *Elsevier Science Ltd*, 2002.

Size theory in Zetasizer Nano User Manual (Man0485-1.1). *Malvern Instrument*, 2013, Ch. 11, p. 1-6.

R

Rietveld, H. M. A profile refinement method for nuclear and magnetic structures. *J. Appl. Crystallogr.*, 1969, 2, 65–71.

Rius, J. Patterson-function direct methods for structure determination of organic compounds from powder diffraction data. XVI. *Acta Cryst.*, 2011, A67, 63-67.

S

Sheldrick. SHELXL-2017/1, Program for the Solution of Crystal Structures, *University of Göttingen, Germany*, 2017.

T

Taylor, H. E. Inductively Coupled Plasmas in Inductively Coupled Plasma-Mass Spectrometry. Practises and Techniques. *Academic Press*, 2001, Ch. 3, p. 15-27.

Thomas, R. Practical Guide to ICP-MS: A Tutorial for Beginners. *CRC Press: Taylor & Francis Group*, 2013.

Thompson, M. CHNS Elemental Analysers. *RSC, AMC Technical Brief*, 2008, 29.

Toby, B. H. EXPGUI, a graphical user interface for GSAS. *J. Appl. Crystallogr.*, 2001, 34(2), 210–213.

V

Vallcorba, O.; Rius, J.; Frontera, C.; Peral, I.; Miravittles, C. DAJUST: a suite of computer programs for pattern matching, space-group determination and intensity extraction from powder diffraction data. *J. Appl. Cryst.*, 2012, 45(4), 844-848.

Visser, J. W. A fully automatic program for finding the unit cell from powder data. *J. Appl. Cryst.*, 1969, 2(3), 89-95.

CHAPTER 3

W

Werner, P.E.; Eriksson, L.; Westdahl, M. TREOR, a semi-exhaustive trial-and-error powder indexing program for all symmetries. *J. Appl. Cryst.*, **1985**, 18(5), 367-370.

Y

Young, N.; Weller, M. T. Diffraction methods and crystallography in Characterisation methods in inorganic chemistry. *Oxford University Press*, **2017a**, Ch. 2, p. 20-65.

Young, N.; Weller, M. T. Nuclear magnetic resonance (NMR) spectroscopy in Characterisation methods in inorganic chemistry. *Oxford University Press*, **2017b**, Ch. 3, p. 66-111.

Young, N.; Weller, M. T. Vibrational spectroscopy in Characterisation methods in inorganic chemistry. *Oxford University Press*, **2017c**, Ch. 4, p. 112-162.

Young, N.; Weller, M. T. X-ray and photoelectron spectroscopy, electron microscopy, and energy dispersive analysis of X-rays in Characterisation methods in inorganic chemistry. *Oxford University Press*, **2017d**, Ch. 6, p. 206-221.

Young, N.; Weller, M. T. Mass spectroscopy, chemical, and thermal analysis techniques in Characterisation methods in inorganic chemistry. *Oxford University Press*, **2017e**, Ch. 7, p. 222-236.

Chapter 4
Transition Metals
Hydroxyphosphonoacetates





UNIVERSIDAD
DE MÁLAGA

Carboxylic groups-containing phosphonic acids, i.e. phosphonocarboxylic acids, are heterofunctional organic linkers which lead to a wide structural variety of metal phosphonates, being the most common topologies the layered and pillared-layered ones (Cabeza & Aranda, 2012).

The commercial available racemic ligand ***R,S* 2-hydroxyphosphonoacetic acid**, [H₂O₃PCH(OH)CO₂H] (hereinafter referred to as HPAA), is a simple low molecular weight acid with a chiral atom and three different coordination groups: hydroxyl, carboxyl and phosphonyl groups (Figure 4.1). The advantageous characteristics of this ligand lie in the high chemical stability, low price, relative low carbon content, safety of use and low toxicity of the degradation products (Bazaga-García et al., 2012). A common feature of this acid is the formation of multiple chelating rings, displaying a wide range of coordination modes with different metal ions. Generally, RT synthesis lead to low-dimensional solids, while hydrothermal reactions result in two- or three-dimensional solids and may even incorporate various alkaline cations as counterions (Cabeza, Olivera-Pastor & Colodrero, 2015). Moreover, this acid possesses a chiral carbon, giving the possibility to prepared non-centrosymmetric metal-organic coordination polymers for possible nonlinear optical applications (Fu et al., 2005a). In addition, HPAA has strong complexation ability for metal ion and thus, it is an excellent corrosion inhibitor (Zhai et al., 2018).

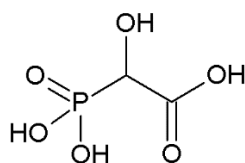


Figure 4.1. Molecular structure of *R,S* 2-hydroxyphosphonoacetic acid (HPAA).




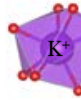
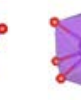

This multidentate organic acid has been widely used for the preparation of a large variety of coordination polymers, with structural arrangements from 1D to 3D, according to the multiple coordination modes it can provide to metal ions.

Bazaga-García et al. (2015) prepared alkali-HPAA derivatives by crystallization, which showed a rich structural diversity depending on the cation size (Table 4.1), from mono-dimensional (Li⁺) through pillared layered structure (Na⁺) to typically 3D frameworks (K⁺ and Cs⁺). These materials presented strong hydrogen bonding networks, making them potential candidates as proton conductors. The highest proton conductivity was observed for Na-HPAA (5.6·10⁻³ S·cm⁻¹ at 98 % RH and 24 °C).

CHAPTER 4

Furthermore, a chiral structure of Cs-HPAA (*S* enantiomer) was obtained from slow crystallization. This could be explained due to the strong hydrogen bonding interactions required for structural stabilization.

Table 4.1. Dimensionality, alkali metals ionic radii and coordination environment and number (Bazaga-García et al., 2015).

Coordination						
	4	5	6	7	9	9
Ionic radii	0.76		1.02	1.38		1.67
Dimensionality	1D		2D	3D		3D

Colodrero et al. (2011) studied the influence of different reaction parameters in preparing various Ca-HPAA derivatives:

- (i) pH values ranging from 1.0 to 7.5 in order to obtain different deprotonation states of the ligand.
- (ii) Temperature of reaction, room temperature and hydrothermal, at 180 °C, to obtain solids with different dimensionalities, the latter conditions favouring higher dimensionality compounds.
- (iii) Incorporation of alkali metal ions (Li⁺ and Na⁺) to synthesise denser modified networks.

They obtained four new crystalline phases (solids 2-5) in addition to that previously reported by Demadis, Papadaki & Císařová (2010), solid (1) (Table 4.2).

Table 4.2. Some details for Ca-HPAA solids (Demadis, Papadaki & Císařová, 2010; Colodrero et al., 2011).

Solid	pH	T (°C)	Dimens.	Composition
(1)	7.3	RT	0D	Ca ₃ (O ₃ PCHOHCO ₂) ₂ ·14H ₂ O
(2)	2.0	RT	2D	Ca(HO ₃ PCHOHCO ₂) ₂ ·3H ₂ O
(3)	0.6-4.6	180	3D	Ca ₅ (O ₃ PCHOHCO ₂) ₂ (HO ₃ PCHOHCO ₂) ₂ ·6H ₂ O
(4)	1.0-4.3	180	3D	CaLi(O ₃ PCHOHCO ₂)
(5)	1.0-7.2	180	2D	Ca ₂ Na(O ₃ PCHOHCO ₂)(HO ₃ PCHOHCO ₂)·1.5H ₂ O

For these compounds, it was found that the trimeric structural motif $\text{Ca}_3(\text{O}_3\text{PCH}(\text{OH})\text{CO}_2)_2$, solid **(1)**, was a central species for deriving the various structures. In this trimeric species, central calcium ion is hexa-coordinated, while the two peripheral calcium ions are octa-coordinated. The central Ca^{2+} is bonded through two pairs of oxygen atoms from the carboxylate and phosphonate groups forming two six-membered rings: Ca-O-C-C-P-O-Ca . The peripheral Ca^{2+} ions are bonded to the hydroxyl group and the other carboxylate oxygen, forming a five-membered ring: Ca-O-C-C-O-Ca .

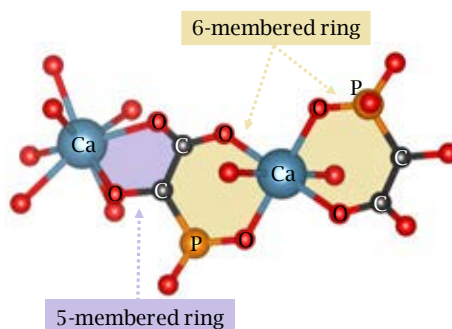


Figure 4.2. A section of the trimeric unit of Ca-HPAA compounds showing the six- and five-membered rings (Colodrero et al., 2011).

Colodrero et al. (2010) reported a series of M(II) hydroxyphosphonoacetates (M= Mg, Co, Ni and Zn) and studied the corresponding structural transformations. Mono-dimensional solids were obtained under room temperature crystallization, $[\text{M}\{\text{HO}_3\text{PCH}(\text{OH})\text{CO}_2\}(\text{H}_2\text{O})_2]_3 \cdot 2\text{H}_2\text{O}$. They transform into 3D structures upon dehydration. By carrying out hydrothermal reactions, a 2D magnesium derivative, $[\text{Mg}\{\text{HO}_3\text{PCH}(\text{OH})\text{CO}_2\}(\text{H}_2\text{O})_2]$, or 3D solids could be synthesised, the latter ones required the presence of sodium and potassium metal ions, as charge-compensating ions.

Fu et al. (2005b) synthesised and characterised four isomorphs layered transition-metal solids by hydrothermal methodology, $\text{M}(\text{CH}(\text{OH})(\text{CO}_2)(\text{PO}_3\text{H}))(\text{H}_2\text{O})_2$ (M= Mn, Fe, Co and Zn). In this case, the metal ion, M(II), is hexacoordinated by six oxygen atoms through M-O coordinate bonds (Figure 4.3a): two oxygen atoms from two water molecules, two phosphonate oxygen atoms from two different ligands and the carboxylate and hydroxyl oxygen atoms from the same ligand. The formation of an extended hydrogen bonds network gives rise to a three dimensional arrangement of layers (Figure 4.3b). For compounds with Mn, Fe and Co, magnetic measurements

showed the presence of antiferromagnetic interactions. Bazaga-García et al. (2012) studied the use of the iron derivative as a heterogeneous Fenton photocatalyst for phenol photodegradation, in the presence of H_2O_2 and UV-A light. A 90% mineralization was reached at 80 min of irradiation, whilst the photocatalyst showed high stability under reaction conditions, with only a little amount of iron species leached to the solution that progressively reabsorbed on particle surface. This iron lixiviation was considered advantageous, as a homogeneous contribution to the photocatalytic process enhanced phenol mineralization. Zhai et al. (2018) reported the use of Zn-HPAA as anticorrosion material. In addition, the anticorrosion properties were improved by the incorporation of a Mo component into the Zn-HPAA layer.

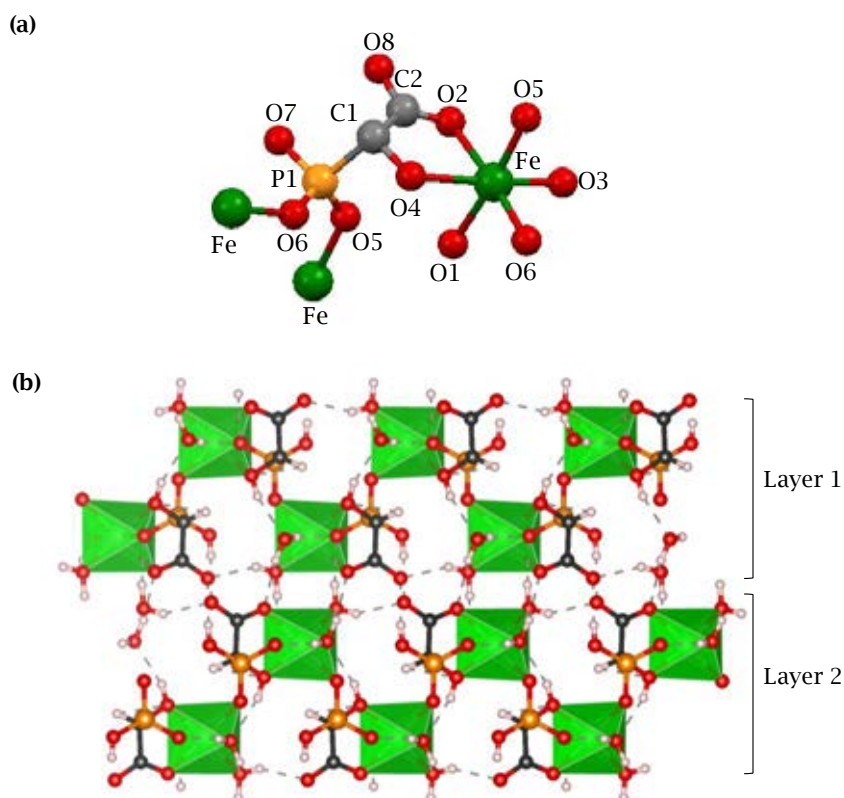


Figure 4.3. (a) Coordination environment of Fe-HPAA and (b) view of the layer packing along *a*-axis (Fu et al., 2005b).

Colodrero et al. (2017) correlated the structural variations with the proton conductivity properties for two series of magnesium and zinc 2-hydroxyphosphonoacetates. Mono dimensional derivatives $[M(\text{OOCCH}(\text{OH})\text{PO}_3\text{H})\cdot 2\text{H}_2\text{O}, \text{M-H}_1\text{HPAA-1D}]$ transformed into two dimensional solids $[M(\text{OOCCH}(\text{OH})\text{PO}_3\text{H})\cdot 2\text{H}_2\text{O}, \text{M-H}_1\text{HPAA-2D}]$ in the measurement conditions (25-80 °C and 95% RH), exhibiting moderate proton conductivities (between $2.1\cdot 10^{-5} \text{ S}\cdot\text{cm}^{-1}$ and $6.7\cdot 10^{-5} \text{ S}\cdot\text{cm}^{-1}$). Moreover, a new 3D compound was reported: $\text{KZn}_6(\text{OOCCH}(\text{OH})\text{PO}_3)_4(\text{OH})\cdot 5\text{H}_2\text{O}$ ($\text{KZn}_6\text{-HPAA-3D}$), where the negatively charged framework was compensated by potassium cations. Upon HCl gas adsorption, $\text{KZn}_6\text{-HPAA-3D}$ was transformed into the 2D derivative ($\text{Zn-H}_1\text{HPAA-2D}$). Post synthesis modifications, such as adsorption of ammonia in the case of the 2D derivatives or HCl for $\text{KZn}_6\text{-HPAA-3D}$, enhanced the proton conductivity of these materials.

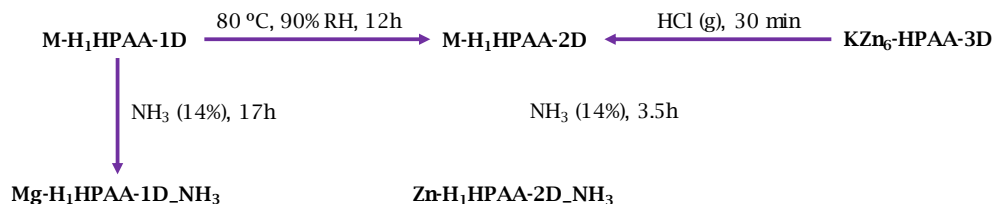


Figure 4.4. Structural transformations for M-HPAA (M= Mg, Zn) (Colodrero et al., 2017).

Other bimetallic derivatives have been also reported. Sun et al. (2006, 2007) synthesised two bimetallic compounds, a 3D $\text{Mg}_{0.5}\text{Cd}[\text{O}_3\text{PCH}(\text{OH})\text{CO}_2]$ and a 2D $\text{Na}_2[\text{Cd}_2(\text{H}_2\text{O})_5(\text{O}_3\text{PCH}(\text{OH})\text{CO}_2)_2]\cdot 2\text{H}_2\text{O}$, where Na^+ acts as a counterion located in one-dimensional channels of the interlayer space. Finally, Fu et al. (2005a) synthesised a 3D open framework, $[(\text{NH}_4)\text{Zn}\{\text{O}_3\text{PCH}(\text{OH})\text{CO}_2\}]$, where NH_4^+ counterbalances the negative charge of the framework.

Colodrero et al. (2012) reported three-dimensional Ln-HPAA solids with general formula: $\text{Ln}_3(\text{H}_{0.75}\text{O}_3\text{PCHOHCOO})_4\cdot x\text{H}_2\text{O}$ (Ln= La, Ce, Pr, Sm, Eu, Gd, Tb and Dy; x = 15–16). Two polymorphic structures, Series I and II, were obtained by slow crystallization at room temperature from very acidic aqueous solutions. These solids presented trimeric units similar to the Ca-HPAA compounds (Figure 4.5). Water-filled 1D channels form in the interlayered region along the *b*-axis. Ln-HPAA solids exhibited proton conductivity, with maximum value for the gadolinium derivative from Series II ($3.2\cdot 10^{-4} \text{ S}\cdot\text{cm}^{-1}$ at 98% RH and 21 °C). These compounds also showed

crystalline-to-amorphous-to-crystalline transformations during dehydration/rehydration cycles, which were followed by photoluminescence spectroscopy.

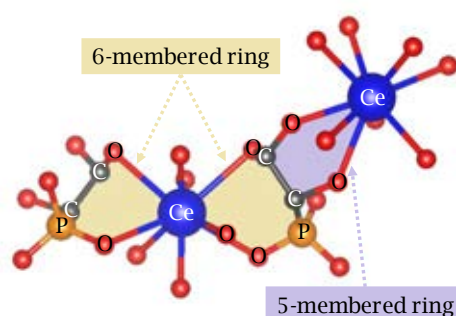


Figure 4.5. A section of the trimeric unit in Ln-HPAA compounds (Colodrero et al., 2012).

In the presence of an auxiliary ligand or template agents, such as ethylenediamine, different compounds have been also reported with the organic ligand HPAA. Dong et al. (2007, 2011) and Li et al. (2007) reported a 3D cadmium derivative with double-stranded helical channels, a 3D magnesium derivative with right-handed helical chains and a 2D antimony derivative synthesised under hydrothermal reaction at 140 °C respectively. Fu, Hu & Wu (2011) reported Zn^{2+} , Co^{2+} and Ba^{2+} derivatives containing secondary ligands and/or a mixture of different metal ions obtained by hydrothermal reactions.

Here, we report a simplified synthesis of Fe^{2+} hydroxyphosphonoacetate as well as the preparation of M(II)-substituted iron derivatives ($M = Mn^{2+}$, Co^{2+} or Zn^{2+}) to investigate their properties as:

- (i) Proton conductors in variable conditions, including the effects of exposure to ammonia vapours.
- (ii) Photocatalysts, in photo-Fenton reactions, intended to remove water pollutants, such as phenol, 4-chlorophenol and methylene blue.

The results of this study have been published in Salcedo et al. (2020).

4.1. Synthesis

Iron and zinc derivatives, as well as the corresponding iron-containing bimetallic solid solutions with Mn^{2+} , Co^{2+} or Zn^{2+} have been synthesised. Although the synthesis of **Fe-** and **Zn-HPAA** was reported by Fu et al. (2005b), an alternative, simplified synthesis procedure has been employed to reduce cost and time of

reaction (from 96 to 24h) as well as removing unnecessary reagents, such as NaF and acetic acid. Moreover, for the Fe(II) derivative, the employment of two metal sources, i.e. $\text{FeSO}_4 \cdot 7\text{H}_2\text{O}$ together with elemental iron, allowed us to achieve a controlled crystallization.

4.1.1. Synthesis of $\text{Fe}[\text{HO}_2\text{PCH}(\text{OH})\text{CO}_2] \cdot 2.5\text{H}_2\text{O}$ (Fe-HPAA)

A mixture of $\text{FeSO}_4 \cdot 7\text{H}_2\text{O}$ (13.9 g; 50 mmol) and granular iron (2.5 g; 44.8 mmol) was added to a HPAA aqueous solution (11.2 mL; 50 mmol of HPAA) in 150 mL of DI water. The mixed solution was stirred under reflux for 1 day. The final pH value of this reaction mixture ranged between 1.0 and 1.3. The obtained solid was filtered, washed with deionized water and dried at 60 °C overnight. Unreacted iron was removed by using a magnet and sieving. The yield of the reaction was 70% based on the iron salt.

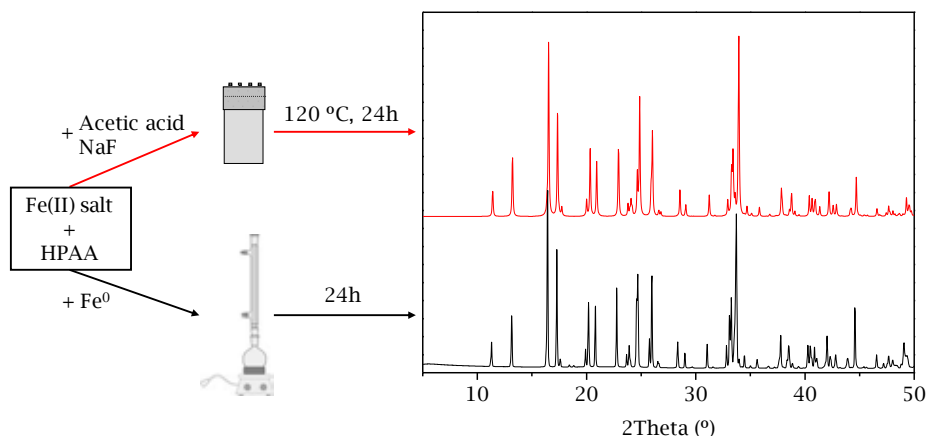


Figure 4.6. A comparison of the proposed, new synthetic methodology for Fe-HPAA (black) with that reported elsewhere (Fu et al., 2005b; red).

4.1.2. Synthesis of $\text{Zn}[\text{HO}_2\text{PCH}(\text{OH})\text{CO}_2] \cdot 2.5\text{H}_2\text{O}$ (Zn-HPAA)

A quantity of $\text{ZnSO}_4 \cdot \text{H}_2\text{O}$ (13.9 g; 50 mmol) was added to a HPAA aqueous solution (11.2 mL; 50 mmol of HPAA) in 150 mL of DI water and this mixture was stirred under reflux for 1 day. The resulting solid was filtered, washed with abundant DI water and dried at 60 °C overnight. The reaction yield was 70% based on the zinc salt.

4.1.3. Synthesis of $\text{Fe}_x\text{M}_{1-x}[\text{HO}_3\text{PCH(OH)CO}_2]\cdot 2.5\text{H}_2\text{O}$ ($\text{Fe}_x\text{M}_{1-x}\text{-HPAA}$)

$\text{Fe}_x\text{M}_{1-x}\text{-HPAA}$ ($\text{M} = \text{Mn}^{2+}$, Co^{2+} and Zn^{2+}) solid solutions were synthesised following the procedure described above for Fe-HPAA but modifying the $\text{Fe}^{2+}/\text{M}^{2+}$ molar ratio of the metal salts and maintaining the same overall metal/ligand molar ratio. In all cases, a fixed amount of granular iron was added (2.5 g; 44.8 mmol). The nominal $[\text{Fe}^0 + \text{Fe}^{2+}]/\text{M}^{2+}$ molar ratios employed were 0.92:0.08, 0.79:0.21, 0.68:0.32 and 0.55:0.45.

4.2. Characterisation

All compounds were extensively characterised by using different techniques such as elemental, thermogravimetric and inductively coupled plasma mass spectrometry analysis, X-ray photoelectron spectroscopy, X-ray powder diffraction and pair distribution function analysis.

4.2.1. Elemental, Thermogravimetric and Inductively Coupled Plasma Mass Spectrometry Analysis

The $\text{Fe}^{2+}/\text{M}^{2+}$ molar ratio of solid solutions samples was determined by inductively coupled plasma mass spectrometry analysis (ICP-MS) Table 4.3 shows the corresponding chemical compositions of all bimetallic solid solutions studied. Elemental analysis for all compounds is given in Appendix II, Table AII.1.

Thermogravimetric analysis of Fe- , Zn- and $\text{Fe}_x\text{Zn}_{1-x}\text{-HPAA}$ samples were recorded from RT to 500 °C with a heating rate of 10 °C·min⁻¹ under air flow. As can be seen in Figure 4.7, dehydration starts at 100-150 °C, while ligand decomposition occurs beyond 200 °C up to about 500 °C, with the Zn(II) derivative sample showing delayed effects and more defined weight loss in comparison to other compositions.

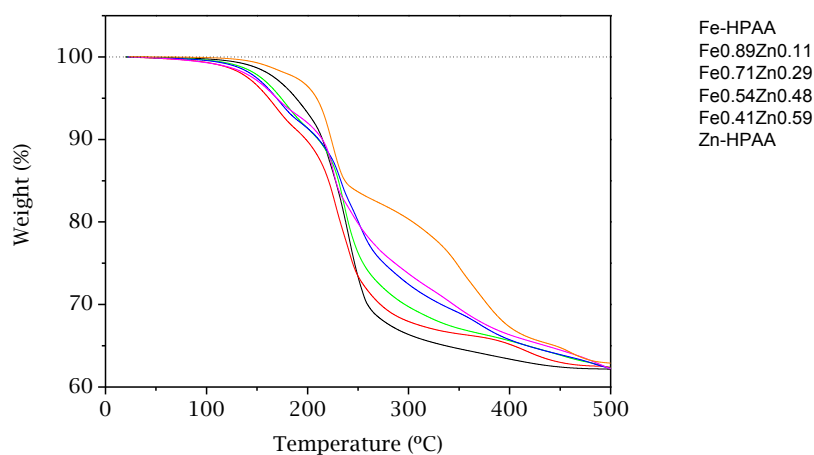


Figure 4.7. Thermal analysis for compounds Fe-HPAA (black), $\text{Fe}_{0.89}\text{Zn}_{0.11}$ -HPAA (red), $\text{Fe}_{0.71}\text{Zn}_{0.29}$ -HPAA (magenta), $\text{Fe}_{0.54}\text{Zn}_{0.46}$ -HPAA (blue), $\text{Fe}_{0.41}\text{Zn}_{0.59}$ -HPAA (green) and Zn-HPAA (orange).

Table 4.3. Chemical composition for $\text{Fe}_x\text{M}_{1-x}$ -HPAA solid solutions (M= Mn^{2+} , Co^{2+} and Zn^{2+}).

Nominal $[\text{Fe}^0+\text{Fe}^{2+}]/\text{M}^{2+}$ molar ratio	Acronym	Stoichiometric
0.92:0.08	$\text{Fe}_{0.89}\text{Zn}_{0.11}$ -HPAA	$\text{Fe}_{0.89}\text{Zn}_{0.11}(\text{HO}_3\text{PCHOHCOO})(\text{H}_2\text{O})_{2.5}$
0.79:0.21	$\text{Fe}_{0.71}\text{Zn}_{0.29}$ -HPAA	$\text{Fe}_{0.71}\text{Zn}_{0.29}(\text{HO}_3\text{PCHOHCOO})(\text{H}_2\text{O})_{2.5}$
0.68:0.32	$\text{Fe}_{0.54}\text{Zn}_{0.46}$ -HPAA	$\text{Fe}_{0.54}\text{Zn}_{0.46}(\text{HO}_3\text{PCHOHCOO})(\text{H}_2\text{O})_{2.5}$
0.55:0.45	$\text{Fe}_{0.41}\text{Zn}_{0.59}$ -HPAA	$\text{Fe}_{0.41}\text{Zn}_{0.59}(\text{HO}_3\text{PCHOHCOO})(\text{H}_2\text{O})_{2.5}$
0.79:0.21	$\text{Fe}_{0.78}\text{Co}_{0.22}$ -HPAA	$\text{Fe}_{0.78}\text{Co}_{0.22}(\text{HO}_3\text{PCHOHCOO})(\text{H}_2\text{O})_{2.5}$
0.68:0.32	$\text{Fe}_{0.66}\text{Co}_{0.34}$ -HPAA	$\text{Fe}_{0.66}\text{Co}_{0.34}(\text{HO}_3\text{PCHOHCOO})(\text{H}_2\text{O})_{2.5}$
0.55:0.45	$\text{Fe}_{0.59}\text{Co}_{0.41}$ -HPAA	$\text{Fe}_{0.59}\text{Co}_{0.41}(\text{HO}_3\text{PCHOHCOO})(\text{H}_2\text{O})_{2.5}$
0.92:0.08	$\text{Fe}_{0.85}\text{Mn}_{0.15}$ -HPAA	$\text{Fe}_{0.85}\text{Mn}_{0.15}(\text{HO}_3\text{PCHOHCOO})(\text{H}_2\text{O})_{2.5}$
0.79:0.21	$\text{Fe}_{0.8}\text{Mn}_{0.2}$ -HPAA	$\text{Fe}_{0.8}\text{Mn}_{0.2}(\text{HO}_3\text{PCHOHCOO})(\text{H}_2\text{O})_{2.5}$

4.2.2. Structural Characterisation

Crystal structure of isostructural compounds **M(II)-HPAA** (M = Fe, Mn, Co and Zn) was previously described by Fu et al. (2005b). The crystal structures of the obtained solids were confirmed by Rietveld refinements. Figure AIII.1 in Appendix III

shows the Rietveld refinement plots for **Fe**- and **Zn-HPAA** using their crystal structure respectively (CCDC no. 285711 and no. 285713).

In order to check if bimetallic compounds correspond to solid solutions, a Rietveld refinement study was also carried out (Figure AIII.2, Appendix III).

As it is shown in Table 4.4, partial substitution of Fe(II) by Zn(II) leads to a subtle reduction in unit cell volume due to the smaller cation size of Zn(II). In addition, the XRPD patterns of the bimetallic compound **Fe_{0.71}Zn_{0.29}-HPAA** differs from that corresponding to a physical mixture of the single derivatives with the same Fe/Zn composition, the latter being characterised by a peak splitting at $2\theta = 16-18^\circ$, which is absent in the former (Figure 4.8). Table 4.4 summaries the main crystallographic data.

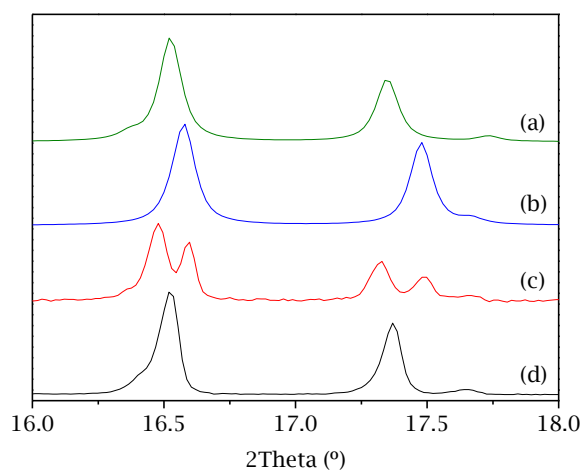


Figure 4.8. Comparison of XRD patterns corresponding to: (a) **Fe-HPAA**, (b) **Zn-HPAA**, (c) 70/30 % w/w **Fe-HPAA/Zn-HPAA** physical mixture and (d) **Fe_{0.71}Zn_{0.29}-HPAA**. (The intensity of the reflections can be affected by preferred orientation due to the layered nature of the solids).

Table 4.4. Selected crystallographic data for $M(II)$ -HPAA and Fe_xZn_{1-x} -HPAA compounds.

Phase	Fe-HPAA	$Fe_{0.88}Zn_{0.11}$ -HPAA	$Fe_{0.71}Zn_{0.29}$ -HPAA	$Fe_{0.54}Zn_{0.46}$ -HPAA	$Fe_{0.41}Zn_{0.59}$ -HPAA	Zn-HPAA
Space group	P 2 ₁ /c	P 2 ₁ /c	P 2 ₁ /c	P 2 ₁ /c	P 2 ₁ /c	P 2 ₁ /c
Chemical formula	$C_2FeO_8PH_8$	$C_2Fe_{0.88}Zn_{0.11}O_8PH_8$	$C_2Fe_{0.71}Zn_{0.29}O_8PH_8$	$C_2Fe_{0.54}Zn_{0.46}O_8PH_8$	$C_2Fe_{0.41}Zn_{0.59}O_8PH_8$	$C_2ZnO_8PH_8$
Formula mass (g·mol ⁻¹)	246.90	247.95	249.67	251.29	252.53	256.44
λ (Å)	0.4124	1.5418	1.5418	1.5418	1.5418	1.5418
a (Å)	5.7580(1)	5.7508(1)	5.75004(9)	5.74238(9)	5.74322(8)	5.72097(9)
b (Å)	15.6192(3)	15.5825(3)	15.5733(2)	15.5573(3)	15.5598(2)	15.5342(2)
c (Å)	7.8938(1)	7.8847(2)	7.8849(2)	7.8745(2)	7.8722(1)	7.8516(1)
β (°)	109.707(1)	109.745(1)	109.869(1)	109.985(1)	110.1420(9)	110.3112(9)
Unit cell volume (Å ³)	668.35(3)	665.02(3)	664.04(2)	661.12(3)	660.47(2)	654.3(2)
Z	4	4	4	4	4	4
No. of independent reflections	1148	707	706	703	703	697
Data/Restraints/Parameters	954/19/75	6191/19/82	1106/19/82	573/19/89	1118/19/46	1102/19/95
R_{wp}	0.0996	0.0139	0.0165	0.0194	0.0230	0.0650
R_p	0.0714	0.0102	0.0117	0.0140	0.0162	0.0493
R_f	0.0722	0.0644	0.0614	0.0470	0.0491	0.0495

4.3. Post-Synthesis Modification

4.3.1. Ammonia Adsorption

As layered solids, **M(II)-HPAA** are amenable to guest molecules adsorption in order to enhance specific properties. Following to a single procedure of tuning proton conductivity conducted by Bazaga-García et al. (2014) for a calcium derivative of the 5-(dihydroxyphosphoryl)isophthalate ligand, we undertook a study of ammonia adsorption, as a post-synthesis modification intended to enhance the proton conductivity of these materials. The goal was to create extended strong H-bond networks with the participation of NH_3 and H_2O , as guest molecules, and the remaining phosphonate acidic groups. Specifically, the procedure consisted of exposing 350 mg of the solid to ammonia vapours (from a 14% ammonia aqueous solution) into a closed container at different exposure times: 0, 1, 5, 12, 24, 36, 42, 48 and 72h. Afterwards, the exceeding adsorbed ammonia was removed in a 98% H_2SO_4 -containing desiccator for 24h (Figure 4.9). Ammonia adsorption leads to partially amorphised derivatives, hereinafter referred to as **Fe-NH₃-xh** or **Fe_{1-x}Zn_x-NH₃-xh**. However, the process is progressive and thus the unreacted crystalline phase remains at exposure times < 72 h (Figure 4.10). These NH_3 -loaded samples were fully characterised by elemental and thermogravimetric analysis, X-ray photoelectron spectroscopy, X-ray powder diffraction, pair distribution function (PDF) analysis and impedance spectroscopy.

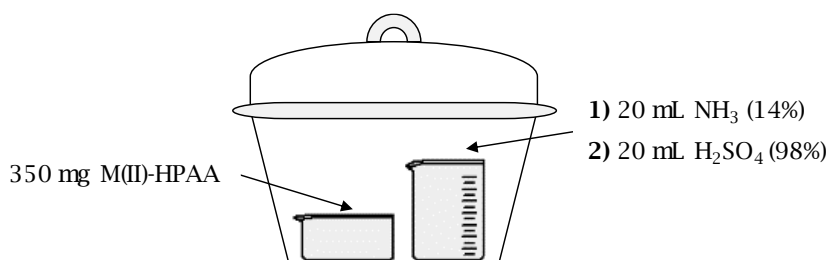


Figure 4.9. Procedures of sample exposure to ammonia vapours and subsequent NH_3 excess removing.

TRANSITION METALS HYDROXYPHOSPHONOACETATES

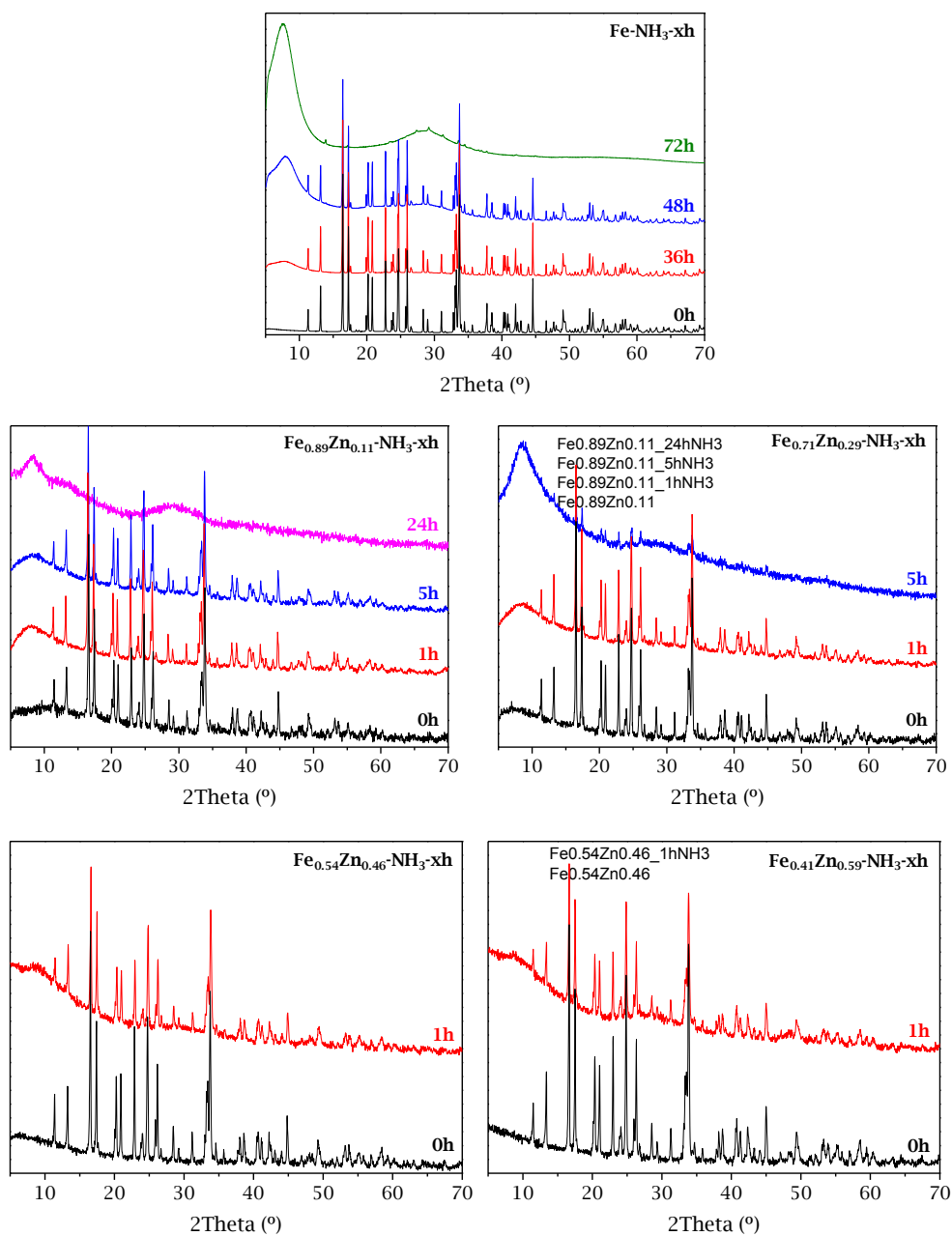


Figure 4.10. X-ray powder diffraction patterns for $\text{Fe-NH}_3\text{-xh}$ and $\text{Fe}_x\text{Zn}_{1-x}\text{-NH}_3\text{-xh}$ derivatives.

The chemical composition of $\text{Fe-NH}_3\text{-xh}$ and $\text{Fe}_x\text{Zn}_{1-x}\text{-NH}_3\text{-xh}$ solids were obtained from their elemental analysis (Table AII.2, Appendix II) and thermal

analysis. Table 4.5 gives a summary of the $\text{Fe-NH}_3\text{-xh}$ and $\text{Fe}_x\text{Zn}_{1-x}\text{-NH}_3\text{-xh}$ composition obtained according to the thermal and elemental analysis results. As can be seen, the maximum adsorption of NH_3 for $\text{Fe}_x\text{Zn}_{1-x}\text{-NH}_3\text{-xh}$ samples was 1.5 mol per formula. Further attempts to increase NH_3 loadings in these materials were unsuccessful due to the hydroscopic nature of the resulting derivatives.

Table 4.5. Chemical composition for $\text{Fe-NH}_3\text{-xh}$ and $\text{Fe}_x\text{Zn}_{1-x}\text{-NH}_3\text{-xh}$ samples.

Acronym	Stoichiometric
Fe-NH₃-0h	$\text{Fe}(\text{HO}_3\text{PCHOHCOO})(\text{H}_2\text{O})_{2.5}$
Fe-NH₃-12h	$\text{Fe}(\text{HO}_3\text{PCHOHCOO})(\text{H}_2\text{O})_{2.5}(\text{NH}_3)_{0.2}$
Fe-NH₃-24h	$\text{Fe}(\text{HO}_3\text{PCHOHCOO})(\text{H}_2\text{O})_{2.5}(\text{NH}_3)_{0.4}$
Fe-NH₃-36h	$\text{Fe}(\text{HO}_3\text{PCHOHCOO})(\text{H}_2\text{O})_3(\text{NH}_3)_{0.75}$
Fe-NH₃-42h	$\text{Fe}(\text{HO}_3\text{PCHOHCOO})(\text{H}_2\text{O})_3(\text{NH}_3)_{0.8}$
Fe-NH₃-48h	$\text{Fe}(\text{HO}_3\text{PCHOHCOO})(\text{H}_2\text{O})_3(\text{NH}_3)_{1.25}$
Fe-NH₃-72h	$\text{Fe}(\text{HO}_3\text{PCHOHCOO})(\text{H}_2\text{O})_3(\text{NH}_3)_{1.75}$
Fe_{0.89}Zn_{0.11}-NH₃-0h	$\text{Fe}_{0.89}\text{Zn}_{0.11}(\text{HO}_3\text{PCHOHCOO})(\text{H}_2\text{O})_{2.5}$
Fe_{0.89}Zn_{0.11}-NH₃-1h	$\text{Fe}_{0.89}\text{Zn}_{0.11}(\text{HO}_3\text{PCHOHCOO})(\text{H}_2\text{O})_3(\text{NH}_3)_{0.2}$
Fe_{0.89}Zn_{0.11}-NH₃-5h	$\text{Fe}_{0.89}\text{Zn}_{0.11}(\text{HO}_3\text{PCHOHCOO})(\text{H}_2\text{O})_3(\text{NH}_3)_{0.5}$
Fe_{0.71}Zn_{0.29}-NH₃-0h	$\text{Fe}_{0.71}\text{Zn}_{0.29}(\text{HO}_3\text{PCHOHCOO})(\text{H}_2\text{O})_{2.5}$
Fe_{0.71}Zn_{0.29}-NH₃-1h	$\text{Fe}_{0.71}\text{Zn}_{0.29}(\text{HO}_3\text{PCHOHCOO})(\text{H}_2\text{O})_3(\text{NH}_3)_{0.6}$
Fe_{0.71}Zn_{0.29}-NH₃-5h	$\text{Fe}_{0.71}\text{Zn}_{0.29}(\text{HO}_3\text{PCHOHCOO})(\text{H}_2\text{O})_3(\text{NH}_3)_{1.5}$
Fe_{0.54}Zn_{0.49}-NH₃-0h	$\text{Fe}_{0.54}\text{Zn}_{0.46}(\text{HO}_3\text{PCHOHCOO})(\text{H}_2\text{O})_{2.5}$
Fe_{0.54}Zn_{0.49}-NH₃-1h	$\text{Fe}_{0.54}\text{Zn}_{0.46}(\text{HO}_3\text{PCHOHCOO})(\text{H}_2\text{O})_3(\text{NH}_3)$
Fe_{0.41}Zn_{0.59}-NH₃-0h	$\text{Fe}_{0.41}\text{Zn}_{0.59}(\text{HO}_3\text{PCHOHCOO})(\text{H}_2\text{O})_{2.5}$
Fe_{0.41}Zn_{0.59}-NH₃-1h	$\text{Fe}_{0.41}\text{Zn}_{0.59}(\text{HO}_3\text{PCHOHCOO})(\text{H}_2\text{O})_3(\text{NH}_3)_{1.3}$

As can be seen in their TG curves (Figure 4.11), increasing NH_3 loadings entail higher low temperature (< 200 °C) weight losses due to removal of the $\text{NH}_3/\text{H}_2\text{O}$ guest species before ligand decomposition starts ($T > 200$ °C).

TRANSITION METALS HYDROXYPHOSPHONOACETATES

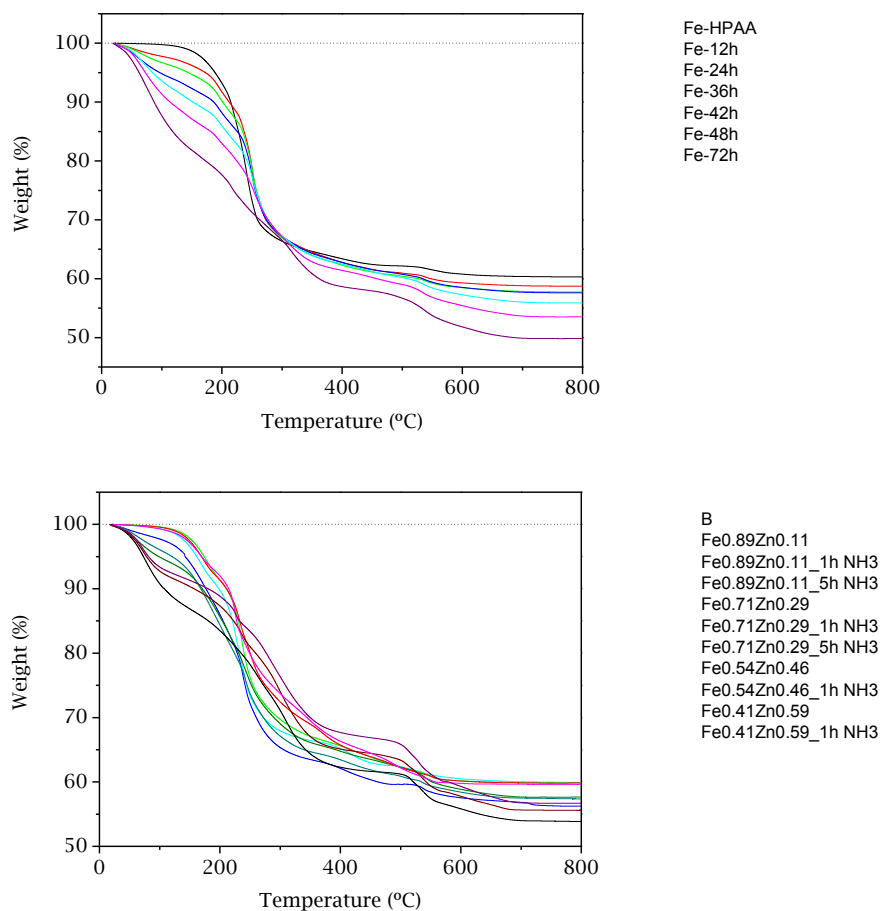


Figure 4.11. Thermal analysis for compounds (top) **Fe-NH₃-xh** [$x = 0$ (black), 12 (red), 24 (green), 36 (blue), 42 (cyan), 48 (magenta) and 72h (purple)] and (bottom) **Fe_{0.89}Zn_{0.11}-NH₃-xh** [$x = 0$ (blue), 1 (cyan) and 5h (dark cyan)], **Fe_{0.71}Zn_{0.29}-NH₃-xh** [$x = 0$ (green), 1 (olive) and 5h (black)], **Fe_{0.54}Zn_{0.29}-NH₃-xh** [$x = 0$ (red) and 1h (wine)] and **Fe_{0.71}Zn_{0.29}-NH₃-xh** [$x = 0$ (pink) and 1h (purple)].

Quantification of the amorphous content in **Fe-NH₃-xh** samples was determined by Rietveld refinement (Rietveld, 1969) using the internal standard method (De la Torre, Bruque & Aranda, 2001). As described in Section 4.2.2., refinements were carried out employing a 33% w/w of TiO₂ as internal standard (NIST 674b). TiO₂ was selected due to its mass adsorption coefficient, similar to those of the samples. Figure AIII.3 in Appendix III shows the final Rietveld plots for the different compositions and Table 4.6 shows selected crystallographic details for the crystalline

CHAPTER 4

fraction of **Fe-NH₃-xh** samples, as well as the amorphous content (A), which was estimated from the following equation:

$$A (\%) = \frac{1 - W_s/R_s}{100 - W_s} \cdot 10^4 \quad \text{Equation 4.1}$$

where W_s is the weighted concentration of the internal standard and R_s stands for the Rietveld analysed concentration of the internal standard (De la Torre, Bruque & Aranda, 2001).

Results indicate that the amorphous fraction increases with higher times of ammonia exposure, in such a way that incorporating 1.25-1.75 mol per formula leads to the practical sample amorphisation.

Table 4.6. Selected crystallographic details and amorphous content for Fe-NH₃-xh compounds.

		Fe-NH ₃ -xh					
x (h)	0	12	24	36	42	48	72
H ₂ O/NH ₃ content	2.5/0	2.5/0.2	2.5/0.4	3/0.75	3/0.8	3/1.25	3/1.75
(mol/formula)							
Space group	P 2 ₁ /c	P 2 ₁ /c	P 2 ₁ /c	P 2 ₁ /c	P 2 ₁ /c	P 2 ₁ /c	-
λ (Å)	0.7093	0.7093	0.7093	0.7093	0.7093	0.7093	-
a (Å)	5.7459(3)	5.7446(3)	5.7456(3)	5.7457(3)	5.7453(3)	5.7432(4)	-
b (Å)	15.556(1)	15.5534(9)	15.556(1)	15.555(1)	15.556(1)	15.551(1)	-
c (Å)	7.8824(5)	7.8801(5)	7.8810(5)	7.8805(5)	7.8798(5)	7.8781(7)	-
β (°)	109.647(3)	109.640(3)	109.634(4)	109.632(4)	109.627(4)	109.635(6)	-
R _{wpr}	0.1040	0.0932	0.0878	0.0778	0.0702	0.0550	-
R _p	0.0784	0.0691	0.0654	0.0575	0.0520	0.0392	-
A (%)	4.7	15.5	23.0	35.1	50.5	75.0	100

Total scattering data analysed by Pair Distribution Function (PDF) methodology provide information about local bonding environments of amorphous, nanoparticles and crystalline phases (Egami & Billinge, 2012). In order to recognise if the amorphous fraction arising from ammonia adsorption is still keeping the local bonding environments of the crystalline phase, synchrotron total scattering data analysed by PDF methodology have been used. Data were collected in the X-ray powder diffraction beamline BL04-MSPD at ALBA synchrotron (Barcelona, Spain) using a wavelength of 0.4124(1) Å (30 keV).

As observed in Figure 4.12, sample with the highest ammonia content, **Fe-NH₃-72h**, did not show larger atomic order beyond 5Å. Nevertheless, local atomic order apparently remained.

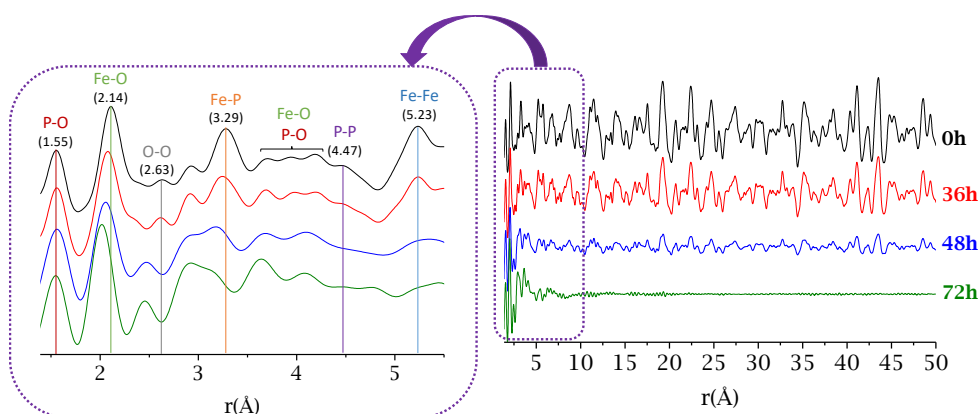


Figure 4.12. (Right) Experimental PDF for **Fe-NH₃-xh** samples at different times (hours) of NH₃ vapours exposure. (Left) Selected interatomic distances are highlighted.

PDF experimental data were obtained and analysed by using PDFgetx3 (Juhas et al., 2013) and PDFGui (Farrow et al., 2007) respectively, employing a $Q_{\text{max}} = 24 \text{ \AA}^{-1}$. A crystalline nickel was employed as standard, from which the instrumental parameter Q_{damp} (0.00273 \AA^{-1}) and Q_{broad} (0.00738 \AA^{-1}) were determined. For the PDF fit of the samples, the following strategy was used. Firstly, a high r -region (30-50 Å) of the crystalline sample, **Fe-NH₃-0h**, was fitted using the crystal structure of **Fe-HPAA** (Fu et al., 2005b) as starting model (CCDC no. 285711). Scale factor, unit cell parameters, atomic displacement parameters (ADPs) and positions of Fe, P and O were optimised. Secondly, the same procedure was followed to fit a new region (from 10 to 30 Å). As the parameters were almost identical, the region from 10 to 50 Å was fitted together.

For low r -region (1.4-10 Å), delta2 (low- r correlated motion peak sharpening factor) was also refined. The final R_w value was 22.2% for the region from 1.4 to 10 Å and 14.5% for the 10-50 Å region. Fit plots are displayed in Figure 4.13.

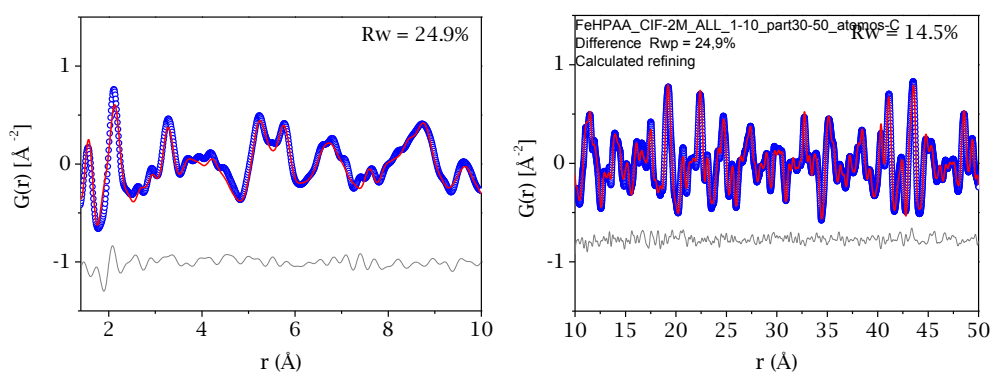


Figure 4.13. Experimental (blue circles) and fitted (red solid lines) PDF fit plots for **Fe-NH₃-0h** at (left) low r -region (1.4-10 Å) and (right) high r -region (10-50 Å).

Values from 10-50 Å region of **Fe-NH₃-0h** were employed for the analysis of the **Fe-NH₃-36h** sample. In this case, only the scale factor, unit cell parameters and ADPs were refined. For low r -region (1.4-10 Å), delta2 (low- r correlated motion peak sharpening factor) was also optimized. The same procedure was employed for **Fe-NH₃-48h** sample, but using the PDF fit of **Fe-NH₃-36h** as starting model. In the 1.4-10 Å region, only the scale factor and unit cell parameters were optimised. All attempts to refine the sp diameter parameter (diameter of the nanoparticle) were unsuccessful. A summary of the PDF analysis results for **Fe-NH₃-xh** (0, 36 and 48 h) is displayed in Table 4.7.

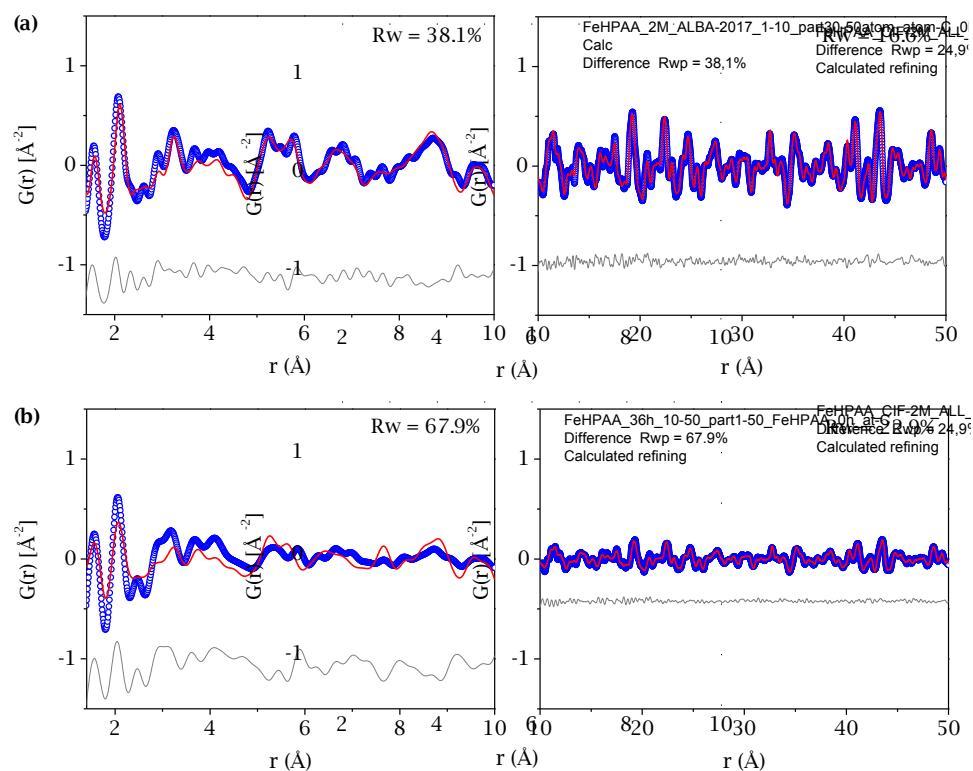


Figure 4.14. Experimental (blue circles) and fitted (red solid lines) PDF fit plots for (a) $\text{Fe-NH}_3\text{-36h}$ and (b) $\text{Fe-NH}_3\text{-48h}$ at (left) low r -region (1.4-10 Å) and (right) high r -region (10-50 Å).

Table 4.7. Selected results from synchrotron PDF analysis of $\text{Fe-NH}_3\text{-xh}$ samples.

x	0h		36h		48h	
Region (Å)	1.4-10	10-50	1.4-10	10-50	1.4-10	10-50
Scale factor	0.3657	0.3334	0.3025	0.2252	0.1969	0.0777
a (Å)	5.7686	5.7584	5.7444	5.7586	5.6606	5.7567
b (Å)	15.6310	15.606	15.6919	15.6039	15.9319	15.6049
c (Å)	7.9111	7.8977	7.8142	7.89768	7.6593	7.8959
β (°)	110.31	109.707	109.8	109.686	110.477	109.683
ADP (Fe)	0.0081	0.0100	0.0099	0.0109	0.0099	0.0113
ADP (P)	0.0082	0.0111	0.0094	0.0112	0.0094	0.0102
ADP (O)	0.0233	0.0224	0.0083	0.0235	0.0083	0.0234
ADP (C)	0.0888	0.0306	0.0567	0.0432	0.0567	0.0437
Delta2	2.3634	-	2.2981	-	2.2981	-
Rw (%)	24.9	14.5	38.1	16.6	67.9	22.9

Data in Table 4.7 reveal that the unit cell parameters as determined in the 10-50 Å region remained practically unchanged, which points to the crystalline phase in **Fe-NH₃-36h** and **Fe-NH₃-48h** samples correspond to an unreacted microcrystalline fraction of the solid. However, the PDF fit for the low *r*-range, 1.4-10 Å increasingly diverges from the starting structural model with NH₃ loadings, which may be interpreted as a result of the loss of short-range order (>5 Å). Interestingly, the first P-O, Fe-O and Fe-P distances (1.55, 2.14 and 3.29 Å respectively) are quite similar for all samples (Figure 4.12), indicating that the iron local environment was essentially preserved upon ammonia exposure. Furthermore, the existence of other crystalline phases that could form due to an eventual decomposition of the ammonia-containing samples is ruled out from the PDF analysis. Another evidence pointing to maintenance of the integrity of Fe(II) phosphonate is provided by the TG-TDA curves. As can be seen in Figure 4.15, **Fe-NH₃-72h** sample displays a thermal behaviour quite similar to that of **Fe-HPAA**.

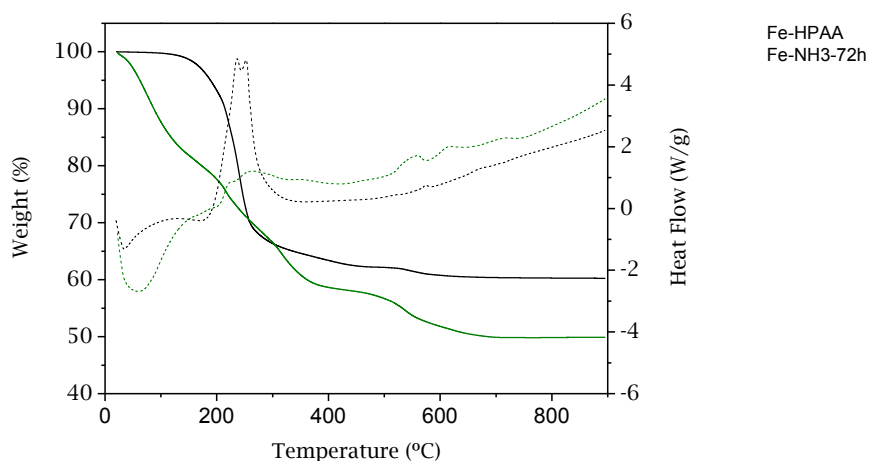


Figure 4.15. TG-TDA curves for **Fe-NH₃-0h** (black) and **Fe-NH₃-72h** (olive).

Moreover, Fe₂P₂O₇ was identified by Rietveld refinement as the resulting product of heating both **Fe-NH₃-0h** and **Fe-NH₃-72h** samples at 700 °C under N₂ (Appendix III, Figure AIII.4), which was carried out using the crystal structure of Co₂P₂O₇ (ICSD no. 2830) as starting model and employing soft constraints to maintain chemically reasonable geometries (Chapter 3, Table 3.2).

Finally, surface characterisation of the NH_3 -loaded samples by X-ray photoelectron spectroscopy (XPS), summarized in Table 4.8, reveals surface Fe(II)/Fe(III) molar ratios quite similar in members of each series at different times of NH_3 exposure, which is taken to mean that ammonia adsorption does not lead to iron oxidation even in the most air-exposed surfaces of the samples.

Table 4.8. Fe(II)/Fe(III) ratio from XPS data for $\text{Fe-NH}_3\text{-xh}$ and $\text{Fe}_x\text{Zn}_{1-x}\text{-NH}_3\text{-xh}$ sample series.

Sample	x (h)	Fe(II)/Fe(III)
Fe-NH₃-xh	12	1.26
	24	1.27
	36	1.37
	42	1.47
	48	1.38
Fe_{0.89}Zn_{0.11}-NH₃-xh	0	2.07
	1	1.79
Fe_{0.71}Zn_{0.29}-NH₃-xh	0	2.31
	1	1.92
Fe_{0.54}Zn_{0.46}-NH₃-xh	0	2.15
	1	1.69
Fe_{0.41}Zn_{0.59}-NH₃-xh	0	1.95
	1	2.29

4.4. Proton Conductivity

All samples were analysed by impedance spectroscopy due to their extended hydrogen bonding networks (Fu et al., 2005b), which make them potential candidates as proton conductor. Moreover, NH_3 -loaded samples were considered of interest for testing the effects of NH_3 adsorption in proton conductivity as it generates important changes in H-bond networks. However, samples with high Zn^{2+} contents were unstable at high relative humidity because of their high hygroscopic nature.

Impedance data were collected as indicated in Section 3.13.2. Figures AIV.1 and AIV.2 in Appendix IV give the plots of complex impedance plane, measured from 80 to 25 °C and 95% RH, for all analysed samples. The total pellet resistance (R_p) was obtained from the intercept of the spike and/or the arc (low-frequency end) on the Z' axis.

Proton conductivity values (Table 4.9) were obtained from the Nyquist plots and the variations with the temperature are given in a traditional Arrhenius plot (Figure 4.16). A gradual enhance of the proton conductivity was observed with increasing ammonia loading, from $1.1 \cdot 10^{-5} \text{ S} \cdot \text{cm}^{-1}$ for **Fe-NH₃-0h** to $6.4 \cdot 10^{-3} \text{ S} \cdot \text{cm}^{-1}$ for **Fe-NH₃-72h** at 80 °C and 95% RH. Solid solution samples exhibited the same behaviour. This increase in proton conductivity may be attributed in principle to higher loading of guest species (NH₃ and H₂O), which can create new proton transfer pathways. The FTIR spectra (Figure 4.17) display a broadening in the stretching vibration bands of H₂O, NH₃/NH₄⁺, carboxylate and phosphonate groups (3400-3100, 1700-1600 and 1200-900 cm⁻¹), which corroborates an enhancement of the hydrogen bond networks caused by the presence of ammonia. In addition, the increment of the intensity observed for the band situated at 1400 cm⁻¹ for **Fe-NH₃-72h** suggests the presence of NH₄⁺ (Oxton, Knop & Falk, 1975).

Table 4.9. Proton conductivity values at 80 °C and 95% RH, activation energy values and H₂O/NH₃ content before and after impedance measurements.

Compound	x (h)	σ (S·cm ⁻¹)	Ea (eV)	H ₂ O/NH ₃ content (mol/formula)	
				Before	After
Fe-NH₃-xh	0	$1.1 \cdot 10^{-5}$	0.36	2.5/0	2.5/0
	12	$2.8 \cdot 10^{-4}$	0.42	2.5/0.2	2.5/0.2
	24	$3.5 \cdot 10^{-4}$	0.41	2.5/0.4	3/0.4
	36	$6.4 \cdot 10^{-4}$	0.41	3/0.75	3/0.5
	42	$8.1 \cdot 10^{-4}$	0.43	3/0.8	3/0.75
	48	$1.2 \cdot 10^{-3}$	0.41	3/1.25	3/1
	72	$1.8 \cdot 10^{-3}$	0.45	3/1.75	3/1.2
Fe_{0.71}Zn_{0.29}-NH₃-xh	0	$4.7 \cdot 10^{-5}$	0.41	2.5/0	2.5/0
	1	$1.9 \cdot 10^{-4}$	0.37	3/0.6	3/0.5
	5	$1.3 \cdot 10^{-3}$	0.43	3/1.5	3/1.1
Fe_{0.41}Zn_{0.59}-NH₃-xh	0	$9.8 \cdot 10^{-6}$	0.44	2.5/0	3/0
	1	$1.5 \cdot 10^{-4}$	0.57	3/1.3	2.5/0.75

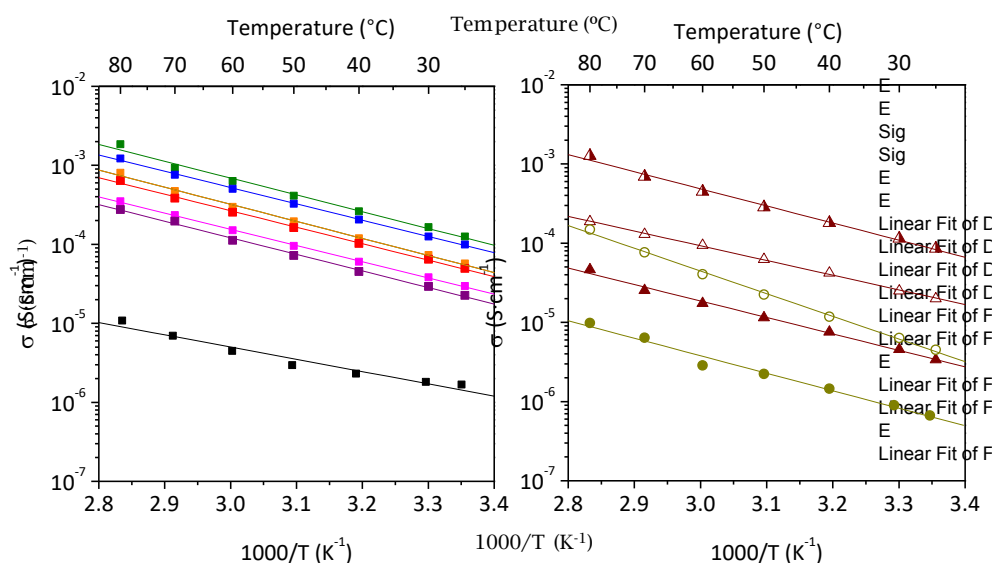


Figure 4.16. Arrhenius plots for (left) $\text{Fe-NH}_3\text{-xh}$ at different ammonia exposure times: 0h (■), 12h (■), 24h (■), 36h (■), 42h (■), 48h (■) and 72h (■) and (right) $\text{Fe}_x\text{Zn}_{1-x}\text{-NH}_3\text{-xh}$: $\text{Fe}_{0.71}\text{Zn}_{0.29}\text{-NH}_3\text{-0h}$ (▲), $\text{Fe}_{0.71}\text{Zn}_{0.29}\text{-NH}_3\text{-1h}$ (△), $\text{Fe}_{0.71}\text{Zn}_{0.29}\text{-NH}_3\text{-5h}$ (▲), $\text{Fe}_{0.41}\text{Zn}_{0.59}\text{-NH}_3\text{-0h}$ (●) and $\text{Fe}_{0.41}\text{Zn}_{0.59}\text{-NH}_3\text{-1h}$ (○).

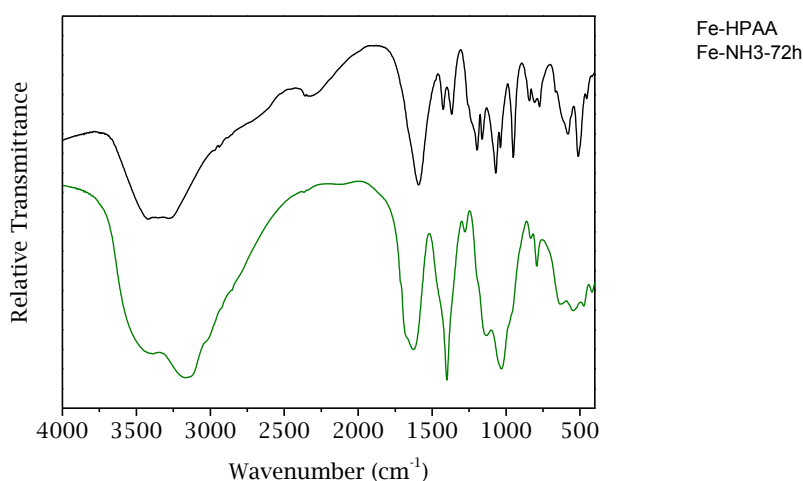


Figure 4.17. FTIR spectra for compounds $\text{Fe-NH}_3\text{-0h}$ (black) and $\text{Fe-NH}_3\text{-72h}$ (olive).

It is significant that the proton conductivity exhibited by $\text{Fe-NH}_3\text{-72h}$ and $\text{Fe}_{0.71}\text{Zn}_{0.29}\text{-NH}_3\text{-5h}$, two samples with equivalent amounts of guest species (NH_3 and

H₂O), are quite similar (Table 4.9), which is taken to mean the essential role of these guest species in determining the proton conductivity behaviour of these solids. The solid solution compounds reached the highest ammonia loading in shorter exposure time than **Fe-HPAA**, but unfortunately they become increasingly hygroscopic with increasing concentration of Zn²⁺ ions in the structure. This could be due to the higher affinity of Zn²⁺, in comparison with Fe²⁺, for ammonia and water molecules.

Activation energy (E_a) values, obtained from the slope of the Arrhenius plots, are all indicative of a Grotthuss-type proton transfer mechanism (E_a < 0.5 eV). It was also demonstrated, as indicated in Table 4.9, that the material compositions remain practically invariable after impedance measurements.

In order to determine the influence of the particle size on proton conductivity, values, a particle size analysis for all samples, before and after impedance measurements, was performed. All samples displayed quiet similar particle size (~1 μm) and not significant changes were observed after impedance measurements (Figures 4.18-20).

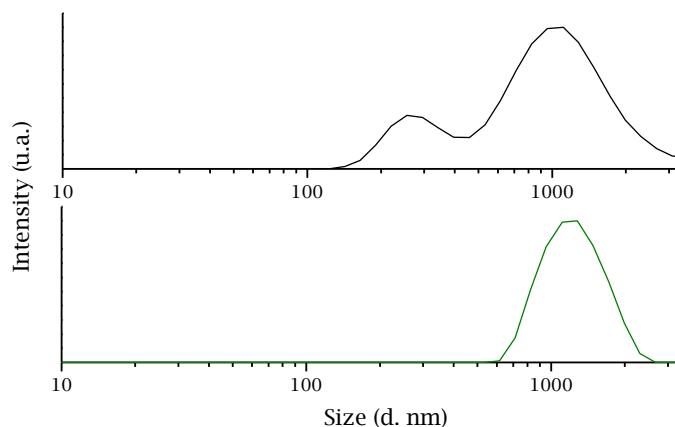


Figure 4.18. Size distribution by intensity for compounds **Fe-NH₃-0h** (black) and **Fe-NH₃-72h** (olive).

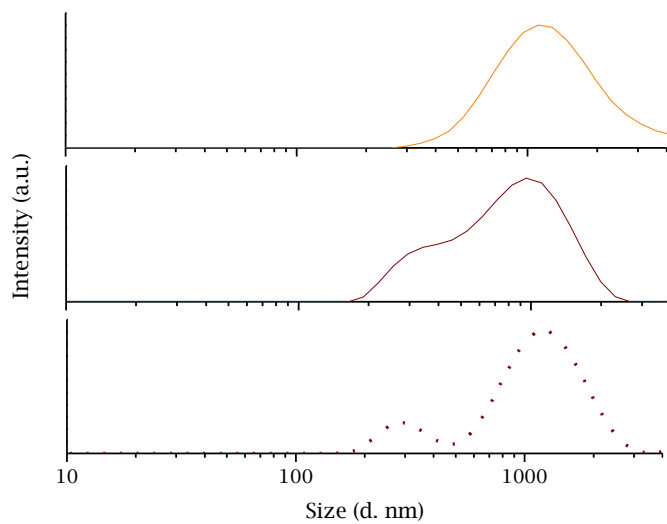


Figure 4.19. Size distribution by intensity for $\text{Fe}_{0.71}\text{Zn}_{0.29}\text{-HPAA}$ (orange) and $\text{Fe}_{0.71}\text{Zn}_{0.29}\text{-NH}_3\text{-5h}$ (wine) before (solid line) and post impedance measurements (dot line).

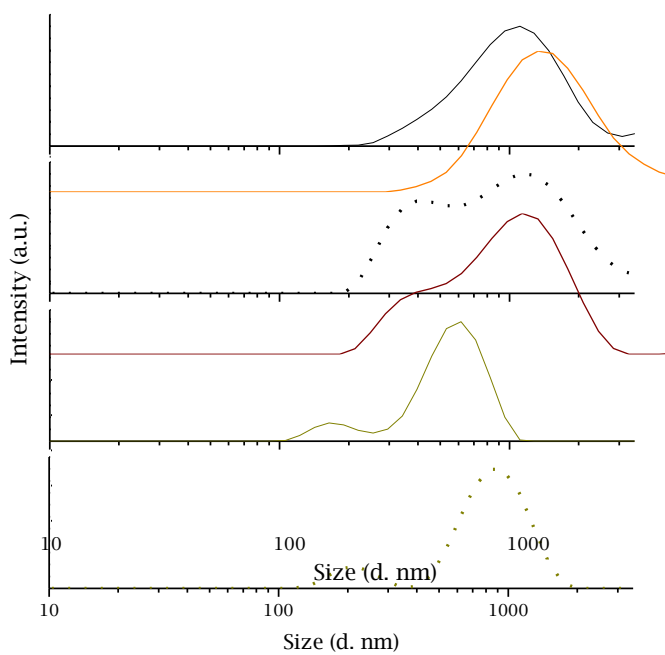


Figure 4.20. Size distribution by intensity before (solid line) and post impedance measurements (dot line) for $\text{Fe}_{0.41}\text{Zn}_{0.59}\text{-HPAA}$ (black) and $\text{Fe}_{0.41}\text{Zn}_{0.59}\text{-NH}_3\text{-1h}$ (dark yellow).

In addition, BET surface areas were measured for samples **Fe-NH₃-0h** and **Fe-NH₃-72h**, but no significant variations were found between them, i.e. the values being characteristics of non-porous solids ($S_{\text{BET}} \sim 2 \text{ m}^2 \cdot \text{g}^{-1}$).

From these data, it can be inferred that the proton conductivity of these materials is rather a result of forming extended H-bond networks, which are greatly facilitated by increasing H₂O/NH₃ loads, than an effect of particle size aggregation. In addition, the proton conductivity values for the studied solids are within the range of values corresponding to many other coordination polymers (Table 1.2).

4.5. Photocatalytic Properties

Photocatalytic properties of **Fe-HPAA** and M(II)-substituted **Fe-HPAA** solid solutions have been studied for photodegradation of phenol, 4-chlorophenol and methylene blue (MB). The former two are highly toxic pollutants present in industrial wastewater (Babuponnusami & Muthukumar, 2011; Clarizia, 2017; Brillas & García-Segura, 2020) and MB is a dye widely employed in textile, paper, printing and other industries (Sharma, 2011; Pouran, Raman & Daud, 2014).

It was already demonstrated (Bazaga-García et al., 2012) that HPAA ligand in the **Fe-HPAA** solid is an oxidation-resistant molecule upon irradiation with UV-A light in the presence of H₂O₂. On the other hand, phenol, organochloride substances and MB are known as recalcitrant pollutants, i.e. they can remain intact in waters for long times, even in the presence of moderate oxidant like H₂O₂. So preliminary assays for phenol degradation indicated that mineralization with H₂O₂ and UV-A light did not take place in 120 minutes of reaction (Bazaga-García et al., 2012).

Regarding to phenol removal, different photocatalytic test conditions were previously optimized studying a wide range of parameters under UV-A light (Bazaga-García, 2015):

- Catalyst load: 220, 500 and 700 mg/L.
- Initial pH: 3.5, 4.0, 5.0 and 6.0.

The selected experimental conditions were the following (Table 4.10):

Table 4.10. Selected experimental conditions for the photocatalytic test.

	Pre-treatment	Treatment
[Pollutant]	0 mg·L ⁻¹	50 mg·L ⁻¹
[H ₂ O ₂]	50 mg·L ⁻¹	500 mg·L ⁻¹
Initial pH	4.0	4.0
[Photocatalyst]	700 mg·L ⁻¹	
Time	30 min	180-240 min

Photocatalytic tests were carried out on a Luzchem CCP-4V photochemical reactor providing of magnetic stirring and equipped with 14 lamps (Figure 4.21). This photoreactor can be computer controlled through CCP-4V software.

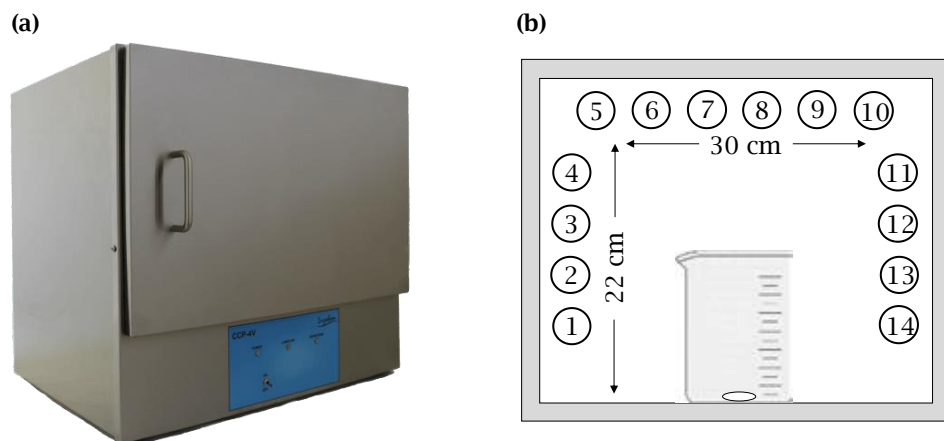


Figure 4.21. (a) Luzchem CCP-4V photoreactor and (b) a schematic diagram of lamps and reaction vessel positioning.

The following procedure was employed for the photocatalytic tests. Firstly, catalyst pre-treatment (700 mg·L⁻¹) under UV-A light (6 Hitachi FL8BL-B lamps, 8W) and with 50 mg·L⁻¹ H₂O₂ during 30 minutes was carry out to enhance its efficiency. This pre-treatment was reported as an effective method to improve the photocatalytic conversion rate (Li et al., 2004; Parkhomchuk, Vanina & Preis, 2008). Then, the photocatalytic test was carried out under visible light (14 Prilux lamps, 8W) at initial pH of 4.0, adding 50 mg·L⁻¹ of phenol or 4-chlorophenol and 500 mg·L⁻¹ of

H₂O₂ (Figure 4.22). Photocatalytic test for MB removal was carried out following the same procedure but without pre-treatment and employing 14 UV-A lamps.

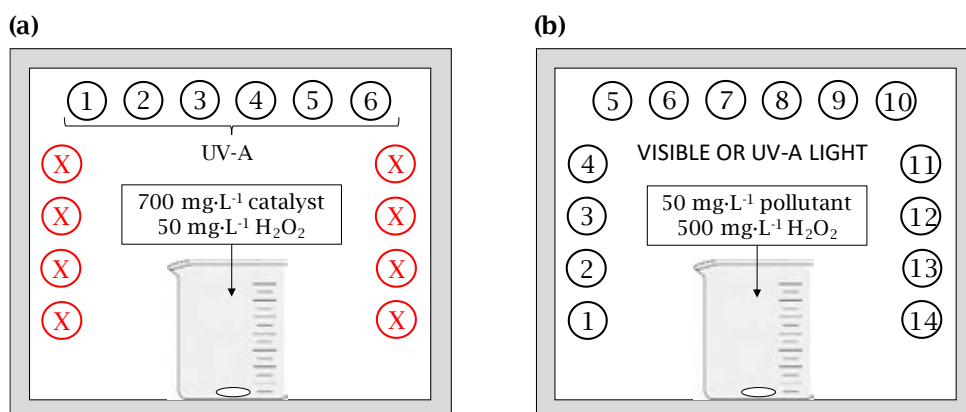


Figure 4.22. Schematic diagrams of the (a) pre-treatment and (b) photocatalytic tests.

In order to carry out different analysis, 8 mL of samples were extracted and filtered at different times of irradiation. In all cases, pollutant photodegradation was followed by measuring total organic carbon (TOC) (Chapter 3, Section 3.1.2).

For phenol degradation, a higher TOC removal rate was achieved at lower reaction times employing UV-A radiation as compared to visible light (~68% against ~32% at 30 minutes of exposure respectively). However, after 180 minutes of reaction, similar percentages of TOC removal were reached under both types of radiation (~95% against ~89%, respectively). Employing solid solution photocatalysts (**Fe_{0.8}Mn_{0.2}**, **Fe_{0.78}Co_{0.22}** or **Fe_{0.71}Zn_{0.29}-HPAA**) under visible irradiation led to TOC removal values quite similar to that corresponding to **Fe-HPAA**. In absence of light, no phenol degradation was noticed (Figure 4.23).

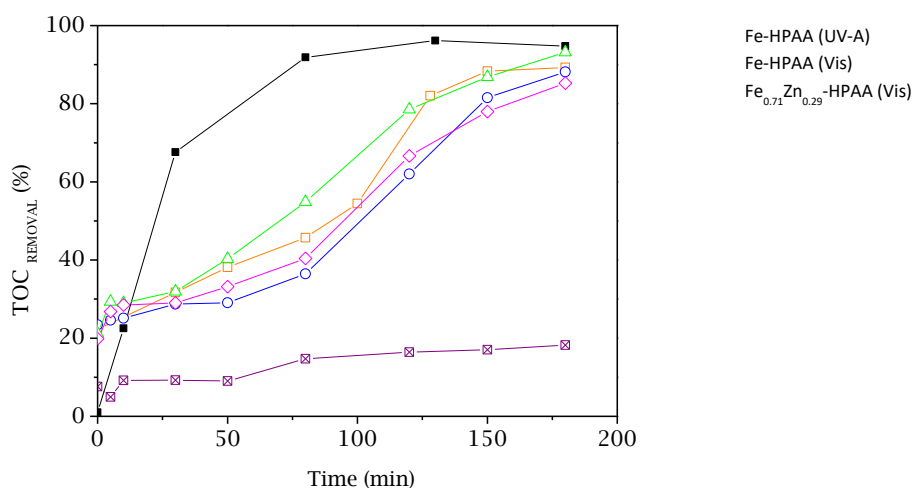


Figure 4.23. Time evolution of phenol removal under UV-A light (■ **Fe-HPAA**), visible light (□ **Fe-HPAA**, △ **Fe_{0.8}Mn_{0.2}-HPAA**, ◇ **Fe_{0.78}Co_{0.22}-HPAA** and ○ **Fe_{0.71}Zn_{0.29}-HPAA**) and in the absence of light (⊠ **Fe-HPAA**).

For 4-chlorophenol photodegradation using the photocatalyst **Fe-HPAA**, TOC removal efficiency was clearly higher under UV-A light (87%) than under visible light (45%), at lower reaction times (50 min). However, a TOC removal of 93% was reached after 240 minutes for both light sources (Figure 4.24). On the other hand, measurements of dissolved chloride, by ion chromatography (Metrohm 883 Basic IC plus), indicated that, independently of the light source used, dechlorination of 4-chlorophenol was quite fast (Figure 4.24). The reaction intermediate products were also analysed by HPLC-MS TSQ Quantum Access Max Thermo Electron device with samples prepared in 3:2 methanol/water mixtures with 5% ammonia (pH= 10). Phenol was identified after 5 minutes of reaction ($m/z= 94$) and the presence of catechol ($m/z= 109$) and hydroquinone ($m/z= 126$) after 10 minutes of reaction suggesting the aromatic ring oxidation.

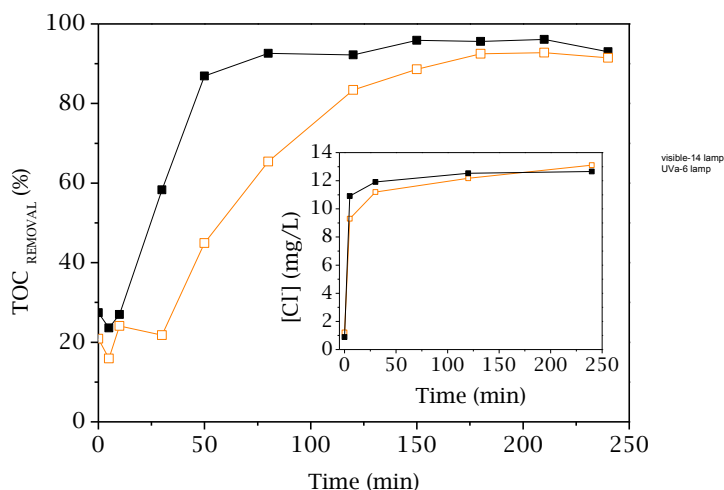


Figure 4.24. Time evolution of 4-chlorophenol removal employing **Fe-HPAA** under UV-A radiation (■) and visible light (□). (Inset) Cl⁻ releasing measurements.

In the case of MB photodegradation, **Fe-HPAA** showed the best results under UV-A light, achieving ~75% of TOC removal at 30 minutes of reaction. No mineralisation took place under visible light. Although with **Fe_{0.71}Zn_{0.29}-HPAA** a similar percentage of TOC removal was achieved at 180 minutes, MB photodegradation was slower at lower times of reactions (Figure 4.25).

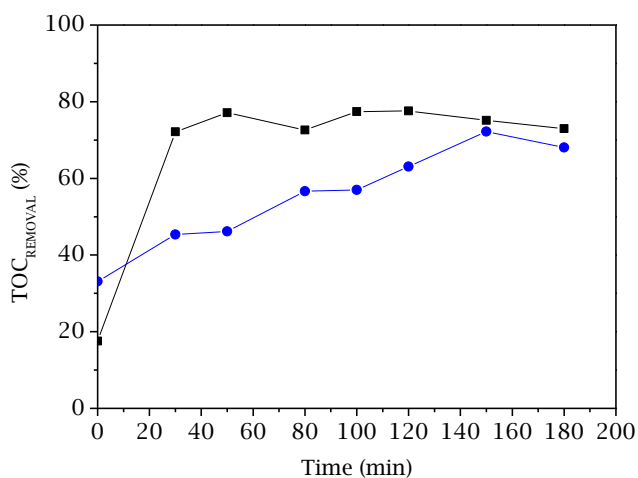


Figure 4.25. Time evolution of methylene blue removal employing **Fe-HPAA** (■) and **Fe_{0.71}Zn_{0.29}-HPAA** (●) under UV-A radiation.

Dissolved metal ions and phosphorous were determined by inductively coupled plasma mass spectroscopy (ICP-MS) on an Optima 7300 DV Perkin-Elmer spectrometer. In view of the ICP-MS results, the stability of these photocatalysts can be considered acceptable, being $\text{Fe}_{0.71}\text{Zn}_{0.21}\text{-HPAA}$ for the phenol photodegradation under visible light which show higher quantities of leached phosphorous ($4.4 \text{ mg}\cdot\text{L}^{-1}$ at 120 min) and metal ions ($5.3 \text{ mg}\cdot\text{L}^{-1}$ Fe and $3.1 \text{ mg}\cdot\text{L}^{-1}$ at 120 min).

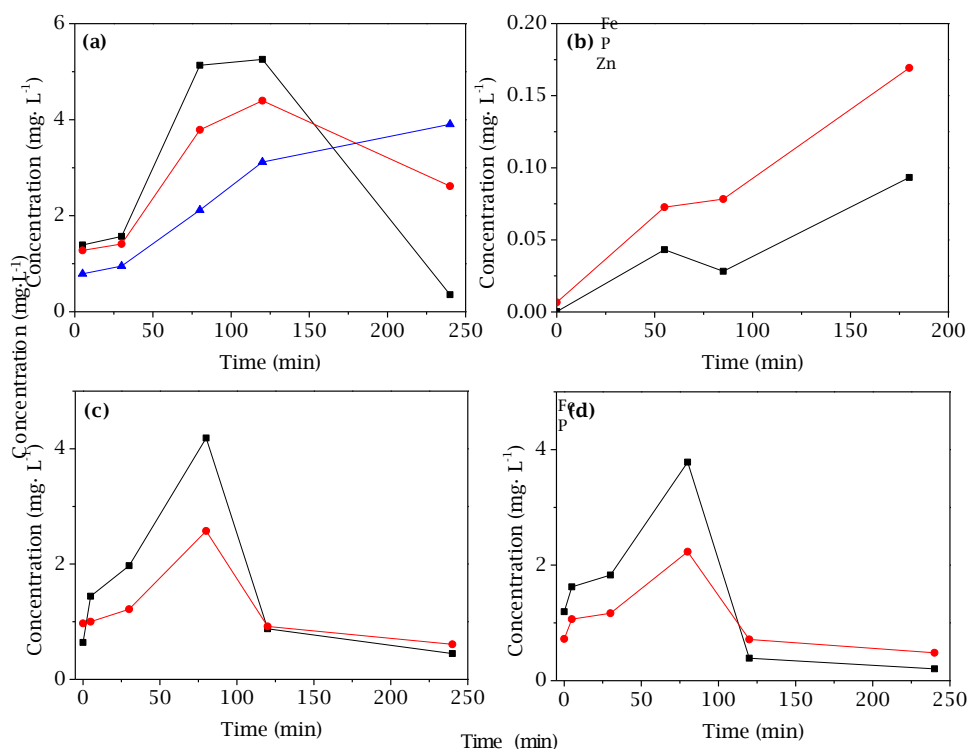
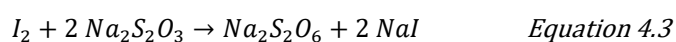
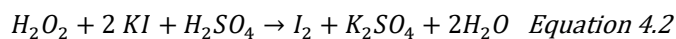


Figure 4.26. Time evolution of total iron (■), phosphorus (●) and zinc (▲) leached for the photocatalytic reactions of: (a) phenol and $\text{Fe}_{0.71}\text{Zn}_{0.21}\text{-HPAA}$ under visible light, (b) methylene blue and Fe-HPAA under UV-A light, 4-chlorophenol and Fe-HPAA under (c) visible light and (d) UV-A light.

Hydrogen peroxide consumption was also monitored during the photodegradation test by iodometric titration (USP technologies, 2020).



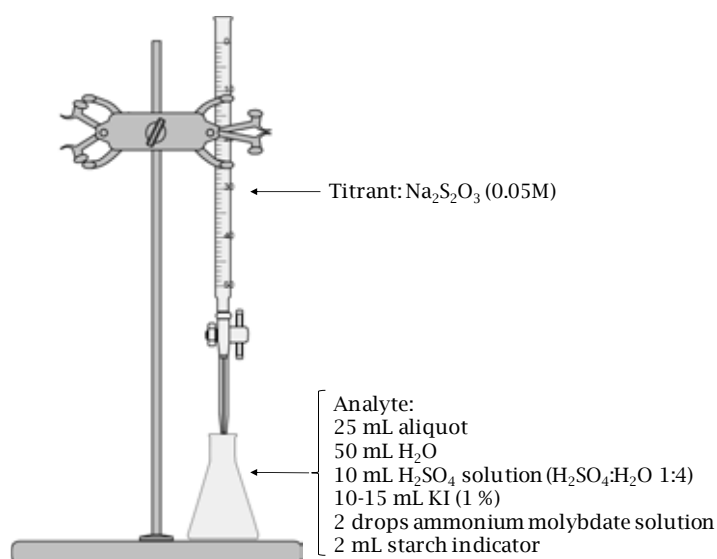


Figure 4.27. Scheme of iodometric titration.

Catalyst recyclability was studied for phenol photodegradation under visible light as a representative test. Firstly, the catalyst was recovered by filtration after the first cycle of the photocatalytic tests. This solid was stirred in a H_2SO_4 solution (80 mL, 10^{-3} M), filtered, washed with plenty of DI water, dried at 60 °C and used in a second cycle. **Fe-HPAA** displayed the same photocatalytic activity after 180 minutes of reaction (Figure 4.28).

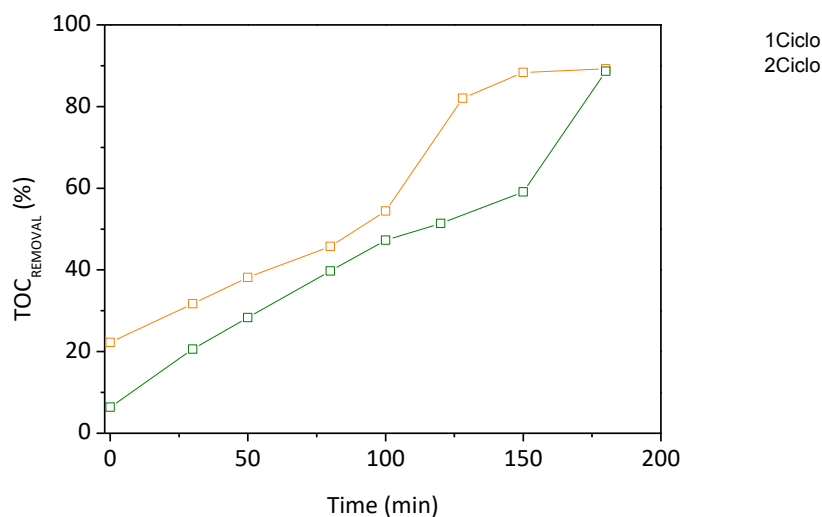


Figure 4.28. Time evolution of TOC removal in different cycles: first (□) and second (□).

Monitoring the photocatalyst **Fe-HPAA** by XRD revealed that the crystalline phase remained stable after conducting the photocatalytic tests (Figure 4.29).

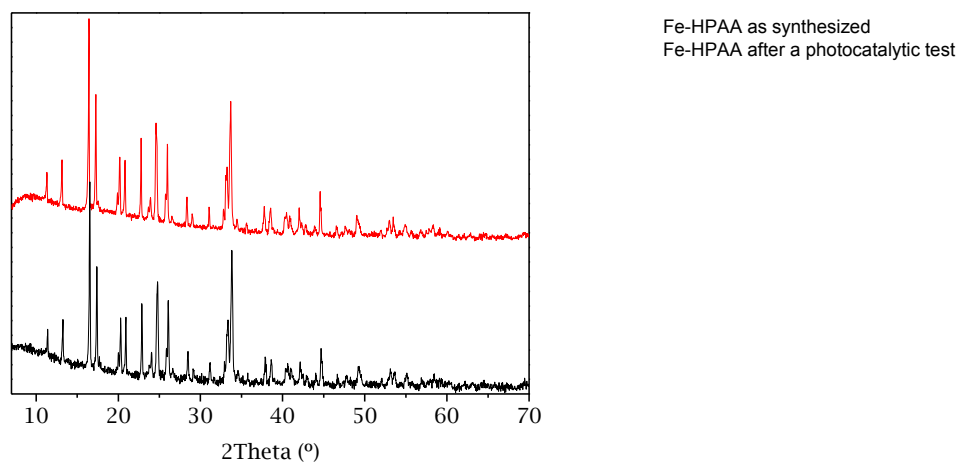


Figure 4.29. X-ray powder diffraction patterns for as synthesised **Fe-HPAA** (red) and after conducting the photocatalytic test under visible irradiation (black).

4.6. Conclusions

- A new, simplified synthesis procedure, alternative to that described in literature, has been employed for the preparation of **Fe-** and **Zn-HPAA**,

$M[\text{HO}_3\text{PCH}(\text{OH})\text{CO}_2]\cdot 2.5\text{H}_2\text{O}$. Iron-containing bimetallic solid solutions, $\text{Fe}_x\text{M}_{1-x}[\text{HO}_3\text{PCH}(\text{OH})\text{CO}_2]\cdot 2.5\text{H}_2\text{O}$ ($M = \text{Mn}^{2+}$, Co^{2+} or Zn^{2+}), have been also synthesised.

- **Fe-HPAA** and **$\text{Fe}_x\text{Zn}_{1-x}$ -HPAA** solids presented a moderate proton conductivity values ($1.1\cdot 10^{-5}$, $4.7\cdot 10^{-5}$ and $9.8\cdot 10^{-6}$ $\text{S}\cdot\text{cm}^{-1}$ at 80 °C and 95% RH for **Fe-NH₃-0h**, **$\text{Fe}_{0.71}\text{Zn}_{0.29}$ -NH₃-0h** and **$\text{Fe}_{0.41}\text{Zn}_{0.59}$ -NH₃-0h**, respectively). A gradual enhancement of the proton conductivity was achieved with increasing $\text{NH}_3/\text{H}_2\text{O}$ loadings up to $1.8\cdot 10^{-3}$ $\text{S}\cdot\text{cm}^{-1}$ (at 80 °C and 95% RH) for **Fe-NH₃-72h**. The local environment of iron in the ammonia-loaded amorphous phase was essentially preserved, as deduced from PDF analysis.
- Bimetallic solid solutions exhibited similar proton conductivity values than **Fe-NH₃-xh** for equivalent amounts of $\text{NH}_3/\text{H}_2\text{O}$. In addition, **$\text{Fe}_x\text{Zn}_{1-x}$ -NH₃-xh** compounds reached highest ammonia loading in shorter exposure times.
- **Fe-HPAA** and **$\text{Fe}_x\text{M}_{1-x}$ -HPAA** ($x > 0.5$) exhibited good photocatalytic properties and recyclability for photodegradation of phenol (~95% at 180 min) and 4-chlorophenol (93% at 240 min) under UV-A as well as visible light. Photodegradation of MB was only possible under UV-A radiation, with a TOC removal of 75% at 30 min.

4.7. References

B

- Babuponnusami, A.; Muthukumar, K. Degradation of Phenol in Aqueous Solution by Fenton, Sono-Fenton and Sono-photo-Fenton Methods. *CLEAN-Soil Air Water*, **2011**, 39(2), 142-147.
- Bazaga-García, M.; Cabeza, A.; Olivera-Pastor, P.; Santacruz, I.; Colodrero, R. M. P.; Aranda, M. A. Photodegradation of Phenol over a Hybrid Organo-Inorganic Material: Iron (II) Hydroxyphosphonoacetate. *J. Phys. Chem. C.*, **2012**, 116, 27, 14526-14533.
- Bazaga-García, M.; Colodrero, R. M. P.; Papadaki, M.; Garczarek, P.; Zoń, J., Olivera-Pastor, P.; Losilla, E. R.; León-Reina, L.; Aranda, M. A. G.; Choquesillo-Lazarte, D.; Demadis, K. D.; Cabeza, A. Guest Molecule-Responsive Functional Calcium Phosphonate Frameworks for Tuned Proton Conductivity. *J. Am. Chem. Soc.*, **2014**, 136(15), 5731-5739.
- Bazaga-García, M.; Papadaki, M.; Colodrero, R. M. P.; Olivera-Pastor, P.; Losilla, E. R.; Nieto-Ortega, B.; Aranda, M. A. G.; Choquesillo-Lazarte, D.; Cabeza, A.; Tuning

CHAPTER 4

Proton Conductivity in Alkali Metal Phosphonocarboxylates by Cation Size-Induced and Water-Facilitated Proton Transfer Pathways. *Chem. Mater.*, **2015**, 27(2), 424-435.

Bazaga-García, M. Multifunctional metal phosphonate frameworks for proton conductivity and photocatalysis. European PhD Thesis, Universidad de Málaga, **2015**.

Brillas, E.; Garcia-Segura, S. Benchmarking recent advances and innovative technology approaches of Fenton, photo-Fenton, electro-Fenton, and related processes: A review on the relevance of phenol as model molecule. *Sep. Purif. Technol.*, **2020**, 237, 116337.

C

Cabeza, A.; Aranda, M. A. G. Metal Carboxyphosphonates in Metal Phosphonates Chemistry. From synthesis to Applications. *RSC*, **2012**, Ch. 4, p. 107-132.

Cabeza, A.; Olivera-Pastor, P.; Colodrero, R. M. P. Hybrid Materials based on Multifunctional Phosphonic Acids in Tailored Organic-Inorganic Materials. *Wiley*, **2015**, Ch. 4, p. 137-191.

Clarizia, L.; Russo, D.; Di Somma, I.; Marotta, R.; Andreozzi, R. Homogeneous photo-Fenton processes at near neutral pH: a review. *Appl. Catal. B: Environ.*, **2017**, 209, 358-371.

Colodrero, R. M.; Olivera-Pastor, P.; Cabeza, A.; Papadaki, M.; Demadis, K. D.; Aranda, M. A. Structural Mapping and Framework Interconversions in 1D, 2D, and 3D Divalent Metal R,S-Hydroxyphosphonoacetate Hybrids. *Inorg. Chem.*, **2010**, 49(2), 761-768.

Colodrero, R. M. P.; Cabeza, A.; Olivera-Pastor, P.; Papadaki, M.; Rius, J.; Choquesillo-Lazarte, D.; García-Ruiz, J. M.; Demadis, K. D.; Aranda, M. A. Common Structural Features in Calcium Hydroxyphosphonoacetates. A High-Throughput Screening. *Cryst. Growth Des.*, **2011**, 11(5), 1713-1722.

Colodrero, R. M. P.; Papathanasiou, K. E.; Stavgianoudaki, N.; Olivera-Pastor, P.; Losilla, E. R.; Aranda, M. A.; León-Reina, L.; Sanz, J.; Sobrados, I.; Choquesillo-Lazarte, D.; García-Ruiz, J. M.; Atienzar, P.; Rey, F.; Demadis, K. D.; Cabeza, A. Multifunctional Luminescent and Proton-Conducting Lanthanide Carboxyphosphonate Open-Framework Hybrids Exhibiting Crystalline-to-Amorphous-to-Crystalline Transformations. *Chem. Mater.*, **2012**, 24(19), 3780-3792.

Colodrero, R. M. P.; Salcedo, I. R.; Bazaga-García, M.; Milla-Pérez, D. F.; Durán-Martín, J. D.; Losilla, E. R.; Moreno-Real, L.; Rius, J.; Aranda, M. A. G.; Demadis, K. D.; Olivera-Pastor, P.; Cabeza, A. Structural variability in M^{2+} 2-hydroxyphosphonoacetate moderate proton conductors. *Pure Appl. Chem.*, **2017**, 89(1), 75-87.

D

De La Torre, A. G.; Bruque, S.; Aranda, M. A. G. Rietveld quantitative amorphous content analysis. *J. Appl. Cryst.*, **2001**, 34(2), 196-202.

Demadis, K. D.; Papadaki, M.; Císařová, I. Single-Crystalline Thin Films by a Rare Molecular Calcium Carboxyphosphonate Trimer Offer Prophylaxis from Metallic Corrosion. *ACS Appl. Mater. Interfaces*, **2010**, 2(7), 1814-1816.

Dong, D. P.; Li, J.; Sun, Z. G.; Zheng, X. F.; Chen, H.; Meng, L.; Zhu, Y. Y.; Zhao, Y.; Zhang, J. Hydrothermal synthesis, crystal structure, and thermal stability of a novel 3D cadmium phosphonate with double-stranded helical channels. *Inorg. Chem. Commun.*, **2007**, 10(9), 1109-1112.

Dong, D. P.; Sun, Z. G.; Tong, F.; Zhu, Y. Y.; Chen, K.; Jiao, C. Q.; Wang, C. L.; Li, C.; Wang, W. N. Synthesis, structure, surface photovoltage and magnetic properties of a novel 3D homochiral manganese phosphonate with right-handed helical chains. *Cryst. Eng. Comm.*, **2011**, 13(10), 3317-3320.

E

Egami, T.; Billinge, S. J. Underneath the Bragg peaks: structural analysis of complex materials. *Elsevier*, **2012**.

F

Farrow, C. L.; Juhás, P.; Liu, J.; Bryndin, D.; Božin, E. S.; Bloch, J.; Proffen, T.; Billinge, S. J. PDFfit2 and PDFgui: computer programs for studying nanostructure in crystals. *J. Phys: Condens. Mat.*, **2007**, 19(33), 335219.

Fu, R.; Zhang, H.; Wang, L.; Hu, S.; Li, Y.; Huang, X.; Wu, X. Nonlinear Optical Activity and High Thermal Stability of a New 3D Open-Framework with Interconnected 24-, 16-, and 8-Atom Channels: $(NH_4)Zn[O_3PCH(OH)CO_2]$. *Eur. J. Inorg. Chem.*, **2005a**, 16, 3211-3213.

Fu, R.; Xiang, S.; Zhang, H.; Zhang, J.; Wu, X. Syntheses, Characterization, and Magnetic Properties of Four New Layered Transition-Metal Hydroxyl- Carboxylate-Phosphonates: $[M(CH(OH)(CO_2)(PO_3H))(H_2O)_2]$ (M= Mn, Fe, Co, Zn). *Cryst. Growth Des.*, **2005b**, 5(5), 1795-1799.

CHAPTER 4

Fu, R.; Hu, S.; Wu, X. Syntheses, crystal structures, thermal stabilities and luminescence of six M (II)-hydroxyphosphonoacetate materials. *J. Solid State Chem.*, **2011**, 184(4), 945-952.

J

Juhàs, P.; Davis, T.; Farrow, C.L.; Billinge, S.J. PDFgetX3: a rapid and highly automatable program for processing powder diffraction data into total scattering pair distribution functions. *J. Appl. Crystallogr.*, **2013**, 46(2), 560-566.

L

Li, F. B.; Li, X. Z.; Ao, C. H.; Hou, M. F.; Lee, S. C. Photocatalytic conversion of NO using TiO₂-NH₃ catalysts in ambient air environment. *Appl. Catal. B: Environ.*, **2004**, 54(4), 275-283.

Li, J.; Meng, L.; Sun, Z. G.; Cui, L. Y.; Zhang, J.; Zhu, Y. Y.; Dong, D. P.; Chen, H.; You, W. S.; Zhu, Z. M. Synthesis and characterizations of a layered antimony (III) phosphonate: [NH₂CH₂CH₂NH₂][Sb₂(O₃PCH(OH)CO₂)₂]. *Inorg. Chem. Commun.*, **2007**, 10(5), 535-537.

O

Oxton, I. A.; Knop, O.; Falk, M. Infrared spectra of the ammonium ion in crystals. I. Ammonium hexachloroplatinate (IV) and hexachlorotellurate (IV). *Can. J. Chem.*, **1975**, 53(18), 2675-2682.

P

Parkhomchuk, E. V.; Vanina, M. P.; Preis, S. The activation of heterogeneous Fenton-type catalyst Fe-MFI. *Catal. Commun.*, **2008**, 9(3), 381-385.

R

Pouran, S. R.; Raman, A. A. A.; Daud, W. M. A. W. Review on the application of modified iron oxides as heterogeneous catalysts in Fenton reactions. *J. Clean. Prod.*, **2014**, 64, 24-35.

S

Salcedo, R. I.; Bazaga-García, M.; Cuesta, A.; Losilla, E. R.; Demadis, K. D.; Olivera-Pastor, P.; Colodrero, R. M. P.; Cabeza, A. NH₃/H₂O-mediated proton conductivity and photocatalytic behaviour of Fe(II)-hydroxyphosphonoacetate and M(II)-substituted derivatives. *Dalton Trans.*, **2020**, 49(13), 3981-3988.

- Sharma, P.; Kaur, H.; Sharma, M.; Sahore, V. A review on applicability of naturally available adsorbents for the removal of hazardous dyes from aqueous waste. *Environ. Monit. Assess.*, **2011**, 183(1-4), 151-195.
- Sun, Z. G.; Cui, L. Y.; Liu, Z. M.; Meng, L.; Chen, H.; Dong, D. P.; Zhang, L. C.; Zhu, Z. M.; You, W. S. Hydrothermal synthesis, crystal structures and characterizations of a novel 3D metal phosphonate: $Mg_{0.5}Cd[O_3PCH(OH)CO_2]$. *Inorg. Chem. Commun.*, **2006**, 9(10), 999-1001.
- Sun, Z. G.; Chen, H.; Liu, Z. M.; Cui, L. Y.; Zhu, Y. Y.; Zhao, Y.; Zhang, J.; You, W. S.; Zhu, Z. M. Synthesis, characterizations, and crystal structure of a novel 2D metal phosphonate: $Na_2[Cd_2(H_2O)_3(O_3PCH(OH)CO_2)_2] \cdot 2H_2O$. *Inorg. Chem. Commun.*, **2007**, 10(3), 283-286.

U

- USP technologies. Iodometric Titration in *Hydrogen Peroxide Technical Library*, 2020. Recovered from <http://www.h2o2.com/technical-library/analytical-methods/default.aspx?pid=70&name=Iodometric-Titration>

Z

- Zhai, T.; Yan, R.; He, W.; Ma, H. Corrosion protection performance of Mo-incorporated 2-hydroxyphosphonoacetic acid- Zn^{2+} complex conversion layers on the cold-rolled steel substrate. *Surf. Coat. Tech.*, **2018**, 351, 50-59.



UNIVERSIDAD
DE MÁLAGA

Chapter 5

Metal Sulfophosphonates





UNIVERSIDAD
DE MÁLAGA

Sulfophosphonic acids are versatile, multifunctional parent linkers for preparing new coordination polymers with specific structural backbones and properties. Therefore, the presence of a strongly acidic sulfonic group makes them potential candidates as proton conductors, which may form part of composite polymeric membranes (Stein, Clearfield & Subramanian, 1996). In addition, the possibility to choose a flexible or rigid ligand gives rise a wide structural variability upon combining properly with metal ions (Sonnauer et al., 2007; Zhang & Fei, 2017; Wöhlbrandt et al., 2019; Du, Xu & Mao, 2006a). Beyer et al. (2017) reported the synthesis of both, rigid and flexible aromatic sulfophosphonic acids, by employing different starting organic precursors (Figure 5.1).

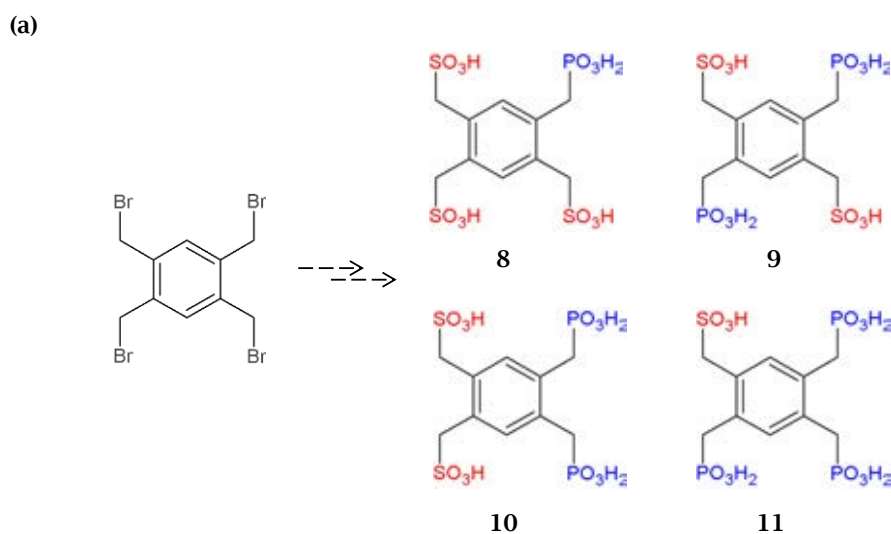


Figure 5.1. (a) Flexible and (b) rigid sulfophosphonic acids as linkers (L) for CPs (Beyer et al., 2017).

(b)

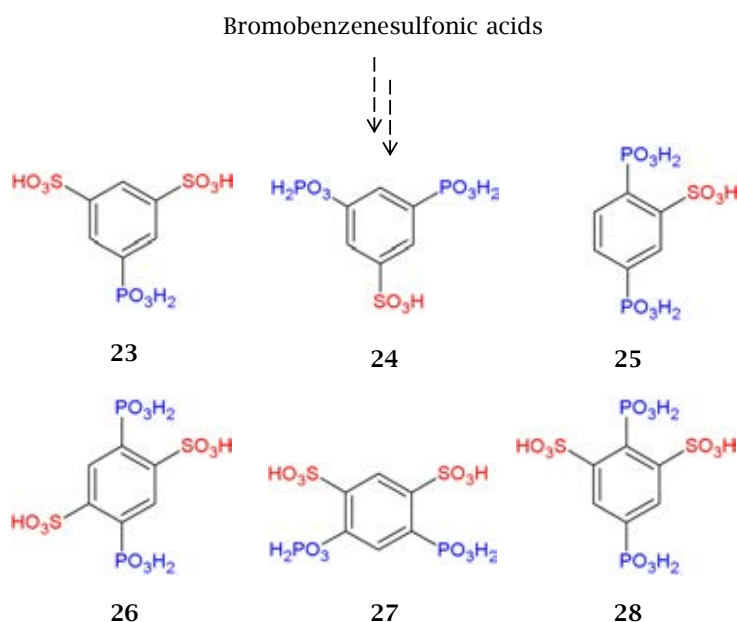


Figure 5.1. (a) Flexible and (b) rigid sulfophosphonic acids as linkers (L) for CPs (Beyer et al., 2017) (Continuation).

Furthermore, compound $[\text{La}_2(\text{H}_2\text{L})_3(\text{H}_2\text{O})_8]$ was synthesised by using acid **9** as an example of proton conductor material, because of the presence in its structure of free hydrogen acceptor and donor groups, together with water molecules within the pores (Beyer et al., 2017).

By using a high-throughput methodology, Norbert Stock research's group have carried out systematic researches of synthesis parameters, such as pH, metal to ligand molar ratio, presence of counterions, etc., influencing the structure and composition of different metal sulfophosphonates. Maniam, Näther & Stock (2010) obtained five new metal phosphonatobenzenesulfonates of Pb(II) and Cu(II) using this method. Wöhlbrandt et al. (2019) reported the synthesis of 2D and 3D divalent metal derivatives (Mg, Ba, Pb and Cd) from the [5-(phosphonomethyl)-2,4-bis(sulfonomethyl)phenyl]methanesulfonic acid. Sonnauer et al. (2007 and 2008) investigated the synthesis of lanthanide, $\text{Ln}(\text{O}_3\text{P-C}_2\text{H}_4\text{-SO}_3)(\text{H}_2\text{O})$ (Ln= La-Dy), and barium, $\text{BaH}(\text{O}_3\text{P-C}_2\text{H}_4\text{-SO}_3)$, derivatives by high-throughput methods. Both structures are built up from chains of MO_6 polyhedra with different connectivity. As opposite to

the case of lanthanide derivatives, the Ba^{2+} derivative structure was shown to present a disordered arrangement of the sulfophosphonate ligand. Eu^{3+} and Tb^{3+} derivatives also exhibited luminescent properties.

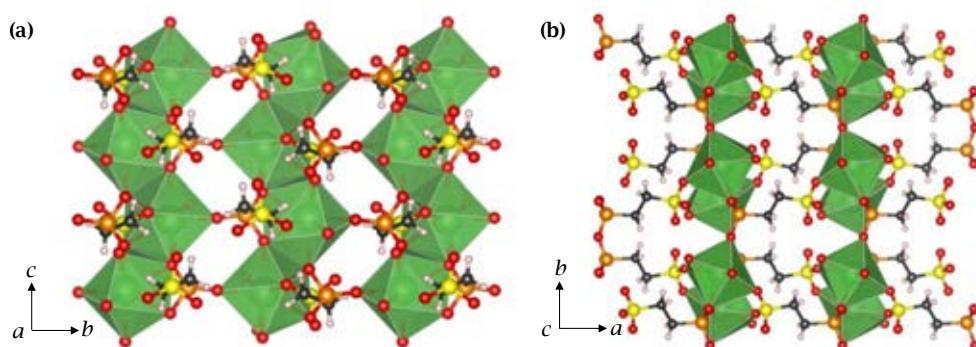


Figure 5.2. Two views of the $La(O_3P-C_2H_4-SO_3)(H_2O)$ framework: (a) a layer formed by 1D chains of edge-sharing LnO_8 polyhedra along c -axis, interconnected through the sulfonate and phosphonate groups and (b) layers bridged by the ethyl groups.

Composite membranes composed of Nafion 117 or sulfonated PEEK, as polymeric matrices, and layered metal sulfophosphonates as fillers, have been considered suitable for using in PEMFC and medium temperature, indirect or direct, methanol fuel cells, because they combine high hydrophilicity, high proton conductivity and exfoliation properties into 0.7-1.2 mm thickness membranes (Alberti & Casciola, 2001).

Zirconium sulfophosphonate chemistry has been widely studied mostly by Alberti and co-workers, as well as other authors. These compounds have been developed by the modification of well-known starting compounds, focusing on α - and γ -type layered derivative structures of zirconium phosphate (Vivani, Costantino & Taddei, 2012).

Stein, Clearfield & Subramanian (1996) reported a series of Zr and Ti phosphate sulfophenylphosphonates, $M(HPO_4)_x(O_3PC_6H_4SO_3H)_{2-x}$, which were obtained by sulfonation. These materials displayed high proton conductivity in a wide range of temperature (up to 100 °C) and relative humidity (from 20 to 85% RH). $Ti(HPO_4)_{0.25}(O_3PC_6H_5)_{0.12}(O_3PC_6H_4SO_3H)_{1.63} \cdot 3.64H_2O$ exhibited the highest proton conductivity value, $1.3 \cdot 10^{-1} S \cdot cm^{-1}$ at 25 °C and 85% RH. Furthermore, compounds with composition $[M(HPO_4)_x(O_3PC_6H_4SO_3H)_{2-x}][M'(O_3P-R-NH_2)_{2-x}]$, M and M' = Ti, Zr, Th, were prepared by self-assembly methods. Their proton conductivity values were lower

than the pure sulfophosphonates but they were likely to use as humidity sensors due to their stability to swelling in aqueous media. The proton conductivity of the as-synthesised $\text{Zr}(\text{HPO}_4)_x(\text{O}_3\text{PC}_6\text{H}_4\text{SO}_3\text{H})_{2-x}$ and ZrPSPH-loaded sulfonated polyetheretherketone (PEEK-S) composite membranes was studied by Bonnet et al. (2000). 40 wt % Zr^{4+} sulfophosphonate/phosphate-loaded composite membrane displayed high proton conductivity values ($\sim 3 \cdot 10^{-2} \text{ S} \cdot \text{cm}^{-1}$ at 100 °C and 100% RH), but slightly lower than those of the as synthesised Zr phosphate sulfophenylphosphonate samples ($\sim 10^{-1} \text{ S} \cdot \text{cm}^{-1}$).

Zima et al. (2010) reported the synthesis and characterisation of zirconium 4-sulfophenylphosphonate, $\text{Zr}(\text{HO}_3\text{SC}_6\text{H}_4\text{PO}_3)_2 \cdot 2\text{H}_2\text{O}$ (ZrSPhP). In comparison with zirconium phosphate sulfophenylphosphonates, as reported by Alberti et al. (2005), ZrSPhP exhibited lower proton conductivity ($10^{-2} \text{ S} \cdot \text{cm}^{-1}$ vs. $6 \cdot 10^{-2} \text{ S} \cdot \text{cm}^{-1}$ at 100 °C and 90% RH), being explained by the ability of the former to incorporate a higher amount of water, as well as by the presence of phosphate groups, which increase the amount of labile protons. Škoda et al. (2018) studied the structure in detail of ZrSPhP and zirconium 4-sulfophenylphosphonate-phenylphosphonates with general formula $\text{Zr}(\text{HO}_3\text{SC}_6\text{H}_4\text{PO}_3)_x(\text{C}_6\text{H}_5\text{PO}_3)_{2-x} \cdot y\text{H}_2\text{O}$ ($x= 0.7-2$; $y= 0$ or 2) employing molecular simulation methods. Regarding to hydrated compounds ($y= 2$), the presence of the water molecules located in the same sheet that oxygen atoms from the sulfonate groups, allow to create extended H-bond networks, what explains the higher proton conductivity of the hydrated forms in comparison with the dehydrated samples. Furthermore, the intercalation capacity of ZrSPhP (Svoboda et al., 2013) and zirconium 4-sulfophenylphosphonates phenylphosphonate (Kopecká et al., 2019) have been studied, proving that they are good host materials for the intercalation of a wide range of basic molecules such as amino alcohols, alkylamines and amino acids.

Alberti, Casciola & Palombari (2000) reported the proton conductivity values of layered metal sulfoarylphosphonates of the α and γ -type as well as some preliminary data for composite membranes prepared with these materials and a polymeric matrix of PEEK-S. The highest proton conductivities were obtained for the most hydrated α and γ -zirconium sulfophenylphosphonates, $\text{Zr}(\text{O}_3\text{PC}_6\text{H}_4\text{SO}_3\text{H})_{0.73}(\text{O}_3\text{PCH}_2\text{OH})_{1.27} \cdot n\text{H}_2\text{O}$ ($n=3-10$) and $\text{ZrPO}_4(\text{O}_2\text{P}(\text{OH})_2)_{0.55}(\text{O}_2\text{P}(\text{OH})\text{C}_6\text{H}_4\text{SO}_3\text{H})_{0.45} \cdot n\text{H}_2\text{O}$ ($n= 5-14$) respectively ($\sim 10^{-2} \text{ S} \cdot \text{cm}^{-1}$ at 20 °C). Moreover, their conductivity remained stable up to 180 °C. Composite membranes exhibited satisfactory textural properties and proton conductivities up to $0.1 \text{ S} \cdot \text{cm}^{-1}$ at 100 °C and 100 % RH.

Zirconium sulfophosphonate, ZrSPP, has been combined with different polymers to produce composite membranes. Kim et al. (2004) prepared Nafion/ZrSPP composite membranes at different filler loading (6.5 and 12.5 wt %), in order to improve the proton conductivity values as compared to the unmodified Nafion membrane. Nafion/ZrSPP (12.5 wt %) composite membrane displayed a proton conductivity of $0.07 \text{ S}\cdot\text{cm}^{-1}$ at $140 \text{ }^\circ\text{C}$ without extra humidification. Li et al. (2010) reported a series of composite membranes using different loads (10, 20 and 30 wt %) of ZrSPP in a sulfonated poly(phthalazinone ether sulfone ketone) polymer matrix, SPPEsk. The proton conductivity of SPPEsk/ZrSPP composite membranes was shown to be higher than that of Nafion 117 membrane in a range of $80\text{-}120 \text{ }^\circ\text{C}$. In addition, SPPEsk/ZrSPP composite membranes displayed high thermal stability and exceptional electrochemical properties, being potential candidates to use in direct methanol fuel cells. They showed lower methanol permeability ($\sim 10^{-8} \text{ cm}^2\cdot\text{s}^{-1}$) than Nafion 117 ($2.4\cdot 10^{-6} \text{ cm}^2\cdot\text{s}^{-1}$).

Melánová et al. (2020) reported the topotactic reaction of γ -zirconium or titanium hydrogen phosphate (γ -ZrP and γ -TiP) with 2-bis(phosphonomethyl)aminoethan-1-sulfonic acid (H_2TDP), giving rise to $\text{Zr}(\text{PO}_4)(\text{H}_2\text{PO}_4)_{1-2x}(\text{H}_2\text{TDP})_x\cdot y\text{H}_2\text{O}$ ($x = 0.15, 0.34, 0.45$) and $\text{Ti}(\text{PO}_4)(\text{H}_2\text{PO}_4)_{1-2z}(\text{H}_2\text{TDP})_z\cdot y\text{H}_2\text{O}$ ($z = 0.41 \pm 0.01$) respectively. The Zr derivative loaded with the smallest amount of H_2TDP , $x = 0.15$, exhibited the highest proton conductivity values, $5.3\cdot 10^{-5} \text{ S}\cdot\text{cm}^{-1}$ at RT.

Jang, Park & Yamazaki (2003) reported the synthesis and proton conductivity properties of sulfonated cerium phenylphosphonate, $\text{Ce}(\text{O}_3\text{PC}_6\text{H}_4\text{SO}_3\text{H})_2\cdot 3.86\text{H}_2\text{O}$. This compound has a similar structure that zirconium sulfophenylphosphonate and displays similar proton conductivity values ($\sigma = 0.026 \text{ S}\cdot\text{cm}^{-1}$ at $175 \text{ }^\circ\text{C}$ and 100% RH). Its proton conductivity was observed to be humidity-dependent and increased by one order of magnitude between 40 and 100% RH.

Recently, Mady, Malmin & Kelland (2019) have reported the use of sulfophosphonates as calcite and barite scale inhibitors in oil and gas industry, which exhibited better compatibilities with calcium brines than phosphonates.

On the other hand, auxiliary ligand-containing metal sulfophosphonates have been also synthesised. For instance, Du et al. (2006a, 2006b, 2007 and 2009) reported the synthesis and characterisation of metal phosphonatobenzenesulfonates employing 1,10-phenanthroline (phen) as the auxiliary ligand. The low dimension of these materials is due to the use of 1,10-phenanthroline, which reduces the coordination sites available for the phosphonate ligand. Maniam & Stock (2011)

reported the synthesis of $[\text{Cu}(\text{HO}_3\text{PC}_6\text{H}_4\text{SO}_3)(\text{C}_{10}\text{H}_8\text{N}_2)] \cdot \text{H}_2\text{O}$ employing 4,4'-bipyridine as auxiliary ligand by high-throughput method.

In this section, transition metals and lanthanide derivatives of the sulfophosphonate ligand **2-[bis(phosphonomethyl)amino]ethanesulfonic acid**, H_5SP , are reported. H_5SP is a phosphonomethylated derivative of taurine (2-aminoethanesulfonic acid). The tris-ammonium, $(\text{NH}_4)_3\text{H}_2\text{SP}$, and pentasodium salts, Na_5SP , were used to synthesise these metal derivatives. These salts were prepared by following the Irani-Moedritzer reaction (Moedritzer and Irani, 1966). The resulting crystalline solids have been full-characterised, and a study of the proton conductivity of these new metal sulfophosphonates, as well as preliminary MEA assays using Nafion-based mixed matrix membranes have been carried out. Some of the results of this study have been published in Bazaga-García et al (2019).

5.1. Synthesis

The synthesis of the ligand was carried out in collaboration with Prof. K. D. Demadis from the Department of Chemistry at the University of Crete (Greece) and Prof. D. Villemin from the Department of Organic Chemistry at University of Caen (France). The pure acid H_5SP is highly hygroscopic, so Na_5SP was isolated by full deprotonation of the SP ligand. Likewise, the ammonium salt, $(\text{NH}_4)_3\text{H}_2\text{SP}$, was obtained by partial deprotonation of H_5SP .

Metal derivatives of this ligand were prepared following two different procedures:

- (i) Hydrothermal/solvothermal synthesis: ***o*-Mn₂HSP**, ***m*-Zn₂HSP**, ***h*-Zn₂HSP**, ***m*-LaH₂SP** and ***o*-LnH₂SP** (Ln= Pr, Nd, Sm, Eu, Gd and Tb) derivatives.
- (ii) Microwave-assisted synthesis: ***o*-Mn₂HSP** and ***o*-EuH₂SP** derivatives.

5.1.1. Synthesis of Divalent Transition Metal Sulfophosphonates

$\text{Mn}_2[(\text{O}_3\text{PCH}_2)_2\text{-NH-(CH}_2)_2\text{-SO}_3] \cdot 3\text{H}_2\text{O}$, ***o*-Mn₂HSP**, was synthesised under hydrothermal conditions. An amount of MnCO_3 (25.7 mg; 0.2236 mmol) was dissolved in 0.45 mL of HCl (1M). Separately, 0.1597 mmol of Na_5SP was dissolved in 0.5 mL of DI water. The manganese solution was added to the ligand solution (Mn: Na_5SP molar ratio of 1.4:1) under constant stirring, appearing a brown precipitate upon mixing. The pH of the mixed solution was adjusted to 3-4.5 with a stock solution of 1M HCl and then, 0.4 mL of EtOH was added (pH ~ 2.5-4.5). The final

mixture was transferred to a Teflon-lined and heated at 150 °C for 96h. Precipitate was isolated by filtration, washed with EtOH and air-dried.

Similar synthetic conditions were then used for the microwave-assisted synthesis, except that the reaction was accomplished in shorter time. The solid was prepared as follows: 51.4 mg of MnCO_3 (0.4472 mmol) was dissolved in 0.45 mL of H_2SO_4 (1M). Separately, 0.3194 mmol of Na_3SP was added to 1 mL of DI water and the pH of the solution was adjusted to 5 with a stock solution of H_2SO_4 (1M) in order to avoid the formation of any precipitate. The manganese solution was added to the ligand solution under constant stirring. Then, 0.8 mL of EtOH was added to the mixed solution (pH ~ 3.4-3.8). Microwave conditions were 160 °C, 850 W, 1200 rpm for 1h. The resulting precipitate was isolated by filtration, washed with EtOH and air-dried.

As shown in Figure 5.3, ***o*-Mn₂HSP** can be obtained in a pH ranging from 2.5 to 4.5 as well as by microwave-assisted synthesis.

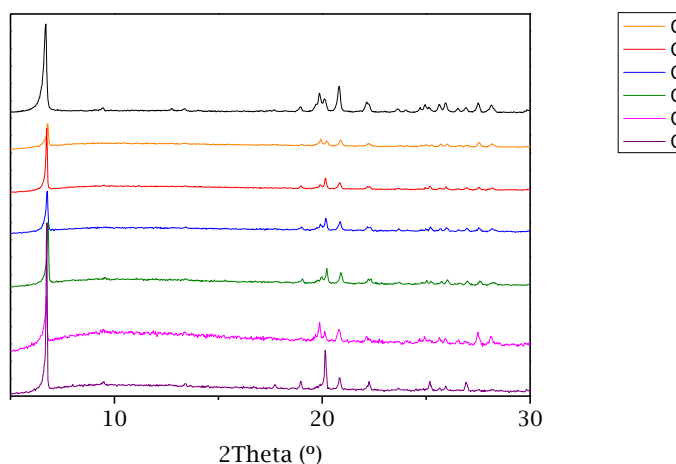


Figure 5.3. XRD patterns of ***o*-Mn₂HSP** obtained by hydrothermal reaction at pH 2.60 (orange), 2.90 (red), 3.12 (blue), 3.51 (olive), 3.75 (pink) and 4.34 (purple) or microwave-assisted synthesis (black).

Synthesis of zinc derivatives was carried out by high-throughput methods, in which different metal to ligand molar ratios and solvent combinations were assayed as below specified:

- $\text{Zn}:(\text{NH}_4)_3\text{H}_2\text{SP}$ molar ratios: 1:2, 1.4:1
- Solvents: EtOH/ H_2O (1:5 and 2:5 v/v) or isopropanol/ H_2O mixture (1:5 or 2:5 v/v).

After optimizing synthesis conditions, two crystalline derivatives were isolated: $\text{Zn}_2[(\text{O}_3\text{PCH}_2)_2\text{-NH-(CH}_2)_2\text{-SO}_3]\text{Zn}_{0,4}(\text{O}_3\text{PCH}_2\text{-NH-CH}_3)_{0,4}(\text{NH}_3)_2 \cdot 4\text{H}_2\text{O}$, ***m*-Zn₂HSP**, and $\text{Zn}_2[(\text{O}_3\text{PCH}_2)_2\text{-NH-(CH}_2)_2\text{-SO}_3] \cdot 7\text{H}_2\text{O}$, ***h*-Zn₂HSP**.

***m*-Zn₂HSP** was obtained only for a Zn:(NH₄)₃H₂SP molar ratio 1:2 using as solvent a mixture of EtOH:H₂O 2:5 (v/v). A quantity of ZnSO₄·7H₂O (0.2298 g; 0.799 mmol) was dissolved in 5 mL of DI H₂O. Separately, 1.597 mmol of (NH₄)₃H₂SP was dissolved in 5 mL of DI water. The zinc solution was added to the ligand solution under constant stirring and 4 mL of EtOH was dropwise added to the mixed solution (pH ~ 4.7). The final solution was transferred to a Teflon-lined and heated at 150 °C for 96 h. The precipitate was isolated by filtration, washed with EtOH and air-dried. As can be observed in Figure 5.5, ***m*-Zn₂HSP** was also obtained using as solvent a mixture of EtOH:H₂O 1:5 (v/v) instead of 2:5. However, this solid exhibited lower crystallinity. Any attempts to synthesise crystalline monophasic compounds by microwave-assisted methods were unsuccessful, obtaining a mixture of phases with poor crystallinity in all cases (Figure 5.5).

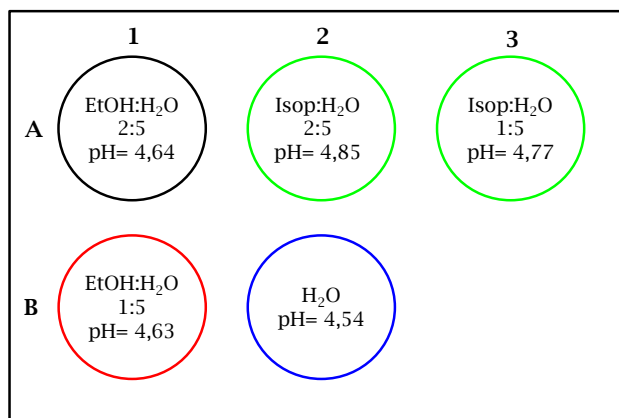


Figure 5.4. Schematic representation of the synthesis conditions used for ***m*-Zn₂HSP** derivative. Green circle indicates that no products were isolated under these synthetic conditions.

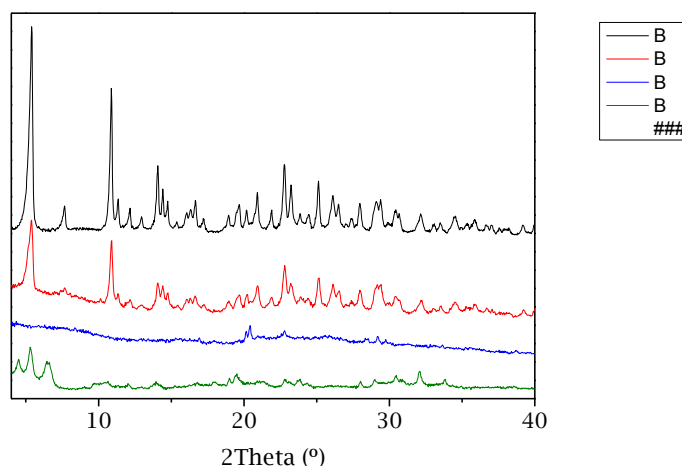


Figure 5.5. XRD patterns of $m\text{-Zn}_2\text{HSP}$ obtained by solvothermal reaction as indicated in Figure 5.4: A1 (black), B1 (red) and B2 (blue) or by microwave-assisted reaction (olive).

The optimal conditions for the $h\text{-Zn}_2\text{HSP}$ synthesis were a $\text{Zn}:(\text{NH}_4)_3\text{H}_2\text{SP}$ molar ratio of 1.4:1 in a mixture of isopropanol: H_2O 1:5 (v/v). Other conditions usually led to the same compound but with lower crystallinity (Figure 5.6). The synthesis was carried out following the same procedure described for $m\text{-Zn}_2\text{HSP}$, but changing the $\text{Zn}:(\text{NH}_4)_3\text{H}_2\text{SP}$ molar ratio and the solvents mixture. A microwave-assisted method was also applied following the same procedure, but at 150 °C, 850 W, 1200 rpm for 30 minutes. However, the resulting solid exhibited lower crystallinity (Figure 5.6).

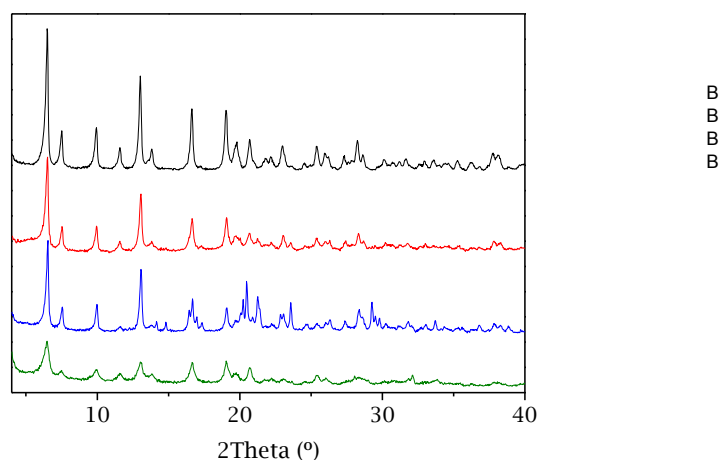


Figure 5.6. XDR patterns of $h\text{-Zn}_2\text{HSP}$ obtained by hydrothermal reaction in solvent mixtures of isopropanol/ H_2O [1:5 (black) and 2:5 (red)] and 2:5 EtOH/ H_2O (blue) or microwave-assisted reaction (olive).

5.1.2. Synthesis of Lanthanide Sulfophosphonates

LnH₂SP compounds, Ln[H(O₃PCH₂)₂-NH-(CH₂)₂-SO₃] \cdot 2H₂O (Ln= La, Pr, Nd, Sm, Eu, Gd and Tb), were prepared by two different procedures:

- (i) Hydrothermal synthesis, for ***m*-LaH₂SP** and ***o*-LnH₂SP** (Ln= Pr, Nd, Sm, Eu, Gd and Tb) derivatives.
- (ii) Microwave-assisted synthesis, for ***o*-EuH₂SP** derivative.

Regarding to hydrothermal synthesis, the conditions were screened by high-throughput methodology in order to optimize the reaction parameters:

- Ln:(NH₄)₃H₂SP or Ln:Na₅SP molar ratios: 1:1, 1:2, 2:1 and 1.5:1.
- Initial pH values: from 0.5 to 4.0.
- Temperature: 140 and 160 °C.
- Solvents: H₂O or H₂O:EtOH mixture (3:1, 1:1 and 1:3).

Hydrothermal synthesis of the lanthanide derivative solids was conducted at 140 °C, using a Ln:(NH₄)₃H₂SP or Na₅SP molar ratio 2:1, pH < 2.0 and H₂O as the solvent. Optimal conditions were used to scale up material synthesis. As an example, the lanthanide solution was prepared by dissolving 0.0799 mmol of the corresponding lanthanide salt (nitrates or chlorides) in 0.5 mL of DI water. Separately, 0.1597 mmol of (NH₄)₃H₂SP or Na₅SP was dissolved in 0.5 mL of DI water. The lanthanide solution was dropwise added to the ligand solution under vigorous stirring and the resulting slurry was re-dissolved by adding a HNO₃ stock solution (0.2 and 0.5 M) to a final pH of 1.2. The obtained solution was transferred to a 5 mL Teflon-lined autoclave, heated at 140 °C for 24h and cooled to RT for 12h. The resulting solid was isolated by filtration, washed twice with DI water and EtOH and air-dried. It is highlighted that other unidentified crystalline phases were obtained for Er³⁺ and Yb³⁺, which were not further characterised.

***o*-EuH₂SP** was prepared by microwave-assisted synthesis as follow: 0.1543 mmol of EuCl₃ \cdot 6H₂O was dissolved in 1.5 mL of DI water. This solution was added dropwise to the ligand solution (0.3087 mmol Na₅SP in 1.5 mL DI water) under stirring. The final pH of the mixture was adjusted to 1.2 in order to re-dissolve the resulting slurry by using a 0.5M stock solution of HCl. The final solution was transferred to a 10 mL glass vial and the reaction was carried out in a microwave reactor at 140 °C, 850W, for 60 minutes and 1200 rpm. The precipitate was isolated by centrifugation, washed with DI water and EtOH and air-dried. This methodology could be extended to other lanthanide derivatives because it considerably shortens the reaction time.

5.2. Characterisation

All compounds were extensively characterised using different techniques.

5.2.1. Elemental Analysis and Thermal Stability

Elemental analysis for transition and lanthanide metal derivatives are given in Appendix II, Table AII.3. C and S percentages found for *m*-LaH₂SP were lower than expected. This could be as consequence of the partial ligand decomposition under the reaction conditions, which was also observed during the ligand salt isolation, as revealed in the ¹³C NMR spectrum (Figure 5.7). In the case of *m*-Zn₂HSP, it appears that partial ligand decomposition also occurs (Table AII.3).

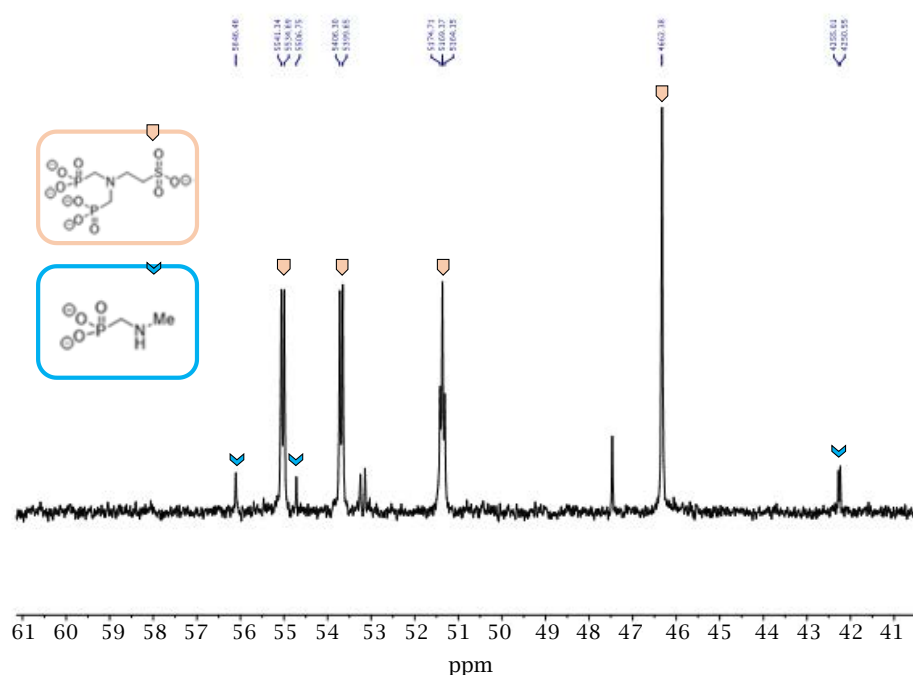


Figure 5.7. ¹³C NMR spectrum of Na₅SP showing the thermal decomposition product.

Thermogravimetric analysis of *o*-Mn₂HSP shows a weight loss from 100 up to 250 °C, corresponding to the loss of three coordinated water molecules (found 12.51%, calc. 11.42%), followed by a second weight loss, from ~ 350 °C, due to the ligand decomposition. The TG curves for both Zn derivatives display similar behaviour, with a first weight loss from RT up to 180-200 °C, due to the irreversible dehydration of the solids (*m*-Zn₂HSP: found 12.59%, calc. 11.59% for 4 water molecules; *h*-Zn₂HSP: found 21.91%, calc. 22.28% for 7 water molecules). According

to the thermogravimetric study, this dehydration process causes amorphisation of the sample (Figure 5.8b). Beyond 280 °C, ligand decomposition occurs (Figure 5.8a).

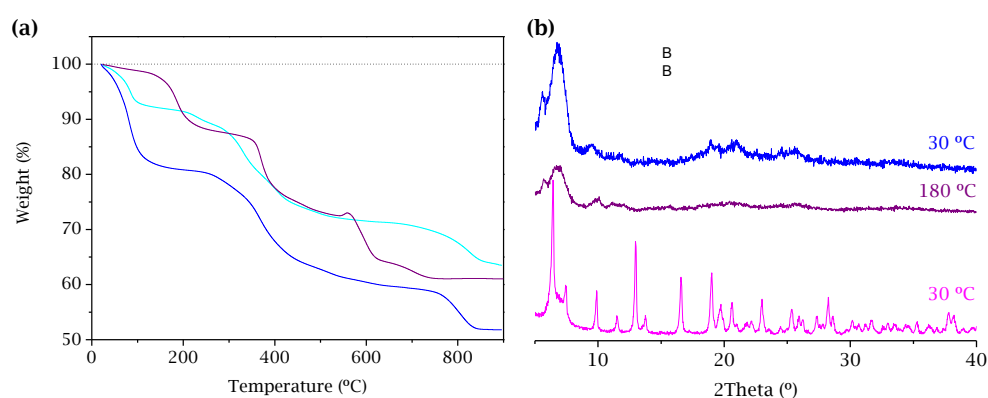


Figure 5.8. (a) Thermal analysis for compounds *o*-Mn₂HSP (purple), *m*-Zn₂HSP (cyan) and *h*-Zn₂HSP (blue) and (b) thermogravimetric patterns for *h*-Zn₂HSP.

Regarding to LnH₂SP compounds, dehydration of *m*-LaH₂SP takes place in two steps (Figure 5.9a). First one, from 50 °C up to ~190 °C, attributed to the loss of the lattice water (found 3.75%, calc. 3.71%) and the second one at 250 °C, corresponding to the loss of the coordination water molecule (found 4.01%, calc. 3.86%). The ligand decomposition starts at ~325 °C. Thermal stability of *m*-LaH₂SP was studied by X-ray powder thermogravimetric analysis. Data were collected at different temperature intervals, from 30 to 270 °C. As can be seen in Figure 5.9b, this solid maintains its crystallinity at least up to 270 °C. Furthermore, it reversibly rehydrates upon exposure at 98% RH for 37 days. It can be concluded that the crystal structure is preserved in the process of dehydration/rehydration.

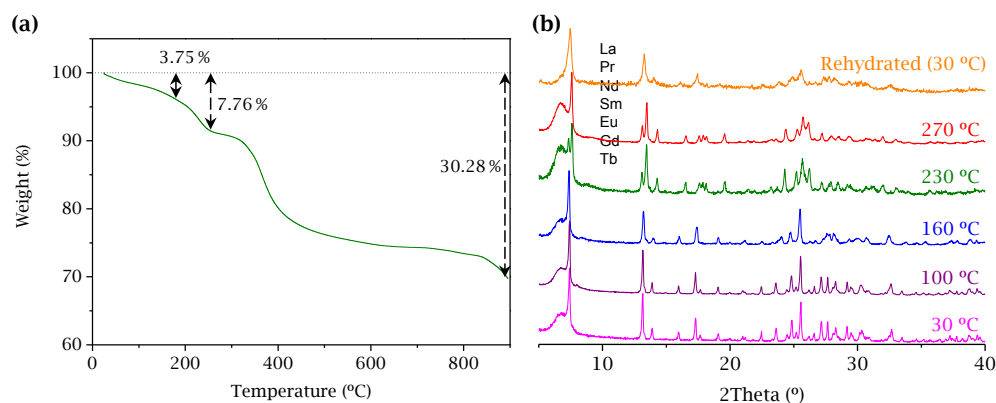


Figure 5.9. (a) Thermal analysis and (b) thermodiffraction patterns for *m*-LaH₂SP.

In the case of *o*-LnH₂SP, dehydration takes place from 30 to 100-150 °C (found 7.12-7.51%, calc. 7.13-7.39%), while the ligand decomposition starts at ~ 350 °C (Figure 5.10a). The decomposition products at 900 °C correspond to LnPO₄. The thermal stability of *o*-SmH₂SP derivative, as representative material, was examined. Thermodiffraction data indicate that *o*-SmH₂SP maintains its crystallinity at least up to 180 °C. It was observed that rehydration is accompanied by a partial loss of crystallinity (Figure 5.10b).

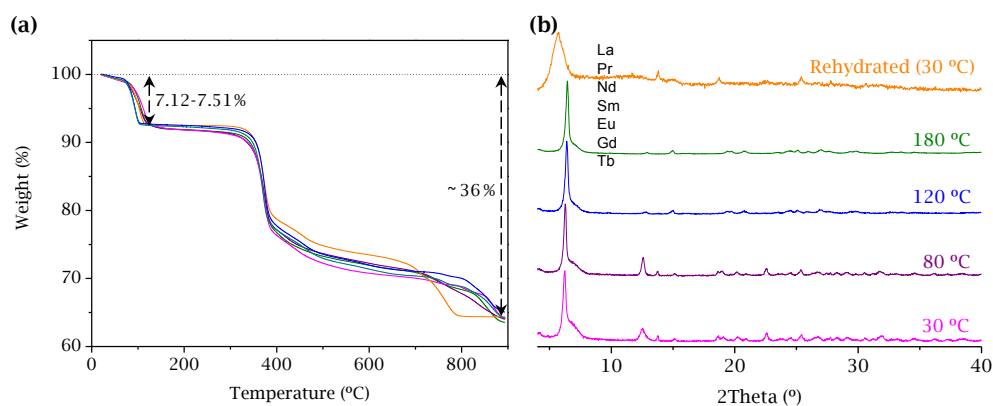


Figure 5.10. (a) Thermal analysis for *o*-LnH₂SP compounds: Pr (olive), Nd (purple), Sm (magenta), Eu (orange), Gd (red) and Tb (blue) and (b) thermodiffraction patterns for *o*-SmH₂SP.

5.2.2. Structural Characterisation

Crystal structure of ***o*-Mn₂HSP**, ***m*-LaH₂SP**, ***o*-PrH₂SP** and ***o*-SmH₂SP** were solved following an *ab initio* methodology from synchrotron X-ray powder diffraction data collected at the BL04-MSPD beamline at ALBA (Barcelona, Spain). Partial structural models were obtained using the program EXPO2014 (Altomare et al., 2013) or by combination of the Patterson function with direct methods (Rius, 2011). The missing atoms were localized by difference Fourier maps.

Crystal structures for ***o*-LnH₂SP** (Ln= Nd, Gd, Eu and Tb) were solved from laboratory powder diffraction patterns (Mo K α_1 0.7093 Å) employing the crystal structure of ***o*-SmH₂SP** as a starting model. Rietveld refinement were carried out to optimize the crystal structures, employing the GSAS package (Larson & Von Dreele, 2004) and soft constraints to maintain chemically reasonable geometries (Chapter 3, Table 3.2).

A summary of selected crystallographic data are given in Table 5.1 and 5.2 and the final Rietveld plots are displayed in Figure 5.11 and Figure AIII.5 (Appendix III). For ***m*-Zn₂HSP** and ***h*-Zn₂HSP**, their powder diffraction patterns were indexed using the program DICVOL (Boultif & Louer, 2004) in a monoclinic [Figures of merits: M(20)= 53.4 and F(20)= 369] and hexagonal unit cells [Figures of merits: M(20)= 47 and F(20) = 252], respectively (de Wolff, 1968; Smith & Snyder, 1979). The Le Bail fits for ***m*-Zn₂HSP** and ***h*-Zn₂HSP** in the proposed space groups are displayed in Figure 5.12.

Table 5.1. Selected crystallographic data for *o*-Mn₂HSP, *m*-Zn₂HSP and *h*-Zn₂HSP compounds.

Phase	<i>o</i> -Mn ₂ HSP	<i>m</i> -Zn ₂ HSP [#]	<i>h</i> -Zn ₂ HSP [#]
Space group	P c n b	P 2 ₁ /a	P 6 ₃ /m c m
Chemical formula	C ₄ Mn ₂ NO ₁₂ P ₂ SH ₁₅	C _{4,8} Zn _{2,4} N _{3,4} O _{14,2} P _{2,4} SH _{25,4}	C ₄ Zn ₂ NO ₁₆ P ₂ S H ₂₃
Formula mass (g·mol ⁻¹)	473.05	621.41	566.02
λ (Å)	0.61976	0.618783	0.61988
a (Å)	26.5105(3)	9.5193(2)	27.1778(6)
b (Å)	10.37266(7)	16.2511(3)	27.1778(6)
c (Å)	10.03046(7)	16.5491(4)	9.2266(3)
α (°)	90.00	90.00	90.00
β (°)	90.00	101.076(2)	90.00
γ (°)	90.00	90.00	120.00
Unit cell volume (Å ³)	2758.22(5)	2512.4(1)	5902.0(2)
Z	8		
No. of independent reflections	8208		
Data/Restraints/Parameters	10417/40/114		
R _{wp}	0.0352	0.0339	0.0419
R _p	0.023	0.0204	0.0271
R _f	0.0249		
CCDC number	2003920		

[#]Le Bail fit data.

Table 5.2. Selected crystallographic data for LnH₂SP compounds.

Phase	<i>m</i> -LaH ₂ SP	<i>o</i> -PrH ₂ SP	<i>o</i> -NdH ₂ SP	<i>o</i> -SmH ₂ SP	<i>o</i> -EuH ₂ SP	<i>o</i> -GdH ₂ SP	<i>o</i> -TbH ₂ SP
Space group	P2 ₁ /c	<i>Pcab</i>	<i>Pcab</i>	<i>Pcab</i>	<i>Pcab</i>	<i>Pcab</i>	<i>Pcab</i>
Chemical formula	C ₄ LaNO ₁₁ P ₂ SH ₁₄	C ₄ PrNO ₁₁ P ₂ SH ₁₄	C ₄ NdNO ₁₁ P ₂ SH ₁₄	C ₄ SmNO ₁₁ P ₂ SH ₁₄	C ₄ EuNO ₁₁ P ₂ SH ₁₄	C ₄ GdNO ₁₁ P ₂ SH ₁₄	C ₄ TbNO ₁₁ P ₂ SH ₁₄
Formula mass (g·mol ⁻¹)	485.07	487.08	490.41	496.53	498.13	503.42	505.09
λ (Å)	0.4124	0.4124	0.7093	0.4124	0.7093	0.7093	0.7093
a (Å)	12.07146(21)	12.9856(1)	12.9311(3)	12.8712(2)	12.8176(5)	12.7829(3)	12.7519(6)
b (Å)	7.51420(13)	27.9504(5)	27.9525(10)	28.0803(7)	27.905(2)	27.9622(8)	27.9883(16)
c (Å)	14.27985(21)	7.1552(1)	7.1194(2)	7.0675(1)	7.0599(2)	7.0407(2)	7.0192(3)
β (Å)	103.0966(12)	90.00	90.00	90.00	90.00	90.00	90.00
Unit cell volume (Å ³)	1261.60(4)	2597.01(7)	2573.36(15)	2554.41(10)	2525.17(26)	2516.59(13)	2505.17(28)
Z	4	8	8	8	8	8	8
No. of independent reflections	1509	7149	2092	1303	1661	2049	2041
Data/Restraints/Parameters	6490/40/118	6323/40/113	4009/40/109	6235/48/111	3970/40/107	4010/40/109	4010/40/107
R _{wp}	0.0621	0.0361	0.0428	0.0617	0.0887	0.0452	0.0671
R _p	0.0440	0.0242	0.0326	0.0410	0.0692	0.0340	0.0490
R _f	0.0225	0.0089	0.0137	0.0242	0.0194	0.0137	0.0178
CCDC number	1922823	1922825	1922824	1922822	1936877	1922821	1922826

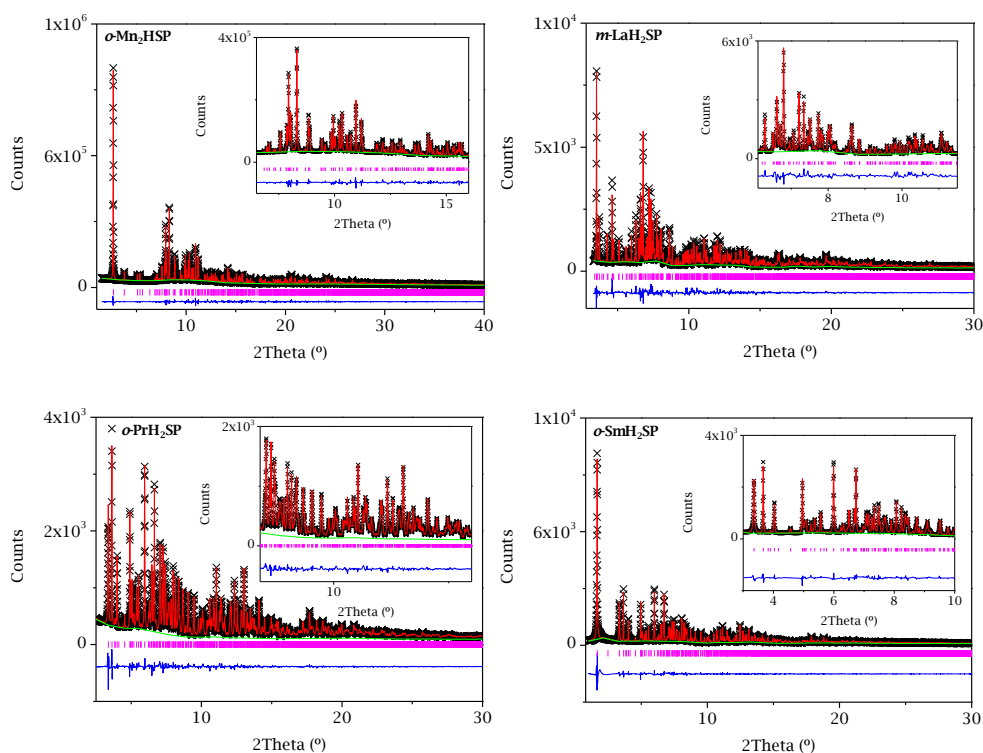


Figure 5.11. Final Rietveld plots for *o*-Mn₂HSP, *m*-LaH₂SP and *o*-LnH₂SP (Ln= Pr and Sm).

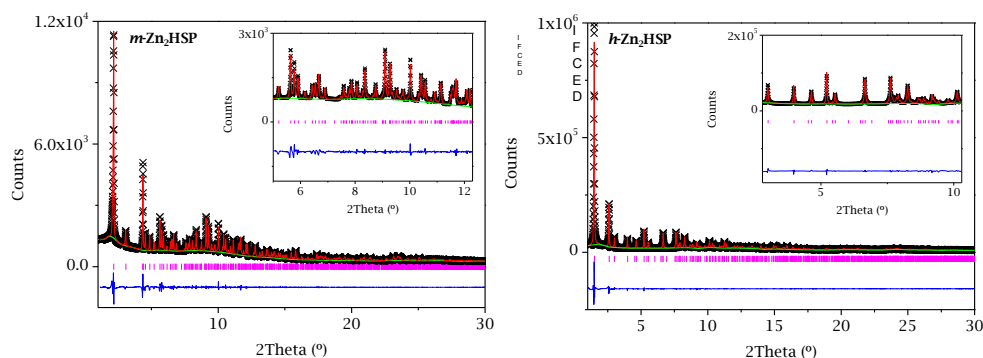


Figure 5.12. Le Bail fits for *m*-Zn₂HSP and *h*-Zn₂HSP.

o-Mn₂HSP is a layered compound that crystallizes in the orthorhombic system. The asymmetric part of the unit cell contains two manganese atoms (Mn1 and Mn2), one amine-ethylsulfonate and two phosphonate groups from the ligand, and four water molecules, two of them in special position (Ow1 and Ow3). The coordination

environment of manganese atoms is octahedral. Mn1 is bonded to three phosphonate oxygen atoms from three different ligands and three water molecules (Ow1, Ow2 and Ow4). Mn2 is coordinated by four phosphonate oxygen atoms from three different ligands and two water molecules (Ow2 and Ow3) (Figure 5.13a). The inorganic layers are built up from edge-sharing Mn(2)O₆ dimers creating zig-zag chains, interconnected by Mn1 octahedra, which share corner with dimers through Ow2 (Figure 5.13b). The ethylsulfonate moiety points to the interlayer region, in an interdigitated arrangement, with the non-coordinated sulfonate groups (O8 and O9) interacting by H-bonds (Figure 5.14 and Table 5.4) with the water molecules (Ow1, Ow2, Ow3 and Ow4) and phosphonate groups of adjacent layers (O2).

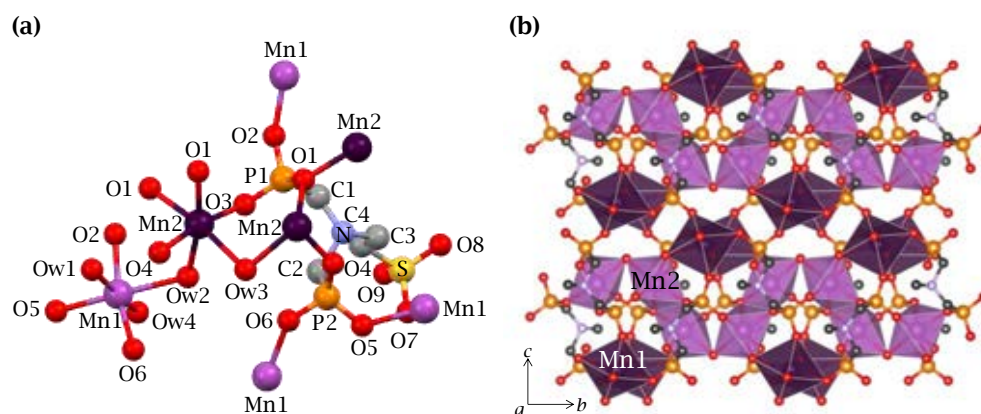


Figure 5.13. (a) Coordination environment and (b) view of the layer of *o*-Mn₂HSP.

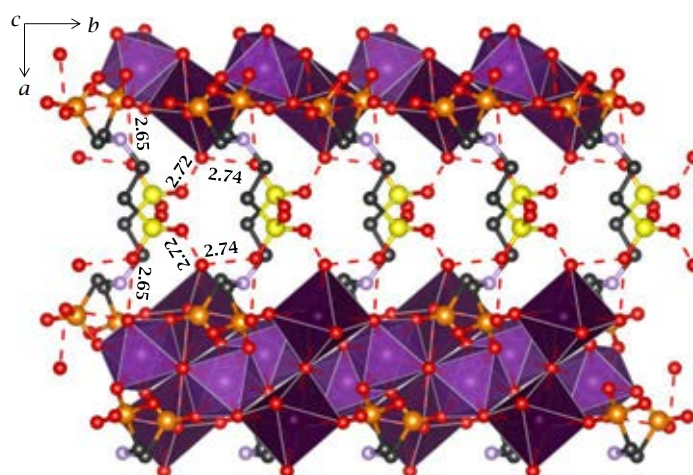


Figure 5.14. H-bonding network within the interlayer region of the ***o*-Mn₂HSP** structure (distances in Å).

***m*-LaH₂SP** is also a bidimensional solid which crystallises in the monoclinic space group $P2_1/c$. Lanthanum ion is octa-coordinated by four oxygen atoms from four phosphonate groups, three oxygen atoms from three sulfonate groups and one oxygen atom (Ow1) from a water molecule. Layers are built up from edge-sharing dimers of LaO₈ polyhedra bridged by phosphonate and sulfonate groups, where this last group connects three metal ions by two oxygen atoms (Figure 5.15b). Oxygen atoms O2 and O3 belonging to the phosphonate group P1 and another one of the sulfonate group (O9), remain uncoordinated and point toward the interlayer region, where a H-bond network is formed with the participation of lattice water (Figure 5.16 and Table 5.3).

Direct coordination of the sulfonate group to lanthanide ions has been also found in both rigid and flexible lanthanide sulfophosphonates (Du, Xu & Mao, 2006a; Sonnauer et al., 2007; Sonnauer & Stock, 2008; Feyand et al., 2010). The rigid ligands preferentially bind lanthanide ions through the phosphonate groups (Du, Xu & Mao, 2006a), except for La³⁺, which may be attributed to the larger size of the latter that makes possible simultaneous coordination with bulky groups.

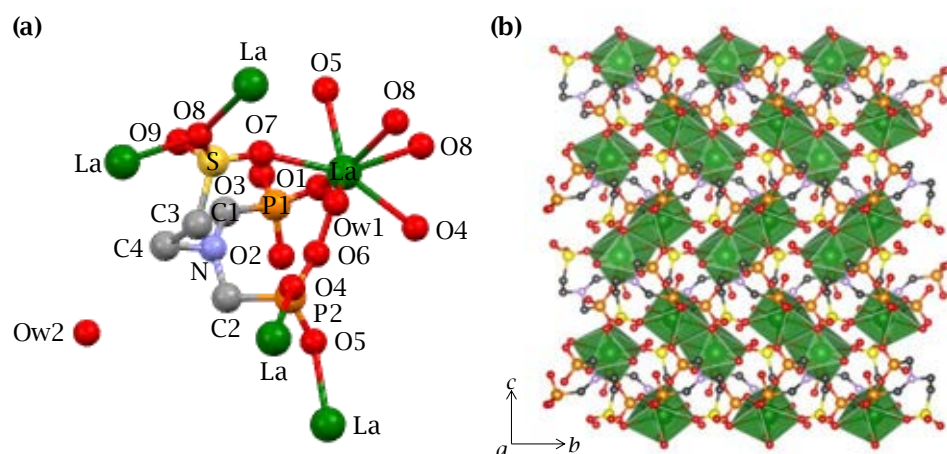


Figure 5.15. (a) Extended asymmetric part of the unit cell with atoms labelled and (b) detail of the connectivity in a single layer for *m*-LaH₂SP.

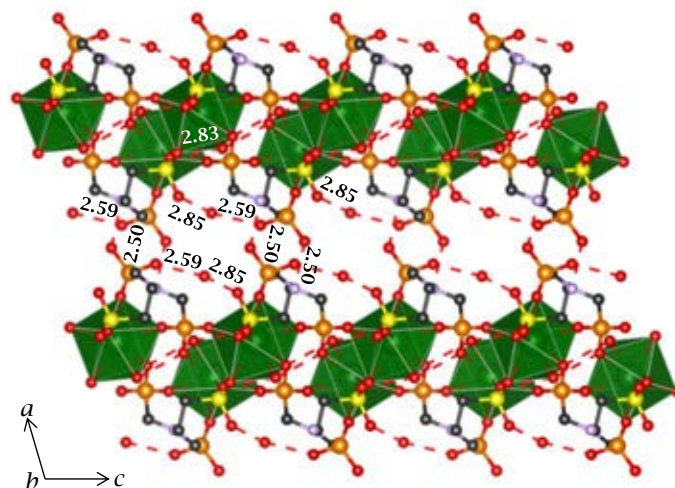


Figure 5.16. H-bonding network within the interlayer region of *m*-LaH₂SP (distances in Å).

Layered *o*-LnH₂SP compounds crystallize in the orthorhombic crystal system. In this structure, the lanthanide ion is octa-coordinated by seven phosphonate oxygen atoms from five different phosphonate groups, two of them bound in a bidentate fashion, and one oxygen atom from a water molecule (Ow1). Layers are formed by edge-sharing LnO₈ polyhedra bridged through the phosphonate groups. Like in *o*-Mn₂HSP but in contrast with *m*-LaH₂SP, the sulfonate group is non-coordinated and points toward the interlayer region (Figure 5.17c). This arrangement facilitates H-

bond interactions with the lattice water molecule and the uncoordinated P-O group, creating extended thus an extended H-bond network (Figure 5.18 and Table 5.3).

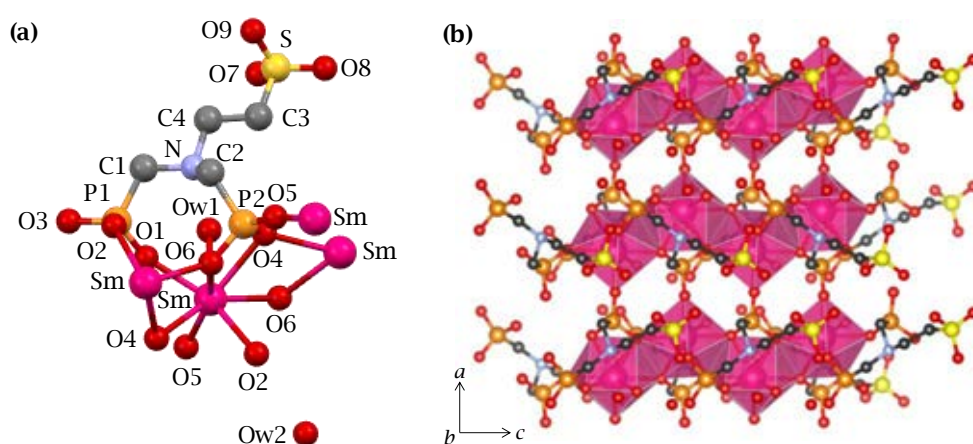


Figure 5.17. (a) Extended asymmetric part of the unit cell with atoms labelled and (b) detail of the connectivity in a single layer for *o*-SmH₂SP.

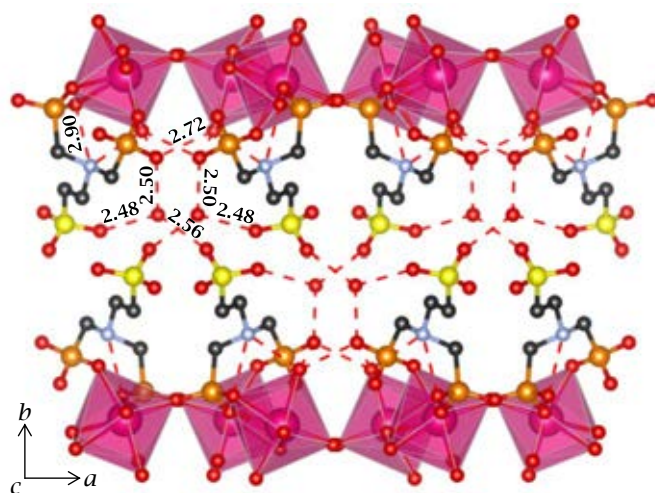


Figure 5.18. H-bonding network within the interlayer region of *o*-SmH₂SP (distances in Å).

Table 5.3. H-bond distances for *o*-Mn₂HSP, *m*-LaH₂SP and *o*-SmH₂SP.

Compound	D...A	D...A (Å)	D...A	D...A (Å)
<i>o</i> -Mn ₂ HSP	O1...O4	3.004(7)	O4...Ow2	2.976(8)
	O1...O4	2.987(8)	O4...Ow3	2.939(6)
	O1...N	3.160(9)	O5...Ow1	3.063(8)
	O2...O4	3.183(9)	O5...Ow2	2.655(8)
	O2...O5	3.219(8)	O5...Ow4	3.146(10)
	O2...N	3.126(10)	O6...Ow1	3.180(9)
	O2...Ow1	2.842(8)	O6...Ow2	3.033(8)
	O2...Ow2	2.969(8)	O6...Ow3	2.483(9)
	O2...Ow4	3.136(9)	O6...Ow4	3.224(10)
	O3...N	3.212(9)	O7...Ow4	3.052(9)
	O3...Ow2	3.068(7)	O8...Ow4	2.730(8)
	O3...Ow3	3.111(10)	O9...Ow2	2.656(9)
	O4...N	2.987(9)	O9...Ow4	2.740(9)
	O4...Ow1	2.635(6)	Ow3...Ow2	3.093(6)
<i>m</i> -LaH ₂ SP	O1...O5	3.152(28)	O5...O8	3.287(31)
	O1...O6	2.898(29)	O5...Ow1	2.921(29)
	O1...O8	3.114(30)	O5...Ow2	3.074(30)
	O1...O9	3.152(32)	O6...O1	2.898(29)
	O2...Ow2	2.595(31)	O6...O7	3.320(31)
	O4...O8	3.200(33)	O6...Ow1	3.155(33)
	O4...Ow1	2.74(4)	O6...Ow1	3.153(29)
	O5...O1	3.152(28)	N...O6	2.924(33)
	O5...O7	2.953(28)	N...O9	3.172(31)
O5...O8	3.151(28)			
<i>o</i> -SmH ₂ SP	O1...O6	2.965(21)	O4...O1	2.908(22)
	O1...Ow1	2.661(22)	O4...Ow1	2.926(24)
	O2...O4	3.037(19)	O6...Ow1	2.918(21)
	O2...O6	3.090(25)	O7...Ow2	2.484(18)
	O2...O6	3.177(22)	O9...Ow2	3.114(21)
	O2...Ow1	3.127(23)	O9...Ow2	2.579(18)
	O3...Ow1	2.694(23)	N...O1	3.039(22)
	O3...Ow1	2.962(23)	N...O4	2.896(22)
	O3...Ow2	2.479(20)	N...Ow1	2.873(24)

5.3. Proton Conductivity

Since the structures of the synthesised metal sulfophosphonates feature extended and well defined H-bond networks, measuring their proton conductivity properties may be of interest, in order to evaluate the effect of ligand connectivity and the contribution of the remaining acidic groups to proton conductivity.

The proton conductivity measurement conditions have been previously mentioned in Section 3.13.2. Impedance spectra were recorded on cooling using stabilisation time of 5h at different temperatures and relative humidity values (Table 5.4). Figures AIV.3-7 in Appendix IV give the complex impedance plane plots, from which the total pellet resistance (R_T) was obtained.

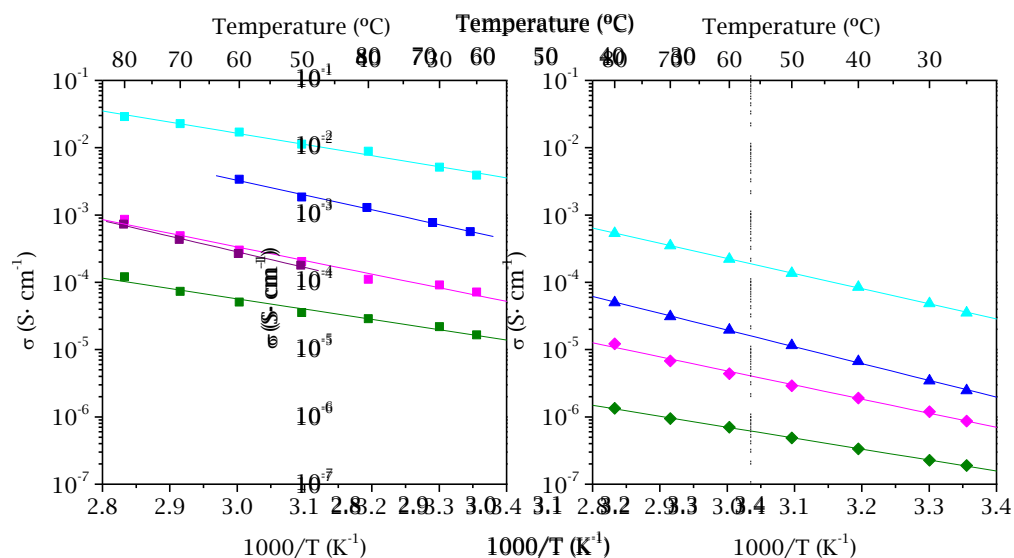


Figure 5.19. Arrhenius plots for σ -Mn₂HSP (purple), m -Zn₂HSP (cyan), h -Zn₂HSP (blue), m -LaH₂SP (olive) and σ -SmH₂SP (magenta) at (left) 95 % RH (■) and (right) 75(▲) and 70 % RH (◆).

Table 5.4. Summary of the proton conductivity and activation energies values of selected materials at 80 °C and different RH values.

Compound	σ (S·cm ⁻¹)	E _a (eV)	% RH
<i>o</i>-Mn₂HSP	7.3·10 ⁻⁴	0.46	95
<i>m</i>-Zn₂HSP	2.9·10 ⁻²	0.44	95
	7.0·10 ⁻³	0.41	90
	3.2·10 ⁻³	0.51	85
	5.4·10 ⁻⁴	0.45	75
<i>h</i>-Zn₂HSP	7.7·10 ⁻³	0.44	95
	2.7·10 ⁻³	0.45	90
	5.8·10 ⁻⁴	0.44	85
	5.0·10 ⁻⁵	0.49	75
<i>m</i>-LaH₂SP	1.2·10 ⁻⁴	0.30	95
	1.3·10 ⁻⁶	0.32	70
<i>o</i>-NdH₂SP	1.1·10 ⁻⁴	0.49	95
<i>o</i>-SmH₂SP	8.6·10 ⁻⁴	0.40	95
	1.2·10 ⁻⁵	0.41	70
<i>o</i>-EuH₂SP	1.2·10 ⁻⁴	0.50	95
<i>o</i>-TbH₂SP	4.4·10 ⁻⁵	0.40	95

The highest proton conductivity values are displayed by ***m*-Zn₂HSP** and ***h*-Zn₂HSP**, ~ 10⁻² S·cm⁻¹ at 80 °C and 95% RH, which is within the range (10⁻³ to 10⁻² S·cm⁻¹) usually found for other metal phosphonate-based coordination polymers as shown in Table 1.2.

The proton conductivities found for the Zn²⁺ derivatives are higher, in more than one order of magnitude, than that of ***o*-Mn₂HSP**. This could be due to the higher water content of Zn²⁺ sulfophosphonates, which may increase the number of H-bonds, favouring the creation of more efficient proton transfer pathways, according to a water-mediated proton transport mechanism (Deng et al., 2020). In fact, a decrease, in more than two order of magnitude, of the proton conductivity was observed for the Zn²⁺ derivatives upon decreasing the RH. In addition, the activation energy values, determined from the Arrhenius plots, suggest a Grotthuss-type proton transport mechanism. Nevertheless, further studies are necessary to establish stronger correlations between the structural characteristics of these solids and proton conductivity.

Regarding to LnH_2SP compounds, ***o*-SmH₂SP** showed the highest proton conductivity value, $\sim 10^{-3} \text{ S}\cdot\text{cm}^{-1}$ at 80 °C and 95% RH, similar to that shown by ***o*-Mn₂HSP** compound. This result suggests that the presence of non-coordinated sulfonate group may be significant to the formation of more efficient proton transfer pathways in the interlamellar region, with shorter H-bonds interactions (Figures 5.14 and 5.18, Table 5.3). In fact, the higher proton conductivity of ***o*-SmH₂SP** with respect to ***m*-LaH₂SP** could be also attributed, in principle, to the contribution that “free” sulfonate groups make to proton transport by establishing more efficient proton transfer pathways (Figure 5.16, Table 5.3). However, the fact that the proton conductivity for the remaining ***o*-LnH₂SP** compounds is close to that of ***m*-LaH₂SP**, is an indication that this property is a combination of various factors and not exclusively dependent on the structural ones. Regarding to the activation energy, the measured values for LnH_2SP compounds are typical of a Grotthuss-type proton transfer mechanism (Table 5.4).

SEM images (Figure 5.20) display elongated platy particles for ***o*-LnH₂SP** (Ln= Nd, Sm, Eu and Tb) samples, showing some significant changes after impedance measurements in both, particle size and morphology, despite that the TG curves (Figure 5.21) did not reveal appreciable changes in weight loss after impedance measurements. For the as synthesised compounds, particle size, determined via dynamic light scattering (DLS), displayed a bimodal distribution with two maxima, ~ 250 and 1000 nm, except for Tb^{3+} derivative which presented just one maximum (~ 700 nm). After impedance measurements, Nd^{3+} and Sm^{3+} derivatives did not show significant variation in particle size, while Eu^{3+} and Tb^{3+} derivatives experienced a notable decrease in particle size distribution, exhibiting a broader distribution centered around 300 and 150 nm, respectively (Figure 7.21).

According to literature (Wong et al., 2017), larger particle size favours higher conductivity, although subtle variations in H-bond lengths and morphology at measurement conditions also may contribute to the total proton conductivity.

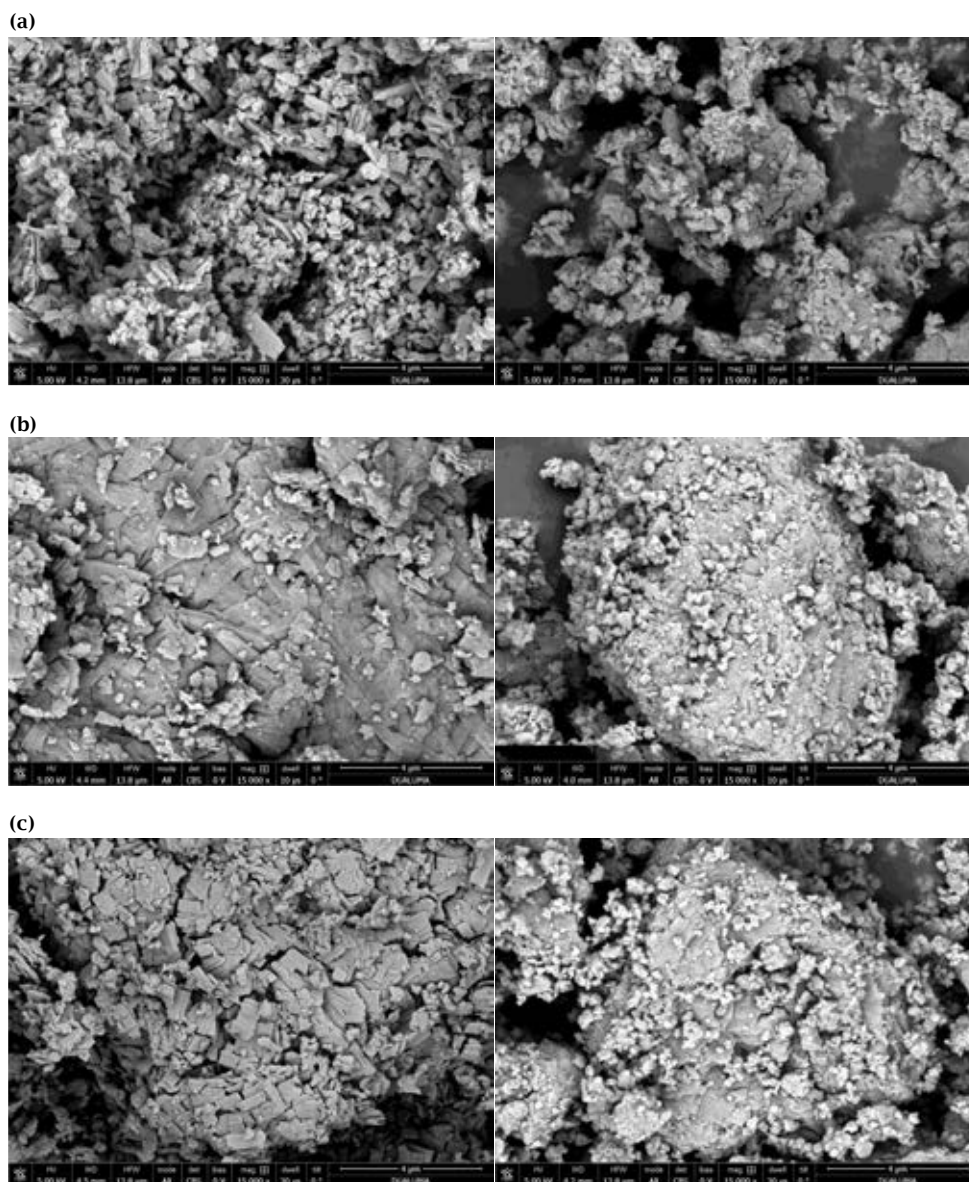


Figure 5.20. SEM images (left) before and (right) after impedance measurements for (a) σ -NdH₂SP, (b) σ -SmH₂SP, (c) σ -EuH₂SP and (d) σ -TbH₂SP samples.

(d)

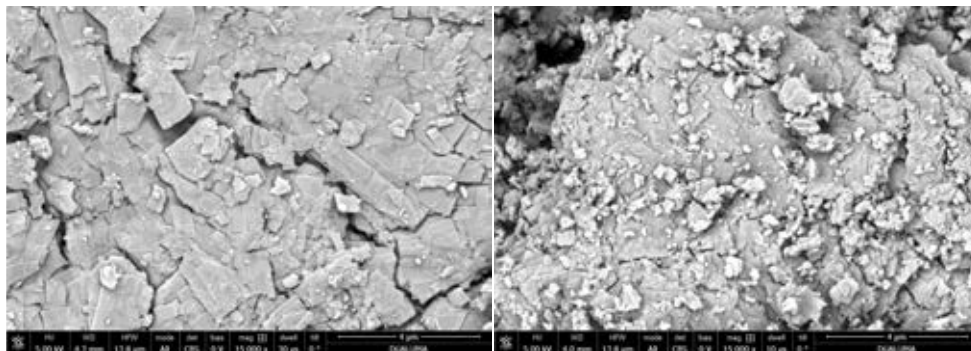


Figure 5.20. SEM images (left) before and (right) after impedance measurements for (a) σ -NdH₂SP, (b) σ -SmH₂SP, (c) σ -EuH₂SP and (d) σ -TbH₂SP samples (Continuation).

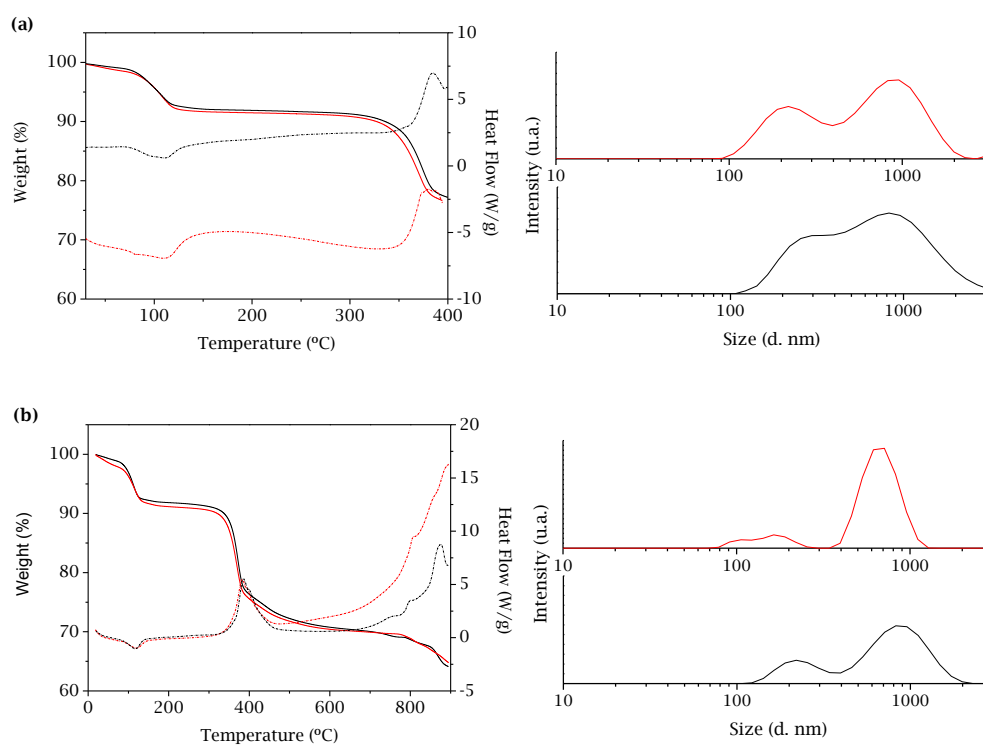


Figure 5.21. (Left) TG curves and (right) particle size distributions for (a) σ -NdH₂SP, (b) σ -SmH₂SP, (c) σ -EuH₂SP and (d) σ -TbH₂SP samples before (black) and after (red) impedance measurements.

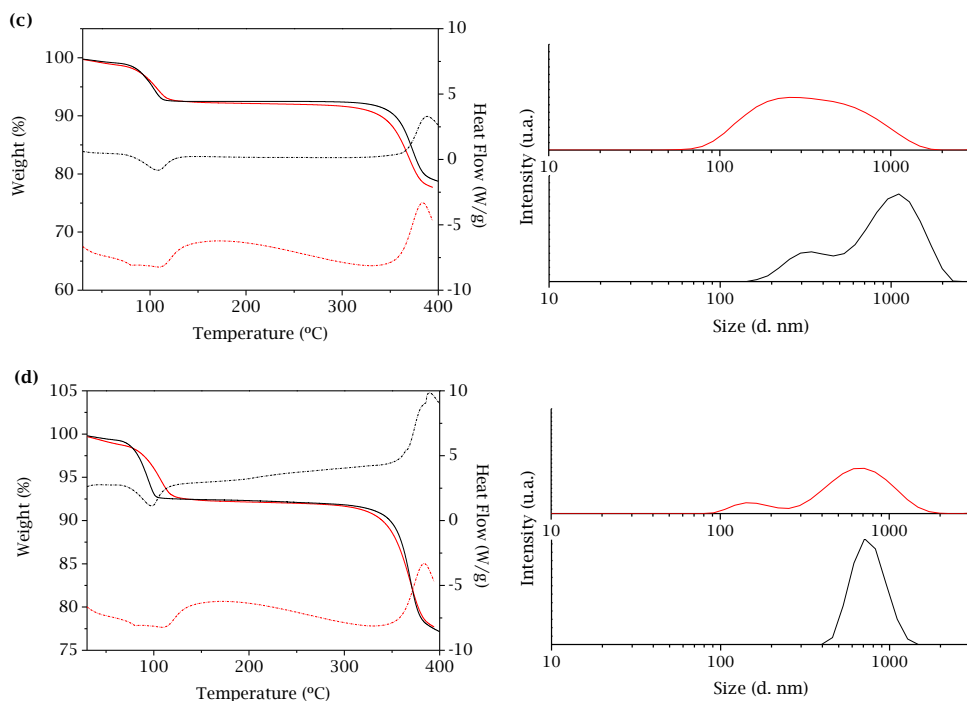


Figure 5.21. (Left) TG curves and (right) particle size distributions for (a) *o*-NdH₂SP, (b) *o*-SmH₂SP, (c) *o*-EuH₂SP and (d) *o*-TbH₂SP samples before (black) and after (red) impedance measurements (Continuation).

5.4. Preparation and Characterisation of Composite Membranes

Preliminary studies of preparation and characterisation of composite membranes for proton exchange membrane fuel cells (PEMFCs) have been carried out in collaboration with the Institute of Science and Technology of Polymers, ICTP-CSIC (Madrid). *o*-SmH₂SP was selected as representative lanthanide derivative for the preparation of composite membranes, using Nafion as supporting polymeric matrix, because of its high performance as proton conductor in a wide range of RH values. In this preliminary study, cast Nafion was not annealed at above the T_g to give the phase separated microstructure and high mechanical stability, as established in other previous studies (Mauritz & More, 2004).

3 and 5 wt % *o*-SmH₂SP-loaded Nafion composite membranes (Nafion/SmH₂SP-X) were prepared. As an example, the preparation procedure is described for composite Nafion/SmH₂SP-3: 18 mg of *o*-SmH₂SP was dispersed in 3 mL of isopropanol using three subsequent cycles of magnetic stirring (10 min) and

sonication (10 min). Then, it was slowly added to a 20 wt % Nafion 1100 EW dispersion (3 g) and mixed using two subsequent cycles of magnetic stirring (5 min) and sonication (5 min). The resulting viscous, homogeneous suspension was casted using a blade (BYK Instruments) onto a polycarbonate plate and air-dried for 2 days. Finally, a 35-40 μm -thickness composite membrane was removed from the plate.

Figure 5.22 displays the XRPD patterns of **Nafion/SmH₂SP-X** membranes together with those of Nafion and as-synthesised ***o*-SmH₂SP**. As can be seen, the characteristic peaks of crystalline ***o*-SmH₂SP** are present in the XRD patterns of **Nafion/SmH₂SP-X** membranes together with a broad reflection between ~ 11 and 21° (2θ) corresponding to the amorphous Nafion membrane.

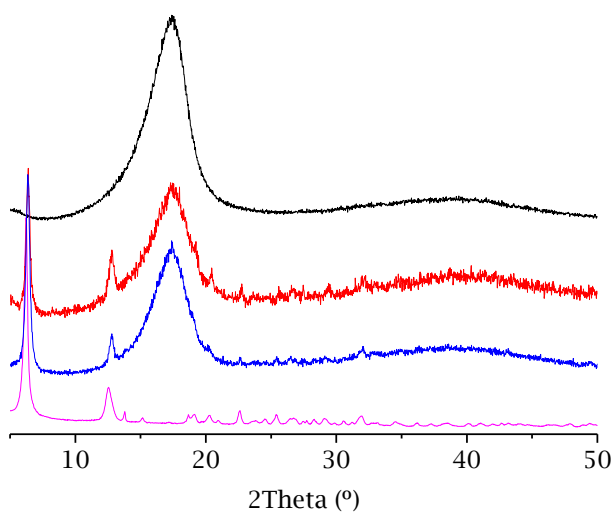


Figure 5.22. XRPD patterns of **Nafion** (black), **Nafion/SmH₂SP-3** (red), **Nafion/SmH₂SP-5** (blue) and ***o*-SmH₂SP** (magenta).

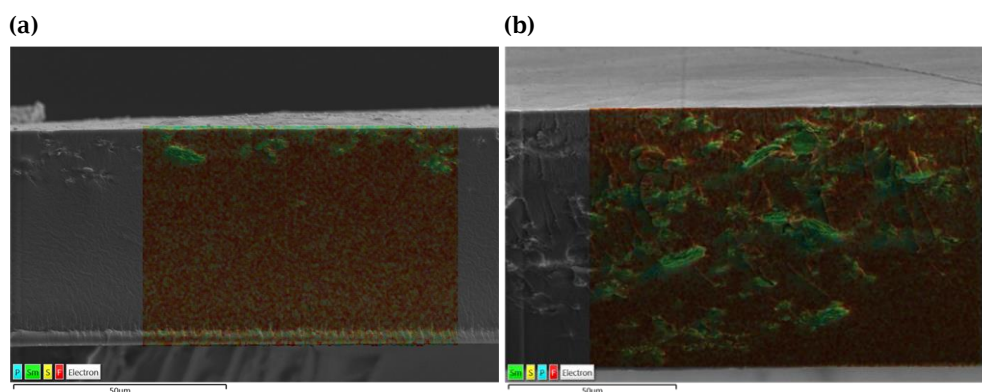
Water uptake measurements were carried out as follows. Firstly, the membranes were dried at 60°C for 12h under vacuum and weighed. Secondly, they were immersed in DI water for 24h; the excess of water was removed with a tissue paper and rapidly weighed. As shown in Table 5.5, water adsorption decreased with increasing load of ***o*-SmH₂SP**.

$$\text{Water uptake (wt \%)} = \frac{\text{Wet membrane (g)} - \text{Dried membrane (g)}}{\text{Wet membrane (g)}} \times 100 \quad \text{Equation 5.1}$$

Table 5.5. Water uptake of Nafion, Nafion/SmH₂SP-3 and Nafion/SmH₂SP-5.

Membrane	Water uptake (%)
Nafion	33.6
Nafion/SmH ₂ SP-3	25.4
Nafion/SmH ₂ SP-5	19.0

The distribution of ***o*-SmH₂SP** particles inside of the polymeric matrix of Nafion was monitored by SEM-EDS. As can be seen in Figure 5.23, there is a uniform distribution of submicrometric particles of ***o*-SmH₂SP** inside the Nafion matrix together with larger particle aggregates, which are especially visible for Nafion/SmH₂SP-5. This may explain that the 3%-loaded composite membrane exhibits higher water uptake (Table 5.6).

**Figure 5.23.** SEM-EDS images for (a) Nafion/SmH₂SP-3 and (b) Nafion/SmH₂SP-5.

In situ through-plane proton conductivity of the membranes were determined on Membrane Electrode Assemblies (MEAs) at 70, 80 and 90 °C and 100% RH (Chapter 3, Section 3.13.2). Equation 5.2 was employed to obtain the through-plane proton conductivity (σ_{TP}), where L is the membrane thickness, R is the resistance and S is the active area of the MEA (5 cm²).

$$\sigma_{TP}(S \cdot cm^{-1}) = \frac{L (cm)}{R (\Omega) \cdot S (cm^2)} \quad \text{Equation 5.2}$$

The resistance was determined from the intersection on the real axis in the Nyquist plots. In order to ensure good data reproducibility, each sample was measured at least five times after it had reached a constant value.

In situ through-plane proton conductivity measurements show slight, but consistent, changes in the behavior of the composite membranes relative to the unmodified Nafion membrane (Del Río, Morales & Escibano, 2014) (Figure 5.24). While the proton conductivity of Nafion decays in the range between 70 and 90 °C, **Nafion/SmH₂SP-X** membranes display a better temperature performance, slightly increasing the conductivity values in the range of 70 to 90 °C and 100% RH, with values of $2.76 \cdot 10^{-2}$ and $2.61 \cdot 10^{-2}$ S·cm⁻¹ for **Nafion/SmH₂SP-3** and **Nafion/SmH₂SP-5** membranes, respectively (Table 5.6). This behavior can be explained as being due to the presence of hydrophilic particles of lanthanide sulfophosphonate, which maintains the hydration degree of the membranes in a wider range of temperature (70-90 °C). Similar results were also reported for Nafion-zirconium phosphate composite membranes functionalized with meta-sulphophenylphosphonic acid (Casciola et al., 2009), although, in this case, high Zr-phosphate loads (20-40 wt %) were needed to make the composite membranes more conductive than pristine Nafion. In addition, the low activation energies (~ 0.1 eV) determined for the **Nafion/SmH₂SP-X** composite membranes are compatible with a Grotthuss-type mechanism and indicative of a highly facilitated proton transport.

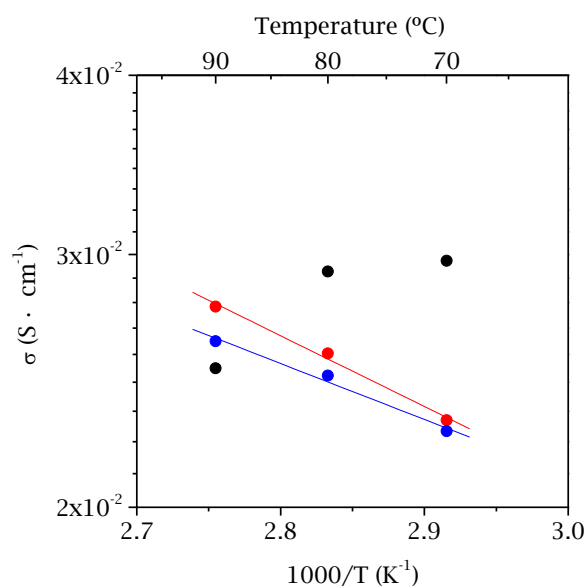


Figure 5.24. Arrhenius plot for **Nafion** membrane (black), **Nafion/SmH₂SP-3** (red) and **Nafion/SmH₂SP-5** (blue) composite membranes at 100% RH.

Table 5.6. Proton conductivity values at 90 °C and 100% RH.

Membrane	σ (S·cm ⁻¹)
Nafion	$2.50 \cdot 10^{-2}$
Nafion/SmH₂SP-3	$2.76 \cdot 10^{-2}$
Nafion/SmH₂SP-5	$2.61 \cdot 10^{-2}$

Initial studies of these composite membranes as proton exchange membrane components of fuel cells (PEMFC) were carried out employing a Scribner 850e multirange fuel cell test system, with a cell temperature of 80 °C, 100% RH and under atmospheric pressure. H₂ and O₂ gas were supplied at 0.2 L·min⁻¹ to the anode and cathode, respectively. The polarization curves were recorded after the single cell had reached stable conditions, that is, potential remained constant over time at a fixed current.

Polarization and power density curves of **Nafion/SmH₂SP-X** composite membranes as well as Nafion membrane as a commercial reference material are shown in Figure 5.25. As can be seen, both **Nafion/SmH₂SP-3** and **Nafion/SmH₂SP-5** composite membranes perform adequately in PEMFC single cells. It should be noted

that the incorporation of 3 wt % of α -SmH₂SP into the Nafion matrix improves the electrochemical behaviour of the pristine Nafion membrane, reaching a maximum current density of 3300 mA·cm⁻² and a maximum power density of 946 mW·cm⁻² (Table 5.7). This appears to be due to the better dispersion of the α -SmH₂SP in the Nafion matrix (Figure 5.23). This also results in a higher water retention capability than that of Nafion/SmH₂SP-5 membrane, even when the α -SmH₂SP load is lower. Therefore, Nafion/SmH₂SP-X composite membranes are potential candidates for their use as electrolytes in PEMFCs. However, these are preliminary results and additional work would be necessary to improve some characteristics such as the dispersion and homogeneity of the fillers.

Table 5.7. Maximum current and power density values.

Membrane	Maximum current density (mA·cm ⁻²)	Maximum power density (mW·cm ⁻²)
Nafion	2900	923
Nafion/SmH ₂ SP-3	3300	946
Nafion/SmH ₂ SP-5	3000	858

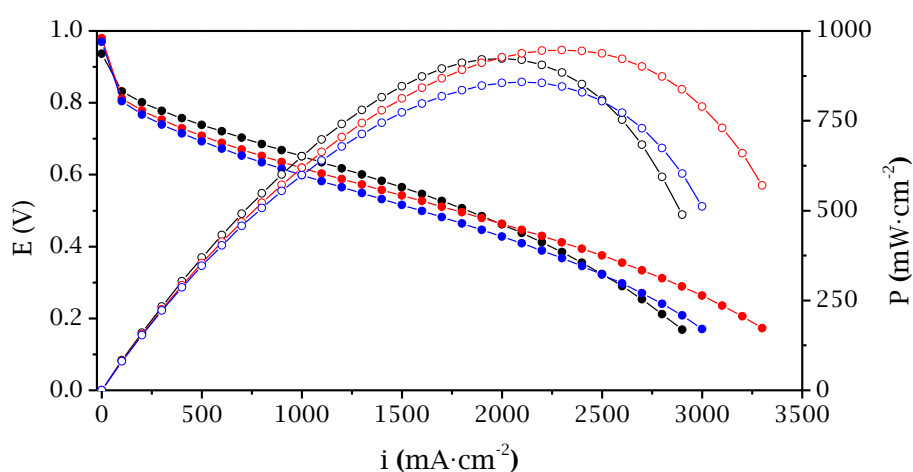


Figure 5.25. Polarization (full) and power density (empty) curves for Nafion (black), Nafion/SmH₂SP-3 (red) and Nafion/SmH₂SP-5 (blue) composite membranes at 80 °C and 100% RH.

After electrochemical tests, cross-sectional SEM images of the corresponding MEAs were taken (Figure 5.26). These images display a uniform **Nafion/SmH₂SP-X** thickness (35-42 μm) and the excellent adhesion between layers, which is indicative that they are stable under operating conditions.

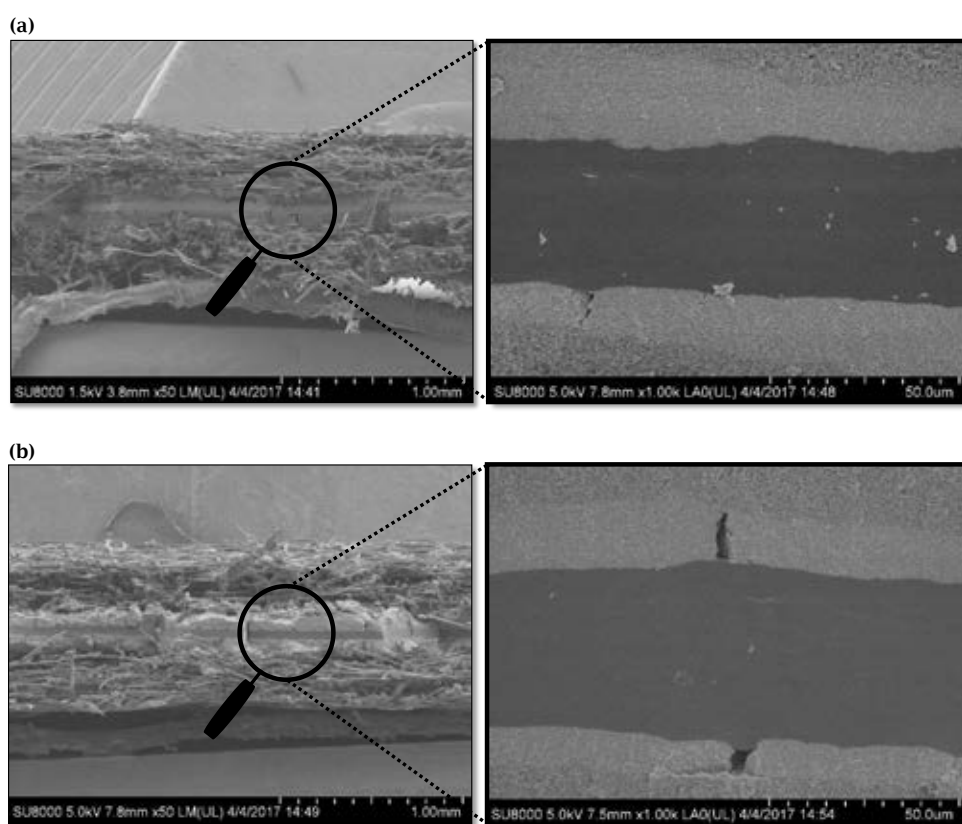


Figure 5.26. Cross-sectional SEM images of MEAs (a) **Nafion/SmH₂SP-3** and (b) **Nafion/SmH₂SP-5**.

5.5. Conclusions

- Divalent transition metals and rare-earth derivatives of the sulfophosphonate ligand 2-[bis(phosphonomethyl)amino]-ethanesulfonic acid can be synthesised by appropriate hydro-, solvothermal and/or microwave-assisted synthesis with the following compositions: $\text{Mn}_2[(\text{O}_3\text{PCH}_2)_2\text{-NH-(CH}_2)_2\text{-SO}_3]\cdot 3\text{H}_2\text{O}$, ***o*-Mn₂HSP**, $\text{Zn}_2[(\text{O}_3\text{PCH}_2)_2\text{-NH-(CH}_2)_2\text{-SO}_3]\text{Zn}_{0.4}[\text{O}_3\text{PCH}_2\text{-NH-CH}_3]_{0.4}(\text{NH}_3)_2\cdot 4\text{H}_2\text{O}$, ***m*-Zn₂HSP**, $\text{Zn}_2[(\text{O}_3\text{PCH}_2)_2\text{-NH-(CH}_2)_2\text{-SO}_3]\cdot 3\text{H}_2\text{O}$, ***o*-Zn₂HSP**, $\text{Zn}_2[(\text{O}_3\text{PCH}_2)_2\text{-NH-(CH}_2)_2\text{-SO}_3]\cdot 3\text{H}_2\text{O}$, ***m*-Zn₂HSP**, $\text{Zn}_2[(\text{O}_3\text{PCH}_2)_2\text{-NH-(CH}_2)_2\text{-SO}_3]\cdot 3\text{H}_2\text{O}$

$\text{SO}_3\text{]}\cdot 7\text{H}_2\text{O}$, ***h*-Zn₂HSP**, and $\text{Ln}[\text{H}(\text{O}_3\text{PCH}_2)_2\text{-NH}(\text{CH}_2)_2\text{-SO}_3]\cdot 2\text{H}_2\text{O}$, ***LnH₂SP*** (Ln= La, Pr, Nd, Sm, Eu, Gd and Tb).

- ***o*-Mn₂HSP** is a 2D solid with an inorganic layer composed of edge-sharing MnO_6 polyhedra and with the ethylsulfonate group pointing towards the interlayer region. ***m*-Zn₂HSP** and ***h*-Zn₂HSP** crystallise in the monoclinic and hexagonal systems, respectively, but their crystal structures still remain unsolved.
- Lanthanide sulfophosphonates exhibit two types of 2D structures: ***m*-LaH₂SP** and ***o*-LnH₂SP** (Ln= Pr, Nd, Sm, Eu, Gd and Tb). Like ***o*-Mn₂HSP**, ***o*-LnH₂SP**, presents a layered structure with the free sulfonic group pointing towards the interlayer region. By contrast, in the structure of ***m*-LaH₂SP** the metal ion is coordinated by the sulfonate group. These differences in metal-ligand binding influence the formation of H-bond networks and create thus different proton transfer pathways in the interlamellar region.
- According to impedance spectroscopy measurements, zinc derivatives exhibit the highest proton conductivity values ($\sim 10^{-2} \text{ S cm}^{-1}$ at 80 °C and 95% RH). Other derivatives such as ***o*-Mn₂HSP** and ***o*-SmH₂SP** exhibit high proton conductivity values, $\sim 10^{-3} \text{ S cm}^{-1}$ at 80 °C and 95% RH, and activation energies typical of a Grotthuss-type proton transfer mechanism.
- Preliminary performances of **Nafion/SmH₂SP-X** composite membranes are indicative that the dispersion of ***o*-SmH₂SP** (X= 3 and 5) inside the matrix of Nafion membrane is a satisfactory way for the preparation of composite membranes, maintaining the high proton conductivity of Nafion at least up to 90 °C. These results make these composite membranes attractive for PEMFCs under operation conditions.

5.6. References

A

- Alberti, G.; Casciola, M.; Palombari, R. Inorgano-organic proton conducting membranes for fuel cells and sensors at medium temperatures. *J. Membr. Sci.*, **2000**, 172(1-2), 233-239.
- Alberti, G.; Casciola, M. Solid state protonic conductors, present main applications and future prospects. *Solid State Ion.*, **2001**, 145(1-4), 3-16.
- Alberti, G.; Casciola, M.; Donnadio, A.; Piaggio, P.; Pica, M.; Sisani, M. Preparation and characterisation of α -layered zirconium phosphate

CHAPTER 5

sulfophenylphosphonates with variable concentration of sulfonic groups. *Solid State Ion.*, **2005**, 176(39-40), 2893-2898.

Altomare, A.; Cuocci, C.; Giacobazzo, C.; Moliterni, A.; Rizzi, R.; Corriero, N.; Falcicchio, A. EXPO2013: a kit of tools for phasing crystal structures from powder data. *J. Appl. Cryst.*, **2013**, 46(4), 1231-1235.

B

Bazaga-García, M.; Salcedo, I. R.; Colodrero, R. M.; Xanthopoulos, K.; Villemin, D.; Stock, N.; López-González, M.; del Río, C.; Losilla, E. R.; Cabeza, A.; Demadis, K. D.; Oliver-Pastor, P. Layered Lanthanide Sulfophosphonates and Their Proton Conduction Properties in Membrane Electrode Assemblies. *Chem. Mater.*, **2019**, 31(23), 9625-9634.

Beyer, O.; Homburg, T.; Albat, M. Stock, N.; Lüning, U. Synthesis of phosphonosulfonic acid building blocks as linkers for coordination polymers. *New J. Chem.*, **2017**, 41(17), 8870-8876.

Bonnet, B.; Jones, D. J.; Roziere, J.; Tchicaya, L.; Alberti, G.; Casciola, M.; Massinelli, L.; Bauerc B.; Peraiod A.; Ramunni, E. Hybrid organic-inorganic membranes for a medium temperature fuel cell. *J. New Mat. Electr. Sys.*, **2000**, 3(2), 87-92.

Boultif, A.; Louer, D. Powder pattern indexing with the dichotomy method. *J. Appl. Cryst.*, **2004**, 37(5), 724-731.

C

Casciola, M.; Capitani, D.; Donnadio, A.; Frittella, V.; Pica, M.; Sganappa, M. Preparation, proton conductivity and mechanical properties of Nafion 117-Zirconium Phosphate Sulphophenylphosphonate composite membranes. *Fuel Cells*, **2009**, 9(4), 381-386.

D

de Wolff, P. D. A simplified criterion for the reliability of a powder pattern indexing. *J. Appl. Crystallogr.*, **1968**, 1(2), 108-113.

Del Río, C.; Morales, E.; Escribano, P. G. Nafion/sPOSS hybrid membranes for PEMFC. Single cell performance and electrochemical characterization at different humidity conditions. *Int. J. Hydrogen Energ.*, **2014**, 39(10), 5326-5337.

- Deng, X.; Hu, J. Y.; Luo, J.; Liao, W. M.; He, J. Conductive Metal–Organic Frameworks: Mechanisms, Design Strategies and Recent Advances. *Topics Curr. Chem.*, **2020**, 378(2), 1-50.
- Du, Z. Y.; Xu, H. B.; Mao, J. G. Rational Design of 0D, 1D, and 3D Open Frameworks Based on Tetranuclear Lanthanide (III) Sulfonate– Phosphonate Clusters. *Inorg. Chem.*, **2006a**, 45(24), 9780-9788.
- Du, Z. Y.; Xu, H. B.; Mao, J. G. Three Novel Zinc (II) Sulfonate– Phosphonates with Tetranuclear or Hexanuclear Cluster Units. *Inorg. Chem.*, **2006b**, 45(16), 6424-6430.
- Du, Z. Y.; Li, X. L.; Liu, Q. Y.; Mao, J. G. Novel cadmium (II) phosphonatophenylsulfonate cluster compounds: Syntheses, structures, and luminescent properties. *Cryst. Growth Des.*, **2007**, 7(8), 1501-1507.
- Du, Z. Y.; Huang, J. J.; Xie, Y. R.; Wen, H. R. Two new 1D structures of copper (II) or yttrium (III) phosphonatobenzenesulfonates using 1, 10-phenanthroline as auxiliary ligand. *J. Mol. Struct.*, **2009**, 919(1-3), 112-116.

F

- Feyand, M.; Nather, C.; Rothkirch, A.; Stock, N. Systematic and In Situ Energy Dispersive X-ray Diffraction Investigations on the Formation of Lanthanide Phosphonatobutanesulfonates: $\text{Ln}(\text{O}_3\text{P-C}_4\text{H}_8\text{-SO}_3)(\text{H}_2\text{O})$ (Ln = La–Gd). *Inorg. Chem.*, **2010**, 49(23), 11158-11163.

J

- Jang, M.; Park, Y.; Yamazaki, Y. Preparation, characterization and proton conductivity of layered cerium sulfophenylphosphonate. *Electrochemistry*, **2003**, 71(8), 691-694.

K

- Kim, Y. T.; Song, M. K.; Kim, K. H.; Park, S. B.; Min, S. K.; Rhee, H. W. Nafion/ZrSPP composite membrane for high temperature operation of PEMFCs. *Electrochim. Acta*, **2004**, 50(2-3), 645-648.
- Kopecká, K.; Melánová, K.; Beneš, L.; Knotek, P.; Mazur, M.; Zima, V. Exfoliation of layered mixed zirconium 4-sulfophenylphosphonate phenylphosphonates. *Dalton Trans.*, **2020**, 49, 3816-3823.

L

- Larson, A. C.; von Dreele, R. B. General structure analysis system (GSAS). Los Alamos National Laboratory Report LAUR, **2004**, 86-748.

CHAPTER 5

Li, Z.; Dong, F.; Xu, L.; Wang, S.; Yu, X. Preparation and properties of medium temperature membranes based on zirconium sulfophenylphosphate/sulfonated poly (phthalazinone ether sulfone ketone) for direct methanol fuel cells. *J. Membr. Sci.*, **2010**, 351(1-2), 50-57.

M

Mady, M. F.; Malmin, H.; Kelland, M. A. Sulfonated Nonpolymeric Aminophosphate Scale Inhibitors—Improving the Compatibility and Biodegradability. *Energy Fuels*, **2019**, 33(7), 6197-6204.

Maniam, P.; Näther, C.; Stock, N. Systematic Hydrothermal Investigation of Metal Phosphonatobenzenesulfonates by High-Throughput Methods. *Eur. J. Inorg. Chem.*, **2010** (24), 3866-3874.

Maniam, P.; Stock, N. Synthesis and Characterization of the Mixed-Linker Copper (II) Coordination Polymer [Cu(HO₃PC₆H₄SO₃)(C₁₀N₂H₈)]·H₂O. *Z. Anorg. Allg. Chem.*, **2011**, 637(9), 1145-1151.

Mauritz, K. A.; Moore, R. B. State of Understanding of Nafion. *Chem. Rev.*, **2004**, 104, 4535-4585.

Melánová, K.; Brus, J.; Zima, V.; Beneš, L.; Svoboda, J.; Kobera, L.; Kutálek, P. Formation of Layered Proton-Conducting Zirconium and Titanium Organophosphonates by Topotactic Reaction: Physicochemical Properties, Proton Dynamics, and Atomic-Resolution Structure. *Inorg. Chem.*, **2020**, 59(1), 505-513

Moedritzer, K.; Irani, R. R. The direct synthesis of α -aminomethylphosphonic acids. Mannich-type reactions with orthophosphorous acid. *J. Org. Chem.*, **1966**, 31(5), 1603-1607.

R

Rius, J. Patterson-function direct methods for structure determination of organic compounds from powder diffraction data. XVI. *Acta Cryst.*, **2011**, 67(1), 63-67.

S

Škoda, J.; Pospíšil, M.; Kovář, P.; Melánová, K.; Svoboda, J.; Beneš, L.; Zima, V. Geometry optimization of zirconium sulfophenylphosphonate layers by molecular simulation methods. *J. Mol.*, **2018**, 24(1), 10.

- Smith, G. S.; Snyder, R. L. FN: A criterion for rating powder diffraction patterns and evaluating the reliability of powder-pattern indexing. *J. Appl. Crystallogr.*, **1979**, 12(1), 60-65.
- Sonnauer, A.; Näther, C.; Höpfe, H. A.; Senker, J.; Stock, N. Systematic investigation of lanthanide phosphonatoethanesulfonate framework structures by high-throughput methods, $\text{Ln}(\text{O}_3\text{P}-\text{C}_2\text{H}_4-\text{SO}_3)(\text{H}_2\text{O})$ (Ln= La– Dy). *Inorg. Chem.*, **2007**, 46(23), 9968-9974.
- Sonnauer, A.; Stock, N. Synthesis and characterization of 2-phosphonoethanesulfonic acid and a barium-hydrogenphosphonatoethanesulfonate— $\text{BaH}(\text{O}_3\text{P}-\text{C}_2\text{H}_4-\text{SO}_3)$. *J. Solid State Chem.*, **2008**, 181(3), 473-479.
- Stein, E.W.; Clearfield, A.; Subramanian, M.A. Conductivity of group IV metal sulfophosphonates and a new class of interstratified metal amino-sulfophosphonates. *Solid State Ion.*, **1996**, 83, 113-124.
- Svoboda, J.; Zima, V.; Melánová, K.; Beneš, L.; Trchová, M. Intercalation chemistry of zirconium 4-sulfophenylphosphonate. *J. Solid State Chem.*, **2013**, 208, 58-64.

V

- Vivani, R.; Constantino, F.; Taddei, M. Zirconium Phosphonates in Metal Phosphonate Chemistry: From Synthesis to Applications, *RSC: London*, **2012**, Ch. 2, p. 45-86.

W

- Wöhlbrandt, S.; Beyer, O.; Reinsch, H.; Ken Inge, A.; Svensson Grape, E.; Lüning, U.; Stock, N. Five New Coordination Polymers with a Bifunctional Phosphonate-Sulfonate Linker Molecule. *Z. Anorg. Allg. Chem.*, **2019**, 645 (10), 732-739.
- Wong, N. E.; Ramaswamy, P.; Lee, A. S.; Gelfand, B. S.; Bladec, K. J.; Taylor, J. M.; Spasyuk, D. M.; Shimizu, G. K. H. Tuning intrinsic and extrinsic proton conduction in metal-organic frameworks by the lanthanide contraction. *J. Am. Chem. Soc.*, **2017**, 139(41), 14676-14683.

Z

- Zhang, G.; Fei, H. Missing metal-linker connectivities in a 3-D robust sulfonate-based metal-organic framework for enhanced proton conductivity. *Chem. Commun.*, **2017**, 53(29), 4156-4159.
- Zima, V.; Svoboda, J.; Melánová, K.; Beneš, L.; Casciola, M.; Sganappa, M.; Brus J.; Trchová, M. Synthesis and characterization of new zirconium 4-sulfophenylphosphonates. *Solid State Ion.*, **2010**, 181(15-16), 705-713.



UNIVERSIDAD
DE MÁLAGA

Chapter 6

Lanthanide Metals Triphosphonates





UNIVERSIDAD
DE MÁLAGA

Aminotris(methylenephosphonic acid), H_6NMP , is an organic ligand which possesses three phosphonic groups in tripodal arrangement. This acid has an excellent chelating ability, forming complex salts with numerous metal compounds. Furthermore, it can bind to metals in different coordinative fashions and states of protonation, which gives rise to a wide diversity of structures, i.e. porous three-dimensional frameworks, layered networks and linear polymers. Both, dense and open-structured lattices have been reported (Cabeza et al., 2002; Clearfield & Demadis, 2012). Under certain specific conditions, quite predictable structure results and, for this reason, this ligand has been largely used in the preparation of crystalline metal phosphonates (Martínez & Farrell, 2017). Moreover, it is commercial available or can be obtained by a Mannich type reaction (Moedritzer & Irani, 1966) of an amine or a suitable ammonium salt, formaldehyde and phosphorous acid, according to the following equation:



Due to its chelating capability and stability, H_6NMP has been widely employed as a chelating agent to prevent scale formation in water systems and to depress metal ions activity (Clearfield & Demadis, 2012). For instance, Tantayakom et al. (2009) studied the effects of the solution pH and the concentration of Mg ions in precipitating Ca- H_6NMP . To investigate its role as a corrosion inhibitor, the thermal stability of several complexes of H_6NMP with copper and zinc ions was monitored (Chausov et al., 2014). This study revealed that all complexes exhibited, in general, high thermal stability, a prerequisite for anticorrosion agents. H_6NMP has been also used to inhibit cathodic reactions on steels. Nakayama (2000) reported the H_6NMP potential to inhibit these reactions on steels in a simulated, $Ca(OH)_2$ -saturated concrete pore solution. Rajendram et al. (1998) studied the system H_6NMP , MoO_4^{2-} and Zn^{2+} as inhibitor of mild steel corrosion in a neutral, aqueous Cl-containing environment, reporting an efficiency of 96%.

By employing H_6NMP , mixed coordination compounds, $[Cu_xNi_{1-x}\{N(CH_2PO_3)_3\}_3]Na_x \cdot nH_2O$ ($x= 0-1$) have been reported (Chausov et al., 2019). Triclinic and monoclinic phases were found depending on the relative occupation of the ions in the structure. The study of H_6NMP -bearing metal transition complexes has been extended for a variety of metal ions, such as chromium, nickel, copper, yttrium and lanthanides (Somov & Chausov, 2015; Somov et al., 2015, 2016, 2019a, b).

The structural variability in hydrothermally synthesised manganese derivatives was studied by Cabeza et al. (2002). In $\text{Mn}[\text{HN}(\text{CH}_2\text{PO}_3\text{H})_3]$, the metal ion is penta-coordinated by phosphonate oxygen atoms, forming a distorted square pyramid, whereas for compound $\text{Mn}[\text{HN}(\text{CH}_2\text{PO}_3\text{H})_3(\text{H}_2\text{O})_3]$, manganese ions are hexa-coordinated by three phosphonate oxygen atoms from two ligands and three water molecules. The manganese atoms are bridged by phosphonates groups forming zigzag chains. Adjacent chains are bonded to each other by hydrogen bonds, giving a corrugated sheet-like structure (Figure 6.1). This structure was found to be quite common, as the Mn(II) derivative is just a member of the isostructural series that includes Co(II), Ni(II), Cu(II) and Cd(II) derivatives, as well as various mixed-metal compounds (Sharma et al., 2001). This observation led to suggest that, irrespective of the metal ion, the H-bond network created is the driving force in determining the final structure of these compounds. On the other hand, $\text{Mn}[\text{HN}(\text{CH}_2\text{PO}_3\text{H})_3(\text{H}_2\text{O})_3]$ was also prepared by mechanochemical synthesis (Akhmetova et al., 2018) (Figure 6.1). The formation of this compound was followed by in situ synchrotron X-ray diffraction, showing a three steps crystallization process, through a non-crystalline intermediate phase. The calcined sample was further investigated as catalyst for the oxygen evolution reaction (OER).

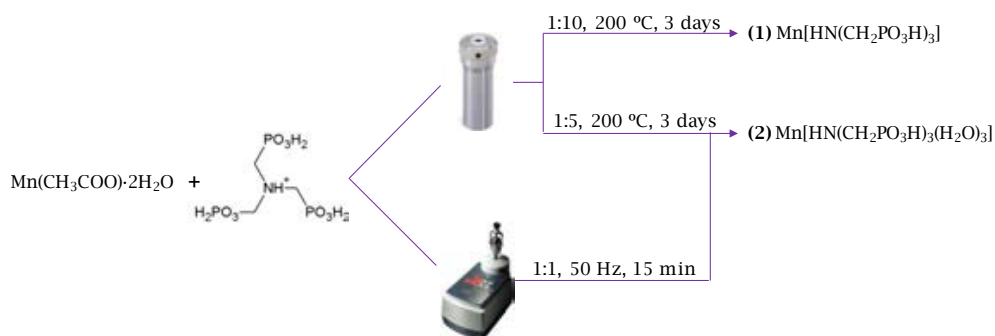


Figure 6.1. Synthesis scheme for Mn compounds (Cabeza et al., 2002; Akhmetova et al., 2018).

Platinum complexes, $[\text{cis-Pt}(\text{NH}_3)_2(\text{NMP})]$ and $[\text{Pt}(\text{R,S-dach})(\text{NMP})]$, have been studied by Bloemink et al. (1994) for their possible applications as antitumor agents.

Our research group previously reported the synthesis, structural characterisation, proton conductivity and luminescent properties of layered chloride-containing lanthanide derivatives (Bazaga-García et al., 2016). This isostructural family of compounds, $\text{Ln}[\text{HN}(\text{CH}_2\text{PO}_3\text{H})_3(\text{H}_2\text{O})_2]\text{Cl} \cdot 2\text{H}_2\text{O}$ ($\text{Ln}^{3+} = \text{La, Pr, Sm, Eu, Gd, Tb}$,

Dy, Ho), was isolated at room temperature in an HCl acidic solution. A 1D, chloride-free Ce^{3+} derivative, formulated as $\text{Ce}_2\{\text{[HN(CH}_2\text{PO}_3\text{H)(CH}_2\text{PO}_3\text{)]}_2(\text{H}_2\text{O)}_4\}\cdot 4.5\text{H}_2\text{O}$, and isostructural with a known lanthanum compound (Mendes et al., 2015), was also isolated at room temperature (Figure 6.2) In these 1D compounds, the metal ion is nona-coordinated by seven phosphonate oxygen atoms and two water molecules. Zig-zag chains along the a -axis are formed by edge-sharing LnO_9 polyhedra. These compounds showed an excellent structural resilience under extreme acidic and moderate basic conditions, as well as in boiling water, for long period of time. Lanthanum derivative also exhibited remarkable catalytic activity in the alcoholysis of styrene oxide with methanol or ethanol and in the acetalization of benzaldehyde with methanol. In the case of 2D compounds, the metal ion is octa-coordinated by six oxygen atoms from three different ligands and two oxygen atoms from water molecules. The positively charged layers are held together by interlayer chloride ions, forming extended hydrogen bond networks. Under the impedance measurement conditions used, i.e. increasing the temperature up to 80 °C and high relative humidity, the 2D materials transform into other chloride-free phases, including the 1D phase, among whose derivatives, the lanthanum compound showed the highest proton conductivity value ($\sigma \sim 2 \cdot 10^{-3} \text{ S}\cdot\text{cm}^{-1}$ at 80 °C and 95% RH). $\text{Gd[HN(CH}_2\text{PO}_3\text{H)}_3(\text{H}_2\text{O)}_2\text{]Cl}\cdot 2\text{H}_2\text{O}$ was found to remain stable under the working conditions, although it exhibited a proton conductivity lower than those of the chloride-free compounds ($\sigma \sim 3 \cdot 10^{-4} \text{ S}\cdot\text{cm}^{-1}$ at 80 °C and 95% RH). A study of the luminescent properties, due to f–f transitions of the lanthanide ions, were also carried out.

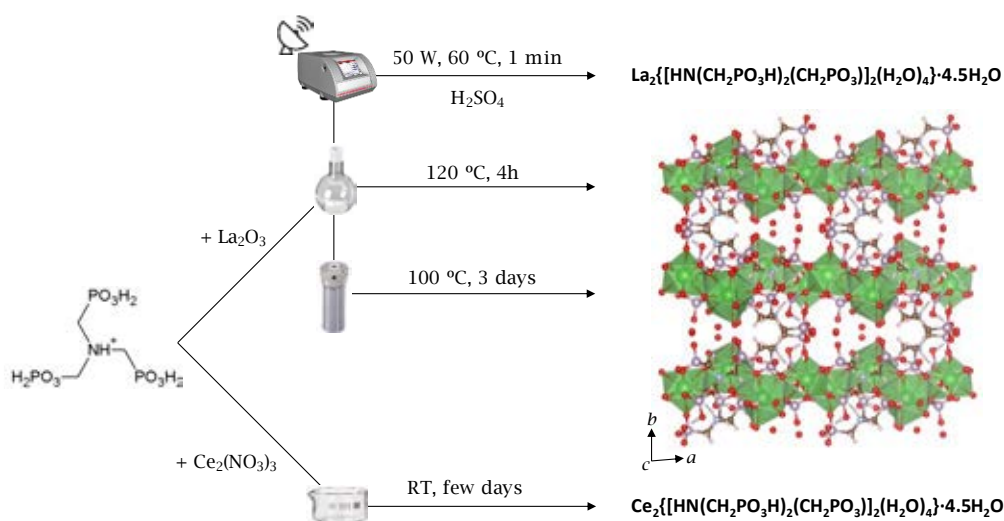


Figure 6.2. Scheme of the synthesis procedures of isostructural 1D lanthanide derivatives (Mendes et al., 2015; Bazaga-García et al., 2016).

The research group of Almeida also reported the synthesis and characterisation of other lanthanide derivatives. On the one hand, a family of isostructural, two-dimensional compounds were synthesised by hydrothermal conditions (Cunha-Silva, 2007), $\text{Ln}(\text{H}_3\text{NMP})\cdot 1.5\text{H}_2\text{O}$ ($\text{Ln}^{3+} = \text{La}, \text{Pr}, \text{Nd}, \text{Sm}$ and Eu). In this structure, the metal ion is octa-coordinated by phosphonate oxygen atoms from four different ligands. Water molecules are placed in the interlayer region instead of entering into the coordination sphere of the metal ion, which is an uncommon structural feature in this type of compounds. Removal of water led to a new phase with shrinkage of the interlayer space. This process is reversible and could be monitored by photoluminescence spectroscopy. However, photoluminescence properties were not modified by the presence of water in the interlayer region. On the other hand, the layered $\text{La}[\text{HN}(\text{CH}_2\text{PO}_3\text{H})_2(\text{CH}_2\text{PO}_3\text{H})_2]$ compound, $\text{La}(\text{H}_3\text{NMP})$, was synthesised by microwave as well as dynamic hydrothermal conditions (i.e., with constant rotation of the autoclaves) (Silva et al., 2011). All attempt to prepare other lanthanide compounds with this composition led to a mixture of phases, in which the predominant phase was that of $\text{La}(\text{H}_3\text{NMP})\cdot 1.5\text{H}_2\text{O}$ in most of the cases. However, incorporating small quantities of the optically active Eu^{3+} and Tb^{3+} ions led to $\text{La}_{0.95}\text{Eu}_{0.05}(\text{H}_3\text{NMP})$ and $\text{La}_{0.95}\text{Tb}_{0.05}(\text{H}_3\text{NMP})$ photoluminescent materials. Regarding to the thermal behaviour, an irreversible structural transformation of $[\text{La}(\text{H}_3\text{NMP})]$ into a dense novel 3D or a

layered 2D material was observed by heating the sample between 300 and 400 °C, which was attributed to a polymerization reaction. Furthermore, this solid was shown to catalyse ring opening of styrene oxide with methanol or ethanol, producing 2-methoxy-2-phenylethanol or 2-ethoxy-2-phenylethanol, respectively. In addition, Silva et al. (2020) have recently reported the synthesis of new layered lanthanide derivatives, with general formula $[\text{Ln}_2(\text{H}_3\text{NMP})_2] \cdot x\text{H}_2\text{O}$ ($\text{Ln}^{3+} = \text{Sm}, \text{Eu}, \text{Tb}, \text{Dy}, \text{Ho}, \text{Er}$ and Yb ; $x=1-4$), through three different methodologies: hydrothermal reaction, microwave-assisted synthesis and one-pot synthesis. The same composition could be also obtained by single-crystal to single-crystal transformation from compound $[\text{Gd}(\text{H}_4\text{NMP})(\text{H}_2\text{O})_2]\text{Cl} \cdot 2\text{H}_2\text{O}$ (Bazaga-García et al., 2016). In a further study, Mendes & Paz (2017) synthesised $[\text{La}_2(\text{H}_4\text{NMP})_2(\text{H}_2\text{O})_3(\text{SO}_4)] \cdot 8\text{H}_2\text{O}$ (**1**) by a microwave methodology. The synthesis was carried out under acidic conditions (sulfuric acid) with the aim to slow down the deprotonation of the ligand and to obtain more porous materials by blocking coordination sites, normally occupied by phosphonic groups. The two dimensional solid (**1**) experiences spontaneous single-crystal to single-crystal transformations, originating the compounds $[\text{La}_2(\text{H}_4\text{NMP})_2(\text{H}_2\text{O})_3(\text{SO}_4)] \cdot 6\text{H}_2\text{O}$ (**2**), $[\text{La}_2(\text{H}_4\text{NMP})_2(\text{H}_2\text{O})_3(\text{SO}_4)] \cdot 2\text{H}_2\text{O}$ (**3**) and $[\text{La}_2(\text{H}_4\text{NMP})_2(\text{H}_2\text{O})_2(\text{SO}_4)] \cdot \text{H}_2\text{O}$ (**4**) by water removal. In addition, compound (**1**) could be regenerated by dipping compound (**4**) in water for 24h. Apart from water content, all of them are structurally similar showing quite similar *a* and *c* cell parameters.

In this chapter, two families of sulfate-containing lanthanide derivatives of the triphosphonic ligand **aminotris(methylenephosphonic acid)**, H_6NMP , are studied. Here we report the synthesis, characterisation and proton conductivity of these compounds, as well as the luminescence properties of bimetallic lanthanide derivatives. In addition, Nafion-based composite membranes, using the lanthanide derivatives as fillers, were prepared to test their performance as components of proton exchange membrane fuel cells (PEMFCs), under operating conditions.

6.1. Synthesis

Two polymorph series have been synthesised by controlled crystallization at 25 °C, giving rise to single crystals. These two families were isolated depending on the $\text{Ln}^{3+}:\text{H}_6\text{NMP}:\text{H}_2\text{SO}_4:\text{H}_2\text{O}$ molar ratios: from 1:5:19.3:3715 up to 1:5:135:3715 for Series **Ln-I** and higher additions of H_2SO_4 (95%) up to 1:5:193:3715 for compounds of Series **Ln-II**. Furthermore, bimetallic solid solutions and anhydrous phase of compounds of Series **Ln-I** were obtained.

6.1.1. Series Ln-I

For the synthesis of compounds of the Series **Ln-I**, $\{\text{Ln}_2[\text{HN}(\text{CH}_2)_3(\text{PO}_3\text{H})_3]_2(\text{H}_2\text{O})_4\}(\text{HSO}_4)_2 \cdot n\text{H}_2\text{O}$ (Ln= Pr, Nd, Sm, Eu, Gd, Tb, Er, Yb; n= 4 - 5), a quantity of lanthanide salt (0.46 mmol) was dissolved in 10 mL of DI water with a volume of H_2SO_4 (95%) ranged between 0.5 and 2.5 (Eu^{3+}) - 3.5 (Pr^{3+}) mL. Separately, 2.30 mmol of H_6NMP (1.5 mL) was added to 20 mL of DI water. Finally, both solutions were mixed. After crystallization at 25 °C in an incubator, crystals or a polycrystalline samples were isolated by filtration, washed with DI water along with ethanol and air-dried. The same synthetic method was used for the bimetallic solid solutions $\{\text{Ln}(1)_{1.6}\text{Ln}(2)_{0.4}[\text{HN}(\text{CH}_2)_3(\text{PO}_3\text{H})_3]_2(\text{H}_2\text{O})_4\}(\text{HSO}_4)_2 \cdot 4\text{H}_2\text{O}$ [Ln(1 and 2) = Eu and Tb], but using a Ln(1):Ln(2) molar ratio of 4:1 for the mixed lanthanide solution and maintaining the same overall lanthanide:ligand molar ratio. Furthermore, a new anhydrous crystalline phase $\{\text{Ln}_2[\text{HN}(\text{CH}_2)_3(\text{PO}_3\text{H})_3]_2\}(\text{HSO}_4)_2$, **Ln-I-230C**, was obtained by heating the as-synthesised sample at 230 °C for 2h. On the other hand, another polymorph, $\{\text{Pr}_2[\text{HN}(\text{CH}_2)_3(\text{PO}_3\text{H})_3]_2(\text{H}_2\text{O})_4\}(\text{HSO}_4)_2 \cdot 4\text{H}_2\text{O}$ (**Pr-I***), was synthesised modifying slightly the $\text{Pr}^{3+}:\text{H}_6\text{NMP}:\text{H}_2\text{SO}_4:\text{H}_2\text{O}$ molar ratio (1:5:95:3000) and following similar synthetic conditions to those reported by Mendes & Paz (2017) albeit without any microwave treatment. A mixture composed of 0.25 mmol of $\text{Pr}(\text{NO}_3)_3 \cdot 6\text{H}_2\text{O}$, 0.217 mL of H_6NMP (0.47 mmol) and 5 mL of DI water was placed into a glass test tube. Finally, 0.5 mL of H_2SO_4 (95%) were added to the solution mixture. After crystallization at RT for several days, crystals were isolated as above described.

6.1.2. Series Ln-II

Synthesis of compounds of Series **Ln-II**, $\text{Ln}[\text{HN}(\text{CH}_2)_3(\text{PO}_3\text{H}_2)(\text{PO}_3\text{H})_2]\text{SO}_4 \cdot 2\text{H}_2\text{O}$ (Ln= Pr, Nd, Eu, Gd, Tb), required H_2SO_4 additions higher than those employed for compounds of Series **Ln-I**. The same quantity of lanthanide salt (0.46 mmol) was dissolved in 10 mL of DI water and between 2.5 (Eu^{3+}) - 3.5 (Pr^{3+}) and 5 mL of H_2SO_4 (95%). This solution was mixed with the H_6NMP solution (2.30 mmol of H_6NMP in 20 mL of DI water). After crystallization at 25 °C in an incubator, solids were isolated as above described. A schematic representation of both synthetic procedure is displayed in Figure 6.3.

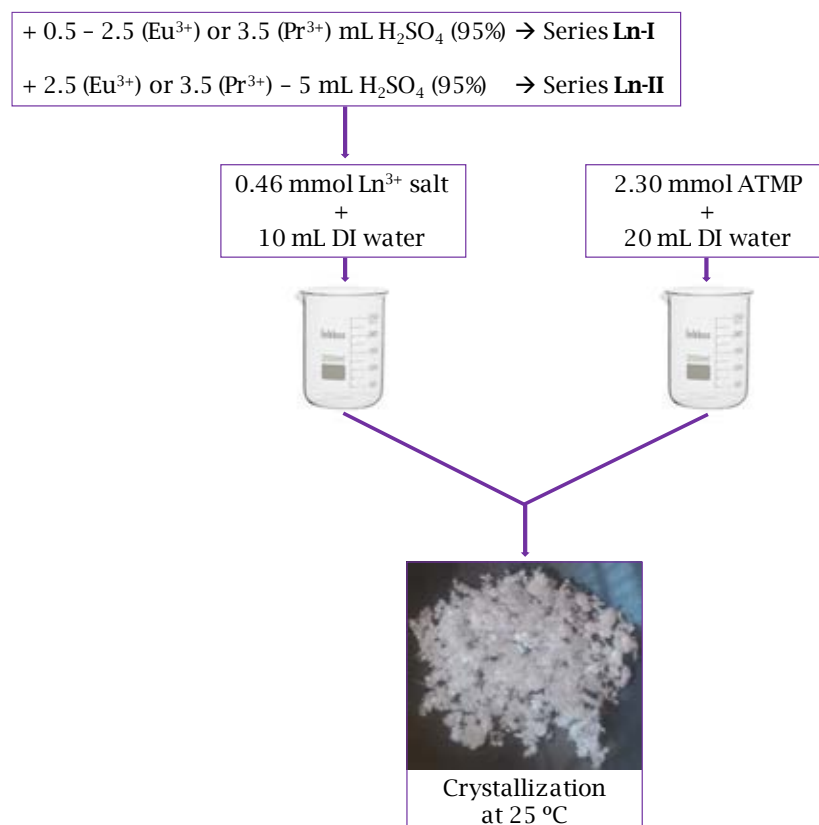


Figure 6.3. Scheme of the synthesis procedure for compounds of Series **Ln-I** and **Ln-II**.

6.2. Characterisation

All compounds were extensively characterised using different techniques.

6.2.1. Elemental and Inductively Coupled Plasma Analysis

Elemental analysis for all as-synthesised compounds are given in Appendix II (Table AII.4).

The Ln(1)/Ln(2) molar ratio of bimetallic solid solutions samples was determined by inductively coupled plasma mass spectrometry analysis (ICP-MS). Table 6.1 shows the chemical composition obtained for the bimetallic solutions.

Table 6.1. Chemical composition for bimetallic solid solutions samples of Series **Ln-I**.

Nominal Ln(1):Ln(2) molar ratio	Acronym	Chemical composition
4:1	Eu _{1.6} Tb _{0.4} -I	{Eu _{1.6} Tb _{0.4} [HN(CH ₂) ₃ (PO ₃ H) ₃] ₂ (H ₂ O) ₄ }(HSO ₄) ₂ ·4H ₂ O
4:1	Tb _{1.6} Eu _{0.4} -I	{Tb _{1.6} Eu _{0.4} [HN(CH ₂) ₃ (PO ₃ H) ₃] ₂ (H ₂ O) ₄ }(HSO ₄) ₂ ·4H ₂ O

6.2.2. Structural Characterisation and Thermal/Chemical Stability

Crystal structures of Pr-I*, Nd, Sm and Tb derivatives from Series **Ln-I** were solved from SCXRD data (Chapter 3, Section 3.4.5).

Synchrotron X-ray powder diffraction data (SXRPD) or laboratory X-ray powder diffraction data (LXRPD) were collected for the remaining compounds of Series **Ln-I** (Ln= Eu, Gd, Er and Yb). Rietveld refinement (Rietveld, 1969) was employed to optimized them, using the crystal structure of **Tb-I**, {Tb₂[HN(CH₂)₃(PO₃H)₃]₂(H₂O)₄}(HSO₄)₂·4H₂O, as a starting model. The refinement was carry out by using the GSAS package (Larson & von Dreele, 2004) with soft constraints to maintain the chemically reasonable geometries for the phosphonate, amine, hydrogensulfate and alkyl groups (Chapter 3, Table 3.2). A summary of selected crystallographic data are given in Table 6.2 and the Rietveld plots for these solids are displayed in Figure AIII.6 (Appendix III). SXRPD data were collected at the beamline BL04-MSPD from ALBA synchrotron (Barcelona, Spain) employing a wavelength of 0.4124(1) Å and equipped with a MYTHEM detector. The capillary was rotated during data collection to improve diffracting particle statistics and patterns were collected over the angular range 0.33–44.5° (2θ). LXRPD data for other compounds of both Series were collected on a θ/θ D8 ADVANCE (Bruker AXS) diffractometer equipped with a Johansson Ge (111) primary monochromator, which allows to use monochromatic Mo radiation, λ = 0.7093 Å.

Crystal structure of **Tb-II** was solved by direct methods using the program EXPO2014 (Altomare et al., 2013). Partial structure model was obtained and the missing atoms were localized by difference of Fourier maps. All crystal structures were optimized by the Rietveld method as described in Chapter 3, Table 3.2. Rietveld plot for Tb-II is displayed in Figure 6.4 and Figure AIII.7 for the other components of this series. Table 6.3 gives some crystallographic data.

Table 6.2. Selected crystallographic data for Ln-I materials.

Phase	Pr-I [#]	Pr-I*	Nd-I	Sm-I	Eu-I
Space Group	P 2 ₁ /c	P 2 ₁ /c	P 2 ₁ /c	P 2 ₁ /c	P 2 ₁ /c
Chemical formula	C ₆ H ₃₈ N ₂ O ₃₄ P ₆ S ₂ Pr ₂	C ₆ H ₃₈ N ₂ O ₃₄ P ₆ S ₂ Pr ₂	C ₆ H ₃₈ N ₂ O ₃₄ P ₆ S ₂ Nd ₂	C ₆ H ₃₈ N ₂ O ₃₄ P ₆ S ₂ Sm ₂	C ₆ H ₃₈ N ₂ O ₃₄ P ₆ S ₂ Eu ₂
Formula mass (g·mol ⁻¹)	1228.13	1228.13	608.39	596.33	1236.26
λ (Å)	1.5418	0.71073	0.71075	0.71073	0.7093
a (Å)	8.5327(2)	8.6510(4)	8.5197(2)	8.6060(3)	8.4993(1)
b (Å)	18.8189(5)	19.5394(9)	19.1826(4)	19.5335(7)	19.4416(3)
c (Å)	10.7340(3)	10.7660(5)	10.7060(3)	10.6850(4)	10.6096(1)
β (°)	109.172(2)	109.922(2)	109.264(3)	109.853(4)	109.5397(9)
V (Å ³)	1628.03(8)	1710.93(14)	1651.71(8)	1689.45(11)	1652.18(5)
Z	2	2	2	2	2
Temperature (K)	298	100	293(2)	293(2)	298
Range data (°)	4.00-69.98	2.27-27.54	2.12-27.46	3.27-29.33	3.70-50.00
Independent reflections		3607	3599	3637	2930
Data / restraints / parameters		3943/51/314	3781/1/170	4360/0/222	4676/48/133
R _{wp}		-	-	-	0.0821
R _p		-	-	-	0.0631
R _F		-	-	-	0.0300
R factor [I > 2σ(I)]		R ¹ = 0.0341; wR ² = 0.0956			-
R factor (all data)		R ¹ = 0.0379; wR ² = 0.1610			-
GoF		1.079	1.108	1.138	-
CCDC number		2003911	2003913	2003912	1980603

^aR₁(F) = Σ||F_o - |F_c||/Σ|F_o|; ^bwR₂(F²) = [Σw(F_o² - F_c²)²/ΣF_o⁴]^{1/2}; *Le Bail fit data.

Table 6.2. Selected crystallographic data for Ln-I materials (Continuation).

Phase	Gd-I	Tb-I	Er-I	Yb-I
Space Group	P 2 ₁ /c	P 2 ₁ /c	P 2 ₁ /c	P 2 ₁ /c
Chemical formula	C ₆ H ₃₈ N ₂ O ₃ P ₆ S ₂ Gd ₂	C ₆ H ₃₈ N ₂ O ₃ P ₆ S ₂ Tb ₂	C ₆ H ₄₀ N ₂ O ₃ P ₆ Er ₂ S ₂	C ₆ H ₄₀ N ₂ O ₃ P ₆ Yb ₂ S ₂
Formula mass (g·mol⁻¹)	1246.83	1250.18	1284.87	1296.43
λ (Å)	0.4124	0.71073	0.7093	0.7093
a (Å)	8.5086(1)	8.4314(2)	8.4562(2)	8.4291(3)
b (Å)	19.4894(4)	19.2357(5)	21.3849(9)	21.4041(12)
c (Å)	10.6123(1)	10.5627(3)	10.3316(2)	10.2876(3)
β (°)	109.5674(7)	109.373(3)	109.7112(15)	109.7420(19)
V (Å³)	1658.19(6)	1616.10(8)	1758.85(12)	1746.97(15)
Z	2	2	2	2
Temperature (K)	298	150.0(2)	298	298
Range data (°)	2.00-20.00	2.71-30.62	4.03-42.01	4.30-42.00
Independent reflections	1032	3244	1907	1888
Data / restraints / parameters	3000/49/111	3715/0/237	3834/65/126	3834/66/129
R_{wp}	0.0720	-	0.1326	0.1209
R_p	0.0561	-	0.1000	0.0905
R_f	0.0198	-	0.0587	0.0450
R factor [I > 2σ(I)]		R1 ^a = 0.0302; wR2 ^a = 0.0572	-	-
R factor (all data)		R1 ^a = 0.0386; wR2 ^a = 0.0597	-	-
GoF	-	1.035	-	-
CCDC number	1980602	1980608	1980605	1980606
^aR1(F) = Σ Fo - Fc /Σ Fo ; ^bwR2(F²) = [Σw(F_o² - F_c²)/ΣF²]^{1/2}.				

Table 6.3. Selected crystallographic data for Ln-II materials.

Phase	Pr-II	Nd-II [#]	Eu-II [#]	Gd-II	Tb-II
Space Group	P-1	P-1	P-1	P-1	P-1
Chemical formula	C ₃ H ₁₅ NO ₁₅ P ₃ PrS	C ₃ H ₁₅ NO ₁₅ P ₃ Nds	C ₃ H ₁₅ NO ₁₅ P ₃ EuS	C ₃ H ₁₅ NO ₁₅ P ₃ GdS	C ₃ H ₁₅ NO ₁₅ P ₃ TbS
Formula mass (g·mol ⁻¹)	571.04	574.38	582.10	587.39	589.06
λ (Å)	1.5406	1.5418	1.5418	0.7093	0.7093
a (Å)	10.1779(4)	10.1853(5)	10.1156(3)	10.1038(5)	10.0792(5)
b (Å)	9.6687(5)	9.6698(5)	9.6128(2)	9.6041(4)	9.5779(4)
c (Å)	9.5553(4)	9.5686(5)	9.4575(2)	9.4144(4)	9.3920(4)
α (°)	110.7290(35)	110.565(4)	110.760(2)	110.6369(26)	110.696(3)
β (°)	111.7803(30)	111.900(3)	111.555(2)	111.6729(24)	111.583(3)
γ (°)	101.453(4)	101.472(4)	101.470(2)	101.5449(33)	101.511(4)
V (Å ³)	755.45(5)	757.35(6)	740.34(3)	734.96(5)	729.91(6)
Z	2	2	2	2	2
Temperature (K)	298	298	298	298	298
Range data (°)	9.56-89.98	4.00-69.98	8.00-69.98	3.50-65.00	4.18-48.00
M(20)	14	14	14.4		
F(20)	29	29	26.4		
Independent reflections	1223			5353	2297
Data / restraints / parameters	4787/57/119			6195/46/119	4430/50/121
R _{wp}	0.1184			0.1213	0.1109
R _p	0.0830			0.0897	0.0835
R _i	0.0683			0.0291	0.0393
CCDC number	2003908			2003909	1980607

[#]Le Bail fit data.

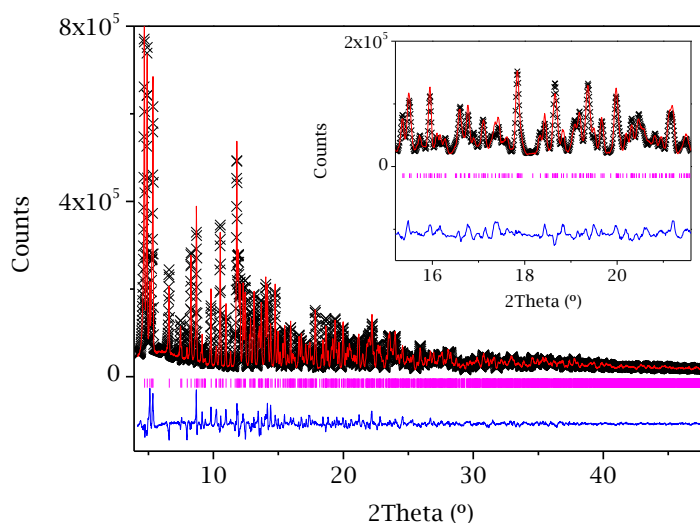


Figure 6.4. Final Rietveld plot for Tb-II.

Crystal structure for **Tb-I-SD** and **Tb-I-230C** was obtained by Rietveld refinement using as starting model the crystal structure of $[\text{La}_2(\text{H}_4\text{NMP})_2(\text{H}_2\text{O})_3(\text{SO}_4)] \cdot 2\text{H}_2\text{O}$ (CCDC no. 1496873, Mendes et al., 2017) and **Tb-I**, respectively (Table 6.4). The Rietveld plots are given in Figure AIII.8 (Appendix III).

Table 6.4. Selected crystallographic data for sulfate-deficient and anhydrous derivatives of Series Ln-I (Ln= Eu, Tb).

Phase	Eu-I-230C	Tb-I-230C	SD-Tb-I
Space Group	P 2 ₁ /c	P 2 ₁ /c	P 2 ₁ /c
Chemical formula	C ₆ H ₂₂ N ₂ O ₂₆ P ₆ Eu ₂ S ₂	C ₆ H ₂₂ N ₂ O ₂₆ P ₆ Tb ₂ S ₂	C ₆ H ₃₄ N ₂ O ₂₆ P ₆ Tb ₂ S ₂
Formula mass (g·mol⁻¹)	1092.14	1106.06	1134.09
λ (Å)	0.7093	0.7093	0.4132
a (Å)	8.887(1)	8.8138(3)	8.5720(2)
b (Å)	16.166(3)	16.0812(7)	16.2769(5)
c (Å)	10.480(1)	10.3891(3)	10.5651(2)
β (°)	109.95(1)	109.9755(19)	109.6499(11)
V (Å³)	1415.1(6)	1383.92(11)	1388.26(7)
Z	2	2	2
Temperature (K)	298	298	298
Range data (°)	2.99-19.97	4.20-47.98	2.00-42.49
Independent reflections	176	2183	7847
Data/restraints/ parameters	774/49/111	4428/51/122	6814/68/131
R_{wp}	0.1046	0.0921	0.0682
R_p	0.0798	0.0684	0.0479
R_f	0.0467	0.0250	0.0188
CCDC number	2003910	1980604	1980609

Isostructural layered compounds of Series **Ln-I**, with general formula $\{\text{Ln}_2[\text{HN}(\text{CH}_2)_3(\text{PO}_3\text{H})_3]_2(\text{H}_2\text{O})_4\}(\text{HSO}_4)_2 \cdot n\text{H}_2\text{O}$ ($\text{Ln} = \text{Pr, Nd, Sm, Eu, Gd, Tb, Er, Yb}$; $n = 4 - 5$), crystallize in the monoclinic crystal system ($P 2_1/c$). The lanthanide ion is octa-coordinated by two coordinated water molecules and four oxygen atoms from four different ligands. Each zwitterion $\text{H}_4\text{NMP}^{2-}$ ligand bonds four Ln^{3+} ions, two bidentately coordinated, forming 8-membered rings, and two other monodentately coordinated, resulting in isolated LnO_8 polyhedra. From the single crystal data, it is interfered that the sulfate species is a hydrogensulfate ion, as three S-O bond lengths are found between 1.466(3) and 1.451(3) Å, whereas the fourth one is much longer at 1.537(3) Å, in agreement with those reported for $\text{Tb}(\text{SO}_4)(\text{HSO}_4)$ (Netzsche et al., 2019). This layered crystal structure is equivalent to that found for $[\text{Ln}(\text{H}_4\text{NMP})(\text{H}_2\text{O})_2]\text{Cl} \cdot 2\text{H}_2\text{O}$ (Bazaga et al., 2016). The non-coordinated hydrosulphate ion, likewise the chloride ion in chloride-containing derivatives, acts as the counterion of positively charged layers and is placed in the interlayered region, together with the lattice water molecules (Ow3 and Ow4). In addition, the HSO_4^- groups interact by hydrogen bond through its four oxygen atoms with the coordinated water (Ow1 and Ow2), lattice water (Ow3 and Ow4), the protonated oxygen atoms from the phosphonate groups (O2, O5 and O8), as well as with the non-protonated phosphonate groups (O3, O6 and O9). These interactions create extended unidirectional H-bonds along the a -axis as displayed in Figure 6.5d (Table 6.5).

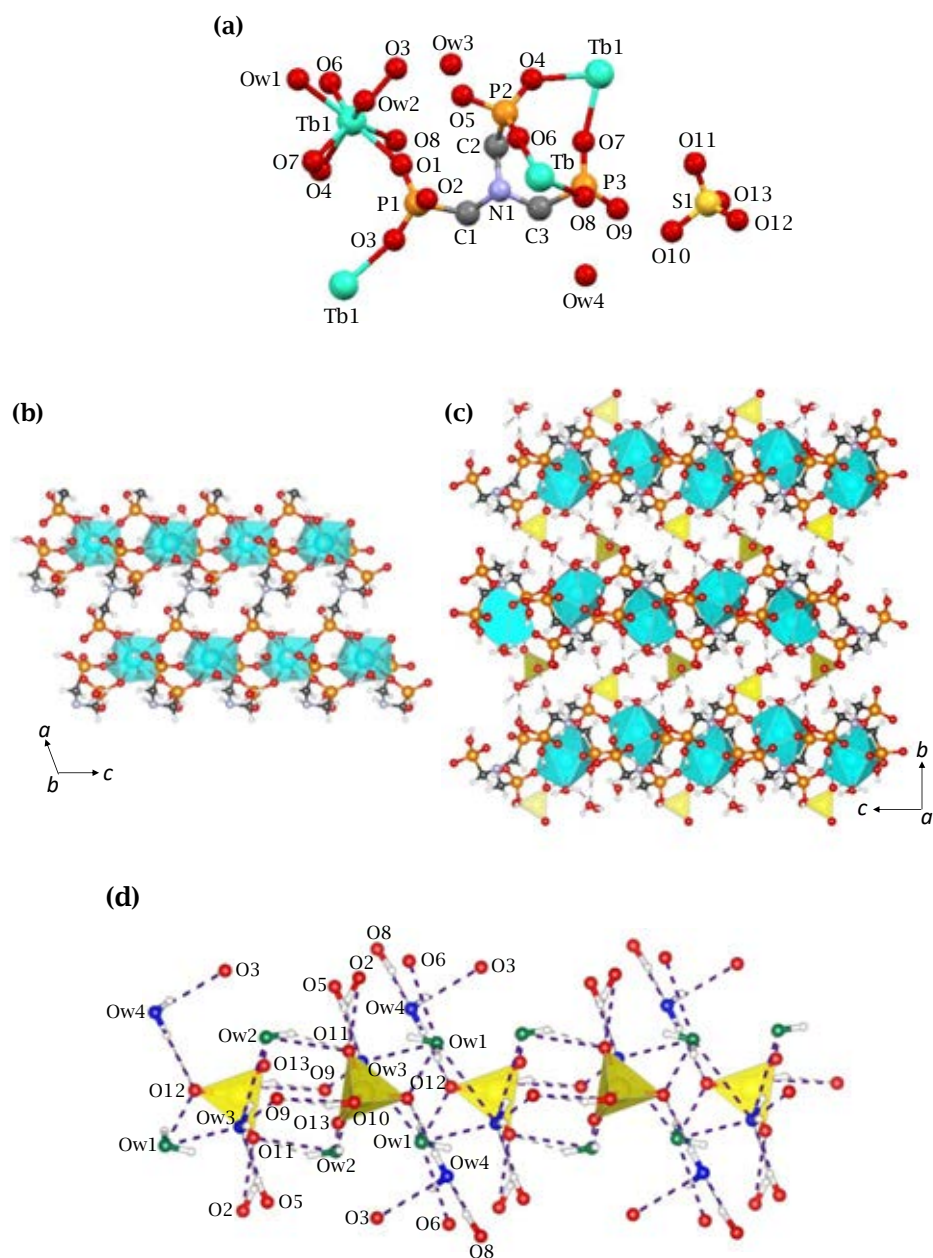


Figure 6.5. (a) Coordination environment of **Tb-I** compound (H atoms are not shown for clarity), (b) connectivity of the ligand in a single layer, (c) view of the 2D packing showing the hydrosulphate ions and water molecules in the interlayer region along *a* axis and (d) unidimensional H-bond networks along *a* axis between sulfate groups (yellow polyhedra), phosphonate oxygen atoms (red), coordinated (green) and lattice water molecules (blue).

Table 6.5. H-bond distances for **Tb-I**.

D-H...A	D-H (Å)	H...A (Å)	D...A (Å)	D-H...A (°)
O8-H8...Ow4	0.98	1.66	2.641(4)	173.3
Ow4-Hw4A...O12 ^{#1}	0.85	1.99	2.823(5)	167.1
Ow4-Hw4B...O3 ^{#2}	0.85	2.16	2.951(4)	154.4
Ow2-Hw2A...O11 ^{#3}	0.86	1.96	2.766(4)	154.7
Ow2-Hw2B...O13 ^{#4}	0.86	1.87	2.672(4)	153.8
O2-H2...O11 ^{#3}	0.82	1.80	2.560(4)	154.0
O5-H5...Ow3	0.82	1.88	2.691(5)	170.1
Ow3-Hw3A...O9 ^{#4}	0.85	2.11	2.901(4)	153.7
Ow3-Hw3B...Ow2 ^{#5}	0.85	2.24	3.005(5)	149.3
Ow1-Hw1A...O12 ^{#6}	0.86	2.20	2.982(4)	151.2
Ow1-Hw1B...Ow3 ^{#7}	0.86	2.14	2.812(4)	133.9
N1-H1...O4 ^{#8}	0.98	2.06	2.938(4)	148.7
O10-H10...O9	0.82	1.71	2.511(4)	166.2
C1-H1A...O13 ^{#9}	0.97	2.29	3.104(5)	140.5

Symmetry transformations used to generate equivalent atoms:

^{#1} -x+2,-y+1,-z+1; ^{#2} x+1,y,z; ^{#3} x-1,-y+1/2,z-1/2; ^{#4} -x+1,y-1/2,-z+3/2; ^{#5} -x,-y,-z+1; ^{#6} x-2,-y+1/2,z-1/2; ^{#7} x-1,y,z; ^{#8} x,-y+1/2,z-1/2; ^{#9} -x+1,-y+1,-z+1.

Crystal structure of **Pr-I***, solved by single crystal data, shows a structural deviation of Series **Ln-I**, exhibiting two sulfate groups with half occupancy. The only difference with compounds of Series **Ln-I** is that one of the two coordinated water molecules is now half-substituted by a monodentate HSO₄⁻ group in the isolated PrO₈ polyhedra. The remaining uncoordinated HSO₄⁻ group is placed in the interlayer region together with two lattice water molecules. The HSO₄⁻ groups interact with both coordinated and lattice water molecules (O10A and O11A) and the oxygen atoms from the phosphonate groups (O7), forming extended unidirectional H-bonds along the *a*-axis (Figure 6.6, Table 6.6).

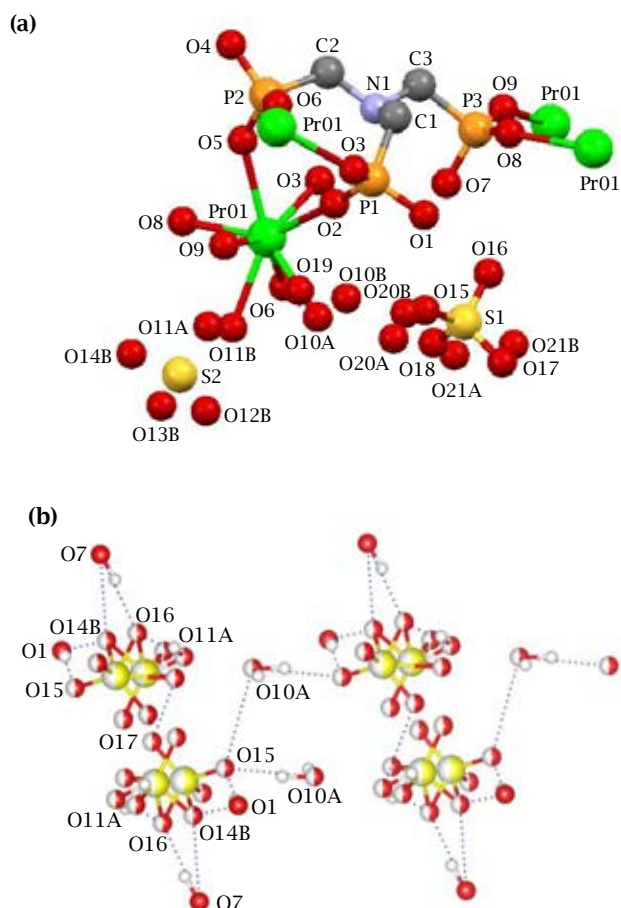


Figure 6.6. (a) Coordination environment of **Pr-I*** (H atoms are not shown for clarity) and (b) unidimensional H-bond networks along *a* axis.

Table 6.6. H-bond distances for **Pr-I***.

D-H...A	D-H (Å)	H...A (Å)	D...A (Å)	D-H...A (°)
O7-H7...O16	0.84	1.78	2.594(8)	161.7
O7-H7...O14B ^{#1}	0.84	1.78	2.498(15)	142.6
O4-H4...O20A ^{#2}	0.84	1.84	2.643(6)	158.7
O1-H1...S2 ^{#1}	0.84	2.59	3.114(6)	122.0
O1-H1...O15	0.84	1.93	2.744(8)	161.9
O1-H1...O14B ^{#1}	0.84	1.98	2.681(17)	139.9

Table 6.6. H-bond distances for Pr-I* (Continuation).

D-H...A	D-H (Å)	H...A (Å)	D...A (Å)	D-H...A (°)
N1-H1A...O3	1.00	2.07	2.938(5)	143.6
O3-H3B... O17 ^{#4}	0.99	2.41	3.092(9)	125.1
C1-H1C...O8	0.99	2.34	3.184(5)	143.1
O11A-H11A...O16 ^{#5}	0.98	1.91	2.855(14)	162.6
O11A-H11B...O17 ^{#6}	0.99	2.08	2.738(13)	122.7
O19-H19A...O5 ^{#7}	0.87	2.04	2.794(5)	144.3
O19-H19B...O9 ^{#8}	0.87	2.19	2.930(5)	142.7
O10A-H10A...O15	0.98	1.75	2.726(11)	171.6
O20A-H20A...O19	0.87	1.84	2.669(6)	157.5
O20B-H20D...O19	0.87	2.06	2.892(18)	158.6

Symmetry transformations used to generate equivalent atoms:

^{#1} x+1,y,z; ^{#2} -x+1,y-1/2,-z+1/2; ^{#3} x,-y+1/2,z+1/2; ^{#4} -x+2,y-1/2,-z+3/2; ^{#5} x-1,y,z; ^{#6} -x+1,-y+1,-z+1; ^{#7} x,-y+1/2,z-1/2; ^{#8} x-1,-y+1/2,z-1/2.

Those compounds of La, [La₂(H₄NMP)₂(H₂O)₃(SO₄)]·nH₂O (n= 2-8), reported by Mendes et al. (2017) can be envisioned as structural analogues of Series Ln-I because they present similar layered features (*a* and *c* parameters; Table 6.2), but with variable interlayer distances (*b* axis) in order to accommodate different contents and arrangements of lattice water molecules and sulfate groups (SO₄²⁻).

Chemical and thermal stability of compounds Ln-I was studied:

- (i) By heating the samples at 230 °C.
- (ii) At high relative humidity (95% RH) and different temperatures.

Thermogravimetric curves for some representative compounds are shown in Figure 6.7a. They were recorded from RT to 700 °C with a heating rate of 10 °C·min⁻¹ under air flow. As can be seen, dehydration takes place from 30 °C up to 280 °C, at which solid decomposition starts. As can be observed in Figure 6.7b and c., the progressively loss of water is accompanied with structural changes, forming a new anhydrous crystalline phase at 230 °C, which remains stable up to 250-270 °C, before ligand decomposition (i.e. for Tb-I, found 11.8 %, calc. 11.5 %). This fact was corroborated by powder X-ray thermodiffraction data collected from RT up to 250 °C, with a heating rate of 5 °C·min⁻¹. The heavier Ln³⁺ derivatives (Ln³⁺= Er and Yb),

with a slightly higher water content, follow a similar behaviour, except that the appearance of partially dehydrated intermediate phases starts at quite lower temperatures (60 °C for Er³⁺) before full dehydration (found 14.3 %, calc. 12.6 %). Therefore, a different weight loss profile is observed in the corresponding TG curves (Figure 6.7a.).

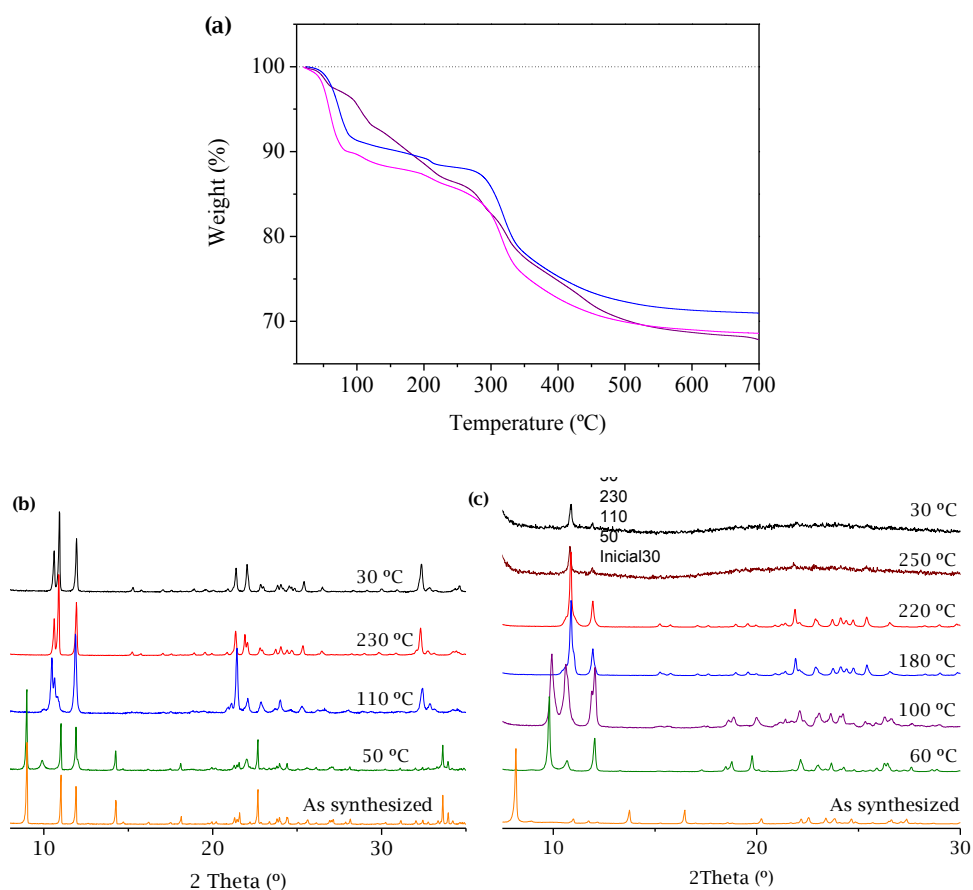


Figure 6.7. (a) Thermal analysis for compounds **Nd-I** (purple), **Tb-I** (blue) and **Er-I** (magenta) and thermodiffraction patterns for (b) **Tb-I** and (c) **Er-I**.

Dehydration of **Ln-I** at 230 °C, to form **Ln-I-230C**, involves changing the function of the hydrogensulfate ion to a more structural role, as a monodentate ligand of the Ln³⁺ ions, while the uncoordinated three other oxygen atoms are located in the interlayer region allowing H-bond interaction with the adjacent layer (Figure 6.8c). This structure is characterised by presenting cell parameters similar to those of the

precursor phase and show the same phosphonate/ Ln^{3+} connectivity within the layer, except that the metal ion is now hepta-coordinated, because of the substitution of two initially coordinated water molecules by the hydrogensulfate ligand (Figure 6.8a). The H-bond interaction of this group with the phosphonate groups of the adjacent layer is established through the oxygen atoms (O1, O3 and O6) of the latter one (Figure 6.8b; Table 6.7).

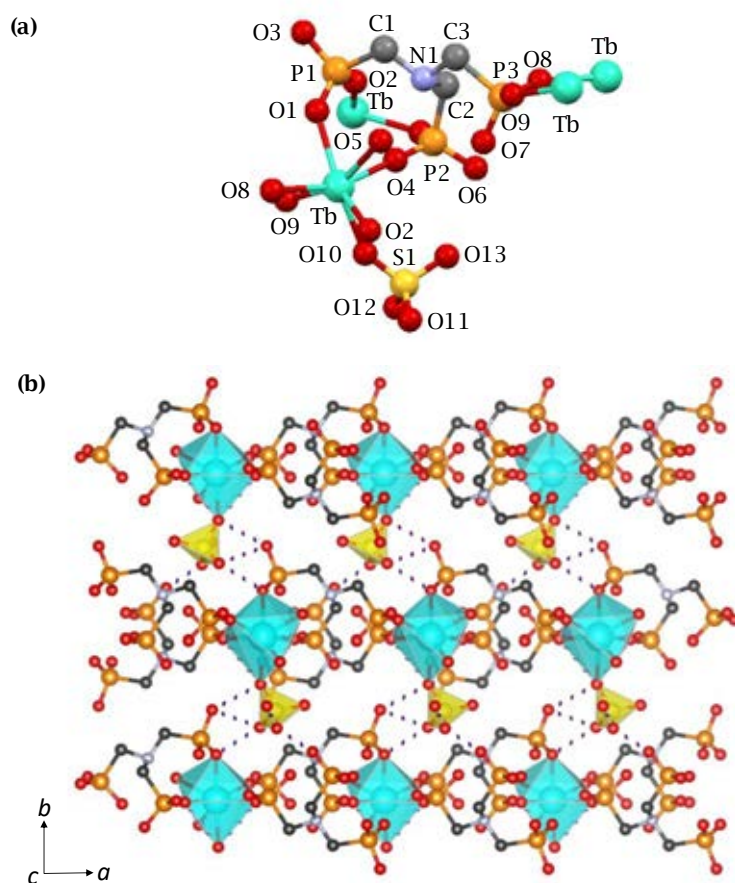


Figure 6.8. (a) Coordination environment of **Tb-I-230C**, (b) view of the 2D adjacent layers with H-bond interactions marked (purple dot lines) and (c) structural transformation of **Tb-I** into **Tb-I-230C**.

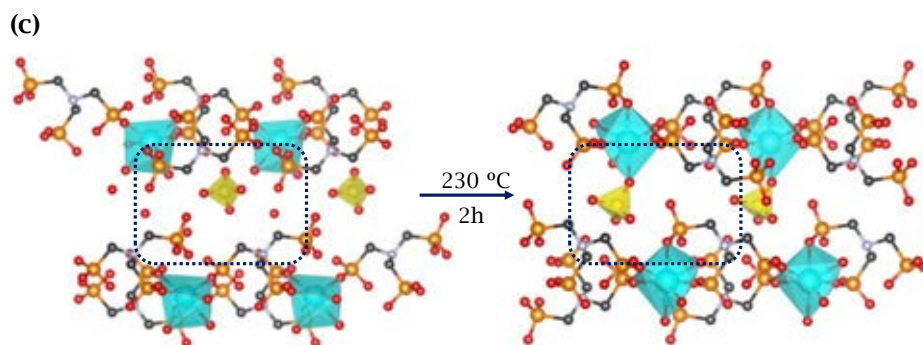


Figure 6.8. (a) Coordination environment of **Tb-I-230C**, (b) view of the 2D adjacent layers with H-bond interactions marked (purple dot lines) and (c) structural transformation of **Tb-I** into **Tb-I-230C** (Continuation).

Table 6.7. H-bond distances for **Tb-I-230C**.

D-H...A	D...A (Å)	D-H...A	D...A (Å)
O1...O12	2.565(29)	O6...O7	2.904(25)
O3...O6	3.195(23)	O6...O11	3.083(20)
O3...O10	2.758(27)	O6...O13	2.873(26)
O3...O11	2.894(28)	O7...O11	2.413(27)
O3...O12	3.053(26)	O9...O10	2.957(24)

Significantly, these changes in lanthanide coordination stabilises the layer structure, thermally and under high humidity conditions, as can be seen in Figure 6.9. Moreover, elemental analysis results showed that this phase is compositionally stable (Appendix II, Table AII.5).

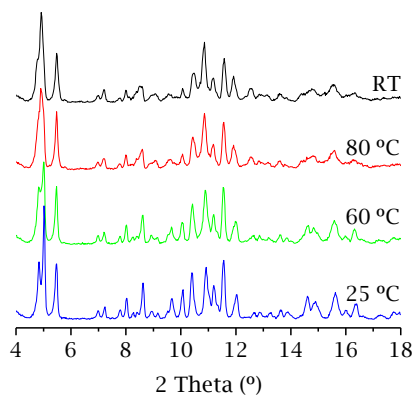


Figure 6.9. Thermodiffraction patterns for **Eu-I-230C** at different temperatures and 95% RH.

On the other hand, at high relative humidity (95% RH) compounds **Ln-I** experience significant and irreversible structural changes upon increasing the temperature, from 25 to 80 °C. Thermodiffraction patterns for **Tb-I** at 95% RH is shown in Figure 6.10 as an example. These structural changes are accompanied by a change in composition, resulting in solids having a sulfate/Ln³⁺ molar ratio reduced to half, $\{\text{Ln}_2[\text{HN}(\text{CH}_2)_3(\text{PO}_3\text{H})_2(\text{H}_2\text{O})_3](\text{SO}_4)_n\cdot n\text{H}_2\text{O}$ (Ln= Pr, Nd, Eu, Gd and Tb; n= 4 - 5), hereinafter referred to as **SD-Ln-I** (SD stands for sulfate-deficient). This change in composition is attributed to a partial dissolution of compounds **Ln-I** under these conditions, with loss of sulfate, accompanied by partial leaching of Ln³⁺ and phosphonate ligand. According to elemental analysis and XRPD patterns (Figure 6.11), **SD-Ln-I** match well with the reported La³⁺ derivative (Mendes et al., 2017). However, for the Yb derivative, sulfate was completely lost, following a quite similar behaviour to that observed for the isorecticular compounds reported by Bazaga-García et al. (2016), $[\text{Ln}(\text{H}_4\text{NMP})(\text{H}_2\text{O})_2]\text{Cl}\cdot 2\text{H}_2\text{O}$.

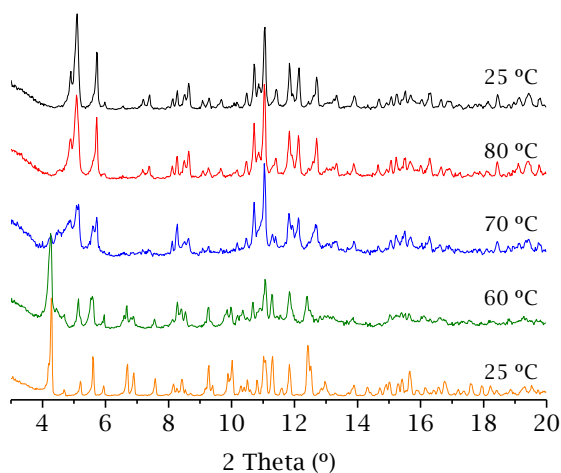


Figure 6.10. Thermodiffraction patterns for **Tb-I** at different temperatures and 95% RH.

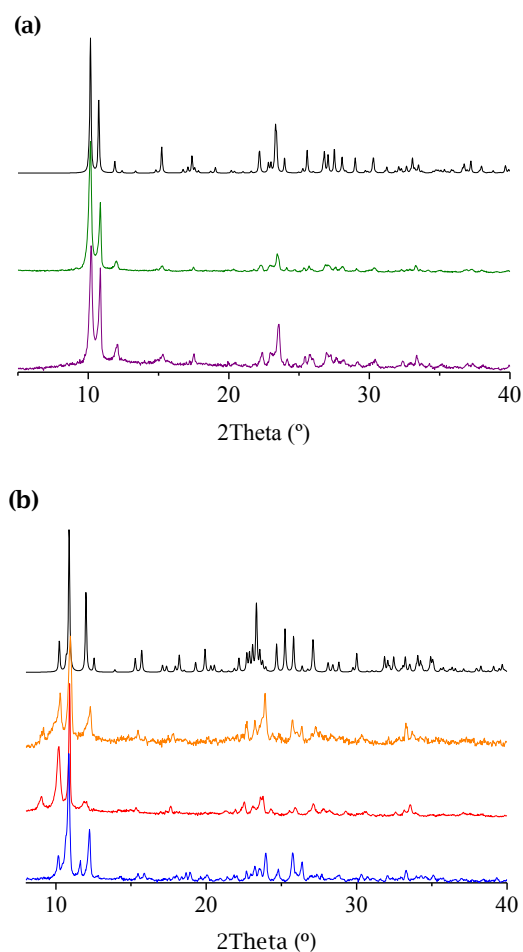


Figure 6.11. XRPD patterns for: (a) **SD-Pr-I** (olive) and **SD-Nd-I** (purple) compared with $[\text{La}_2(\text{H}_4\text{NMP})_2(\text{H}_2\text{O})_3(\text{SO}_4)] \cdot 6\text{H}_2\text{O}$ (black; CCDC no. 1496872); (b) **SD-Gd-I** (orange), **SD-Eu-I** (red) and **SD-Tb-I** (blue) compared with $[\text{La}_2(\text{H}_4\text{NMP})_2(\text{H}_2\text{O})_3(\text{SO}_4)] \cdot 2\text{H}_2\text{O}$ (black; CCDC no. 1496873).

As revealed for the terbium derivative, transformation of **Tb-I** into **SD-Tb-I** does not imply a change in the connectivity of the ligand, but simply deprotonation of the HSO_4^- . In the structure of **SD-Tb-I**, Tb^{3+} is also octa-coordinated as in compounds Ln-I, but one of the two coordinated water molecules is now half-substituted by the SO_4^{2-} group. This group binds Tb^{3+} in a monodentate fashion and its three uncoordinated oxygen atoms point towards the interlayer region, interacting with the non-coordinated oxygen atoms O3 and O6 from the phosphonate groups, as well as with the coordinated (Ow1) and the lattice (Ow3) water molecules, through H-bonds. This

H-bond interaction extends along the a -axis, and these pathways are interconnected through lattice water Ow2, in the c -axis direction, creating extended H-bond networks (Figure 6.12), different to those already described for the compounds Ln-I (Table 6.8).

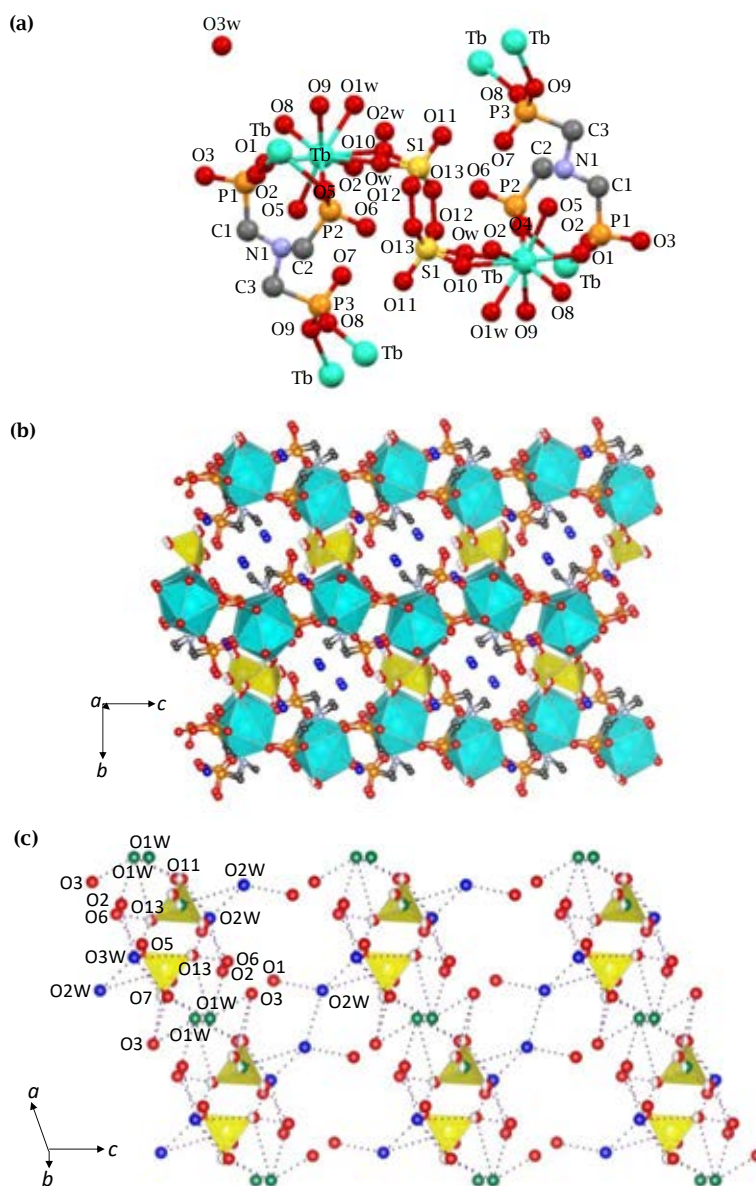


Figure 6.12. (a) Coordination environment of **SD-Tb-I**, (b) packing of the crystal structure with lattice water molecules in blue and (c) H-bond networks between sulfate groups (yellow polyhedra), phosphonate oxygen atoms (red), coordinated (green) and lattice water molecules (blue).

Table 6.8. H-bond distances for **SD-Tb-I**.

D-H...A	D...A (Å)	D-H...A	D...A (Å)
O1W...O3	2.902(20)	O7...O3W	2.679(11)
O1W...O6	3.178(22)	O10...O3	3.131(31)
O1W...O7	3.193(22)	O11...Ow	2.536(29)
O1W...O11	2.535(20)	O11...O3W	2.635(20)
O1W...O13	3.136(25)	O12...O3W	2.501(22)
Ow...O2W	3.12(4)	O12...O2W	2.835(33)
O1...O2W	3.016(23)	O13...Ow	2.583(33)
O2...O3W	2.793(21)	O13...Ow	2.89(4)
O3...O11	2.858(26)	O13...O3W	2.897(32)
O6...O12	2.551(24)	O13...O3W	3.169(29)
O6...O13	2.411(24)	O3W...O5	3.055(23)
O7...O11	2.414(20)	O2W...O2W	2.910(32)

The abnormally short distances found for **SD-Tb-I** and **Tb-II** suggest the formation of linear H-bonds, where H is in an intermediate position between two oxygen atoms (Emsley, 1980). However, some errors in the atomic position of the oxygen atoms are not disposable due to the limitation of the refinements using X-ray powder diffraction data in presence of heavy atoms.

As above described, by increasing the addition of sulphuric acid added, new layered isostructural compounds, $\text{Ln}[\text{HN}(\text{CH}_2)_3(\text{PO}_3\text{H}_2)(\text{PO}_3\text{H})_2]\text{SO}_4 \cdot 2\text{H}_2\text{O}$ (Series **Ln-II**, with Ln= Pr, Nd, Eu, Gd, Tb), were obtained. These solids crystallize in the triclinic crystal system ($P\bar{1}$). Layers are composed of edge-sharing dimeric Ln_2O_{14} polyhedra running along the diagonal to the *bc* plane, interconnected by sulfate-bridged ions (Figure 6.13b). Lanthanide environment is octa-coordinated (Figure 6.13a), in which phosphonate P1 bridges two lanthanide ions through O1 and O2, phosphonate P2 acts simultaneously as chelate for one of the two lanthanide ions and bridging two metal ions through a single oxygen atom (O6), giving rise to the formation of Ln_2O_{14} dimers, whereas the third phosphonate only coordinates monodentately to the lanthanide ions. This structure contains two lattice water molecules, which interact with the layers through H-bond (Figure 6.13d; Table 6.9).

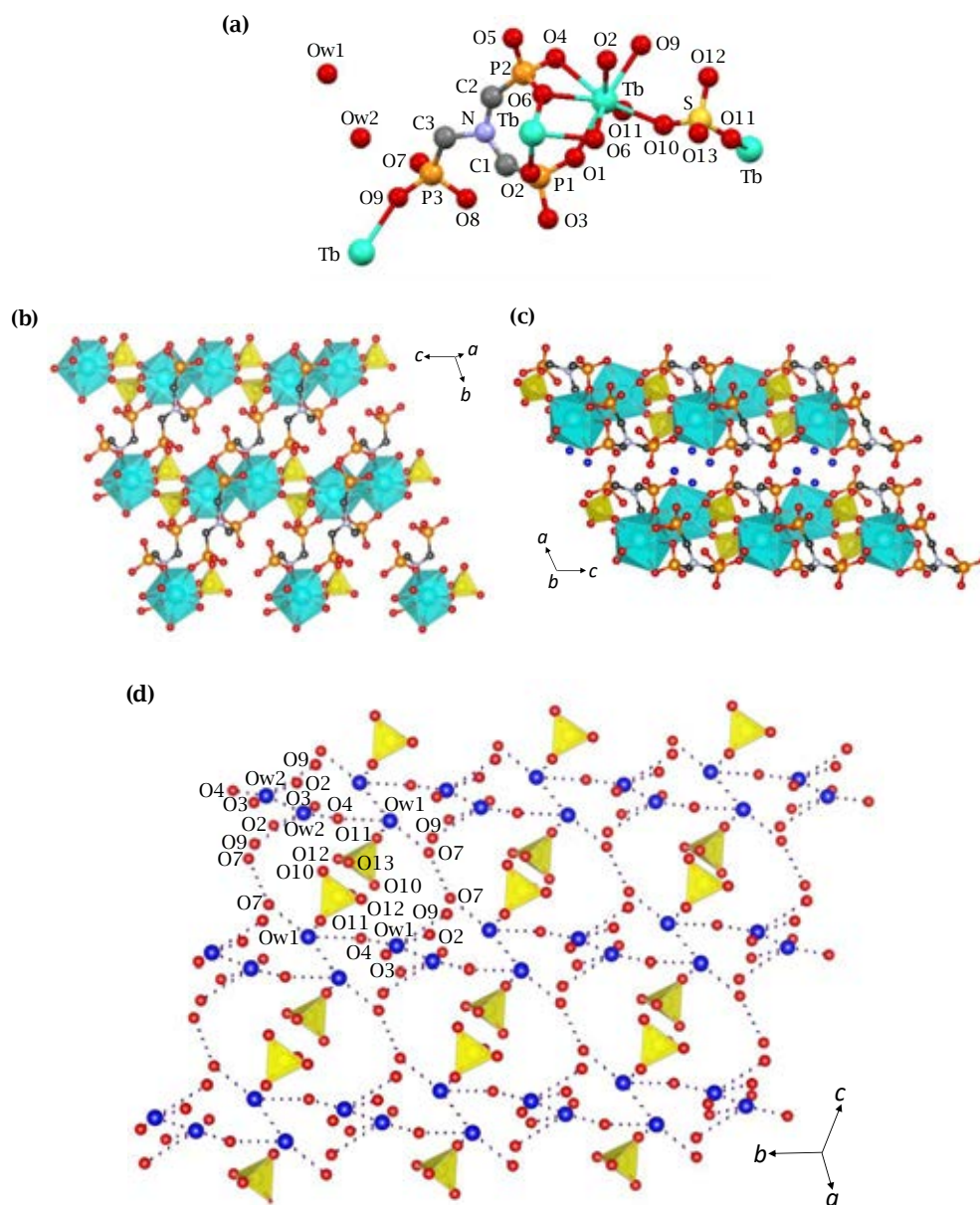


Figure 6.13. (a) Coordination environment of **Tb-II**, (b) view of the connectivity of Tb_2O_{14} dimers through the sulfate and phosphonates groups in a single layer, (c) layered packing with lattice water molecules in blue and (d) H-bond interactions in the bc plane between sulfate groups (yellow polyhedra), phosphonate oxygen atoms (red) and lattice water molecules (blue).

Table 6.9. H-bond distances for **Tb-II**.

D-H...A	D...A (Å)	D-H...A	D...A (Å)
O1...O8	3.115(31)	O8...O12	3.475(27)
O1...O11	2.896(30)	O9...O19	2.18(4)
O2...Ow2	2.77(4)	O9...Ow2	3.18(4)
O3...O12	3.23(4)	O10...O10	2.79(5)
O3...Ow2	2.491(28)	O11...Ow1	3.00(4)
O4...Ow1	2.93(4)	Ow1...Ow1	2.97(6)
O4...Ow2	3.03(4)	Ow2...Ow2	2.96(6)
O7...Ow1	2.67(4)		

As done for compounds **Ln-I**, compounds **Ln-II** were investigated for their chemical and thermal stability. TG curves reveal a unique low temperature weight loss corresponding to removal of the two lattice water molecules (i.e. for **Tb-II**, found 7.0%, calc. 6.0%). In addition, X-ray powder thermodiffraction data showed that this solid is stable up to 140 °C, from which it tends to amorphise upon dehydration (Figure 6.14).

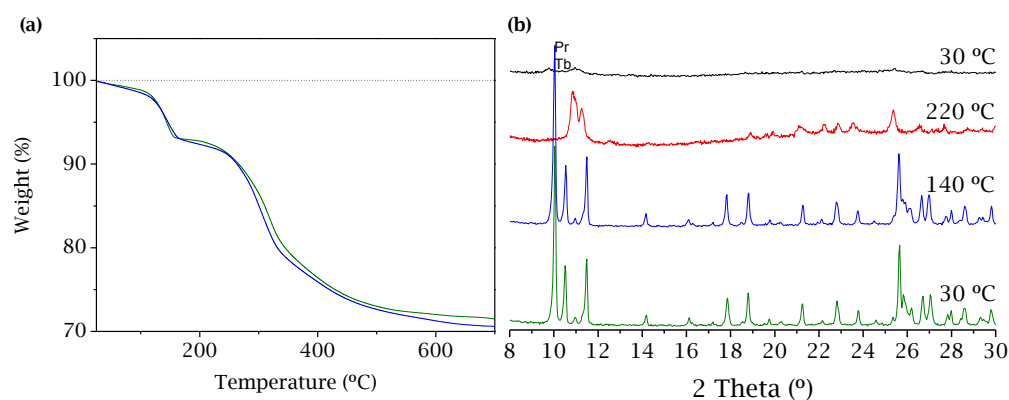


Figure 6.14. (a) Thermal analysis for **Pr-II** (olive) and **Tb-II** (blue) and (b) thermodiffraction patterns for **Tb-II**.

In contrast to compounds of Series **Ln-I**, those of Series **Ln-II** remain stable under wet conditions (95% RH) and 80 °C (Figure 6.15).

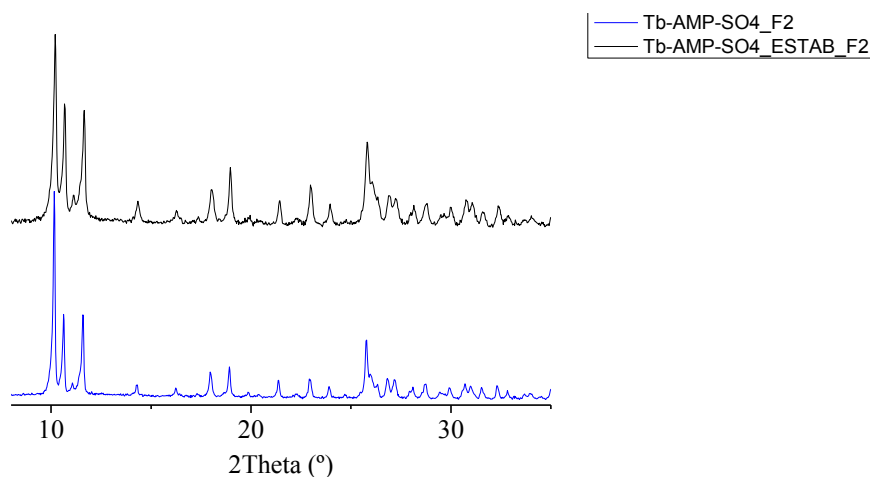


Figure 6.15. X-ray powder diffraction patterns for **Tb-II** as synthesised (blue) and after 89h at 80 °C and 95 %RH (black).

6.3. Proton Conductivity

It was reasoned that incorporating sulfate anions would enhance proton conductivity as compared with the analogous Cl⁻ containing compounds, because chiefly to the formation of stronger extended H-bonding networks. Proton conductivity has been evaluated at 75 and 95 % RH. Solids of Series **Ln-I** are unstable under the measurement conditions. However, the resulting sulfate-deficient derivatives (**SD-Ln-I**), as well as solids of Series **Ln-II** are stable and exhibit robust extended H-bond networks. On the other hand, the anhydrous solids of Series **Ln-I** stabilise the highest sulfate content in the structure, becoming also promising candidates as proton conductors. By contrast, anhydrous solids of Series **Ln-II** adsorb water in such a way that cause pellet deformation, according to preliminary stability tests.

Proton conductivity measurements were carried out as indicated in Section 3.13.2. AC impedance data were collected on an AUTOLAB PGSTAT302N or a HP4284A impedance analyser over the frequency range from 10⁶ or 10⁵ Hz to 20 Hz and an applied voltage of 0.35 or 1 V, respectively. Impedance spectra were recorded on cooling using stabilisation time of 5h at different temperature intervals from 80 to 25 °C and at 75 or 95% RH. Complex impedance plane plots are shown in Appendix IV (Figure AIV.8 and AIV.9), from which the total pellet resistance (R_p) was obtained. Furthermore, for **SD-Pr-I** and **SD-Tb-I**, samples were kept at 80 °C and 95% RH for 80–90 h, washed with DI water and dried at air.

As shown in Figure 6.16, all solids exhibit high proton conductivity values, ranging from $1.1 \cdot 10^{-3}$ to $3.6 \cdot 10^{-2}$ S \cdot cm $^{-1}$ at 80 °C and 95% RH, very close to those of Nafion[®] (Del Río, Morales & Escribano, 2014). In addition, these values are higher than those found for the isorecticular compound $[\text{Gd}(\text{H}_4\text{NMP})(\text{H}_2\text{O})_2]\text{Cl} \cdot 2\text{H}_2\text{O}$ (3.10^{-4} S \cdot cm $^{-1}$ at 80 °C and 95 % RH; Bazaga-García et al., 2016). This enhancement of the proton conductivity is due to the higher propensity of the sulfate anions to establish H-bonding interactions with available species, such as water molecules and phosphonate groups. As a typical behaviour of water-mediated proton conductors, the proton conductivity decreased at lower values of relative humidity (Deng et al., 2020). In all cases, the activation energy values (Table 6.10), obtained from the slope of the Arrhenius plots (Figure 6.16), are indicative of a Grotthuss-type proton transfer mechanism, which can be related with the existence of H-bond networks formed by interaction among phosphonate groups, sulfate groups and water molecules.

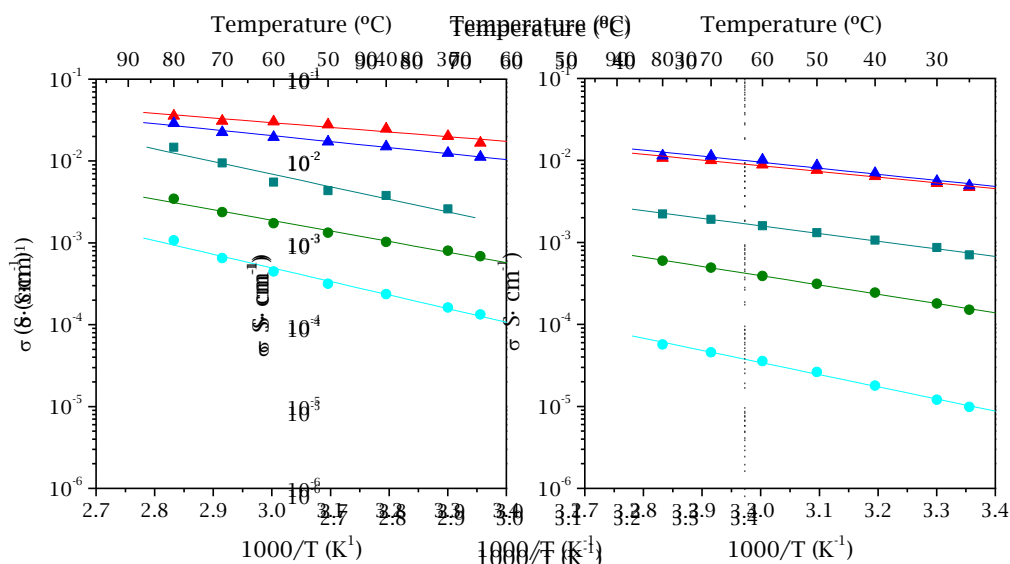


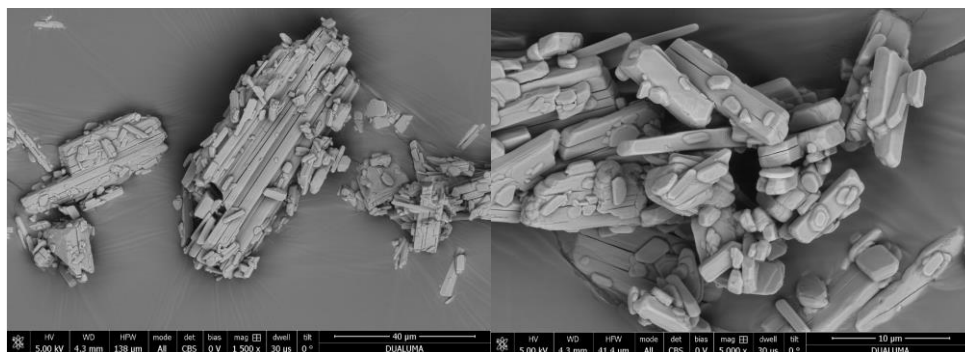
Figure 6.16. Arrhenius plots for SD-Tb-I (■), Tb-I-230C (▲), Eu-I-230C (▲), Pr-II (●) and Tb-II (●) at (left) 95 and (right) 75% RH.

Table 6.10. Summary of the proton conductivity and activation energies values at 80 °C, and 95 and 75% RH.

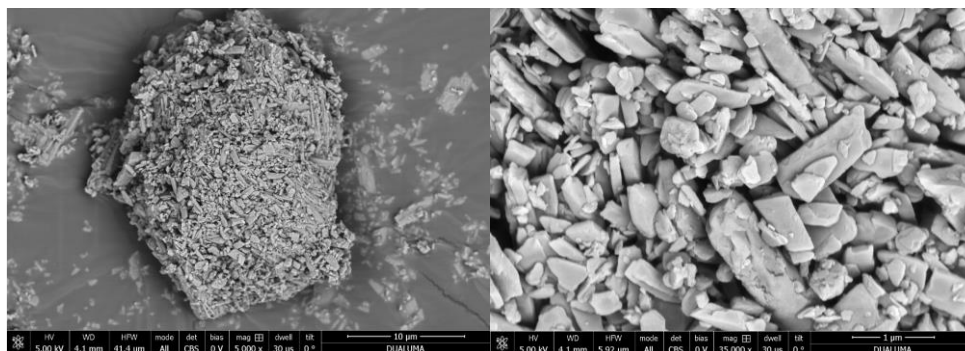
Sample	95% RH		75% RH	
	σ (S·cm ⁻¹)	E _a (eV)	σ (S·cm ⁻¹)	E _a (eV)
SD-Tb-I	1.5·10 ⁻²	0.31	2.2·10 ⁻³	0.18
Eu-I-230C	3.6·10 ⁻²	0.11	1.1·10 ⁻²	0.14
Tb-I-230C	2.9·10 ⁻²	0.14	1.1·10 ⁻²	0.17
Pr-II	3.5·10 ⁻³	0.26	6.0·10 ⁻⁴	0.22
Tb-II	1.1·10 ⁻³	0.33	5.7·10 ⁻⁵	0.29

SD-Tb-I exhibits higher proton conductivity values than members of Series **Ln-II** due to the higher availability of sulfate oxygen atoms to establish H-bond networks. Regarding to SEM images, compounds of both Series exhibit similar morphological features (Figure 6.17). They are constituted by aggregates of elongated platy particles.

(a)



(b)

**Figure 6.17.** SEM images of as synthesised **Eu-I** (a) and **Tb-II** (b).

The heat treatment of samples belonging to Series **Ln-I**, at 230 °C during 2h, leading to full sulfate-content materials, resulted in an enhancement of proton conductivity, as compared with sulfate-deficient solids. However, dehydration does not preclude further water uptake during the impedance measurements, as observed by thermal analysis (Figure 6.18b), the composition of rehydrated **Tb-I-230C** being compatible with the formula $\{\text{Ln}_2[\text{HN}(\text{CH}_2)_3(\text{PO}_3\text{H})_2]_2\}(\text{HSO}_4)_2 \cdot 6\text{H}_2\text{O}$ (weight loss found 8.5%, calculated, 8.9%). According to XRD patterns, post-impedance samples may be composed of the intact crystalline phase plus an amorphous component, possibly responsible for water uptake.

All samples were monitored by TG and XRPD analyses to ensure that no appreciable changes occurred after impedance measurements (Figures 6.18).

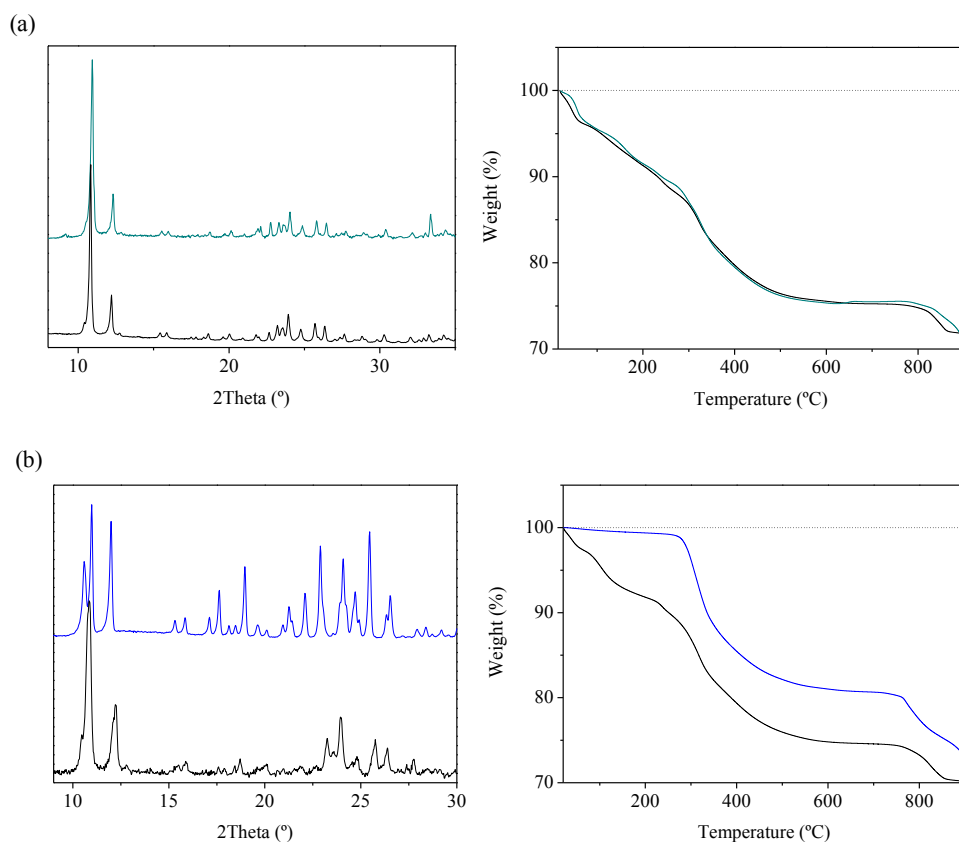


Figure 6.18. X-ray powder diffraction patterns (left) and thermal analysis (right) before (blue) and after (black) proton conductivity measurements for (a) **SD-Tb-I**, (b) **Tb-I-230C** and (c) **Tb-II**.

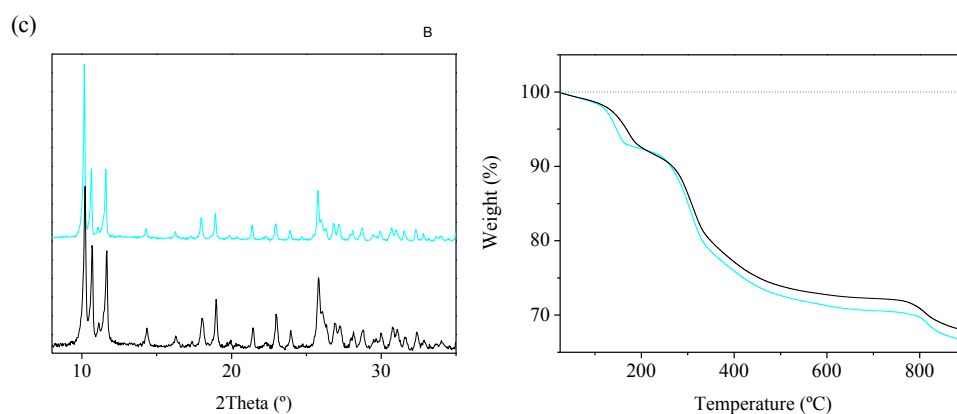


Figure 6.18. X-ray powder diffraction patterns (left) and thermal analysis (right) before (blue) and after (black) proton conductivity measurements for (a) **SD-Tb-I**, (b) **Tb-I-230C** and (c) **Tb-II** (Continuation).

6.4. Preparation and Characterisation of Composite Membranes

Preliminary studies of preparation and characterisation of composite membranes for proton exchange membrane fuel cells (PEMFCs) have been carried out in collaboration with the Institute of Science and Technology of Polymers, ITCP-CSIC (Madrid). **Eu-I-230C**, **SD-Eu-I** and **Tb-II** were selected as representative derivatives from Series **Ln-I** and **Ln-II** for the preparation of Nafion-based composite membranes. 3% (w/w) (**Eu-I-230C**, **SD-Eu-I** or **Tb-II**)-loaded Nafion composite membranes, i.e. **Nafion/Eu-I-230C**, **Nafion/SD-Eu-I** and **Nafion/Tb-II**, were prepared as follows. 18 mg of the corresponding lanthanide derivative (**Eu-I-230C**, **SD-Eu-I** or **Tb-II**) were dispersed in 3 mL of 2-propanol via magnetic stirring (10 min) and sonication (10 min) in six subsequent cycles. Then, this suspension was carefully added to 3 g of 20 wt % Nafion solution in a flask under magnetic stirring up to obtaining a viscous homogeneous suspension. Membranes were prepared by casting using a Blade (BYK Instruments) onto a polycarbonate plate that was allowed to air-dry for 48 hours. Finally, the obtained membranes (with thickness of 50 μm) was peeled off from the polycarbonate plate.

Figure 6.19 displays the XRD patterns of **Nafion/Eu-I-230C**, **Nafion/SD-Eu-I** and **Nafion/Tb-II** composite membranes, compare with that of Nafion and those corresponding to **Eu-I-230C**, **SD-Eu-I** and **Tb-II** samples. As can be observed, the

characteristic peaks of crystalline **Eu-I-230C**, **SD-Eu-I** or **Tb-II** compounds are present in the XRD patterns of the composite membranes, together with a broad reflection between ~ 11 and 21° (2θ) corresponding to the amorphous Nafion membrane (black).

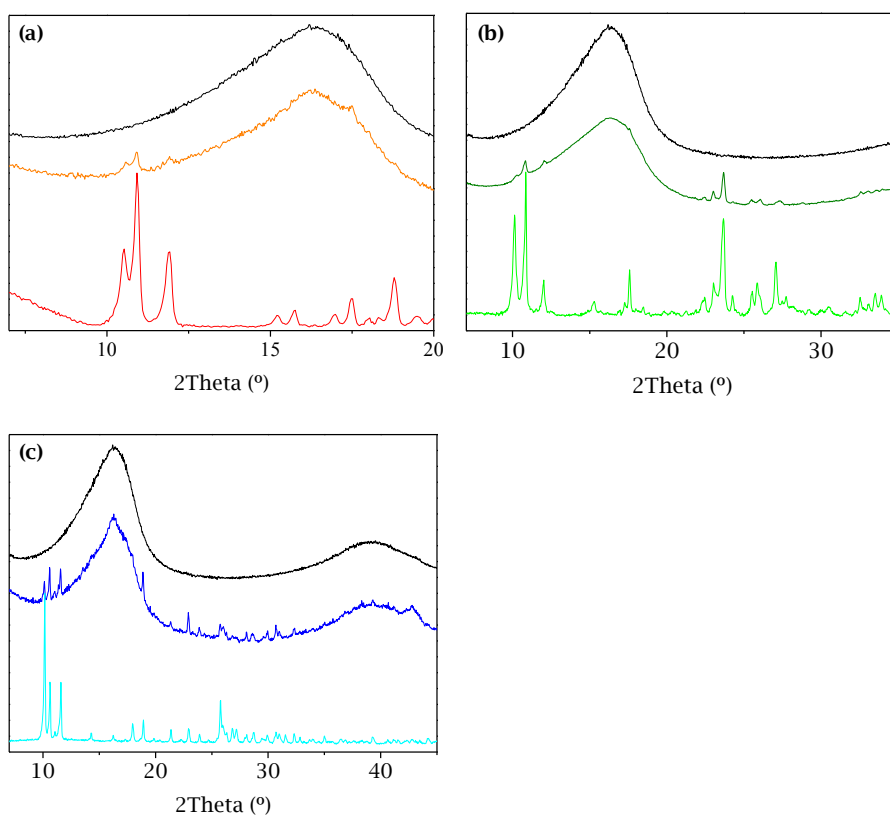


Figure 6.19. XRPD patterns of (a) **Eu-I-230C** (red), **Nafion/Eu-I-230C** composite membrane (orange) and Nafion membrane (black); (b) **SD-Eu-I** (green), **Nafion/SD-Eu-I** composite membrane (olive) and Nafion membrane (black) and (c) **Tb-II** (cyan), **Nafion/Tb-II** composite membrane (blue) and Nafion membrane (black)

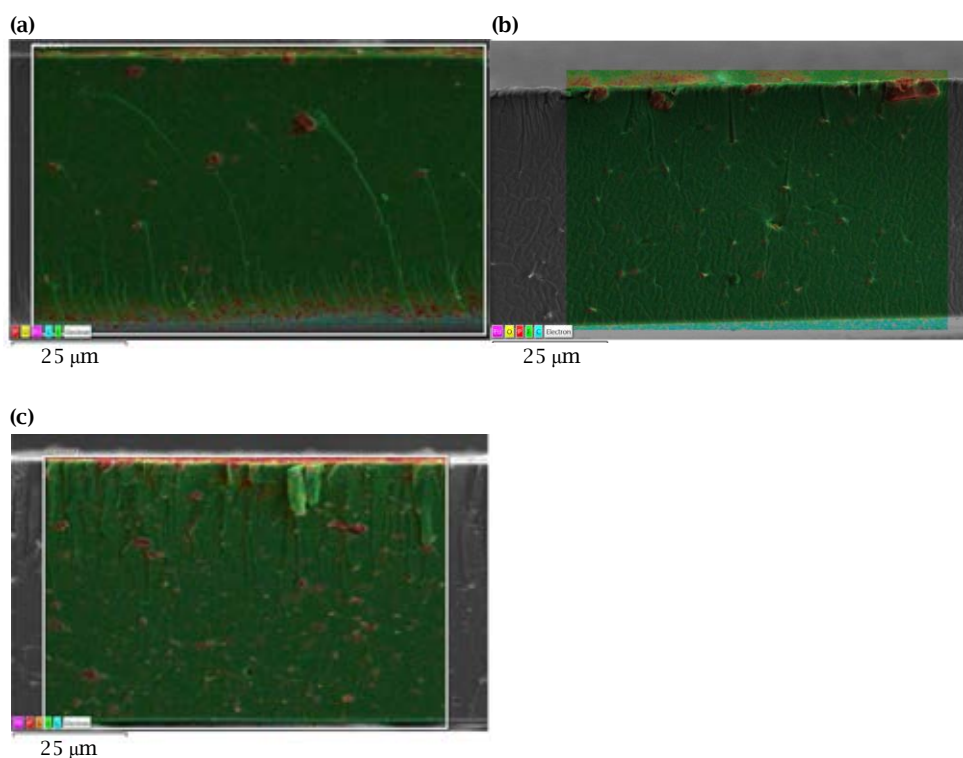
For water uptake measurements, the membranes were dried at 60°C for 12h and weighed. Then, they were immersed in DI water for 24h; the excess of water was removed with a tissue paper and rapidly weighed.

$$\text{Water uptake (wt. \%)} = \frac{\text{Wet membrane (g)} - \text{Dried membrane (g)}}{\text{Wet membrane (g)}} \times 100 \quad \text{Equation 6.2}$$

Table 6.11. Water uptake of Nafion, Nafion/Eu-I-230C and Nafion/Tb-II.

Membrane	Water uptake (%)
Nafion	35.3
Nafion/Eu-I-230C	32.3
Nafion/Tb-II	24.4

As can be seen in the SEM-EDS images of both Nafion/Eu-I-230C, Nafion/SD-Eu-I and Nafion/Tb-II composite membranes (Figure 6.20), Eu-I-230C, SD-Eu-I and Tb-II particles are uniform distributed inside the polymeric matrix of Nafion.

**Figure 6.20.** SEM-EDS images for (a) Nafion/Eu-I-230C, (b) Nafion/SD-Eu-I and (c) Nafion/Tb-II.

In situ through-plane conductivity of the membranes was determined on the MEAs at 70, 80 and 90 °C and 100% RH (Chapter 3, Section 3.13.2). Equation 6.2 was employed to obtain the through-plane proton conductivity (σ_{TP}), where L is the membrane thickness, R is the resistance and S is the active area of the MEA (5 cm²).

$$\sigma_{TP} (S \cdot cm^{-1}) = \frac{L (cm)}{R (\Omega) \cdot S (cm^2)} \quad \text{Equation 6.2}$$

The resistance was determined from Nyquist plots and it corresponds to the intercept with the real axis in the Nyquist plots.

As can be seen in Figure 6.21, Nafion-based composite membranes exhibit in situ through-plane proton conductivity values similar to the unmodified Nafion membrane. In addition, the same behaviour is observed at 90 °C where all membranes exhibit a small decay of the proton conductivity values due to the loss of the optimal hydration degree of the membranes.

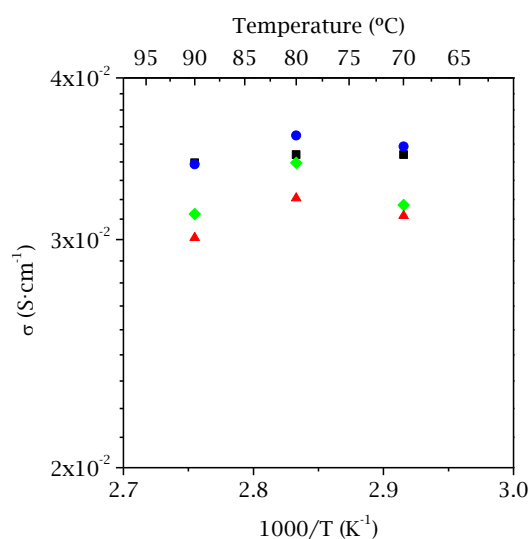


Figure 6.21. Arrhenius plot for unmodified Nafion membrane (black square), **Nafion/Eu-I-230C** (red triangles), **Nafion/SD-Eu-I** (green diamonds) and **Nafion/Tb-II** (cyan circles) composite membranes at 100% RH.

Composite membranes were evaluated as proton exchange membranes for fuel cells. These tests were performed employing a Scribner 850e multirange fuel cell test system with H₂ as fuel and O₂ as an oxidant. Both gas were supplied at 0.2 L·min⁻¹. The maximum current and power densities were determined at 100% RH, under atmospheric pressure and three different cell temperatures (70, 80 and 90 °C).

Figure 6.22 shows the polarization and power density curves of **Nafion/Eu-I-230C**, **Nafion/SD-Eu-I** and **Nafion/Tb-II** composite membranes as well as those of the pure Nafion membrane, as commercial reference material. The incorporation of **Eu-I-230C**, **SD-Eu-I** or **Tb-II** into the Nafion polymeric matrix leads to composite membranes that perform satisfactorily in PEMFCs. All composite membranes improve the electrochemical features relative to the pure Nafion membrane at 70 °C (Figure 6.22a.), reaching a maximum current density of 3201, 3601 and 3800 mA·cm⁻² and a maximum power density of 866, 1012 and 1008 mW·cm⁻² for **Nafion/Eu-I-230C**, **Nafion/SD-Eu-I** and **Nafion/Tb-II** respectively, while the corresponding values for pure Nafion are 2600 mA·cm⁻² and 840 mW·cm⁻². At higher temperature values, **Nafion/Eu-I-230C** and **Nafion/SD-Eu-I** exhibit similar behavior than the pure Nafion membrane. On the other hand, **Nafion/Tb-II** exhibits the best results of maximum current and power density in the entire range of measured temperatures (Table 6.12).

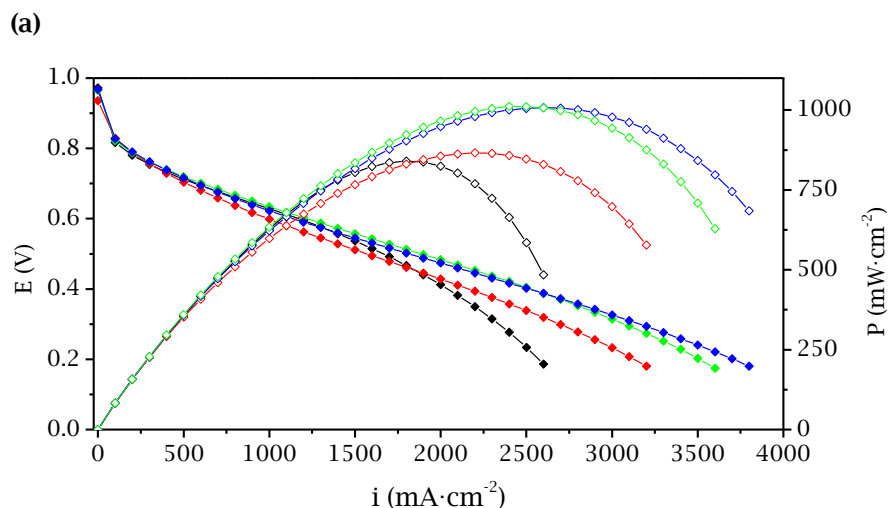


Figure 6.22. Polarization (full) and power density (empty) curves for Nafion (black), **Nafion/Eu-I-230C** (red) and **Nafion/Tb-II** (blue) composite membranes at 100% RH and different temperatures: (a) 70, (b) 80 and (c) 90 °C.

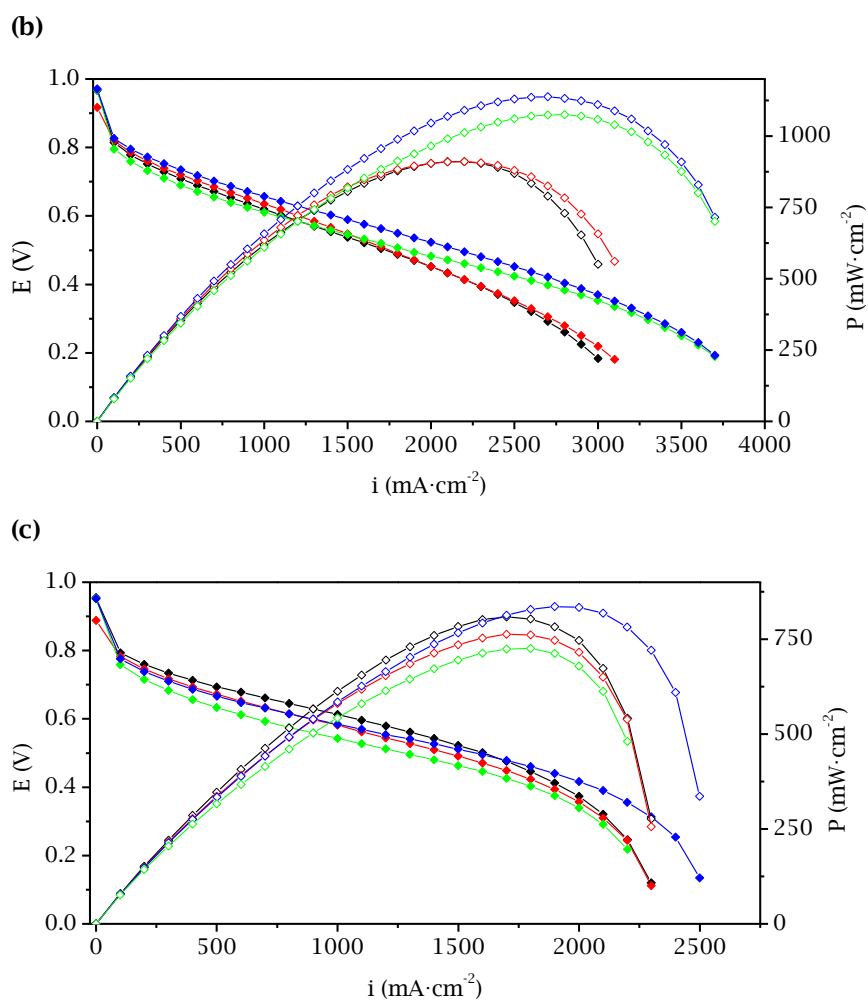


Figure 6.22. Polarization (full) and power density (empty) curves for Nafion (black), Nafion/Eu-I-230C (red) and Nafion/Tb-II (blue) composite membranes at 100% RH and different temperatures: (a) 70, (b) 80 and (c) 90 °C (Continuation).

Table 6.12. Maximum current and power density values.

Membrane	Max. current density			Current density (0.6V)			Max. power density		
	(mA·cm ⁻²)			(mW·cm ⁻²)			(mW·cm ⁻²)		
	70 °C	80 °C	90 °C	70 °C	80 °C	90 °C	70 °C	80 °C	90 °C
Nafion	2600	3000	2299	1200	1099	1099	840	910	809
Nafion/Eu-I-230	3201	3100	2299	1000	1200	900	866	910	763
Nafion/SD-Eu-I	3601	3700	2000	1200	1099	700	1012	1075	725
Nafion/Tb-II	3800	3700	2499	1099	1400	900	1008	1138	836

6.5. Luminescent Properties

Photoluminescence (PL) spectra of selected powder samples were carried out in collaboration with Prof. Gary Hix from the University of Wolverhampton (U.K.). A Carl Zeiss-Axio Imager A2m optical microscope was employed in fluorescence mode using a HBO 100 mercury lamp. The PL signal was collected by Ocean Optics QE Pro spectrometer connected to the microscope via a fibre optic waveguide.

In all of them, the emission is due to the direct excitation of the lanthanide ion. The H_6NMP and HSO_4^- or SO_4^{2-} ligands play no detectable role in the emission of light. It is of interest that unlike many lanthanide containing compounds there is little evidence of concentration quenching, which is commonly observed in condensed structure types such as oxide materials. This can perhaps be explained by the fact that the crystal structure of these materials keeps the lanthanide ions at a reasonable distance from one another and that the structure does not give rise to an electronic structure that would readily re-adsorb any light emitted by the ions.

For **Tb-I**, the spectrum of the emission show the expected emission lines centred around the most intense $^5\text{D}_4 \rightarrow ^7\text{F}_5$ transition which is at 452 nm with a shoulder at 546 nm. The data are tabulated for each of the transitions observed. In addition, under Hg lamp illumination, **Tb-I** displays a characteristic green emission as shown in Figure 6.23.

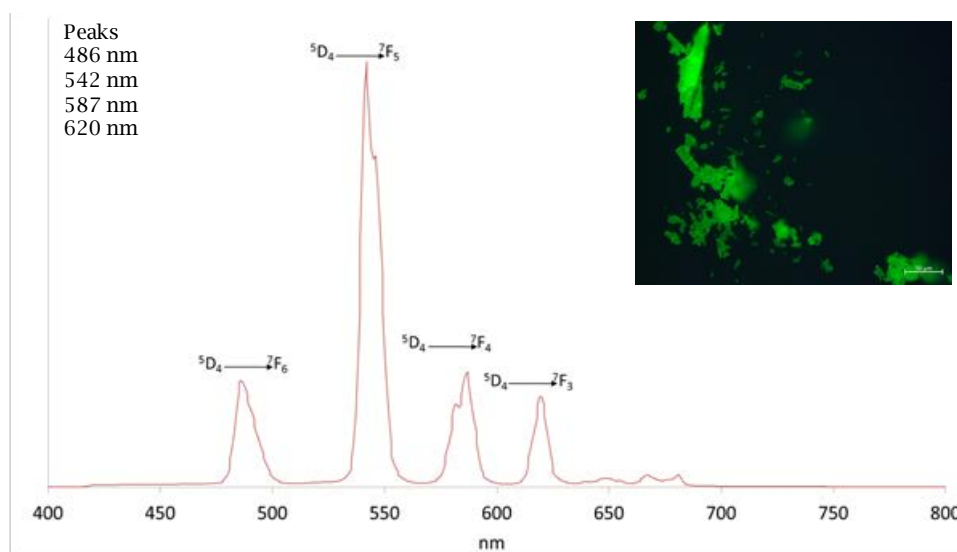


Figure 6.23. PL spectra ($\lambda_{\text{ex}} = 355 \text{ nm}$) for **Tb-I** and (inset) and its image under Hg lamp illumination.

In the case of **Tb_{0.8}Eu_{0.2}-I**, its spectrum contains lines arising from both the Eu and Tb atoms which are tabulated beneath. As can be seen, the positions of the Tb lines (black labels) are unshifted with respect to the Tb only material. The 593 nm line associated with the Eu $^5D_0 \rightarrow ^7F_1$ transition appears as a shoulder on the line derived from the Tb $^5D_4 \rightarrow ^7F_4$ transition which is observed at 583 nm. Similarly, the peak around 620 nm is of much greater intensity in the mixed metal system than in the Tb only sample as this is a superposition of the Eu $^5D_0 \rightarrow ^7F_2$ and Tb $^5D_4 \rightarrow ^7F_3$ transitions. The line observed at 697 nm coming from the Eu $^5D_0 \rightarrow ^7F_4$ transition is not observed in the spectrum of the Tb only sample (Figure 6.24).

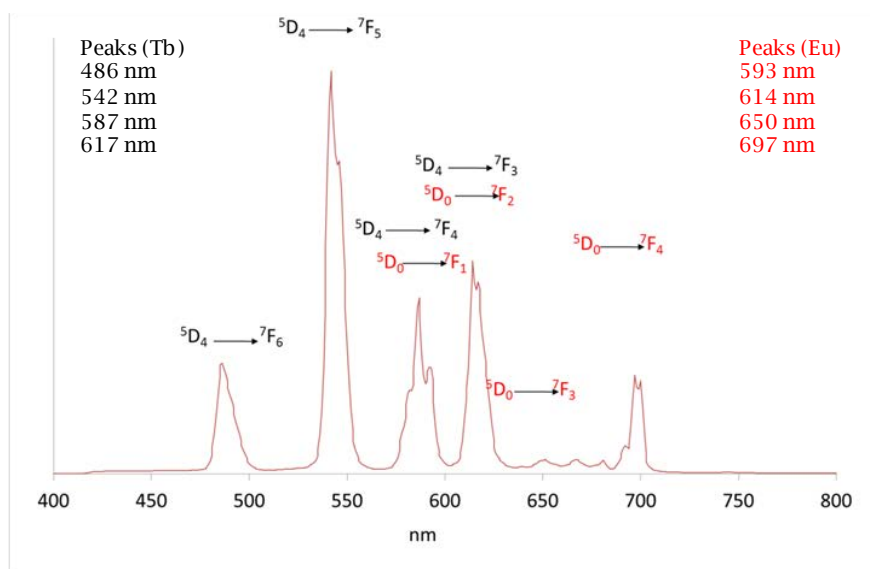


Figure 6.24. PL spectra ($\lambda_{ex}= 355$ nm) for **Tb_{0.8}Eu_{0.2}-I**.

This sample again demonstrates the characteristic green emission that is associated with the Tb in the sample when illuminated with an Hg lamp. The pictures show the sample under natural light (darkfield image) and illuminated by the Hg lamp.

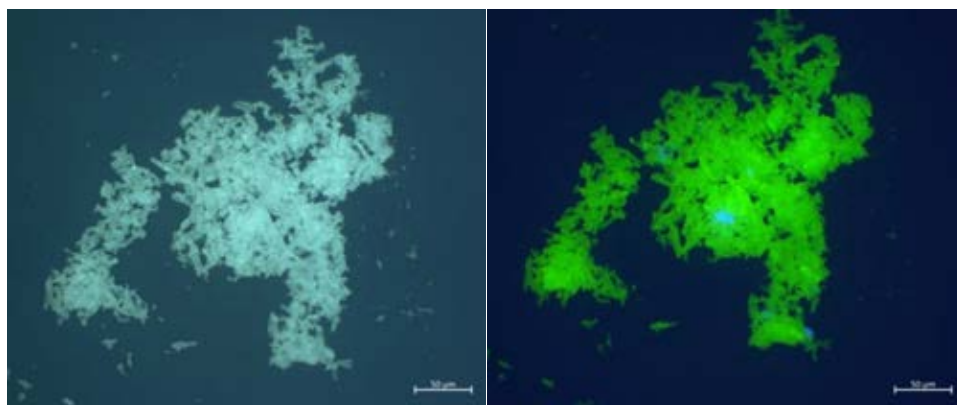


Figure 6.25. $\text{Tb}_{0.8}\text{Eu}_{0.2}\text{-I}$ under natural light and illuminated with a Hg lamp.

In the spectrum of $\text{Tb}_{0.2}\text{Eu}_{0.8}\text{-I}$ sample, as would be expected, the Eu lines are more intense. However it is notable that even with the much lower concentration of Tb present in the sample, the most intense peak is the Tb $^5\text{D}_4 \rightarrow ^7\text{F}_5$ transition, which demonstrates the greater relative intensity of the emission from Tb when compared to Eu. This is evidenced further in the overlapping peak around 620 nm (Eu $^5\text{D}_0 \rightarrow ^7\text{F}_2$ and Tb $^5\text{D}_4 \rightarrow ^7\text{F}_3$ transitions), where the compositional change to much greater Eu content does not have an appreciable affect upon the relative intensity of the aggregated peak with respect to the peak at 542 nm (Tb $^5\text{D}_4 \rightarrow ^7\text{F}_5$ transition). However, there is a more pronounced splitting of the composite peak which differentiates the Eu and Tb contributions, which arises from the increased contribution of the Eu emission to this line.

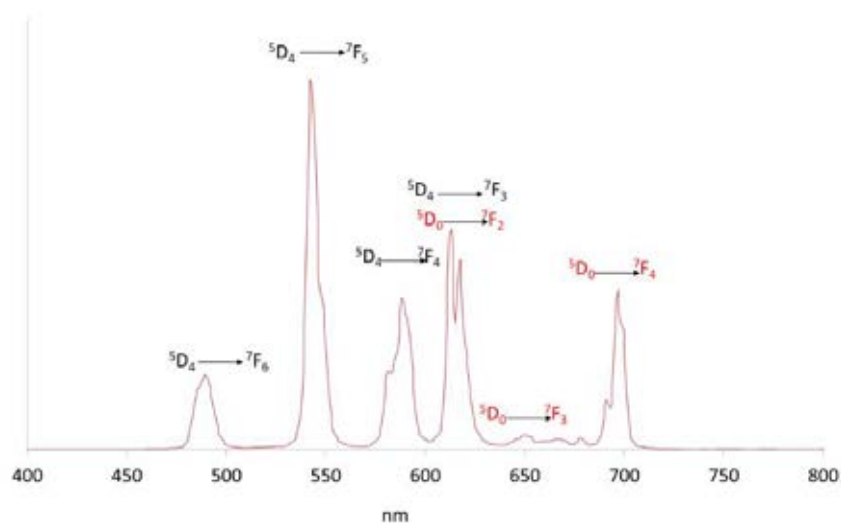


Figure 6.26. PL spectra (λ_{ex} = 355 nm) for $Tb_{0.2}Eu_{0.8}$ -I.

6.6. Conclusions

- Two polymorph series, $\{Ln_2[HN(CH_2)_3(PO_3H)_3]_2(H_2O)_4\}(HSO_4)_2 \cdot nH_2O$ ($Ln = Pr, Nd, Sm, Eu, Gd, Tb, Er, Yb$; $n = 4-5$; Series **Ln-I**) and $Ln[HN(CH_2)_3(PO_3H_2)(PO_3H)_2]SO_4 \cdot 2H_2O$ ($Ln = Pr, Nd, Eu, Gd, Tb$; Series **Ln-II**) have been isolated by slow crystallization at 25 °C depending on the Ln^{3+} : $H_6NMP:H_2SO_4:H_2O$ molar ratios. Compounds of Series **Ln-II** necessitated higher amounts of H_2SO_4 (95%) to be obtained.
- Members of Series **Ln-I** present a layered crystal structure equivalent to that of $[Ln(H_4NMP)(H_2O)_2]Cl \cdot 2H_2O$, with uncoordinated hydrogensulfate ions placed in the interlayer region, as a layer charge-compensating species. On the other hand, layers in compounds of Series **Ln-II** are composed of edge-sharing dimeric Ln_2O_{14} polyhedra, interconnected by bridge sulfate ions.
- For compounds of Series **Ln-I**, heating at 80 °C under high relative humidity (95% RH), resulted in structurally different compounds, having half the sulfate/ Ln^{3+} molar ratio, with the sulfate anion being in deprotonated form. Conversely, compounds of Series **Ln-II** remained stable under these conditions. In addition, thermal treatment at 220-230 °C in furnace led to the anhydrous derivatives, preserving the initial Ln :phosphonate:sulfate molar ratios. While members of Series **Ln-I** evolve to a new crystalline

anhydrous phase with the latter heat treatment, members of Series **Ln-II** transformed into amorphous anhydrous solids.

- Compounds of both Series, **Ln-I** and **Ln-II**, exhibit high proton conductivity values, ranging from $1.1 \cdot 10^{-3}$ to $3.6 \cdot 10^{-2}$ S·cm⁻¹ at 80 °C and 95% RH.
- Preliminary studies on **Nafion/Eu-I-230C**, **Nafion/SD-Eu-I** and **Nafion/Tb-II** composite membranes, as components of proton exchange membrane fuel cells (PEMFCs), have revealed that these mixed matrix membranes exhibit power and current densities values higher than that of only Nafion membrane, while maintaining a high proton conductivity, similar to that of Nafion, in the range of 70-90 °C and 100 % RH.
- Luminescence spectra recorded for selected bimetallic solid solutions of Series **Ln-I**, showed the characteristics transitions attributed to the lanthanide ions.

6.7. References

A

Altomare, A.; Cuocci, C.; Giacobazzo, C.; Moliterni, A.; Rizzi, R.; Corriero, N; Falcicchio, A. EXPO2013: a kit of tools for phasing crystal structures from powder data. *J. Appl. Cryst.*, **2013**, 46, 1231-1235.

Akhmetova, I.; Schutjajew, K.; Wilke, M.; Buzanich, A.; Rademann, K.; Roth, C.; Emmerling, F. Synthesis, characterization and in situ monitoring of the mechanochemical reaction process of two manganese (II)-phosphonates with N-containing ligands. *J. Mater. Sci.*, **2018**, 53(19), 13390-13399.

B

Bazaga-García, M.; Angeli, G. K.; Papathanasiou, K. E.; Salcedo, I. R.; Olivera-Pastor, P.; Losilla, E. R.; Choquesillo-Lazarte, D.; Hix, G. B.; Cabeza, A.; Demadis, K. D. Luminescent and Proton Conducting Lanthanide Coordination Networks Based On a Zwitterionic Tripodal Triphosphonate. *Inorg. Chem.*, **2016**, 55(15), 7414-7424.

Bloemink, M. J.; Keppler, B. K.; Zahn, H.; Dorenbos, J. P.; Heetebrij, R. J.; Reedijk, J. New Antitumor Platinum Compounds Linked to Amino Phosphonic Acids Which Lose the Phosphonate and Tertiary Amine Ligand upon Binding to Nucleic Acids. *Inorg. Chem.*, **1994**, 33(6), 1127-1132.

CHAPTER 6

C

- Cabeza, A.; Ouyang, X.; Sharma, C. K.; Aranda, M. A.; Bruque, S.; Clearfield, A. Complexes formed between nitrilotris (methylenephosphonic acid) and M^{2+} transition metals: isostructural organic– inorganic hybrids. *Inorg. Chem.*, **2002**, 41(9), 2325-2333.
- Chausov, F. F.; Zakirova, R. M.; Somov, N. V.; Petrov, V. G.; Aleksandrov, V. A.; Shumilova, M. A.; Naimushima, E. A.; Shabanova, I. N. Thermal stability and thermal decomposition mechanism of nitrilotris (methylene phosphonate) complexes of copper and zinc with varied coordination. *Russ. J. Appl. Chem.*, **2014**, 87(8), 1031-1037.
- Chausov, F. F.; Lomova, N. V.; Somov, N. V.; Kazantseva, I. S.; Kholzakov, A. V.; Sapozhnikov, G. V.; Zakirova, R. M. Competitive formation of crystalline phases and its structural properties within the system $[Cu_xNi_{(1-x)}\{N(CH_2PO_3)_3\}]Na_n \cdot nH_2O$ ($x=0 \dots 1$). *J. Cryst. Growth*, **2019**, 524, 125187.
- Clearfield, A.; Demadis, K. D. Metal Phosphonate Chemistry: From Synthesis to Applications, *RSC: London*, **2012**.
- Cunha-Silva, L.; Mafra, L.; Ananias, D.; Carlos, L. D.; Rocha, J.; Almeida Paz, F. A. Photoluminescent Lanthanide– Organic 2D Networks: A Combined Synchrotron Powder X-ray Diffraction and Solid-State NMR Study. *Chem. Mater.*, **2007**, 19(14), 3527-3538.

D

- Del Río, C.; Morales, E.; Escribano, P. G. Nafion/sPOSS hybrid membranes for PEMFC. Single cell performance and electrochemical characterization at different humidity conditions. *Int. J. Hydrogen Energ.*, **2014**, 39(10), 5326-5337.
- Deng, X.; Hu, J. Y.; Luo, J.; Liao, W. M.; He, J. Conductive Metal–Organic Frameworks: Mechanisms, Design Strategies and Recent Advances. *Topics Curr. Chem.*, **2020**, 378(2), 1-50.

E

- Emsley, J. Very strong hydrogen bonding. *Chem. Soc. Rev.*, **1980**, 9(1), 91-124.

L

- Larson, A. C.; von Dreele, R. B. General structure analysis system (GSAS). Los Alamos National Laboratory Report LAUR, **2004**, 86–748.

M

- Martínez, R. J.; Farrell, J. Understanding Nitrilotris(methylenephosphonic acid) reactions with ferric hydroxide. *Chemosphere*, **2017**, 175, 490-496.
- Mendes, R. F.; Silva, P.; Antunes, M. M.; Valente, A. A.; Paz, F. A. A. Sustainable synthesis of a catalytic active one-dimensional lanthanide-organic coordination polymer. *Chem. Commun.*, **2015**, 51(54), 10807-10810.
- Mendes, R. F.; Paz, F. A. A. Dynamic breathing effect in metal-organic frameworks: Reversible 2D-3D-2D-3D single-crystal to single-crystal transformation. *Inorg. Chim. Acta*, **2017**, 460, 99-107.
- Moedritzer, K.; Irani, R. R. The direct synthesis of α -aminomethylphosphonic acids. Mannich-type reactions with orthophosphorous acid. *J. Org. Chem.*, **1966**, 31(5), 1603-1607.

N

- Nakayama, N. Inhibitory effects of nitrilotris (methylenephosphonic acid) on cathodic reactions of steels in saturated $\text{Ca}(\text{OH})_2$ solutions. *Corros. Sci.*, **2000**, 42(11), 1897-1920.
- Netzsch, P.; Bariss, H.; Bayarjargal, L.; Höpfe, H. A. $\text{Tb}(\text{HSO}_4)(\text{SO}_4)$ - a green emitting hydrogensulfate sulfate with second harmonic generation response. *Dalton Trans.*, **2019**, 48(43), 16377-16383.

R

- Rajendran, S.; Apparao, B. V.; Mani, A.; Palaniswamy, N. Corrosion inhibition by ATMP-molybdate- Zn^{2+} system in low chloride media. *Anti-Corros. Method. M.*, **1998**, 45(1), 25-30.
- Rietveld, H. M. A Profile Refinement Method for Nuclear and Magnetic Structures. *J. Appl. Crystallogr.*, **1969**, 2(2), 65-71

S

- Sharma, C. K.; Clearfield, A.; Cabeza, A.; Aranda, M. A.; Bruque, S. Deprotonation of Phosphonic Acids with M^{2+} Cations for the Design of Neutral Isostructural Organic-Inorganic Hybrids. *J. Am. Chem. Soc.*, **2001**, 123(12), 2885-2886.
- Silva, P.; Vieira, F.; Gomes, A. C.; Ananias, D.; Fernandes, J. A.; Bruno, S. M.; Soares, R.; Valente, A. A.; Rocha, J.; Paz, F. A. A. Thermal transformation of a layered multifunctional network into a metal-organic framework based on a polymeric organic linker. *J. Am. Chem. Soc.*, **2011**, 133(38), 15120-15138.

CHAPTER 6

- Silva, P.; Mendes, R. F.; Fernandes, C.; Gomes, A. C.; Ananias, D.; Remião, F.; Borges, F.; Valente, A. A.; Paz, F. A. A. Multifunctionality and cytotoxicity of a layered coordination polymer. *Dalton Trans.*, **2020**, 49(13), 3989-3998.
- Somov, N. V., & Chausov, F. F. Structure of complexes of nitrilo tris methylene phosphonic acid with copper, $[\text{CuN}(\text{CH}_2\text{PO}_3)_3(\text{H}_2\text{O})_3]$ and $\text{Na}_4[\text{CuN}(\text{CH}_2\text{PO}_3)_3]_2 \cdot 19\text{H}_2\text{O}$, as bactericides and inhibitors of scaling and corrosion. *Crystallogr. Rep.*, **2015**, 60(2), 210-216.
- Somov, N. V.; Chausov, F. F.; Zakirova, R. M.; Fedotova, I. V.; Shumilova, M. A.; Aleksandrov, V. A.; Petrov, V. G. Synthesis, structure, and properties of the stabilized coordination chrome (II) complex with nitrilotris (methylenephosphonic) acid $[\text{Cr}^{\text{II}}(\text{H}_2\text{O})_3-\mu\text{-NH}(\text{CH}_2\text{PO}_3\text{H})_3]$. *Russ. J. Coord. Chem.*, **2015**, 41(10), 688-694.
- Somov, N. V.; Chausov, F. F.; Zakirova, R. M.; Fedotova, I. V. Synthesis, structure, and properties of nickel complexes with nitrilotris (methylenephosphonic acid) $[\text{Ni}(\text{H}_2\text{O})_3\text{N}(\text{CH}_2\text{PO}_3\text{H})_3]$ and $\text{Na}_4[\text{Ni}(\text{H}_2\text{O})\text{N}(\text{CH}_2\text{PO}_3)_3] \cdot 11\text{H}_2\text{O}$. *Crystallogr. Reports*, **2016**, 61(2), 216-224.
- Somov, N. V.; Chausov, F. F.; Lomova, N. V.; Zakirova, R. M.; Petrov, V. G.; Zhiron, D. K.; Shumilova, M. A. Yttrium Coordination Compounds with Nitrilotris (Methylenephosphonic Acid). *Russ. J. Coord. Chem.*, **2019a**, 45(5), 361-370.
- Somov, N. V.; Chausov, F. F.; Lomova, N. V.; Zakirova, R. M.; Fedotova, I. V.; Petrov, V. G.; Shumilova, M. A.; Zhiron, D. K. Nitrilotris (methylenephosphonic) Complexes of Lanthanides $[\text{Na}(\text{H}_2\text{O})_x]_2[\text{Ln}^{\text{III}}\text{Na}_6\text{H}(\text{H}_2\text{O})_{10}\{\text{N}(\text{CH}_2\text{PO}_3)_3\}_2] \cdot n\text{H}_2\text{O}$ ($\text{Ln}^{\text{III}} = \text{Pr, Nd}$). *Russ. J. Coord. Chem.*, **2019b**, 45(1), 47-55.
- Sone, Y.; Ekdunge, P.; Simonsson, D. Proton conductivity of Nafion 117 as measured by a four-electrode AC impedance method. *J. Electrochem. Soc.*, **1996**, 143(4), 1254-1259.

T

- Tantayakom, V.; Fogler, H. S.; De Moraes, F. F.; Bualuang, M.; Chavadej, S.; Malakul, P. Study of Ca-ATMP Precipitation in the Presence of Magnesium Ion. *Langmuir*, **2009**, 20(6), 2220-2226.

Chapter 7
Alkali & Alkaline Earth
Metals Tetrphosphonates





UNIVERSIDAD
DE MÁLAGA

Phosphonic acids containing the amino-bis(methylenephosphonate) moiety are versatile ligands to obtain novel metal-organic derivatives with a great variety of topologies, including closely packed three-dimensional, pillared layered networks or layered solids, which usually may present free acidic groups in their structures. These solids feature unique properties for a wide range of applications such as proton conductivity, ion-exchange, heterogeneous catalysis, photoluminescence, etc (Clearfield & Demadis, 2012).

Some of the structural features, which make attractive the use of aminomethylenephosphonates, lie in the flexibility of the polymethylene chain linked to the N atoms and the zwitterionic character of these molecules, since at pH < 10 the basic N atom is always protonated (Cardiano et al., 2017). Furthermore, they can be prepared from primary amines by the Moedritzer-Irani reaction (also called Mannich-type condensation), which is a simple and economic method and reasonably pure products can be obtained by recrystallization, although with some limitations when the acids are very soluble in water (Firmino et al., 2018).

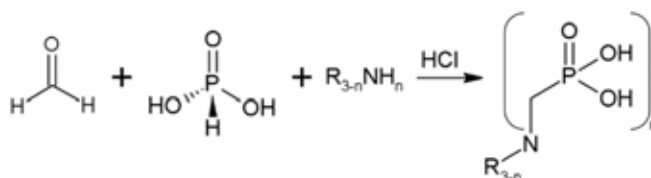


Figure 7.1. Mannich-type condensation.

Employing diamines, a particular group of diaminotetraphosphonates can be prepared, where the N atoms are connected with a systematically elongated polymethylene chain ($n = 2-12$), whereas the two ends of the molecule are identical, with an amino-bis(methylenephosphonate) on each side (Figure 7.2) (Villemin & Didi, 2015).

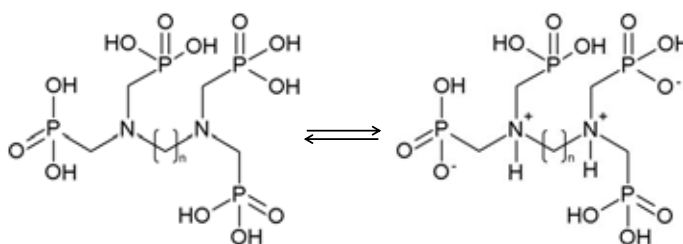


Figure 7.2. General structure of the tetraphosphonate family members in the zwitterionic form.

Following this procedure, many metal alkyldiamine-tetrakis(methylenephosphonates) have been prepared. For instance, with the ligand EDTMP ($n=2$), Ga(III), ^{153}Sm , ^{175}Yb and ^{177}Lu complexes, suitable as therapeutic radiopharmaceutical for treatment and/or palliation of bone metastases cancer, have been reported (Su, Qiu & Jia, 2005; Singh et al., 1989; Eary et al., 1993; Holmes, 1992; Mathew et al., 2004; Ando et al., 1998; Chakraborty et al., 2007). Three dimensional $[\text{M}^{\text{II}}(\text{TDTMP})\cdot 2\text{H}_2\text{O}]$ solids ($\text{M}^{\text{II}} = \text{Mg}$, Ca , Mn , Fe , Co , Ni , Zn and Cd ; $n=4$) have been synthesised by high-throughput methodology. In these compounds, M^{2+} ions are surrounded by six phosphonate groups to form eight-membered rings by alternating $\text{M}^{\text{II}}\text{O}_6$ and PO_3C polyhedra, with the layers connected by the organic groups (Stock & Bein, 2004; Stock, Rauscher & Bein, 2004). By increasing the alkyl chain length of the ligand to $n = 8$ (ODTMP), 3D ultramicroporous magnesium derivatives have been obtained: $\text{MgH}_6\text{ODTMP}\cdot 2\text{H}_2\text{O}(\text{DMF})_{0.5}$ (**1**) by hydrothermal reaction and $\text{MgH}_6\text{ODTMP}\cdot 2\text{H}_2\text{O}$ (**2**) and $\text{MgH}_6\text{ODTMP}\cdot 6\text{H}_2\text{O}$ (**3**) upon H_2O and DMF removal and subsequent rehydration (Colodrero et al. 2012a). These solids have been shown to exhibit high CO_2 selectivity from CO_2/CH_4 mixtures. In addition, solid (**3**) displayed high proton conductivity ($\sigma = 1.6\cdot 10^{-3} \text{ S}\cdot\text{cm}^{-1}$ at 19°C and 100% RH).

Regarding the ligand **hexamethylenediamine-N,N,N',N'-tetrakis(methylenephosphonic acid)** (hereinafter referred to as HDTMP), a variety of multifunctional solids have been reported. The two dimensional calcium derivative, $\text{Ca}[(\text{HO}_3\text{PCH}_2)_2\text{NH}(\text{CH}_2)_6\text{NH}(\text{CH}_2\text{PO}_3\text{H})_2]\cdot 2\text{H}_2\text{O}$ (CaH_6DTMP), is remarkable for its reversible breathing mechanism, i.e. the capability of the network to reversibly uptake $\text{NH}_3/\text{H}_2\text{O}$ (Figure 7.3) (it can accommodate up to 10 $\text{NH}_3/\text{H}_2\text{O}$ molecules in the interlamellar space) through a subtle structural adjust occurring in the layers upon adsorption-desorption of the guest molecules (Colodrero et al., 2009). The intercalation process of NH_3 from concentrated aqueous solution (28%) gave rise to other three new compounds: $\text{CaH}_6\text{DTMP}\cdot 6\text{H}_2\text{O}\cdot 4\text{NH}_3$, $\text{CaH}_6\text{DTMP}\cdot 1.5\text{H}_2\text{O}\cdot 1.5\text{NH}_3$ and $\text{CaH}_6\text{DTMP}\cdot 5\text{NH}_3$.

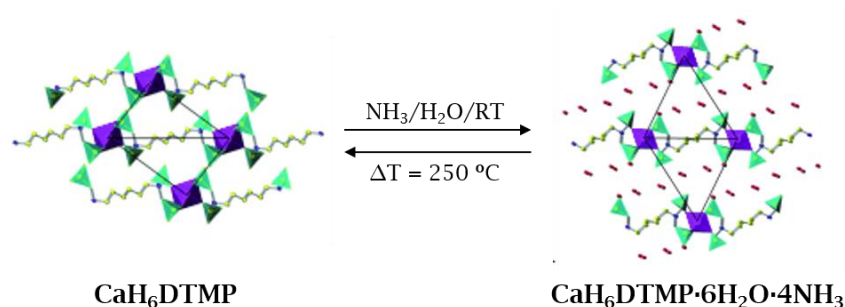


Figure 7.3. The reversible intercalation of $\text{NH}_3/\text{H}_2\text{O}$ in CaH_6DTMP (Colodrero et al., 2009).

Demadis, Mantzaridis & Lykoudis (2006) reported a 3D zinc derivative: $\{\text{Zn}[(\text{HO}_3\text{PCH}_2)_2\text{N}(\text{H})-(\text{CH}_2)_6\text{N}(\text{H})(\text{CH}_2\text{PO}_3\text{H})_2]\cdot\text{H}_2\text{O}\}_n$, Zn-HDTMP. The distorted octahedral environment of Zn^{2+} is formed exclusively by phosphonate oxygen atoms. This solid offers excellent corrosion protection for carbon steel (~170% reduction in the corrosion rate). Other anticorrosion passive films of M-HDTMP (M= Sr^{2+} and Ba^{2+}) have been also reported by Demadis et al. (2009). Isostructural Sr^{2+} and Ba^{2+} derivatives are composed of corrugated sheets, made up by zig-zag chains, where the metal ions exhibit an octacoordinated environment and the ligand HDTMP is monodeprotonated, which allows for a H-bond interaction of the phosphonic groups with lattice water.

The room temperature-synthesised 3D ultramicroporous lanthanum material, namely $\text{La}[(\text{O}_3\text{PCH}_2)(\text{HO}_3\text{PCH}_2)\text{N}(\text{H})(\text{CH}_2)_6\text{N}(\text{H})(\text{CH}_2\text{PO}_3\text{H})_2]\cdot 7\text{H}_2\text{O}$, $\text{La}(\text{H}_5\text{DTMP})\cdot 7\text{H}_2\text{O}$, is built of LaO_6 polyhedra chains, which are formed exclusively by six oxygen atoms of bridging phosphonate groups. This solid contains 1D channels filled with lattice water molecules that interact with the protonated phosphonate groups through hydrogen bonds. Such configuration originates effective proton conducting pathways ($\sigma = 8\cdot 10^{-3} \text{ S}\cdot\text{cm}^{-1}$, at 24 °C and 98% relative humidity, and $E_a = 0.25 \text{ eV}$). Moreover, this solid presents a strong irreversible NO adsorption capacity. Upon dehydration, the crystalline compounds $\text{La}(\text{H}_5\text{DTMP})\cdot 2\text{H}_2\text{O}$ and $\text{La}(\text{H}_5\text{DTMP})$ were obtained (Figure 7.4), which feature highly corrugated layers with different degrees of conformational flexibility of the organic chain. The anhydrous solid, however, was not found to revert to the fully hydrated phase upon exposure the sample over a saturated NaCl solution (Colodrero et al., 2012b).

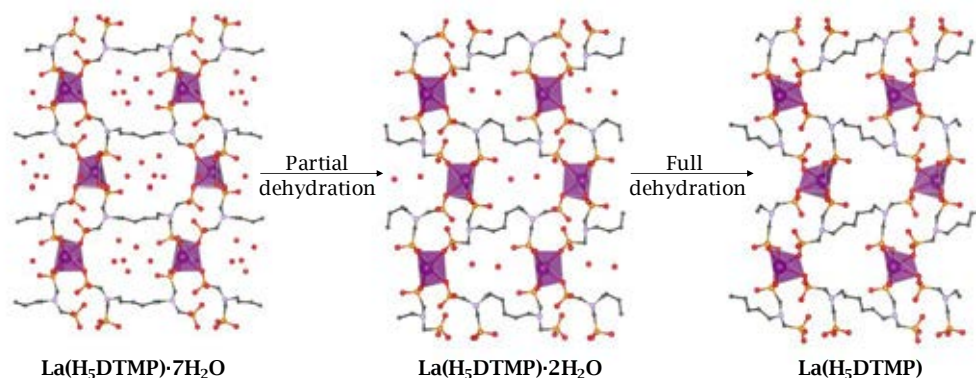


Figure 7.4. Progressive structural changes of $\text{La}(\text{H}_3\text{DTMP}) \cdot 7\text{H}_2\text{O}$ upon dehydration.

Mendes et al. (2017) reported a new photoluminescent family of 3D lanthanide derivatives, $[\text{Ln}_2(\text{SO}_4)_2(\text{HO}_3\text{PCH}_2)_2\text{N}(\text{H})(\text{CH}_2)_6\text{N}(\text{H})(\text{CH}_2\text{PO}_3\text{H})_2(\text{H}_2\text{O})_4] \cdot 10\text{H}_2\text{O}$ ($\text{Ln} = \text{Eu}, \text{Sm}, \text{Gd}$), prepared by the addition of sulfuric acid to the reaction media. These solids were obtained by microwave irradiation (80 °C), which was claimed to reduce significantly the reaction time, from 2 months to 15 min, respect to the conventional methodology. Sulfuric acid is believed to be essential in the formation of these solids by competing with the ligand for metal coordination positions. In this structure, the Ln^{3+} ion is octacoordinated, surrounded by four oxygen phosphonate atoms, two coordination water molecules and one sulfate ion in a typical bidentate coordination fashion. Layers are built up from alternating MO_8 and PO_3C polyhedra in the plane *ab*. These 2D layers are connected by the organic linker alkyl chain, originating a compact 3D structure. The pores of the structure are occupied by disordered water molecules (Figure 7.5).

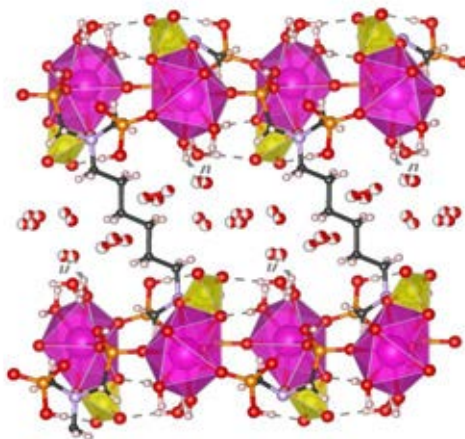


Figure 7.5. View of the packing of $[\text{Eu}_2(\text{SO}_4)_2(\text{HO}_3\text{PCH}_2)_2\text{N}(\text{H})(\text{CH}_2)_6\text{N}(\text{H})(\text{CH}_2\text{PO}_3\text{H})_2(\text{H}_2\text{O})_4]\cdot 10\text{H}_2\text{O}$ along a -axis.

The synthesis methodologies, structural diversity and properties showed by lanthanide tetraphosphonic-based metal-organic frameworks have been recently reviewed (Firmino et al., 2018).

In this section, the synthesis, structural features and properties, mainly gas adsorption and proton conductivity, of alkali ($M^+ = \text{Li}^+, \text{Na}^+, \text{K}^+, \text{Rb}^+$ and Cs^+) and Mg^{2+} derivatives of the tetraphosphonate ligand **hexamethylenediamine- $\text{N},\text{N},\text{N}',\text{N}'$ -tetrakis(methylenephosphonic acid)**, HDTMP, are studied. In addition, some post-synthesis modifications are also discussed as alternative method to improve the proton transfer mechanisms. The results of this study have been published in the papers Salcedo et al. (2018) and Colodrero et al. (2018).

7.1. Synthesis

These compounds were synthesised by two different methods:

- (i) Crystallization at room temperature, for the alkali metal derivatives ($M = \text{Li}^+, \text{Na}^+, \text{K}^+, \text{Rb}^+$ and Cs^+).
- (ii) Hydrothermal or microwave-assisted synthesis, for magnesium derivative.

7.1.1. Synthesis of Alkali Metal Tetraphosphonates

All alkali metal derivatives were obtained by mixing the aqueous solutions of the HDTMP acid with the solution of the corresponding alkali salt or hydroxide in

different molar ratios (Table 7.1). The final colourless solution was placed in a glass test tube and a quantity of EtOH as a co-solvent was then carefully layered on top of the aqueous layer with a Pasteur pipette in order to facilitate crystallization in the mixed H₂O/EtOH layer (Figure 7.6). After a couple of weeks, large colourless needle-like crystals appeared which were isolated by filtration, washed with EtOH and air-dried.

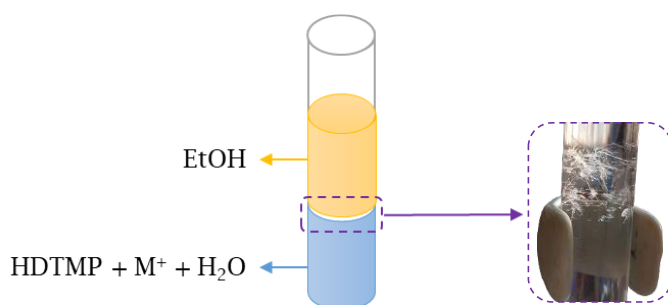


Figure 7.6. M(I)-HDTMP synthesis scheme.

Among all of the M(I):HDTMP molar ratios tested, only monophasic solids were isolated when this ratio was 2:1, except for the lithium derivative, which was synthesised using a 1:1 molar ratio. Other synthesis conditions, such as hydrothermal or microwave-assisted did not lead to any solid. The crystallization time can be reduced by passing a current of nitrogen through the solvent using a Stuart SBH CONC/1 sample concentrator.

Table 7.1. Summary of the quantities used for each reagent.

SAMPLE	SOLUTION 1		SOLUTION 2		CO-SOLVENT
	HDTMP (mmol)	H ₂ O (mL)	Alkali salt or hydroxide (mmol)	H ₂ O (mL)	EtOH (mL)
Li-HDTMP-4W	1	20	1	10	20
Na-HDTMP	2	20	4	10	20
K-HDTMP	2	20	4	10	20
Rb-HDTMP	2	10	4	5	30
Cs-HDTMP	0.3	20	0.6	5	30

For the lithium derivative, a new anhydrous crystalline phase (**Li-HDTMP-0W**) was also obtained by heating the as-synthesised solid (**Li-HDTMP-4W**) at 200 °C for 2 h. The dehydration/rehydration transformation is reversible as below discussed. Table 7.2 sums up some characteristics of the isolated M(I)-HDTMP compounds.

Table 7.2. Composition and some structural characteristics of **M(I)-HDTMP** compounds (SC = single crystal; P = powder).

Acronym	Stoichiometric	Structure	Space group
Li-HDTMP-4W	$\text{Li}_2(\text{HO}_3\text{PCH}_2)_2\text{NH}(\text{CH}_2)_6\text{NH}(\text{CH}_2\text{PO}_3\text{H})_2 \cdot 4\text{H}_2\text{O}$ (SC)	1D	$\text{P}\bar{1}$
Li-HDTMP-0W	$\text{Li}_2(\text{HO}_3\text{PCH}_2)_2\text{NH}(\text{CH}_2)_6\text{NH}(\text{CH}_2\text{PO}_3\text{H})_2$ (P)	2D	$\text{P}\bar{1}$
Na-HDTMP	$\text{Na}_2(\text{HO}_3\text{PCH}_2)_2\text{NH}(\text{CH}_2)_6\text{NH}(\text{CH}_2\text{PO}_3\text{H})_2 \cdot 6\text{H}_2\text{O}$ (SC) $\text{Na}_2(\text{HO}_3\text{PCH}_2)_2\text{NH}(\text{CH}_2)_6\text{NH}(\text{CH}_2\text{PO}_3\text{H})_2 \cdot 8\text{H}_2\text{O}$ (P)	1D	$\text{P}\bar{1}$
K-HDTMP	$\text{K}_2(\text{HO}_3\text{PCH}_2)_2\text{NH}(\text{CH}_2)_6\text{NH}(\text{CH}_2\text{PO}_3\text{H})_2 \cdot 8\text{H}_2\text{O}$ (SC)	2D	$\text{P}2_1/c$
Rb-HDTMP	$\text{Rb}(\text{H}_2\text{O}_3\text{PCH}_2)_2\text{NH}(\text{CH}_2)_6\text{NH}(\text{CH}_2\text{PO}_3\text{H})_2(\text{H}_2\text{O})_2 \cdot 2\text{H}_2\text{O}$ (SC)	3D	$\text{C}2/c$
Cs-HDTMP	$\text{Cs}(\text{H}_2\text{O}_3\text{PCH}_2)_2\text{NH}(\text{CH}_2)_6\text{NH}(\text{CH}_2\text{PO}_3\text{H})_2(\text{H}_2\text{O})_2 \cdot 2\text{H}_2\text{O}$ (SC)	3D	$\text{P}\bar{1}$

7.1.2. Synthesis of Magnesium Tetrakisphosphonates

Synthesis conditions of magnesium derivatives were screened by high-throughput methodology in order to optimize the following parameters:

- Mg:HDTMP molar ratios: 1:1, 1:2 2:1, 3:2, 4:1.
- Initial pH values: 0.5 - 6.5.
- Temperature conditions: 130, 140 and 180 °C.
- Solvents: H_2O or DMF/ H_2O mixture (2:1 v/v or 4:1 molar).

A home-designed parallel-synthesis system consisting of 6 or 36 Teflon reactor chambers in a 3x2 or 6x6 array was employed. Reactors had an inner diameter of 19 mm, a depth of 18 mm and a total volume of 5 mL (Figure 7.7a). A thin sheet of Teflon covered the reaction vessels, which were then placed in an aluminium autoclave (Figure 7.7b) (Colodrero et al., 2010).

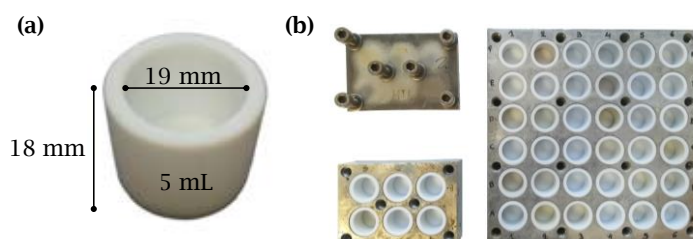


Figure 7.7. (a) Image of the a reaction vessel and (b) details of the home-designed parallel-synthesis systems.

Two crystalline monophasic derivatives were isolated, **Mg-HDTMP-1** and **Mg-HDTMP-2** (Table 7.3).

Mg-HDTMP-1 was obtained in aqueous solution only for 1:2 Mg:HDTMP molar ratio and pH 1, at 140 °C during 7 days. Other synthesis conditions gave rise to a mixture of phases. In addition, a third crystalline anhydrous phase, **Mg-HDTMP-1deh**, was obtained upon heating **Mg-HDTMP-1** at 180 °C.

Mg-HDTMP-2 was isolated from a hydrothermal (Mg:HDTMP molar ratio of 1:2.8, 180 °C, 5 days) or a solvothermal (DMF/H₂O mixture 2:1 v/v, Mg:HDTMP molar ratio of 1:4, 130 °C, 3 days) reaction. The optimal pH was 2.1.

The same synthetic conditions were then used for the microwave-assisted synthesis of **Mg-HDTMP-1** and **Mg-HDTMP-2**, which resulted in a fast method (30 min) leading to higher yields.

Table 7.3. Composition and some structural characteristics of **Mg-HDTMP** compounds.

Acronym	Stoichiometric	Structure	Space group
Mg-HDTMP-1	$\{\text{Mg}[(\text{HO}_3\text{PCH}_2)_2\text{NH}(\text{CH}_2)_6\text{NH}(\text{CH}_2\text{PO}_3\text{H})_2]\cdot\text{H}_2\text{O}\}_n$	3D	P $\bar{1}$
Mg-HDTMP-1deh	$\{\text{Mg}[(\text{HO}_3\text{PCH}_2)_2\text{NH}(\text{CH}_2)_6\text{NH}(\text{CH}_2\text{PO}_3\text{H})_2]\}_n$	3D	C2/c
Mg-HDTMP-2	$\{\text{Mg}[(\text{HO}_3\text{PCH}_2)_2\text{NH}(\text{CH}_2)_6\text{NH}(\text{CH}_2\text{PO}_3\text{H})_2]\}_n$	3D	P $\bar{1}$

7.2. Characterisation

All compounds were extensively characterised using the following techniques.

7.2.1. Elemental and Thermogravimetric Analysis

Elemental analysis for alkali metal and magnesium derivatives are given in Appendix II (Table AII.6).

Thermogravimetric analysis were recorded from RT to 900 °C at a heating rate of 10 °C·min⁻¹ under air flow. For alkali derivatives (Figure 7.8), water loss took place between 50 (K-HDTMP) and 100 °C (Li- and Cs-HDTMP) until 300 °C. For Li-HDTMP, an additional weight loss was observed in the range of 220-300 °C, which can be attributed to partial condensation of POH groups. In the cases of Na- and Rb-HDTMP polycrystalline samples, higher water content, as compared to the corresponding single crystals, was observed (Table 7.4). This result may be explained by the coexistent of phases with different water content, in agreement with the presence of some extra diffraction peaks in their XRPD patterns.

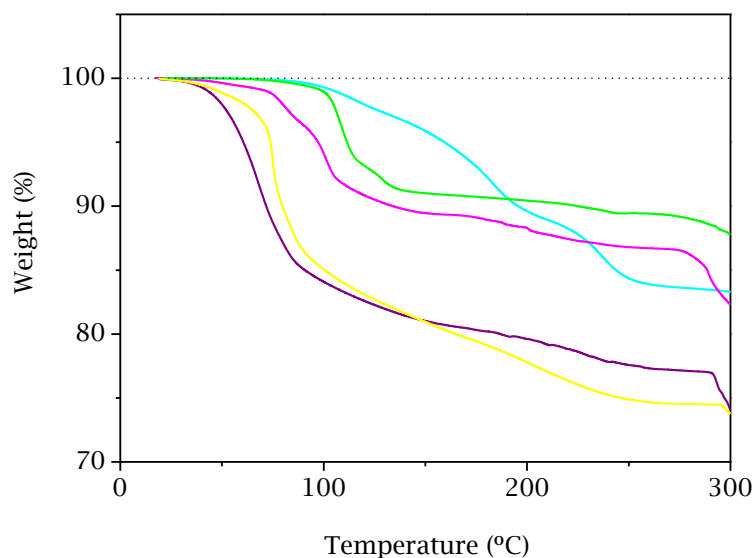


Figure 7.8. Thermal analysis for compounds: Li-HDTMP-4W (cyan), Na-HDTMP (yellow), K-HDTMP (purple), Rb-HDTMP (magenta) and Cs-HDTMP (green).

Regarding to the magnesium compounds (Figure 7.9), solid Mg-HDTMP-1 dehydrates between 135 °C and 180 °C, with an associate weight loss of 3.79% (calculated: 3.38%); whereas solid Mg-HDTMP-2 does not show any appreciable weight loss in this temperature range from TG analysis, which confirms its anhydrous nature. For both Mg²⁺ derivatives, the ligand decomposition starts above 320 °C.

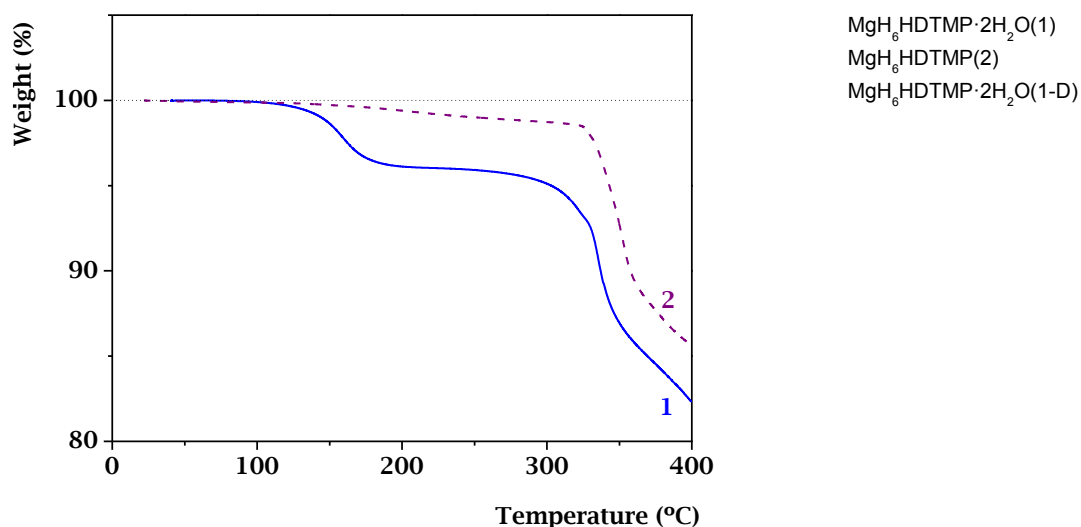


Figure 7.9. Thermal analysis for compounds **Mg-HDTMP-1** (blue) and **Mg-HDTMP-2** (purple).

Table 7.4. Observed (TG) and calculated water weight loss (%) at 200 °C for **M(I)**- and **M(II)**-HDTMP compounds.

Sample	Observed	Calculated
Li-HDTMP-4W	15.2	12.5
Na-HDTMP	22.4	18.7
K-HDTMP	20.4	20.2
Rb-HDTMP	12.9	11.1
Cs-HDTMP	9.6	10.3
Mg-HDTMP-1	3.79	3.38

7.2.2. Structural Characterisation

The crystal structures of alkali metal compounds, except that of the anhydrous lithium derivative, were solved from single crystal X-ray diffraction data (Chapter 3, section 3.4.5).

The crystal structure of **Li-HDTMP-0W** was obtained by Rietveld refinement from synchrotron X-ray powder diffraction data collected at the ID15A beamline at the ESRF (Grenoble, France) with a wavelength of 0.18972(1) Å. The crystal structure of **Li-HDTMP-4W** was used as starting model. The refinement was carry out by using

the GSAS package (Larson & Von Dreele, 2004) with soft constraints to maintain the chemically reasonable geometries for the phosphonate, amine groups and alkyl chain (see Chapter 3, Table 3.2). A summary of crystallographic data is given in Table 7.5 and the Rietveld plot for **Li-HDTMP-0W** is displayed in Figure 7.10.

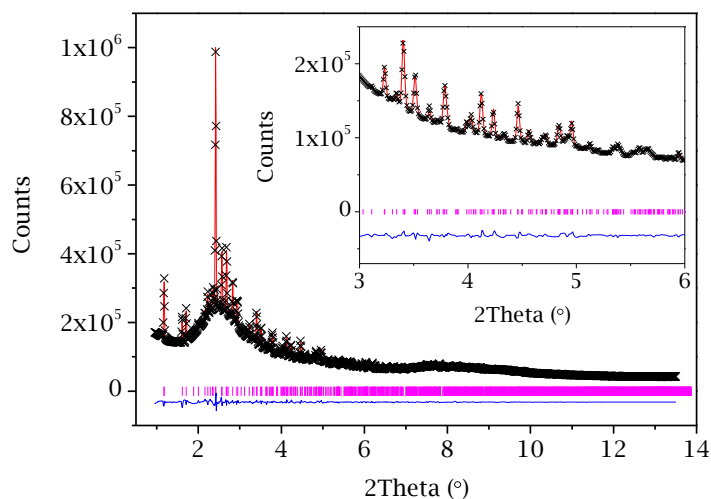


Figure 7.10. Final Rietveld plot for **Li-HDTMP-0W**.

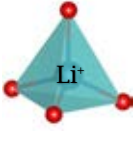
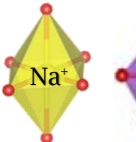
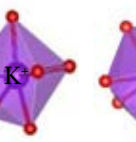
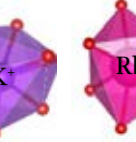
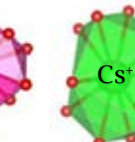

These compounds show a rich structural diversity, which depend on the cation size, from monodimensional (such as Li^+ and Na^+) through layered (K^+) to pillared-layered structures (Rb^+ and Cs^+). The effect of the alkali metals ionic radii is reflected on the M-O bond distances and the coordination number of the metal centre (both of them increase with the ionic radius) (Table 7.6).

Li-HDTMP-4W is a monodimensional solid, in which the lithium ion is tetrahedrally coordinated by four oxygen atoms from two water molecules and two different HDTMP ligands. Such coordination mode creates 30-membered rings through the interaction of two phosphonate groups of each ligand with two lithium ions. These rings further extend into ribbons by coordinating the remaining phosphonate groups of the ligand to other lithium ions. In addition, the rings are stabilized by intramolecular hydrogen bonding between phosphonate groups. (Figure 7.11a). The ribbons, in turn, are connected between themselves by H-bonds (Table 7.7) of phosphonate groups with the protonated amine group and water molecules (Figure 7.11b).

Table 7.5. Selected crystallographic data for M(O)-HDTMP compounds.

Phase	Li-HDTMP-4W	Li-HDTMP-0W	Na-HDTMP	K-HDTMP	Rb-HDTMP	Cs-HDTMP
Space group	P $\bar{1}$	P $\bar{1}$	P $\bar{1}$	P2 ₁ /c	C2/c	P $\bar{1}$
Chemical formula	Li ₂ P ₄ O ₁₆ N ₂ C ₁₀ H ₃₄	Li ₂ P ₄ O ₁₂ N ₂ C ₁₀ H ₂₆	Na ₂ P ₄ O ₂₃ N ₂ C ₁₀ H ₄₈	K ₂ P ₄ O ₂₀ N ₂ C ₁₀ H ₄₂	RbP ₄ O ₁₆ N ₂ C ₁₀ H ₃₅	CS ₂ P ₄ O ₁₆ N ₂ C ₁₀ H ₃₅
Formula mass (g·mol⁻¹)	576.16	504.10	734.36	712.53	648.75	696.19
λ (Å)	0.71073	0.18972	0.71073	0.71073	0.71073	0.71073
a (Å)	5.9728(6)	5.9014(4)	7.6682(1)	7.7178(1)	6.0257(5)	6.0072(2)
b (Å)	9.4557(9)	9.2693(7)	11.5335(1)	33.0373(4)	14.1011(7)	7.6864(2)
c (Å)	11.0182(11)	9.5123(7)	18.0768(2)	11.7577(1)	28.762(2)	14.8250(4)
α (Å)	74.418(7)	85.902(4)	97.378(1)	90.000	90.000	86.677(2)
β (Å)	76.170(7)	77.676(5)	94.792(1)	103.709(1)	94.816(3)	78.906(2)
γ (Å)	84.313(7)	85.588(6)	101.705(1)	90.000	90.000	67.611(2)
Unit cell volume (Å³)	581.622(10)	506.04(8)	1542.61(3)	2912.52(6)	2435.25(6)	621.01(3)
Z	1	2	2	4	4	1
No. of reflections	10054	2254	9784	8877	4773	3748
No. of independent reflections	1693		7729	7448	3984	2722
Data/Restraints/Parameters	1719/7/175	1428/33/97	7729/28/457	7448/22/409	3984/10/189	2722/8/176
GoF	0.991	-	1.052	1.036	1.039	1.024
R factor [$I > 2\sigma(I)$]	^a R ₁ = 0.0578	-	^a R ₁ = 0.0368	^a R ₁ = 0.0287	^a R ₁ = 0.0328	^a R ₁ = 0.0344
	^w R ₂ = 0.1399	-	^w R ₂ = 0.0905	^w R ₂ = 0.0666	^w R ₂ = 0.0791	^w R ₂ = 0.0676
R factor (all data)	^a R ₁ = 0.0904	-	^a R ₁ = 0.0527	^a R ₁ = 0.0393	^a R ₁ = 0.0436	^a R ₁ = 0.0580
	^w R ₂ = 0.1595	-	^w R ₂ = 0.0981	^w R ₂ = 0.0713	^w R ₂ = 0.0838	^w R ₂ = 0.0759
R_{wp}	-	0.0115	-	-	-	-
R_p	-	0.0220	-	-	-	-
R_F	-	0.0427	-	-	-	-
CCDC number	1584820	1584815	1584819	1584817	1584816	1584818

Table 7.6. Alkali metals ionic radii, coordination environment and number.

						
Coordination	4	6	6	8	8	10
Ionic radii	0.76	1.02	1.38	1.38	1.48	1.67

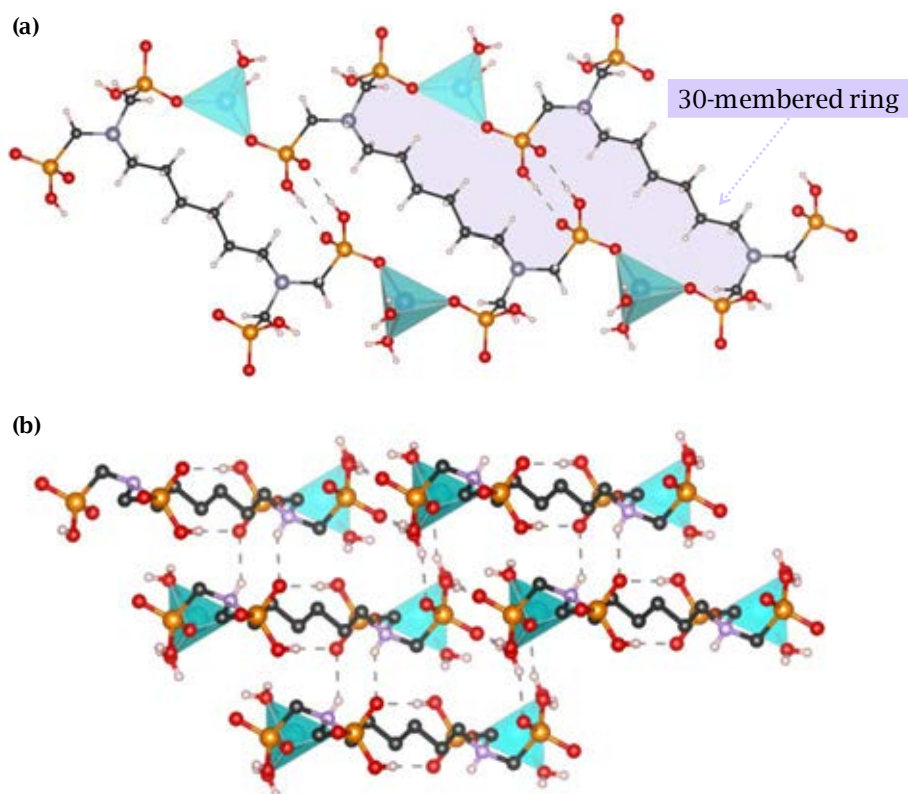
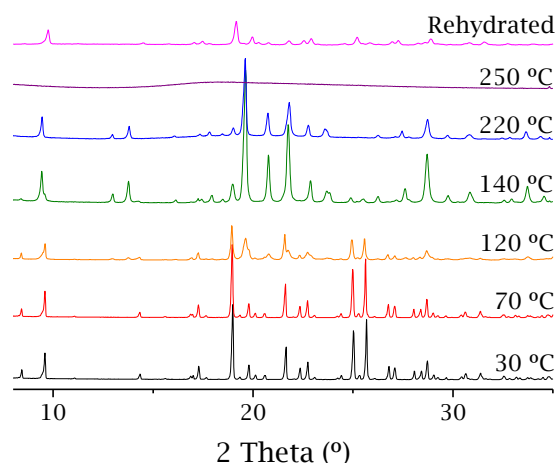

Figure 7.11. View of (a) a single ribbon and (b) ribbons packing along *b* axis in the structure of Li-HDTMP-4W (C-H bonds are not shown).

Table 7.7. Summary of the hydrogen bonding data for **Li-HDTMP-4W**.

D-H...A	D-H (Å)	H...A (Å)	D...A (Å)	D-H-A (°)	Symmetry operator for A
O1-H1o...O2	0.827(19)	1.77(2)	2.593(4)	178(5)	-x+1, -y+1, -z
O5-H5o...O4	0.819(19)	1.81(2)	2.624(4)	175(5)	-x+2, -y+1, -z+1
O7-H7a...O2	0.815(19)	1.91(2)	2.727(4)	178(5)	-x+1, -y+1, -z
O7-H7b...O3	0.828(19)	2.01(2)	2.806(4)	162(4)	-x+2, -y+1, -z
O8-H8a...O7	0.831(19)	2.03(3)	2.827(5)	161(6)	-x+1, -y+2, -z
O8-H8b...O5	0.810(20)	2.19(2)	2.996(4)	169(5)	x-1, y, z
N1-H1n...O4	0.861(18)	2.05(3)	2.794(4)	145(4)	-x+1, -y+1, -z+1

Thermal stability of **Li-HDTMP-4W** was studied by X-ray powder thermodiffraction, from RT up to 250 °C and a heating rate of 5 °C·min⁻¹. According to the TG curve (Figure 7.8), lithium derivative is stable up to 120 °C, above which the solid starts to loss water and a crystalline anhydrous phase (**Li-HDTMP-0W**) develops at the expenses of the former one. This phase becomes amorphous about 250 °C (Figure 7.12).

**Figure 7.12.** Thermodiffraction patterns for **Li-HDTMP-4W**.

Upon rehydration, slowly under ambient conditions or quickly (5h) at 80 °C and 95% RH, the initial crystalline phase, **Li-HDTMP-4W**, is retrieved; indicating that this

dehydration/rehydration process is fully reversible, in the range of temperatures studied (Figure 7.13).

Li-HDTMP-0W presents a bidimensional structure as a result of the condensation of the ribbon-like chains, but the tetra-coordinated environment of lithium is still maintained by binding to phosphonate oxygen atoms exclusively. In addition, the formation of edge-sharing LiO_6 dimers along a -axis gives rise to the appearance of 8-membered rings in the layers (Figure 7.14).

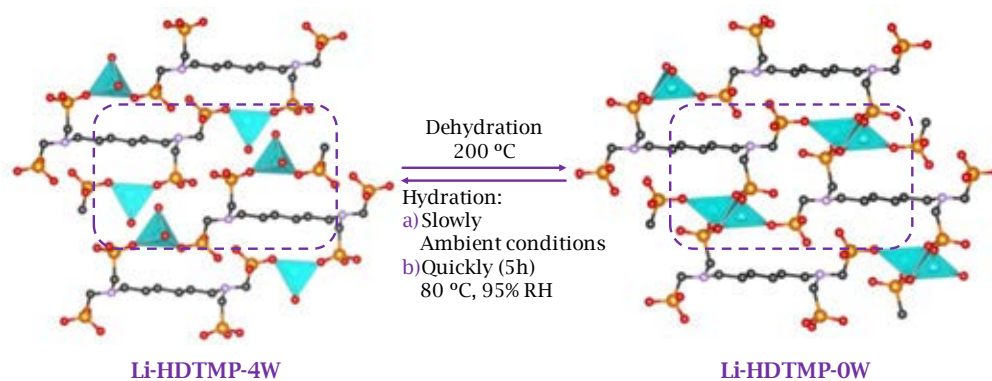


Figure 7.13. Reversible structural transformation of **Li-HDTMP** compounds.

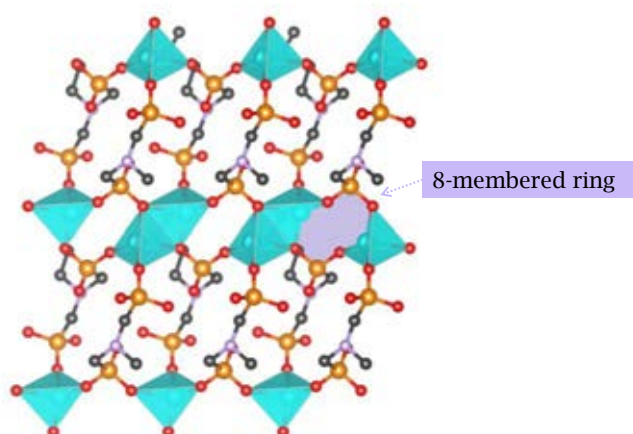


Figure 7.14. View along c axis of the 8-membered rings in the layers of **Li-HDTMP-0W**.

Na-HDTMP is also a monodimensional solid that crystallizes in the triclinic crystal system ($P\bar{1}$) with three crystallographically independent sodium ions in the

lattice. All of them are hexa-coordinated by six oxygen atoms (Na1: four from water molecules and two from two different ligand molecules; Na2: five from water molecules and one from a phosphonate moiety; Na3: all of them from water molecules). By sharing edge and face, Na1 and Na2 polyhedra form 1D-ribbons along *a*-axis, whereas Na3 acts as a counter ion, $[\text{Na}(\text{H}_2\text{O})_6]^+$, of the negatively charged ribbons (Figure 7.15).

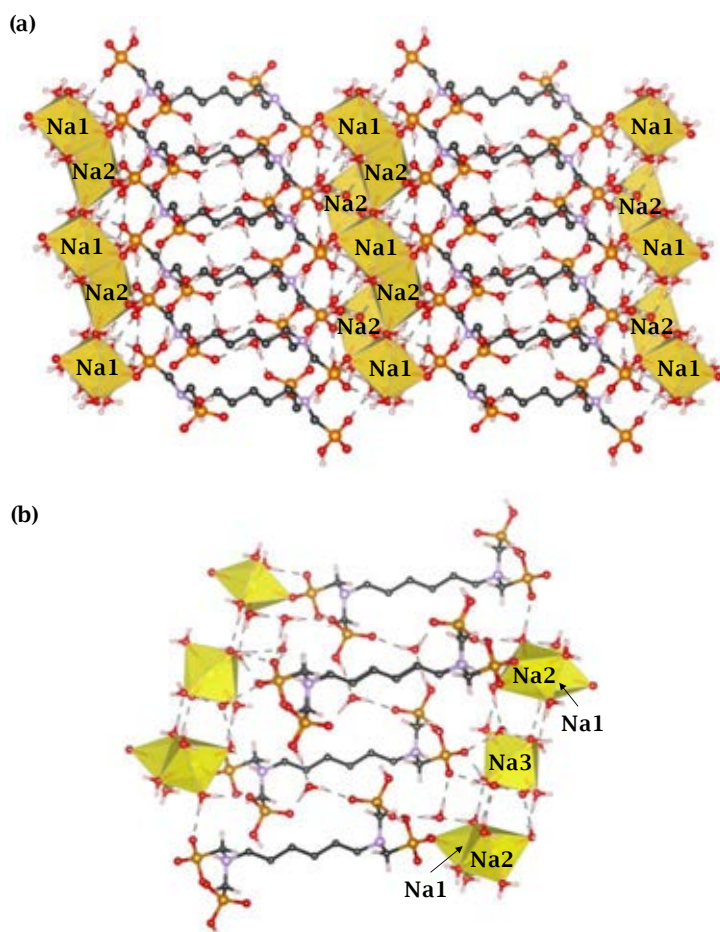


Figure 7.15. View of (a) the 1D-ribbons along *b* axis and (b) the 3D-packing in Na-HDTMP (some C-H bonds are not shown).

The structure of **K-HDTMP** contains two crystallographically independent potassium ions, one (K1) octa-coordinated and another one (K2) hexa-coordinated. K1 is coordinated by five water molecules and three phosphonate oxygen atoms from

two different ligand molecules and K2, by five water molecules and one phosphonate oxygen atom. Dimers are formed by face-sharing K1 and K2 polyhedral through three oxygen atoms which are connected to each other by one bridged water molecule giving rise to chains. The zig-zag layers generated are held together through hydrogen bonds assisted by lattice H₂O molecules located between them.

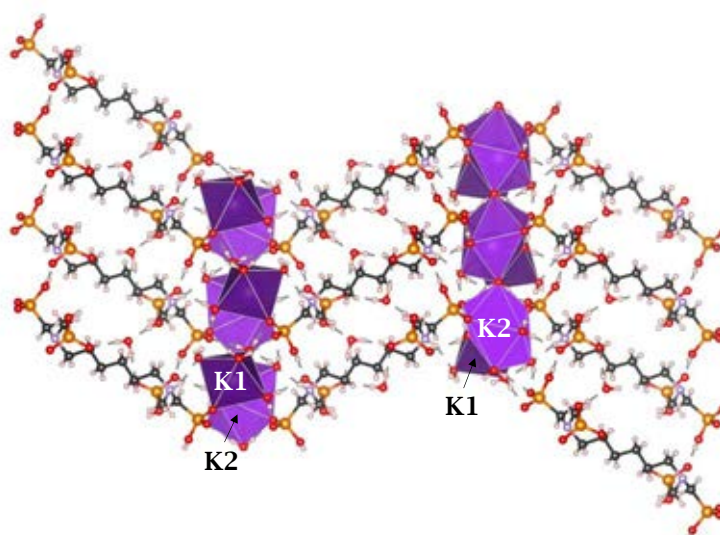


Figure 7.16. Layers packing viewed along *a* axis for **K-HDTMP**.

The alkali metal ion in **Rb-** and **Cs-HDTMP** derivatives feature octa- and deca-coordinated MO_x environments, respectively [six (Rb⁺) or eight (Cs⁺) oxygen atoms from four different ligands and two others from water molecules]. In the case of **Rb-HDTMP**, sheets are formed by isolated Rb⁺ polyhedra bridged by phosphonate groups and sheet packing is established through the connection of the organic linker to adjacent sheets. In contrast, the sheets of **Cs** derivative are formed by edge-sharing Cs⁺ polyhedra bridged by phosphonate groups. As result of this connectivity, pillared layered structures are formed in both cases, with the lattice water being placed in between the sheets and taking part of a hydrogen bond network.

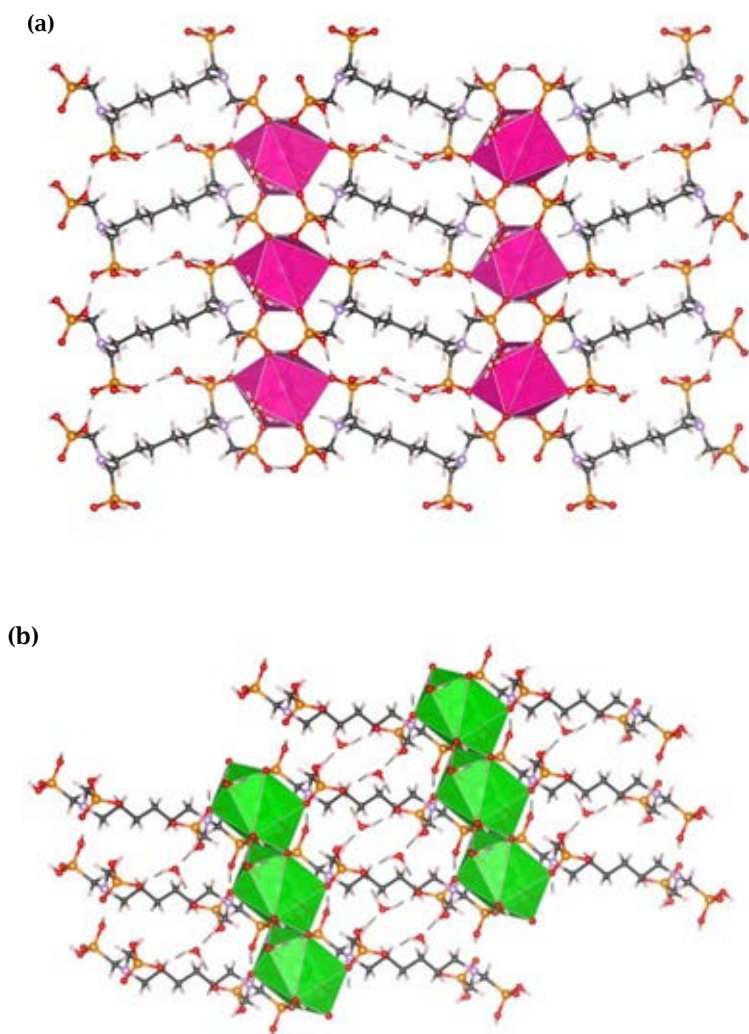


Figure 7.17. View of the pillared layered structure of (a) **Rb-HDTMP** along a axis and (b) **Cs-HDTMP** along b axis (C-H bonds are not shown).

The structures of **Mg-HDTMP-1** and **Mg-HDTMP-2** were solved following an *ab initio* methodology using laboratory X-ray powder diffraction data. The integrated intensities were extracted using the program DAJUST (Vallcorba et al., 2012) and the crystal structures were solved by direct methods using the program XLENS (Rius, 2011). For compound **Mg-HDTMP-1**, a starting structural model with 31 atoms in the asymmetric unit cell was obtained. For compound **Mg-HDTMP-2**, carbon atoms from the alkyl chain were localized by difference of Fourier maps. Both structural models

were optimized by the Rietveld method (Rietveld, 1969) using the GSAS package (Larson & von Dreele, 2004) with soft constraints to maintain the chemically reasonable geometries for the phosphonate, alkyl chain and amine groups (Chapter 3, Table 3.2).

The solid **Mg-HDTMP-1deh** was indexed using the DICVOL06 program (Boultif & Louer, 2004) in the monoclinic system with unit cell parameters: $a = 23.4649 \text{ \AA}$, $b = 8.6857 \text{ \AA}$, $c = 9.6130 \text{ \AA}$, $\beta = 99.253^\circ$ and figures of merits: $M(20) = 32.9$ and $F(20) = 77.7$ (de Wolff, 1968; Smith & Snyder, 1979). The extinction conditions were consistent with the space group $C 2/c$. Given the similitude found between these unit cell parameters and space group with those reported for $\text{Mg-ODTMP}\cdot 2\text{H}_2\text{O}\cdot (\text{DMF})_{0.5}$ ($\text{MgP}_4\text{O}_{12}\text{N}_2\text{C}_{12}\text{H}_{30}\cdot 2\text{H}_2\text{O}\cdot 0.5\text{DMF}$; CCDC no. 815762; Colodrero et al., 2012a), the crystal structure of the latter was used as starting model for Rietveld refinement. Crystallographic data for all Mg^{2+} derivatives compounds are shown in Table 7.8 and the final Rietveld plots appear in Figure 7.18.

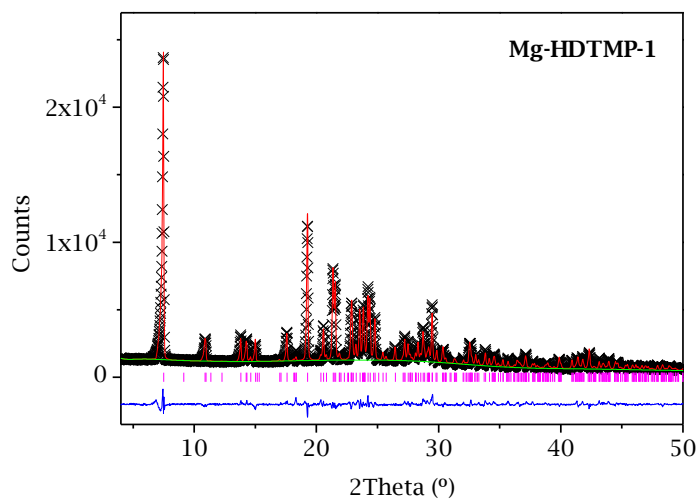


Figure 7.18. Rietveld plots for Mg derivatives **Mg-HDTMP-1**, **Mg-HDTMP-1deh** and **Mg-HDTMP-2**.

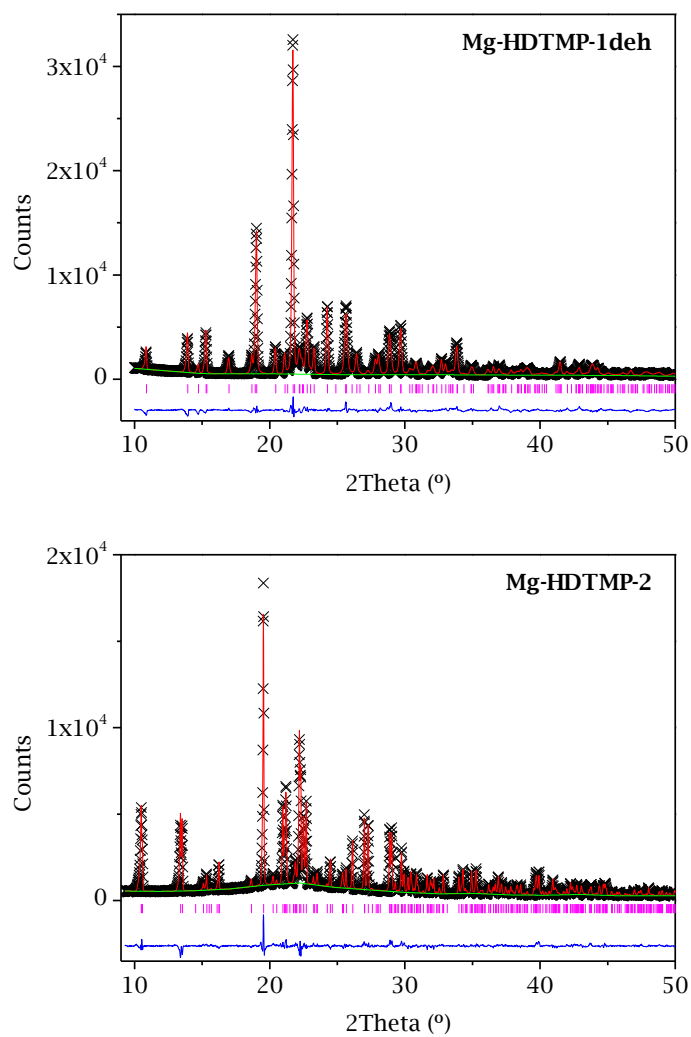


Figure 7.18. Rietveld plots for Mg derivatives Mg-HDTMP-1, Mg-HDTMP-1deh and Mg-HDTMP-2 (Continuation).

Table 7.8. Selected crystallographic data for Mg-HDTMP compounds.

Phase	Mg-HDTMP-1	Mg-HDTMP-1 deh	Mg-HDTMP-2
Space group	$P\bar{1}$	C2/c	$P\bar{1}$
Chemical formula	$MgP_4O_{13}N_2C_{10}H_{28}$	$MgP_4O_{12}N_2C_{10}H_{26}$	$MgP_4O_{12}N_2C_{10}H_{26}$
Formula mass ($g \cdot mol^{-1}$)	532.54	514.52	514.52
λ (Å)	1.5406	1.5406	1.5406
a (Å)	12.5276(3)	23.469(1)	12.362(2)
b (Å)	9.70223(2)	8.6872(4)	9.0720(1)
c (Å)	8.62223(2)	9.6165(5)	9.5525(1)
α (Å)	91.917(1)	90.0	90.6651(8)
β (Å)	70.621(1)	99.219(4)	106.7290(9)
γ (Å)	86.485(2)	90.0	111.8975(8)
Unit cell volume (Å^3)	985.16(4)	1935.3(2)	943.45(2)
Z	2	4	2
Temperature (K)	298	493	298
No. of independent reflections	2043	588	1947
Data/Restraints/ Parameters	5710/65/132	4147/33/75	5398/63/135
R_{wp}	0.0474	0.0812	0.0617
R_p	0.0361	0.0602	0.0482
R_f	0.0654	0.0500	0.0425
CCDC number	1855415	1855416	1855417

Mg-HDTMP-1 and Mg-HDTMP-2 crystallize in the triclinic system, while solid Mg-HDTMP-1deh is monoclinic. All of them present pillared layered structures.

Mg-HDTMP-1 exhibits two crystallographically independent magnesium ions in special positions, both hexacoordinated by six oxygen atoms from six different ligand molecules. Layers are built up from isolated magnesium octahedral. Each amino-*bis*(methylenephosphonate) moiety links three magnesium ions, bridging two

of them through one phosphonate group and connecting the third metal ion by the another adjacent phosphonate group (Figure 7.19a). In this framework, alkyl chains are placed in between the layers along the *a* axis to form a pillared layered structure, in whose interlayer space lattice water is located. (Figure 7.19b).

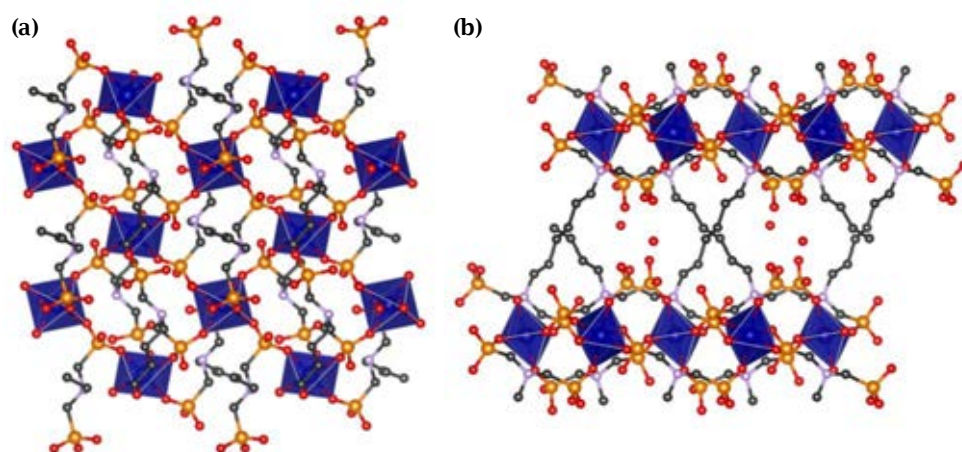


Figure 7.19. View of (a) the layers of **Mg-HDTMP-1** along *a* axis and (b) the 3D packing along *b* axis.

Upon dehydration, by heating at 180 °C, a new, anhydrous phase (**Mg-HDTMP-1deh**), isoreticular with $\text{MgH}_6\text{ODTMP}\cdot 2\text{H}_2\text{O}(\text{DMF})_{0.5}$ was obtained (Colodrero et al., 2012a). The layers are formed in the *bc* plane by isolated Mg^{2+} octahedra surrounded by six phosphonate oxygen atoms from six different ligands (Figure 7.20a). There are two crystallographically independent P atoms, P1 and P2. P1 is connected to the magnesium ion through one oxygen atom (O1), being the remaining two phosphonate oxygen atoms uncoordinated (O2 and O3). On the other hand, P2 bridges two magnesium ions through two oxygen atoms (O4 and O5), while the third oxygen atom is uncoordinated (O6). Neighbouring layers are connected along the *a* axis by the organic linker, with the alkyl chains in cross-diagonal fashion, which results in a pillared layered structure (Figure 7.20b). Viewed along the *b* axis, 1D channels form in the interlayer region.

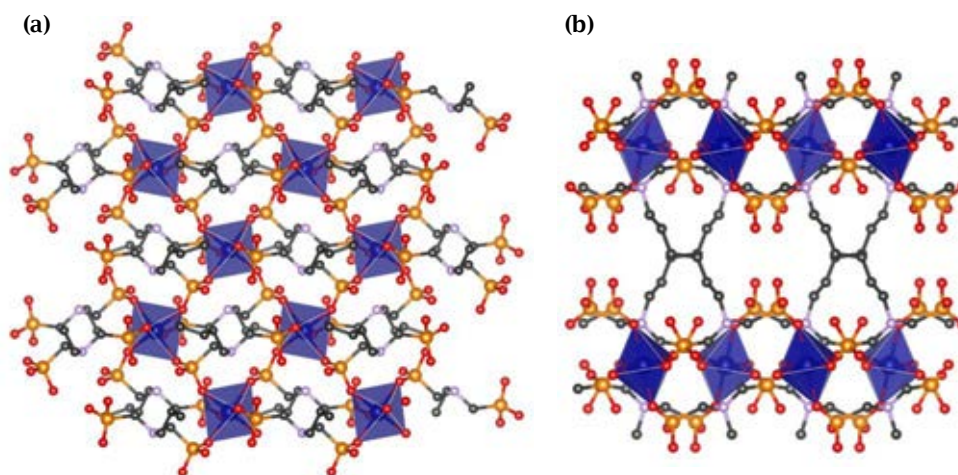


Figure 7.20. View of (a) the layers along axis-*a* and (b) the 3D packing along axis-*c* of **Mg-HDTMP-1deh**.

This process of dehydration/rehydration is reversible in as much as **Mg-HDTMP-1** can be regenerated upon equilibrating **Mg-HDTMP-1deh** at room temperature.

In **Mg-HDTMP-2**, magnesium is also octahedrally coordinated by six phosphonate oxygen atoms from four different ligands, which gives rise to layers composed of isolated magnesium octahedra interconnected to each other by the alkyl chains.

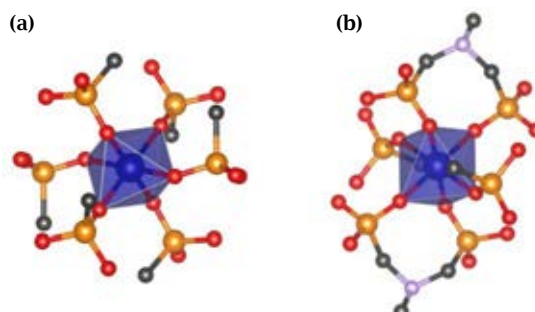


Figure 7.21. Coordination environments of (a) **Mg-HDTMP-1** and (b) **Mg-HDTMP-2**.

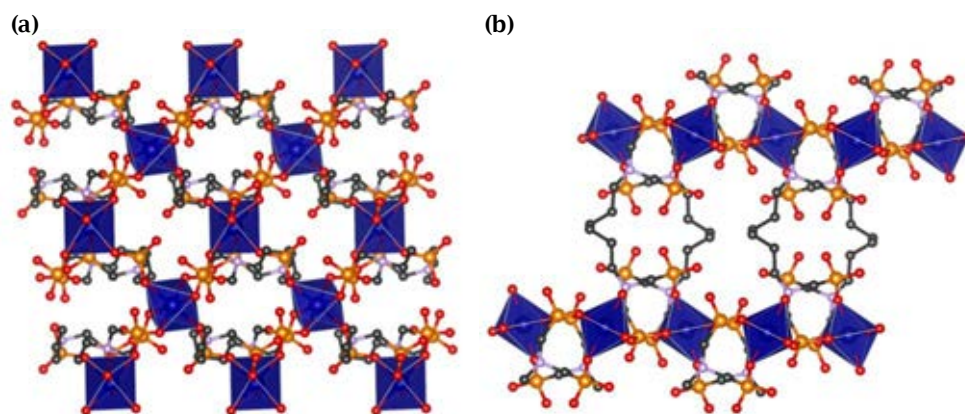


Figure 7.22. View of (a) the Mg-HDTMP-2 layers along axis-*a* and (b) the 3D packing along axis-*c*.

Although water, as lattice water, is an essential contributor to the formation of the hydrogen bond network in Mg-HDTMP-1; its absence, in the structure of solid Mg-HDTMP-2, does not impede generating strong hydrogen bonds, which are established among proximal free POH groups (Table 7.9).

Table 7.9. H-bond distances for Mg-HDTMP-1, Mg-HDTMP-1deh and Mg-HDTMP-2.

Compound	D...A	D...A (Å)	D...A	D...A (Å)
Mg-HDTMP-1	O1...O2	2.534(8)	O5...N2	3.067(13)
	O1...O3	2.507(8)	O5...H ₂ O	2.606(17)
	O1...O9	2.946(12)	O6...O12	2.940(13)
	O1...O11	2.823(12)	O7...O8	2.555(8)
	O2...O3	2.526(8)	O7...O9	2.543(8)
	O2...O6	2.483(12)	O7...O10	2.647(12)
	O3...O6	2.944(12)	O7...H ₂ O	2.841(15)
	O3...O12	2.883(13)	O8...O9	2.532(8)
	O3...N1	2.820(12)	O9...O11	2.831(11)
	O4...O5	2.536(8)	O10...O11	2.553(8)
	O4...O6	2.521(8)	O10...O12	2.503(8)
	O4...H ₂ O	2.585(14)	O11...O12	2.499(8)
	O5...O8	2.631(12)	O11...N2	3.080(11)

Table 7.9. H-bond distances for **Mg-HDTMP-1**, **Mg-HDTMP-1deh** and **Mg-HDTMP-2** (Continuation).

Compound	D...A	D...A (Å)	D...A	D...A (Å)
Mg-HDTMP-1deh	O1...O2	2.430(10)	O4...O5	2.946(13)
	O1...O3	2.597(9)	O4...O5	2.433(9)
	O1...O4	2.983(10)	O4...O6	2.377(9)
	O1...O5	2.990(11)	O4...N	3.146(14)
	O2...O3	2.512(10)	O5...O6	2.525(9)
	O3...O6	2.950(11)	O5...N	2.840(14)
Mg-HDTMP-2	O1...O2	2.560(7)	O5...O11	2.454(10)
	O1...O3	2.530(7)	O6...O7	2.830(11)
	O1...O7	2.862(11)	O6...N2	2.791(12)
	O1...O12	3.044(11)	O7...O8	2.570(7)
	O2...O3	2.491(7)	O7...O9	2.483(7)
	O2...O6	2.896(13)	O7...N2	3.059(13)
	O2...O7	2.962(10)	O8...O9	2.533(8)
	O2...N2	3.011(12)	O9...N1	3.052(12)
	O3...O9	2.901(10)	O9...O10	2.938(9)
	O3...O10	2.909(10)	O10...N1	2.736(12)
	O3...O12	2.862(12)	O10...O11	2.540(7)
	O4...O5	2.559(7)	O10...O12	2.531(7)
	O4...O6	2.556(7)	O11...O12	2.548(7)
	O5...O6	2.506(7)		

7.2.3. Gas Adsorption Characterisation

N₂ and CO₂ adsorption isotherms for degassed **Mg-HDTMP-1** and **Mg-HDTMP-2** were measured in a Micrometric ASAP 2020 instrument. Samples were degassed under 5 · 10⁻⁶ bar at 220 °C for 12 h. N₂ adsorption was collected at 77 K and analysed by the Brunauer-Emmett-Teller (BET) method giving surface areas typical of non-porous solids (≤ 4 m²·g⁻¹). Additionally, CO₂ adsorption was collected at 273K and 1 bar. The surface areas, deduced by Dubinin-Radushkevich (DR) equation, for **Mg-HDTMP-1** and **Mg-HDTMP-2** were 55 m²·g⁻¹ and 11 m²·g⁻¹ respectively (0.105 and 0.05 mmol · g⁻¹ of CO₂ adsorbed). By increasing the alkyl chain length of the ligand to eight

(ODTMP), ultramicroporous magnesium derivatives were reported (Colodrero et al., 2012a). The anhydrous derivative, **MgH₆ODTMP**, presented higher surface areas (180 m²·g⁻¹) and CO₂ adsorption capacity (0.8 mmol·g⁻¹) values while N₂ adsorption was very low (4 m²·g⁻¹). This indicates that **MgH₆ODTMP** could be useful for CO₂/N₂ separation as opposed to compounds **Mg-HDTMP-1** and **Mg-HDTMP-2**.

Structural studies under different CO₂ pressure (10.5-1 bar) and temperatures (from RT up to 200 °C) was carry out for **Mg-HDTMP-1deh**. These tests were realized in ALBA synchrotron (Barcelona, Spain) using the ICP-ITQ-ICIQ-ALBA capillary flow cell (Figure 7.23). The dehydration of the solid was obtained by heating the capillary containing the sample at 200 °C and under a 3 bars CO₂ gas flow. X-ray powder diffraction data were collected using a wavelength of 0.6160 Å. As can be observed in Figure 7.24, at high CO₂ pressures, up to 10.5 bars, this solid behaves as a guest-responsive framework. This is revealed by the splitting of low angle diffraction peaks under CO₂ degassing from 10.5 to 1 bar, which can be attributed to different conformations of the pillaring alkyl chains (Figure 7.24). This phenomenon together with the partial amorphisation prevented from the auto-indexing of the powder pattern. These changes are irreversible after adsorption/desorption processes.

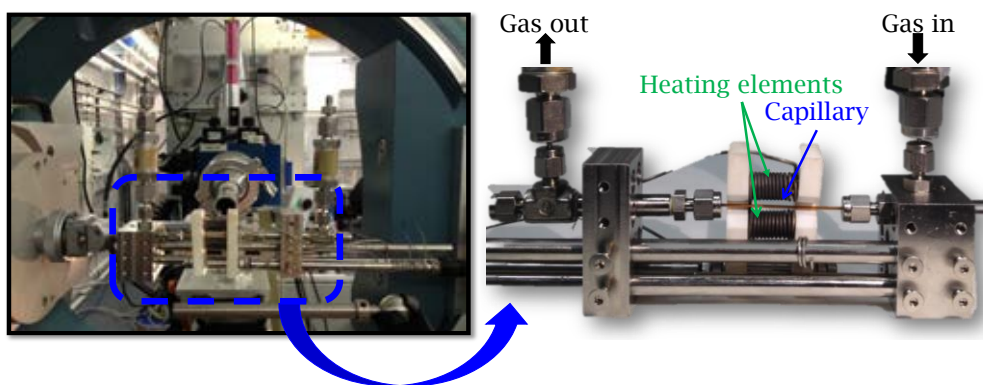


Figure 7.23. ICP-ITQ-ICIQ-ALBA capillary flow cell installed at the BL04-MSPD beamline from ALBA synchrotron.

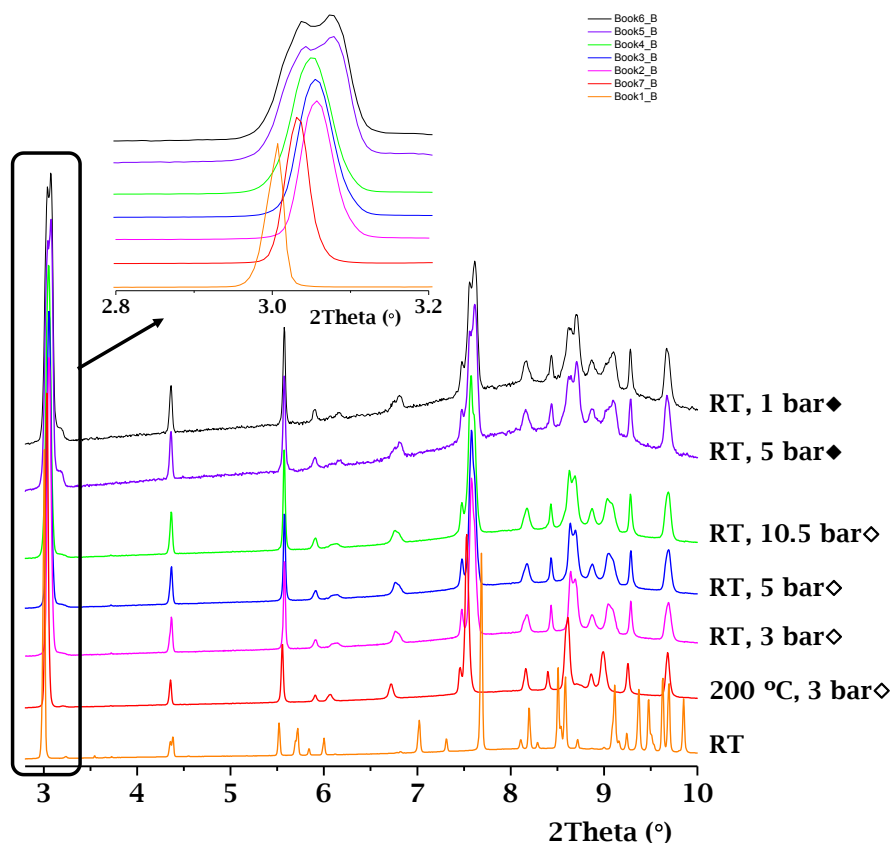


Figure 7.24. Synchrotron X-ray powder diffraction patterns for Mg-HDTMP-1 at different CO₂ pressures (◇ adsorption and ◆ desorption) and temperatures.

7.3. Post-Synthesis Modification

The above-mentioned structural features of Li-HDTMP, Mg-HDTMP-1 and Mg-HDTMP-2 make them attractive to study possible proton transfer pathways, not only in the pristine structures, but also by appropriate post-synthesis modifications in order to correlate the proton conductivity properties with the structural changes in these solids. For this purpose, samples (200 mg) of each solid were exposed to ammonia vapours (from 14% NH₃ aqueous solutions) into a closed container for 2 or 5h (for lithium and magnesium derivatives respectively). Subsequently, the samples were dried with 98% H₂SO₄ for 24h. A similar procedure was previously used for Ca₂[(HO₃PC₆H₃COOH)₂]₂[(HO₃PC₆H₃(COO)₂H)(H₂O)₂]₂·5H₂O, Ca-PiPhtA-I (Bazaga-García et al., 2014), leading to an increase of proton conductivity in more than one order of magnitude, from 5.7·10⁻⁴ to 6.6·10⁻³ S·cm⁻¹ at 80 °C and 95% relative humidity.

Upon NH_3 adsorption, **Li-HDTMP-4W** undergoes a partial amorphisation and new peaks can be observed together with those of the initial crystalline phase (Figure 7.25).

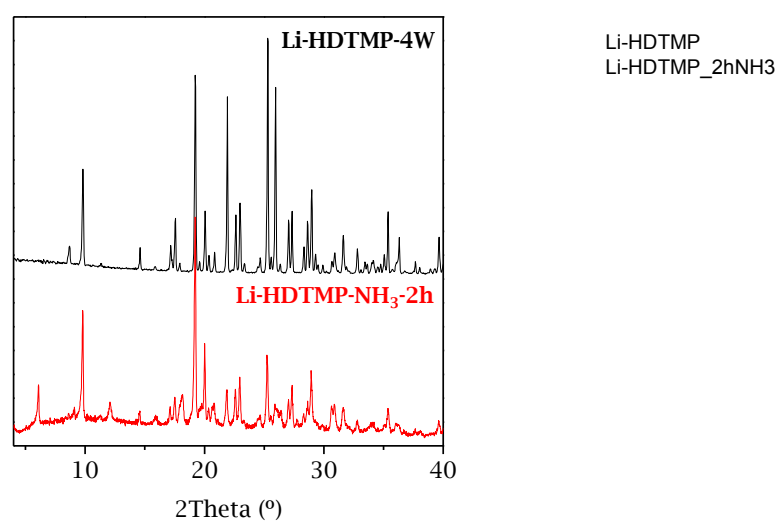


Figure 7.25. X-ray powder diffraction patterns for **Li-HDTMP-4W** (black) and **Li-HDTMP-NH₃-2h** (red).

In the case of the magnesium derivatives, although NH_3 adsorption leads to partial amorphisation (derivatives 3 and 4 respectively), the original crystalline phases are still present (Figure 7.26).

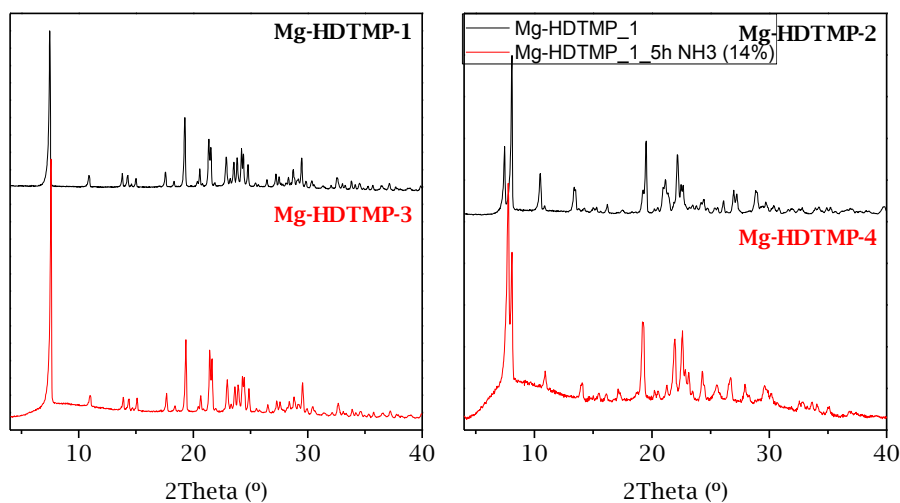


Figure 7.26. X-ray powder diffraction patterns for **Mg-HDTMP-1**, **-2**, **-3** and **-4**.

These new compounds were characterised by elemental and thermogravimetric analysis, X-ray powder diffraction data, Rietveld-determined particle size and impedance spectroscopy.

Weight loss and elemental analysis results are shown in Table AII.7 (Appendix II).

Crystallite size can be determined indirectly from the XRD peak broadening analysis. There are different methods for this calculation, such as Williamson-Hall (W-H), Warren-Averbach and Balzar methods. Regarding to W-H method, the crystallite size determination is performed employing the FWHM of the diffraction peak (Nath, Singh & Das, 2000). This analysis was carried out by Rietveld refinement using HighScore Plus v4.6a software (PANalytical B. V.) and LaB₆ as the standard for the determinations of the instrumental resolution function.

Upon exposure to ammonia vapours, the average particle size of **Mg-HDTMP-3** remains quite similar to that of **Mg-HDTMP-1**. However, a significant reduction in the average particle size was found for **Mg-HDTMP-4** as compared to **Mg-HDTMP-2**, which suggests a different reactivity against NH₃ of solids **Mg-HDTMP-1** and **Mg-HDTMP-2**.

Table 7.10. Particle size as determined by the Rietveld method.

Acronym	Stoichiometric	Particle size (Å)
Mg-HDTMP-1	Mg[(HO ₃ PCH ₂) ₂ NH(CH ₂) ₆ NH(CH ₂ PO ₃ H) ₂].H ₂ O	1162
Mg-HDTMP-3	Mg[(HO ₃ PCH ₂) ₂ NH(CH ₂) ₆ NH(CH ₂ PO ₃ H) ₂](NH ₃) _{1.5} .4H ₂ O	1425
Mg-HDTMP-2	Mg[(HO ₃ PCH ₂) ₂ NH(CH ₂) ₆ NH(CH ₂ PO ₃ H) ₂]	1190
Mg-HDTMP-4	Mg[(HO ₃ PCH ₂) ₂ NH(CH ₂) ₆ NH(CH ₂ PO ₃ H) ₂](NH ₃) _{2.5} .7H ₂ O	758

7.4. Proton Conductivity

Alkali metal- and **Mg-HDTMP** solids are potential candidates as proton conductors due to the presence of hydrogen bonding networks in their crystal structures. However, preliminary stability tests indicated that ammonia-containing magnesium derivatives and **Li-HDTMP-NH₃-2h** as well as the alkali metal compounds, except **Li-HDTMP-4W**, were hygroscopic at high relative humidity. Therefore, their proton conductivity properties could not be studied. As comparison, the proton conductivity properties of the acid ligand **HDTMP** have been also studied.

Proton conductivity measurements were carried out as have been previously reported in Section 3.13. In this case, an AUTOLAB PGSTAT302N analyser was employed over the frequency range from 10^5 to 20 Hz with an applied voltage of 0.35 V. AC impedance data were collected over upon cooling using a stabilization time of 5h at different temperature intervals from 80 to 25 °C and at 60, 75 or 95% RH. Figure AIV.10 (Appendix IV) gives the plots of complex impedance plane, measured from 80 to 30 °C and 95% RH, for all analysed samples. The total pellet resistance (R_T) was obtained from the intercept of the spike and/or the arc (low-frequency end) on the Z' axis.

Figure 7.27 displays hydrogen bond interactions corresponding to the ligand, in which the phosphonic and protonated amino groups are involved. However, the as-synthesised **Li-HDTMP-4W** shows higher proton conductivity values ($7.6 \cdot 10^{-4} \text{ S} \cdot \text{cm}^{-1}$) than the free **HDTMP** ligand ($2.0 \cdot 10^{-4} \text{ S} \cdot \text{cm}^{-1}$) at 80 °C and 95% RH. This enhancement is thought to be due to the role played by coordinated water in the structure of the lithium derivative, which generates extended proton transport pathways by contributing to establish additional hydrogen bond interactions with the phosphonic groups.

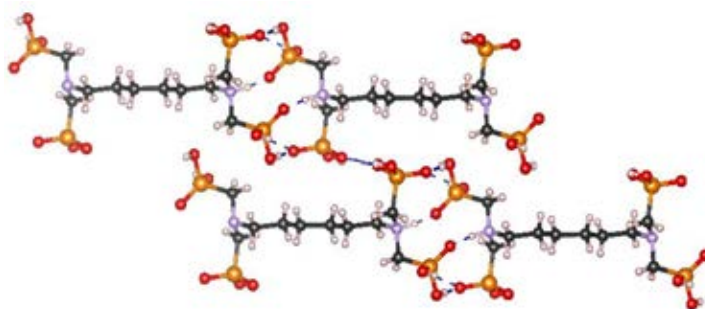


Figure 7.27. View along a -axis of hydrogen bond interactions in the structure of ligand **HDTMP**.

As shown in Figure 7.13, **Li-HDTMP-0W** rehydrates to **Li-HDTMP-4W** upon preheating the sample at 80 °C and 95% RH for 5 hours. Interestingly, the rehydrated sample shows higher proton conductivity values ($4.4 \cdot 10^{-3} \text{ S} \cdot \text{cm}^{-1}$) than the as-synthesised **Li-HDTMP-4W** ($7.6 \cdot 10^{-4} \text{ S} \cdot \text{cm}^{-1}$). The same behaviour occurs with magnesium derivatives, whose rehydrated form exhibits a proton conductivity ($6.6 \cdot 10^{-5} \text{ S} \cdot \text{cm}^{-1}$) that it is fourfold that of the as-synthesised **Mg-HDTMP-1** ($1.6 \cdot 10^{-5} \text{ S} \cdot \text{cm}^{-1}$).

In order to understand this behaviour, the average particle size was determined by the Rietveld method and their TG curves compared. After impedance measurements, a half particle size reduction was determined for as synthesised **Li-HDTMP-4W** and the rehydrated form (Table 7.11). For **Mg-HDTMP-1**, no significant variations in particle size were observed. Rehydrated compounds present the same water content than as synthesised samples. However, the TG analyses display subtle variations in the water loss (Figure 7.28 and 7.29), suggesting changes in hydrogen bond interactions between the lattice water molecules and the framework after rehydration. These modifications could change the acidity of acid groups and water mobility, what would justify the enhancement of the proton conductivity values for the rehydrated samples.

Table 7.11. Rietveld-determined particle size.

Sample	Particle size (Å)	
	Before impedance measurements	After impedance measurements
As synthesised Li-HDTMP-4W	~1400	~700
Rehydrated Li-HDTMP-4W	~1200	~600
Mg-HDTMP-1	~1200	~1300
Mg-HDTMP-2	~1200	~1000

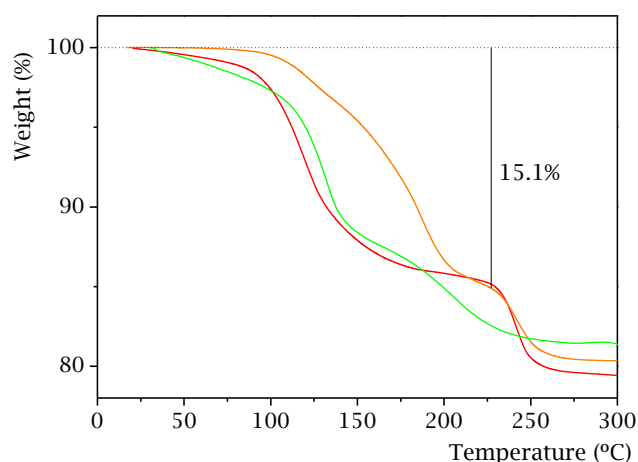


Figure 7.28. Thermal analysis for: as synthesised **Li-HDTMP-4W** (orange), **Li-HDTMP-4W** after impedance measurements (red) and the rehydrated form (green).

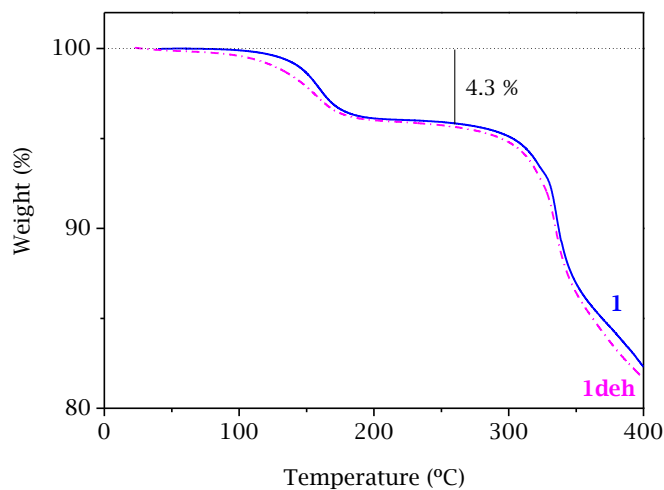


Figure 7.29. Thermal analysis for compounds **Mg-HDTMP-1** (blue) and the rehydrated form (magenta).

In addition, solid state ^1H -MAS-NMR spectra for Li-HDTMP-4W, Li-HDTMP-0W and the rehydrated compound were collected using a Bruker Ascend-600 spectrometer equipped with a 2.5 mm MAS probe. These spectra consist of broad bands, which were deconvoluted into a several components using the DMFIT program (Massiot et al., 2002). The signals at ~ 5.0 ppm, 8.6 ppm and 11.0 ppm are attributed to bound water, P-OH and N-H $^+$ groups, respectively (Colodrero et al., 2012c; Florecia-Crespi et al., 2018). For all compounds, ^1H -MAS-NMR spectra were quite similar (Figure 7.30, Table 7.12).

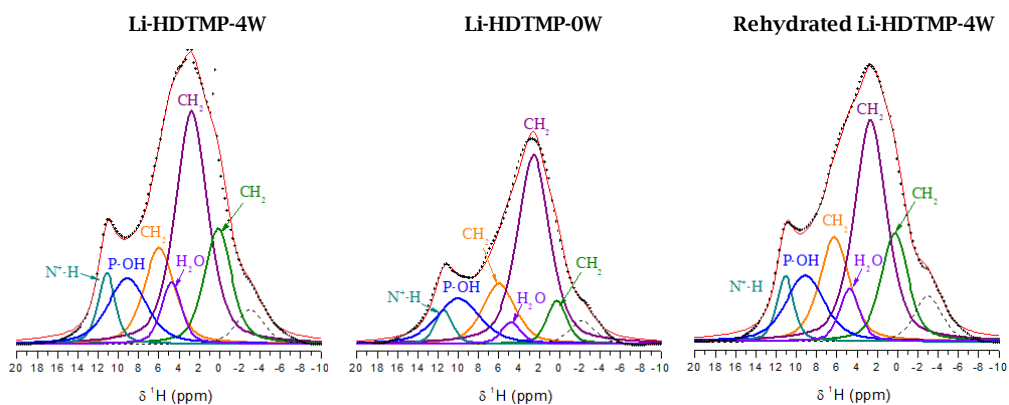


Figure 7.30. Solid state ^1H -MAS-NMR spectra for Li-HDTMP-4W, Li-HDTMP-0W and rehydrated Li-HDTMP-4W.

Table 7.12. ¹H-SS-NMR data and band assignments for ligand **HDTMP** and **Li-HDTMP** samples.

Compound	δ (ppm)	Calculated integral (%)[*]	Assignment
HDTMP	13.22	7.31	P-(OH) ₂
	12.11	5.48	P-(OH) ₂
	11.11	6.84	N-H ⁺
	9.54	12.58	P-OH
	5.61	20.84	CH ₂
	2.39	38.18	CH ₂
	0.2	8.76	CH ₂
Li-HDTMP-0W	11.44	4.92	N-H ⁺
	10.00	16.65	P-OH
	5.97	16.66	CH ₂
	4.80	3.61	H ₂ O
	2.56	51.08	CH ₂
	0.25	7.07	CH ₂
Rehydrated Li-HDTMP-4W	11.08	6.29	N-H ⁺
	9.12	14.37	P-OH
	6.23	17.53	CH ₂
	4.73	5.76	H ₂ O
	2.67	39.81	CH ₂
	0.27	16.21	CH ₂
Li-HDTMP-4W	11.14	6.67	N-H ⁺
	9.11	13.82	P-OH
	5.95	15.73	CH ₂
	4.73	6.59	H ₂ O
	2.76	40.43	CH ₂
	0.14	16.76	CH ₂

* Renormalized without the signal probe.

The activation energy values determined from the Arrhenius plot (Figure 7.31) for **HDTMP** ligand, as synthesised **Li-HDTMP-4W**, rehydrated lithium derivative, **Mg-HDTMP-1**, rehydrated **Mg-HDTMP-1deh** and **Mg-HDTMP-2** indicate that a Grotthuss-type proton transfer mechanism operates at high humidity (95% RH). At lower relative

humidity (60 and 75% RH), the proton conductivity decreased (Table 7.13), which is a typical behaviour of proton conductors, and for as synthesised **Li-HDTMP-4W**, rehydrated **Li-HDTMP-4W** and rehydrated **Mg-HDTMP-1deh** the proton transfer mechanism changed from a Grotthuss-type to a vehicular one (activation energy > 0.5 eV).

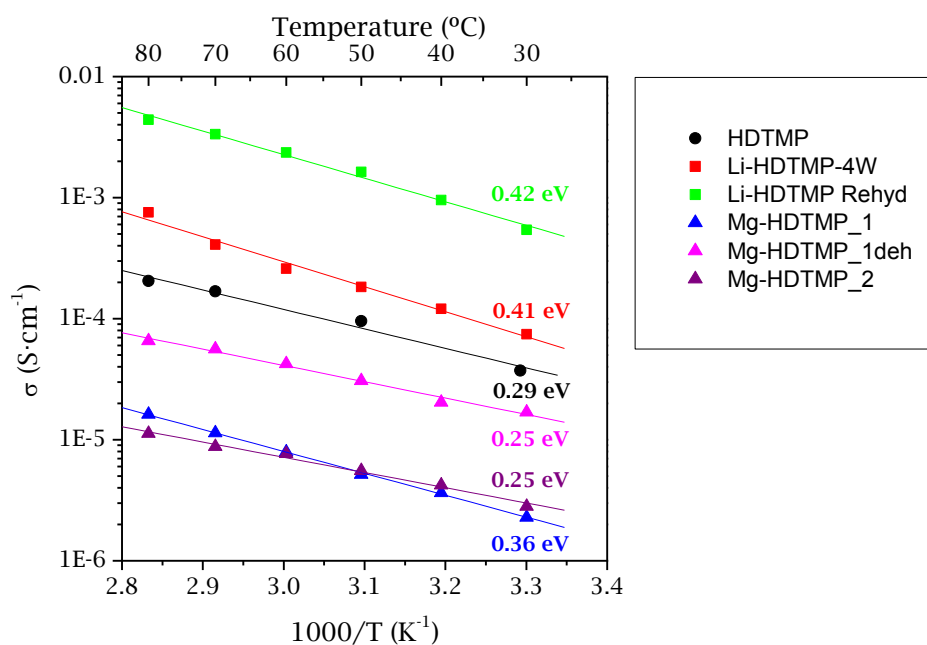


Figure 7.31. Arrhenius plots for **HDTMP** acid (black), **Li-HDTMP-4W** (red), **rehydrated Li-HDTMP-4W** (green), **Mg-HDTMP-1** (blue), **rehydrated Mg-HDTMP-1deh** (magenta) and **Mg-HDTMP-2** (purple).

The moderate proton conductivity exhibited by the **Mg-HDTMP** compounds contrasts with the high proton conductivity observed for the highly hydrated metal derivatives, **La-HDTMP-7H₂O** (Colodrero et al., 2012b) and **Mg-ODTMP-6H₂O** (Colodrero et al., 2012a) (Table 7.13). The higher water content appears to induce efficient H-bond networks, necessary for establishing more extended proton transfer pathways.

Table 7.13. Summary of the proton conductivity and activation energies values of selected materials.

Compound	σ (S·cm ⁻¹)	E _a (eV)	T (°C)	RH (%)
HDTMP	2.0·10 ⁻⁴	0.29	80	95
	6.2·10 ⁻⁷	0.42	80	60
Li-HDTMP-4W	7.6·10 ⁻⁴	0.41	80	95
	4.0·10 ⁻⁶	0.54	80	60
Rehydrated Li-HDTMP-4W	4.4·10 ⁻³	0.42	80	95
	2.5·10 ⁻⁵	0.74	80	60
Mg-HDTMP-1	1.6·10 ⁻⁵	0.36	80	95
	4.4·10 ⁻⁷	0.45	80	75
Rehydrated Mg-HDTMP-1deh	6.6·10 ⁻⁵	0.35	80	95
	4.7·10 ⁻⁷	0.59	80	75
Mg-HDTMP-2	9.8·10 ⁻⁶	0.35	80	95
	6.5·10 ⁻⁷	0.38	80	75
La-HDTMP·7H ₂ O	8·10 ⁻³	0.25	19	98
Mg-ODTMP·6H ₂ O	1.6·10 ⁻³	0.31	19	100

7.5. Conclusions

- Alkali (from Li to Cs) and magnesium derivatives of the tetraphosphonate ligand HDTMP have been synthesised using different methodologies: (i) crystallization at RT for the alkali metal derivatives and (ii) hydro-/solvothermal or microwave-assisted synthesis for magnesium derivatives.
- Alkali derivatives exhibit a rich structural diversity induced by the cation size, from 1D (Li⁺ and Na⁺) through 2D (K⁺) to pillared-layered structures (Rb⁺ and Cs⁺). Magnesium derivatives present pillared layered structures.
- Mg-HDTMP-1** and **2** exhibited low CO₂ adsorption capacities (0.105 and 0.05 mmol·g⁻¹, respectively) attributed to the short alkyl chain which prevent from the accommodation of the adsorbed guest molecules. In addition, **Mg-HDTMP-1deh** behaves as a guest-responsive framework upon CO₂ adsorption at high pressure (10.5 bar).

- Impedance spectroscopy measurements indicate that **Li-HDTMP-4W** and **Mg-HDTMP-1** solids exhibit moderate proton conductivity values, which are enhanced by almost one order of magnitude upon reversible dehydration/rehydration process ($4.4 \cdot 10^{-3} \text{ S} \cdot \text{cm}^{-1}$ and $6.6 \cdot 10^{-5} \text{ S} \cdot \text{cm}^{-1}$ at 80 °C and 95% RH, respectively). This enhancement of the proton conductivity can be attributed to subtle changes in the H-bond networks formed after rehydration.

7.6. References

A

Ando, A.; Ando, I.; Tonami, N.; Kinuya, S.; Kazuma, K.; Kataiwa, A.; Nakagawa, M.; Fujita, N. ^{177}Lu -EDTMP: a potential therapeutic bone agent. *Nucl. Med. Commun.*, **1998**, 19(6), 587-591.

B

Bazaga-García, M.; Colodrero, R. M. P.; Papadaki, M.; Garczarek, P.; Zoń, J.; Olivera-Pastor, P.; Losilla, E. R.; León-Reina, L.; Aranda, M. A. G.; Choquesillo-Lazarte, D.; Demadis, K. D.; Cabeza, A. Guest Molecule-Responsive Functional Calcium Phosphonate Frameworks for Tuned Proton Conductivity. *J. Am. Chem. Soc.*, **2014**, 136(15), 5731-5739.

Boultif, A.; Louer, D. Powder pattern indexing with the dichotomy method. *J. Appl. Cryst.* **2004**, 37, 724-731.

C

Cardiano, P.; Cigala, R. M.; Cordaro, M.; De Stefano, C.; Milea, D.; Sammartano, S. On the complexation of metal cations with “pure” diethylenetriamine-N, N, N', N', N''-pentakis (methylenephosphonic) acid. *New J. Chem.*, **2017**, 41(10), 4065-4075.

Chakraborty, S.; Das, T.; Banerjee, S.; Balogh, L.; Chaudhari, P. R.; Sarma, H. D.; Polyák, A.; Máthé, D.; Venkatesh, M.; Janoki, G.; Pillai, M. R. A. ^{177}Lu -EDTMP: a viable bone pain palliative in skeletal metastasis. *Cancer Biother. Radio.*, **2007**, 23(2), 202-213.

Clearfield, A.; Demadis, K. D. Metal phosphonate chemistry: From synthesis to applications. *RSC: London*, **2012**.

Colodrero, R. M. P.; Cabeza, A.; Olivera-Pastor, P.; Infantes-Molina, A.; Barouda, E.; Demadis, K. D.; Aranda, M. A. “Breathing” in Adsorbate-Responsive Metal Tetraphosphonate Hybrid Materials. *Chem. Eur. J.*, **2009**, 15(27), 6612-6618.

- Colodrero, R. M.; Olivera-Pastor, P.; Cabeza, A.; Papadaki, M.; Demadis, K. D.; Aranda, M. A. Structural Mapping and Framework Interconversions in 1D, 2D, and 3D Divalent Metal R, S-Hydroxyphosphonoacetate Hybrids. *Inorg. Chem.*, **2010**, 49(2), 761-768.
- Colodrero, R. M. P.; Olivera-Pastor, P.; Losilla, E. R.; Hernández-Alonso, D.; Aranda, M. A.; Leon-Reina, L.; Rius, J.; Demadis, K. D.; Moreau, B.; Villemin, D.; Palomino, M.; Rey, F.; Cabeza, A. High Proton Conductivity in a Flexible, Cross-Linked, Ultramicroporous Magnesium Tetrakisphosphate Hybrid Framework. *Inorg. Chem.*, **2012a**, 51(14), 7689-7698.
- Colodrero, R. M. P.; Olivera-Pastor, P.; Losilla, E. R.; Aranda, M. A.; Leon-Reina, L.; Papadaki, M.; McKinlay, A. C.; Morris, R. E.; Demadis, K. D.; Cabeza, A. Multifunctional lanthanum tetrakisphosphates: Flexible, ultramicroporous and proton-conducting hybrid frameworks. *Dalton Trans.*, **2012b**, 41(14), 4045-4051.
- Colodrero, R. M. P.; Papathanasiou, K. E.; Stavgianoudaki, N.; Olivera-Pastor, P.; Losilla, E. R.; Aranda, M. A.; León-Reina, L.; Sanz, J.; Sobrados, I.; Choquesillo-Lazarte, D.; García-Ruiz, J. M.; Atienzar, P.; Rey, F.; Demadis, K. D.; Cabeza, A. Multifunctional Luminescent and Proton-Conducting Lanthanide Carboxyphosphonate Open-Framework Hybrids Exhibiting Crystalline-to-Amorphous-to-Crystalline Transformations. *Chem. Mater.*, **2012c**, 24(19), 3780-3792.
- Colodrero, R. M. P.; Salcedo, I. R.; Bazaga-García, M.; Barouda, E.; Papadaki, M.; Papathanasiou, K. E.; Hernández-Alonso, D.; Rius, J.; Aranda, M. A. G.; Losilla, E. R.; Olivera-Pastor, P.; Demadis, K. D.; Cabeza, A. High-Throughput Synthesis of Pillared-Layered Magnesium Tetrakisphosphate Coordination Polymers: Framework Interconversions and Proton Conductivity Studies. *Inorganics*, **2018**, 6(3), 96.

D

- de Wolff, P. D. A simplified criterion for the reliability of a powder pattern indexing. *J. Appl. Crystallogr.*, **1968**, 1(2), 108-113.
- Demadis, K. D.; Mantzaridis, C.; Lykoudis, P. Effects of structural differences on metallic corrosion inhibition by metal– polyphosphonate thin films. *Ind. Eng. Chem. Res.*, **2006**, 45(23), 7795-7800.

CHAPTER 7

Demadis, K. D.; Barouda, E.; Raptis, R. G.; Zhao, H. Metal Tetrakisphosphate “Wires” and Their Corrosion Inhibiting Passive Films. *Inorg. Chem.*, **2009**, 48(3), 819-821.

E

Eary, J. F.; Collins, C.; Stabin, M.; Vernon, C.; Petersdorf, S.; Baker, M; Ferency, S.; Addison, S. J., Appelbaum, F. Samarium-153-EDTMP biodistribution and dosimetry estimation. *J. Nucl. Med.*, **1993**, 34(7), 1031-1036.

F

Firmino, A. D. G.; Figueira, F.; Tomé, J. P. C.; Almeida-Paz, F. A.; Rocha, J. Metal-Organic Frameworks assembled from tetrakisphosphonic ligands and lanthanides. *Coord. Chem. Rev.*, **2018**, 355, 133-149.

Florencia-Crespi, A.; Byrne, A. J.; Vega, D.; Chattah, A. K.; Monti, G. A.; Lázaro-Martínez, J. M. Generation and Stability of the gem-Diol Forms in Imidazole Derivatives Containing Carbonyl Groups. Solid-State NMR and Single-Crystal X-ray Diffraction Studies. *J. Phys. Chem. A*, **2018**, 122, 601-609.

H

Holmes, R. A. [¹⁵³Sm] EDTMP: a potential therapy for bone cancer pain. *Semin. Nucl. Med.*, **1992**, 22(1), 41-45.

L

Larson, A. C.; von Dreele, R. B. General structure analysis system (GSAS). Los Alamos National Laboratory Report LAUR, 2004, 86-748.

M

Massiot, D., Fayon, F.; Capron, M.; King, I.; Le Calvé, S.; Alonso, B.; Durand, J-O.; Bujoli, B.; Gan, Z.; Hoatson, G. Modelling one- and two-dimensional solid-state NMR spectra. *Magn. Reson. Chem.*, **2002**, 40(1), 70-76.

Mathew, B.; Chakraborty, S.; Das, T.; Sarma, H. D.; Banerjee, S.; Samuel, G.; Venkatesh, M.; Pillai, M. R. A. ¹⁷⁵Yb labeled polyaminophosphonates as potential agents for bone pain palliation. *Appl. Radiat. Isot.*, **2004**, 60(5), 635-642.

Mendes, R. F.; Ananias, D.; Carlos, L. D.; Rocha, J.; Paz, F. A. A. Photoluminescent Lanthanide-Organic Framework Based on a Tetrakisphosphonic Acid Linker. *Crystal Cryst. Growth Des.*, **2017**, 17(10), 5191-5199.

N

Nath, D.; Singh, F.; Das, R. X-ray diffraction analysis by Williamson-Hall, Halder-Wagner and size-strain plot methods of CdSe nanoparticles-a comparative study. *Mater. Chem. Phys.*, **2020**, 239, 122021.

R

Rietveld, H. M. A profile refinement method for nuclear and magnetic structures. *J. Appl. Crystallogr.*, **1969**, 2, 65–71.

Rius, J. Patterson-function direct methods for structure determination of organic compounds from powder diffraction data. XVI. *Acta Cryst.*, **2011**, A67(1), 63-67.

S

Salcedo, I. R.; Colodrero, R. M. P.; Bazaga-García, M.; Vasileiou, A.; Papadaki, M.; Olivera-Pastor, P.; Infantes-Molina, A.; Losilla, E. R.; Mezei, G.; Cabeza, A.; Demadis, K. D. From light to heavy alkali metal tetraphosphonates (M= Li, Na, K, Rb, Cs): Cation size-induced structural diversity and water-facilitated proton conductivity. *Cryst. Eng. Comm.*, **2018**, 20(47), 7648-7658.

Singh, A.; Holmes, R. A.; Farhangi, M.; Volkert, W. A.; Williams, A.; Stringham, L. M.; Ketring, A. R. Human Pharmacokinetics of Samarium-153 EDTMP in Metastatic Cancer. *J. Nucl. Med.*, **1989**, 30(11), 1814-1818.

Smith, G. S.; Snyder, R. L. FN: A criterion for rating powder diffraction patterns and evaluating the reliability of powder-pattern indexing. *J. Appl. Crystallogr.*, **1979**, 12(1), 60-65.

Stock, N.; Bein, T. High-Throughput Synthesis of Phosphonate-Based Inorganic–Organic Hybrid Compounds under Hydrothermal Conditions. *Angew. Chem.*, **2004**, 116(6), 767-770.

Stock, N.; Rauscher, M.; Bein, T. Inorganic–organic hybrid compounds: hydrothermal synthesis and characterization of a new three-dimensional metal tetraphosphonate $\text{Mn}[(\text{HO}_3\text{PCH}_2)\text{N}(\text{H})(\text{CH}_2)_4(\text{H})\text{N}(\text{CH}_2\text{PO}_3\text{H}_2)]$. *J. Solid State Chem.*, **2004**, 177(3), 642-647.

Su, M.; Qiu, Y.; Jia, W. A pilot study of antitumor effect of gallium ethylenediaminetetramethylene phosphonate [Ga(III)-EDTMP] in tumor-bearing rats. *Adv. Ther.*, **2015**, 22(4), 297-306.

CHAPTER 7

V

- Vallcorba, O.; Rius, J.; Frontera, C.; Peral, I.; Miravittles, C. DAJUST: a suite of computer programs for pattern matching, space-group determination and intensity extraction from powder diffraction data. *J. Appl. Cryst.*, **2012**, 45(4), 844-848.
- Villemin, D.; Didi, M. A. Aminomethylenephosphonic Acids Syntheses and Applications (A Review). *Orient. J. Chem.*, **2015**, 31, 1-12.

Chapter 8

Conclusions & Future Prospects





UNIVERSIDAD
DE MÁLAGA

8.1. Conclusions

- A variety of crystalline multifunctional alkali metal-, divalent metal- and lanthanide-phosphonates, as well as some bimetallic derivatives have been synthesised from the phosphonate-based ligands: *R,S* 2-hydroxyphosphonoacetic acid (HPAA), 2-[bis(phosphonomethyl)amino]ethanesulfonic acid (H₃SP), aminotris(methylenephosphonic acid) (H₆NMP) and hexamethylenediamine-*N,N,N',N'*-tetrakis(methylenephosphonic acid) (HDTMP). Solids were obtained by employing both, room temperature crystallisation and hydrothermal/solvothermal reactions. For the latter processes, a high-throughput methodology was applied in order to optimise the synthesis conditions.

- Layered Fe(II)- and bimetallic Fe(II)-based 2-hydroxyphosphonoacetates exhibit remarkable properties as Photo-Fenton catalysts and proton conductors. These materials constitute an example of multifunctional solids by taking advantage of both, the metal ion -for its redox properties and reactivity- and the ligand -for its acidic properties-. As photocatalysts, the Fe(II) derivatives are efficient in degradation of recalcitrant pollutant, such as phenol, 4-chlorophenol and methylene blue (MB). The phenols were mineralised under UV-A as well as visible light in the presence of H₂O₂, with TOC removals near 90%, although a longer reaction time (150 min or more against 80 min) was necessitated with visible light. While MB, only could be partially mineralised (75%) under UV-A light. In addition, Fe(II)-hydroxyphosphonoacetate and derivatives have been shown to exhibit NH₃/H₂O-mediated proton conductivity which increases with the amount adsorbed of these two guest species up to a limit of 1.75 mol NH₃ per formula for **Fe-NH₃-72h**. Upon ammonia adsorption solids become increasingly amorphous, but PDF studies revealed that the local Fe(II) environment was still preserved.

- Metal-sulfophosphonates, more specifically those of Mn²⁺ and Ln³⁺, present layered structures, in which the sulfonate moiety can act as a bridging group such as in ***m*-LaH₂SP** or it is in protonated form contributing to enhance extended H-bond networks (***o*-LnH₂SP** and ***o*-Mn₂HSP**), a structural feature

important in determining the proton conductivity properties of these materials. *m-Zn₂HSP* and *h-Zn₂HSP* are among the most proton conductive materials studied ($\sim 10^{-2}$ S·cm⁻¹ at 80 °C and 95% RH), notwithstanding, their structures still remain unsolved. The structurally different lanthanide sulfophosphonates *m-LaH₂SP* and *o-LnH₂SP* have been compared to establish valuable structure-properties relationships. From these correlations it was inferred that uncoordinated sulfonate groups, thus exerting an important role to connect other functional groups and/or guest molecules into extended H-bond networks, assist to enhance proton conductivity, other characteristics being similar. In these solids, the proton conductivity was most a result of structural features, but other various factors, such as heating under high relative humidity and particle aggregate size made also a contribution.

- Two series of layered sulfate-containing lanthanide aminotris (methylenephosphonate) compounds have been isolated, i.e. Ln-I and Ln-II, which differ most significantly in the structural role played by the sulfate anion. In Series **Ln-I**, this anion is present as a charge-compensating hydrogensulfate species in the interlayer space, while in Series **Ln-II** it acts as a bridging ligand connecting Ln₂O₁₄ dimers in the layer. As a result of these structural differences, the two series of compounds display remarkable distinctive properties in chemical stability and proton conductivity. Solids of Series **Ln-I** evolve to sulfate-deficient networks upon heating under high relative humidity. These sulfate-deficient structures remain stable under the impedance measurement conditions and displayed proton conductivity values as high as 10⁻² S·cm⁻¹ at 80 °C and 95% RH. Also interesting was the fact that upon heating in furnace at 230 °C, solids of Series **Ln-I** transform into a crystalline anhydrous phase, which showed the highest proton conductivity up to 3.6·10⁻² S·cm⁻¹ at 80 °C and 95% RH, attributed to the ability to adsorb water. All these structural transformations were related to the different modes in which Ln³⁺ are coordinated by the sulfate species. Solids of Series **Ln-II** also displayed high proton conductivity values, up to 3.5·10⁻³ S·cm⁻¹ at the same measurement conditions.

- Alkali metal and alkaline-earth metal tetrakisphosphonates, derived from the acid HDTMP, showed a wide structural diversity, from 1D (Li⁺ and Na⁺) to 3D/pillared-layered (Cs⁺, Rb⁺ and Mg²⁺), through layered structures (K⁺), which is thought to be induced by the size of the cation. Hydrated phases of Li⁺ and Mg²⁺ derivatives transformed to another crystalline anhydrous phase. Interestingly, the dehydration/rehydration process was fully reversible, in the range of temperatures studied and subtle changes in the H-bond networks implied an enhancement of almost one order of magnitude in their proton conductivity.
- Most of the studied materials displayed a Grotthuss-type proton transfer mechanism according to the E_a values found (≤ 0.5) and their proton conductivity could be enhanced by post-synthesis treatments. In addition, some of them, particularly ***o*-SmH₂SP**, **Eu-I-230C**, **SD-Eu-I** and **Tb-II**, could be successfully used as filler in Nafion[®]-base composite membranes showing excellent performances in MEAs, even higher than pure Nafion[®] membranes, under operating conditions of PEMFCs.

8.2. Future Prospects

Although the phosphonate chemistry makes it difficult to predesign structures with desired dimensionalities, continuous advances in phosphonate-based ligand synthesis have provided a number of multifunctional linkers for metal ions, to yield new metal phosphonate materials having specific predetermined properties, some of which are quite attractive to face some of the most intricate challenges in the area of solid state chemistry, such as those related to a sustained use and production of energy and other environmental issues. Therefore, it is expected that by appropriate combinations of metal ions, possessing specific chemical features, e.g. redox and/or catalytic, luminescence properties, etc., with multifunctional phosphonate ligands, providing variable coordinative modes into robust networks/frameworks, will continue broadening the field of metal phosphonate chemistry in the next years. In particular, metal phosphonates are especially interesting as proton conductor materials, as they can be easily prepared from acidic conditions and are affordable for further post-synthesis modifications. Most of the metal phosphonates studied possess structures

with extended H-bond networks and present moderate to high proton conductivity. More specifically, lanthanide phosphonates are prominent materials because their coordination properties contribute to enhance proton conductivity in different ways, e.g. allowing the presence of bound and lattice water, creating positively charged layers, and hence, the inclusion of secondary ligands that further contribute to define proton transfer pathways, besides to their ability of coordinating different functional groups, depending on synthesis conditions. Lanthanide phosphonates have been also demonstrated to enhance desired properties of Nafion-based mixed membranes in MEAs under the operation conditions of PEMFCs. Taking into consideration these premises, we foresee some of the future research lines to be implemented:

- Synthesis of suitable single crystals of ***m*-Zn₂HSP** and ***h*-Zn₂HSP** in order to establish structure-property relationships.
- Preparation and characterisation of new metal (lanthanide) phosphonates, functionalised with other anions different to Cl⁻ and SO₄²⁻ in order to study their influence on their proton conductivity properties.
- Preparation and characterisation of new composite membranes, by extending the types of fillers to other metal phosphonate candidates, such as ***o*-Mn₂HSP**, ***m*-Zn₂HSP** and ***h*-Zn₂HSP**, and of polymeric matrices (Nafion, polyvinylphosphonic acids, chitosan, etc.).
- Studying the mechanical properties of the composite membranes prepared.
- To study the performance of composite membranes under PEMFCs operating conditions.
- Using transition metal phosphonates as precursors of PEMFCs electrocatalysts, derived from pyrolytic treatments.

Capítulo 8

Conclusiones & Perspectivas Futuras





UNIVERSIDAD
DE MÁLAGA

8.1. Conclusiones

- Se han sintetizado una gran variedad de fosfonatos cristalinos de metales alcalinos, divalentes y lantánidos, así como algunos derivados bimetálicos a partir de los ácidos: *R,S* 2-hidroxifosfonoacético (HPAA), 2-[bis(fosfonometil)amino]-etanosulfónico (H₂SP), aminotris(metilenfosfónico) (H₆NMP) y hexametilendiamina-*N,N,N',N'*-tetrakis(metilenfosfónico) (HDTMP). Estos sólidos se han obtenido mediante cristalización a temperatura ambiente y/o reacción hidrotermal/solvotermal. En este último caso, las condiciones óptimas de síntesis se establecieron siguiendo una metodología de síntesis en paralelo o “high-throughput”.
- Tanto el derivado de Fe(II), **Fe-HPAA**, como los derivados bimetálicos de Fe(II), **Fe_xM_{1-x}-HPAA**, del ácido *R,S* 2-hidroxifosfonoacético mostraron buenas propiedades como catalizadores foto-Fenton así como conductores protónicos. Estos materiales constituyen un ejemplo de sólidos multifuncionales, aprovechando tanto las características del ion metálico –por sus propiedades redox y su reactividad– como del ligando –por sus propiedades ácidas–. Como fotocatalizadores, los derivados de Fe(II) mostraron una gran eficiencia en la degradación de contaminantes recalcitrantes, tales como el fenol, 4-clorofenol y el azul de metileno (MB). La mineralización del fenol y del 4-clorofenol se llevó a cabo bajo radiación UV-A así como luz visible en presencia de H₂O₂, con porcentajes de eliminación cercanos al 90% aunque a mayores tiempos de reacción (180 minutos frente a 80 minutos bajo radiación UV-A). En el caso del MB, solo pudo ser parcialmente mineralizado (75%) bajo radiación UV-A. Por otro lado, el hidroxifosfonoacetato de Fe(II) y sus derivados presentan una conductividad protónica mediada por las especies huéspedes NH₃/H₂O, la cual aumenta de manera gradual al aumentar la cantidad de ambas especies adsorbidas hasta un máximo de 1.75 mol NH₃ y 3 mol H₂O por fórmula para el **Fe-NH₃-72h**. Tras la adsorción de amoníaco, la fracción amorfa de estos sólidos va aumentando. Sin embargo, mediante el estudio de PDF se comprobó que el entorno local del Fe(II) se conservaba.

- Los sulfofosfonatos de Mn^{2+} y Ln^{3+} presentan una estructura laminar, donde el grupo sulfonato puede actuar como ligando puente, caso del *m-LaH₂SP*, o estar protonado, como en *o-LnH₂SP* y en *o-Mn₂HSP*, lo cual contribuye a reforzar las redes de enlace de hidrógeno, una característica importante para la conductividad protónica. Ambos derivados de Zn, *m-Zn₂HSP* y *h-Zn₂HSP*, presentaron los mayores valores de conductividad protónica ($\sim 10^{-2}$ S·cm⁻¹ at 80 °C and 95% RH). Sin embargo, sus estructuras cristalinas aún no están resueltas. Se han estudiado las diferencias estructurales entre *m-LaH₂SP* y *o-LnH₂SP*, con el fin de establecer relaciones entre su estructura y sus propiedades. A partir de estas correlaciones, se puede deducir que el grupo sulfonato no coordinado desempeña un papel importante para conectar otros grupos funcionales y/o moléculas huéspedes mediante redes de enlaces de hidrógeno, lo que puede ayudar a mejorar la conductividad protónica. En estos materiales, la conductividad se debió principalmente a las características estructurales, aunque también se vio afectada por otros factores como el calentamiento a alta humedad relativa o el tamaño de los agregados de partículas.
- Se han sintetizado dos series polimórficas de derivados laminares de lantánidos del ácido aminotris(metilenfosfónico) en las que se incorpora sulfato, **Ln-I** y **Ln II**, siendo su principal diferencia el papel estructural que desempeña este anión. En la Serie **Ln-I**, el sulfato está presente como hidrogenosulfato, actuando como compensador de cargas en el espacio interlaminar, mientras que en la Serie **Ln-II** actúa como ligando puente, conectando los dímeros Ln₂O₁₄ en la lámina. Como resultado de estas diferencias estructurales, los compuestos de ambas series muestran distinta estabilidad química y conductividad protónica. Los sólidos de la serie **Ln-I** evolucionan hacia una fase sulfato deficiente al calentarlos a alta humedad relativa, **SD-Ln-I**. Estos sólidos permanecen estables bajo las condiciones de medida de impedancia, mostrando unos altos valores de conductividad protónica (10^{-2} S·cm⁻¹ a 80 °C y 95% RH). Otro aspecto interesante es que al calentar a 230 °C los sólidos de la Serie **Ln-I**, se obtiene una nueva fase cristalina y anhidra, la cual presenta los mayores valores de conductividad protónica ($3.6 \cdot 10^{-2}$ S·cm⁻¹ a 80 °C y 95% RH) gracias a la capacidad de adsorber agua. Todas estas transformaciones estructurales se

deben a los diferentes modos en los que el Ln^{3+} se encuentra coordinado por las especies sulfato. Los sólidos de la Serie **Ln-II** también exhiben altos valores de conductividad, hasta $3.5 \cdot 10^{-3} \text{ S} \cdot \text{cm}^{-1}$ en las mismas condiciones de operación.

- Los tetrafosfonatos de metales alcalinos y alcalinotérreos, derivados del ácido HDTMP, han mostrado una amplia diversidad estructural: desde monodimensionales (Li^+ y Na^+), pasando por sólidos laminares (K^+), hasta estructuras tridimensionales (Cs^+ , Rb^+ y Mg^{2+}), la cual se relaciona con el tamaño del catión. Las medidas de impedancia indican que las fases hidratadas de los derivados de Li^+ y Mg^{2+} presentan una conductividad protónica moderada. Mediante tratamiento térmico ambas fases evolucionan a otras fases cristalinas anhidras. Sin embargo, el proceso de deshidratación/rehidratación es completamente reversible en el intervalo de temperaturas estudiadas y conlleva cambios sutiles en las redes de enlace de hidrógeno que implican un aumento de la conductividad protónica en casi un orden de magnitud.
- La mayoría de los materiales estudiados presentan valores de energía de activación bajos ($< 0.5 \text{ eV}$), típicos de un mecanismo de transporte protónico tipo Grotthuss, y su conductividad protónica pudo ser mejorada mediante tratamientos post-síntesis. Además, algunos de ellos, en particular **$\sigma\text{-SmH}_2\text{SP}$** , **Eu-I-230C**, **SD-Eu-I** y **Tb-II**, se han probado con éxito en membranas mixtas, empleando Nafion® como matriz polimérica. Estas membranas han mostrado un excelente rendimiento en las condiciones de operación habituales de las pilas de combustible (PEMFCs), incluso mejorando el de la propia membrana de Nafion sin modificar.

8.1. Perspectivas futuras

Aunque la química de los fosfonatos dificulta el diseño previo de estructuras con dimensiones deseadas, los continuos avances en la síntesis de ligandos basados en fosfonatos han proporcionado una serie de ligandos multifuncionales que permiten la síntesis de nuevos fosfonatos metálicos con propiedades específicas predeterminadas. Algunas de estas propiedades son

CAPÍTULO 8

muy atractivas para enfrentar algunos de los desafíos más complejos en el área de la química del estado sólido, como por ejemplo el uso y producción sostenible de energía, así como otros problemas medioambientales. Por ello, se espera que mediante la combinación apropiada de iones metálicos que posean características químicas específicas, como por ejemplo propiedades redox y/o catalíticas, luminiscentes, etc., con ligandos fosfonatos multifuncionales, los cuales proporcionan distintos modos de coordinación en redes/estructuras robustas, se continúe ampliando el campo de la química de los fosfonatos metálicos en los próximos años. En particular, los fosfonatos metálicos son especialmente interesante como conductores protónicos, ya que pueden ser fácilmente preparados en condiciones ácidas y se pueden llevar a cabo modificaciones post-síntesis. La mayoría de los fosfonatos metálicos estudiados poseen estructuras con redes de enlaces extendidos y presentan valores moderados/altos de conductividad protónica. Más específicamente, los fosfonatos de lantánidos son potenciales candidatos debido a que sus propiedades de coordinación contribuyen a aumentar la conductividad protónica de diferentes maneras, por ejemplo, permitiendo la presencia de moléculas de agua coordinadas y sin coordinar, creando capas cargadas positivamente y, por tanto, la inclusión de ligandos secundarios que contribuyen aún más a definir las rutas de transferencia de protones, además de la capacidad de coordinar diferentes grupos funcionales, dependiendo de las condiciones de síntesis. También se ha demostrado que los fosfonatos lantánidos aumentan las propiedades de las membranas compuestas basadas en Nafion en ensamblajes de membrana-electrodos (MEAs) bajo las condiciones de operación de las PEMFCs. Teniendo en cuenta estas premisas, prevemos algunas de las futuras líneas de investigación a implementar:

- Síntesis de monocristales adecuados de $m\text{-Zn}_2\text{HSP}$ y $h\text{-Zn}_2\text{HSP}$ para establecer relaciones entre sus estructuras y sus propiedades.
- Preparación y caracterización de nuevos fosfonatos lantánidos funcionalizados con otros aniones distintos a Cl^- y SO_4^{2-} con el fin de estudiar su influencia en sus propiedades de conductividad protónica.

CONCLUSIONES & PERSPECTIVAS FUTURAS

- Preparación y caracterización de membranas mixtas, extendiendo los tipos de carga a otros fosfonatos metálicos, como ***o*-Mn₂HSP**, ***m*-Zn₂HSP** y ***h*-Zn₂HSP**, y matrices poliméricas (Nafion, ácidos polivinilfosfónicos, chitosan, etc.).
- Estudio de las propiedades mecánicas de las membranas mixtas preparadas.
- Estudio de las prestaciones de las membranas mixtas bajo condiciones de operación de las PEMFCs.
- Empleo de fosfonatos de metales de transición como precursores de electrocatalizadores en PEMFCs, derivados de pirólisis.



UNIVERSIDAD
DE MÁLAGA

Appendices



UNIVERSIDAD
DE MÁLAGA

Appendix I

Abbreviations





UNIVERSIDAD
DE MÁLAGA

ABBREVIATIONS

AOPs	Advanced Oxidation Processes
CP	Coordination Polymer
Ea	Activation Energy
EtOH	Ethanol
FT-IR	Fourier Transformation Infrared Spectroscopy
HDTMP	Hexamethylenediamine-N,N,N',N'-tetrakis(methylenephosphonic acid)
H ₆ NMP	Aminotris(methylenephosphonic acid)
HPAA	R,S 2-hydroxyphosphonoacetic acid
H ₅ SP	2-[bis(phosphonomethyl)amino]-ethanesulfonic acid
IC	Inorganic Carbon
ICP-MS	Inductively Coupled Plasma Mass Spectrometry
LXRPD	Laboratory X-Ray Powder Diffraction
MB	Methylene Blue
MEA	Membrane Electrode Assembly
MOF	Metal Organic Framework
MP	Metal Phosphonate
NMR	Nuclear Magnetic Resonance
PCP	Porous Coordination Polymer
PDF	Pair Distribution Function
PEEK	Polyetheretherketone
PEEK-S	Sulfonated polyetheretherketone
PEMFC	Proton-Exchange Membrane Fuel Cell
phen	1,10-phenanthroline
RH	Relative humidity
RT	Room temperature
SCXRD	Single Crystal X-Ray Diffraction
SEM	Scanning Electron Microscopy
SP	Sulfophosphate
SPPEK	Sulfonated poly(phthalazinone ether sulfone ketone)
TC	Total Carbon
TG-DTA	Thermogravimetric and differential thermal analysis
TOC	Total Organic Carbon

APPENDIX I

XPS	X-Ray Photoelectron Spectroscopy
XRD	X-Ray Diffraction
XRPD	X-Ray Powder Diffraction

Appendix II

CHNS Elemental Analysis





UNIVERSIDAD
DE MÁLAGA

Table AII.1. Elemental analysis for **M-HPAA** solids and the corresponding solid solutions.

Sample	%C		%H	
	Found	Calc.	Found	Calc.
Fe-HPAA	9.011	9.424	2.935	3.163
Fe_{0.89}Zn_{0.11}-HPAA	9.043	9.385	2.648	3.150
Fe_{0.71}Zn_{0.29}-HPAA	9.030	9.323	2.763	3.129
Fe_{0.54}Zn_{0.46}-HPAA	8.953	9.264	2.797	3.110
Fe_{0.41}Zn_{0.59}-HPAA	8.795	9.220	2.828	3.095
Zn-HPAA	8.874	9.084	2.725	3.049

Table AII.2. Elemental analysis for **M(II)-HPAA** solids.

Sample	x (h)	%C		%H		%N	
		Found	Calc.	Found	Calc.	Found	Calc.
Fe-NH₃-xh	12	9.046	9.300	3.147	3.356	1.071	1.085
	24	8.967	9.179	3.285	3.543	1.953	2.141
	36	8.638	8.974	3.587	3.860	3.777	3.925
	42	8.669	8.946	3.595	3.904	4.257	4.173
	48	8.340	8.423	3.838	4.506	5.998	6.139
	72	7.615	8.179	4.629	4.890	8.796	8.346
Fe_{0.89}Zn_{0.11}-NH₃-xh	1	8.821	8.951	2.814	3.606	0.912	1.044
	5	8.559	8.784	3.652	3.870	2.529	2.561
Fe_{0.71}Zn_{0.29}-NH₃-xh	1	8.634	8.699	3.520	3.942	3.007	3.044
	5	7.912	8.242	4.435	4.669	7.227	7.209
Fe_{0.54}Zn_{0.46}-NH₃-xh	1	8.321	8.419	3.910	4.239	4.935	4.909
Fe_{0.41}Zn_{0.59}-NH₃-xh	1	8.164	8.236	4.083	4.458	6.264	6.243

APPENDIX II

Table AII.3. Elemental analysis results for ***o*-Mn₂HSP**, ***m*-Zn₂HSP**, ***h*-Zn₂HSP** and **LnH₂SP** compounds.

Sample	%C		%H		%N		%S	
	Found	Calc.	Found	Calc.	Found	Calc.	Found	Calc.
<i>o</i>-Mn₂HSP	9.48	9.77	3.16	3.46	2.90	2.85	6.10	6.52
<i>m</i>-Zn₂HSP	9.14	9.28	3.64	4.12	7.16	7.66	4.70	5.16
<i>h</i>-Zn₂HSP	8.36	8.53	3.59	4.12	2.55	2.49	5.40	5.68
<i>m</i>-LaH₂SP	8.58	9.91	2.63	2.91	2.98	2.89	5.36	6.61
<i>o</i>-PrH₂SP	9.64	9.86	2.89	2.90	3.11	2.88	6.64	6.58
<i>o</i>-NdH₂SP	9.43	9.68	2.92	2.88	3.08	2.86	6.38	6.54
<i>o</i>-SmH₂SP	9.22	9.68	2.91	2.84	2.99	2.82	6.21	6.46
<i>o</i>-EuH₂SP	9.83	10.01	2.48	2.52	2.95	2.92	6.70	6.68
<i>o</i>-GdH₂SP	9.41	9.54	2.84	2.80	2.81	2.78	6.19	6.40
<i>o</i>-TbH₂SP	9.32	9.51	2.78	2.79	2.76	2.77	6.39	6.35

Table AII.4. Elemental analysis for compounds of Series **Ln-I** and **Ln-II**.

SAMPLE	% C		% H		% N		% S		
	Found	Calc.	Found	Calc.	Found	Calc.	Found	Calc.	
SERIES I	Pr (n=4)	5.87	5.94	2.77	3.16	2.36	2.31	5.10	5.28
	Nd (n=4)	5.88	5.90	2.99	3.14	2.32	2.29	4.98	5.25
	Sm (n=4)	5.66	5.84	3.17	3.11	2.27	2.27	5.75	5.20
	Eu (n=4)	5.46	5.78	2.91	3.07	2.25	2.25	5.02	5.14
	Gd (n=4)	5.58	5.75	3.00	3.21	2.26	2.23	5.40	5.11
	Tb (n=4)	5.58	5.76	3.00	3.06	2.27	2.24	5.18	5.13
	Er (n=5)	5.24	5.61	2.85	3.14	2.13	2.18	5.42	5.13
	Yb (n=5)	5.27	5.56	3.37	3.11	2.20	2.16	4.49	4.95
	Eu _{1.6} Tb _{0.4}	5.36	5.82	3.01	3.09	2.18	2.26	4.80	5.18
	Tb _{1.6} Eu _{0.4}	5.43	5.78	2.99	3.07	2.36	2.25	5.10	4.87
SERIES II	Pr	5.89	6.31	2.62	2.65	2.42	2.45	5.78	5.62
	Eu	6.09	6.19	2.70	2.60	2.54	2.41	5.73	5.51
	Nd	6.27	6.08	2.63	2.89	2.44	2.36	4.58	5.41
	Gd	5.38	6.13	2.60	2.57	2.23	2.38	5.80	5.46
	Tb	6.14	6.12	2.62	2.57	2.27	2.38	5.74	5.44

Table AII.5. Elemental analysis for anhydrous compounds of Series Ln-I.

SAMPLE	% C		% H		% N		% S	
	Found	Calc.	Found	Calc.	Found	Calc.	Found	Calc.
Eu-I-230	6.38	6.60	1.89	2.03	2.58	2.57	4.87	5.87
Tb-I-230	6.29	6.52	1.88	2.01	2.52	2.53	6.47	5.80

Table AII.6. Elemental analysis for M(I)-HDTMP and Mg-HDTMP derivatives.

Sample	%C		%H		%N	
	Found	Calc.	Found	Calc.	Found	Calc.
Li-HDTMP-4W	20.40	20.85	5.83	5.95	5.02	4.86
Na-HDTMP	17.31	17.65	5.79	6.22	4.17	4.12
K-HDTMP	16.76	16.85	5.75	5.94	4.01	3.93
Rb-HDTMP	17.08	17.54	5.01	5.74	4.10	4.09
Cs-HDTMP	17.13	17.25	4.89	5.07	4.10	4.02
Mg-HDTMP-1	22.25	22.55	5.30	5.30	5.29	5.26
Mg-HDTMP-1deh	22.90	23.34	5.13	5.09	5.42	5.44
Mg-HDTMP-2	23.06	23.34	5.21	5.09	5.30	5.44

Table AII.7. Elemental analysis and weight loss for Li- and Mg-HDTMP derivatives.

Sample	NH ₃ /H ₂ O content	%C		%H		%N		Weight loss (%)	
		Found	Calc.	Found	Calc.	Found	Calc.	Found	Calc.
Li-HDTMP-NH₃-2h	2.0/8	17.97	17.76	6.31	7.30	8.01	8.28	22.22	20.23
Mg-HDTMP-3	1.5/4	19.38	19.62	6.33	6.34	7.91	8.01	11.30	11.76
Mg-HDTMP-4	2.5/7	17.57	17.58	6.77	7.01	9.38	9.23	18.60	18.44



UNIVERSIDAD
DE MÁLAGA

Appendix III

Final Rietveld Plots





UNIVERSIDAD
DE MÁLAGA

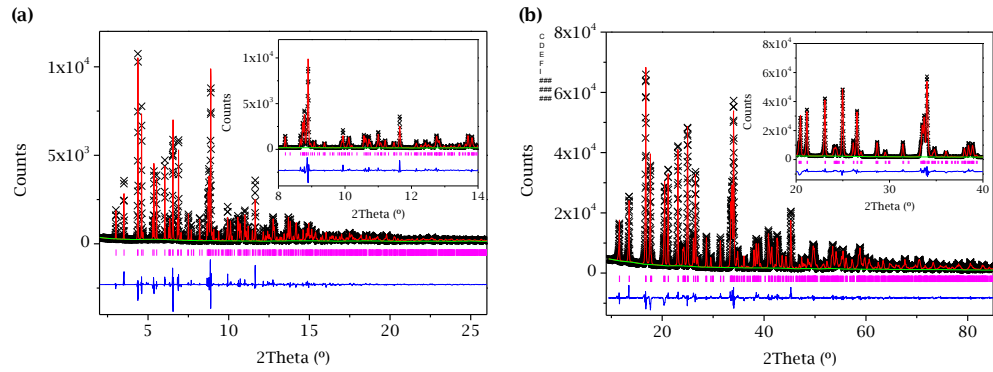


Figure AIII.1. Final Rietveld plots for (a) Fe-HPAA and (b) Zn-HPAA.

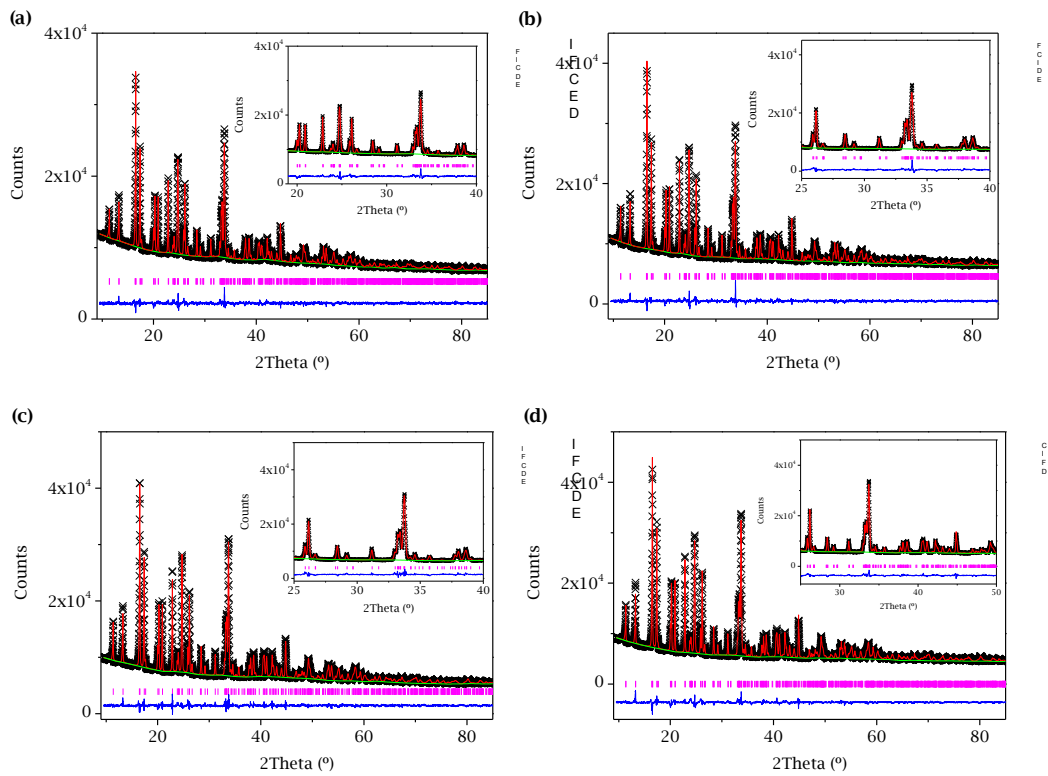


Figure AIII.2. Final Rietveld plots for (a) $\text{Fe}_{0.89}\text{Zn}_{0.11}$ -HPAA, (b) $\text{Fe}_{0.71}\text{Zn}_{0.29}$ -HPAA, (c) $\text{Fe}_{0.54}\text{Zn}_{0.46}$ -HPAA and (d) $\text{Fe}_{0.41}\text{Zn}_{0.59}$ -HPAA.

APPENDIX III

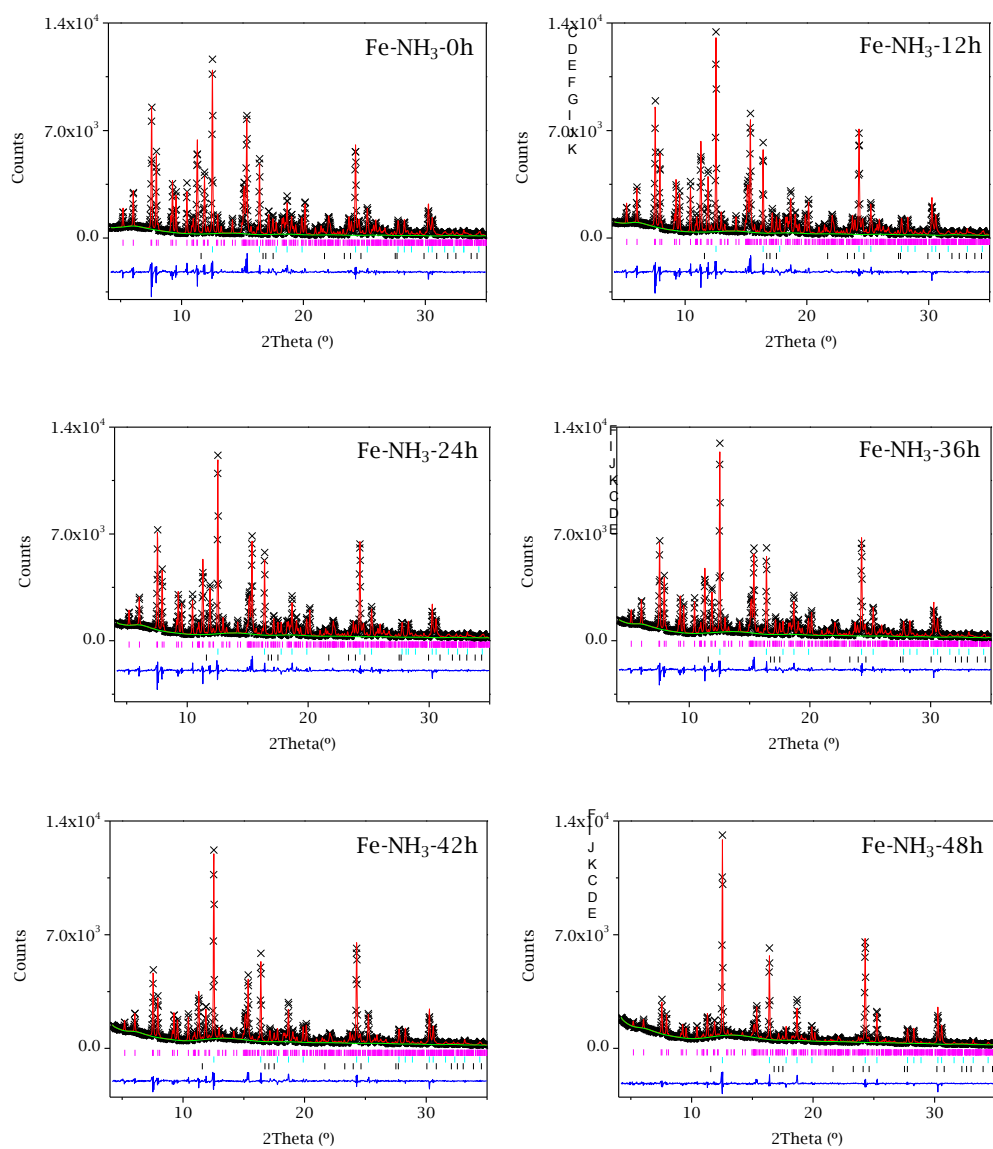


Figure AIII.3. Rietveld plots for Fe-NH₃-xh samples.

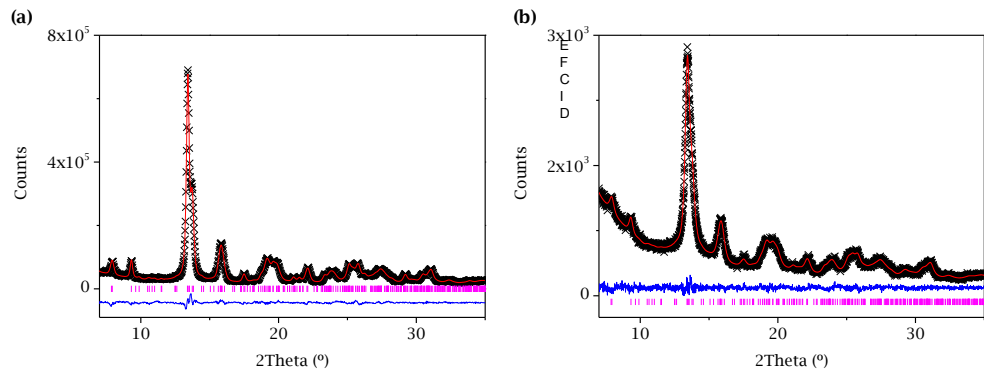


Figure AIII.4. Rietveld refinement plot for $\text{Fe}_2\text{P}_2\text{O}_7$ obtained by calcination at 700 °C under N_2 of (a) Fe-HPAA and (b) Fe- NH_3 -72h.

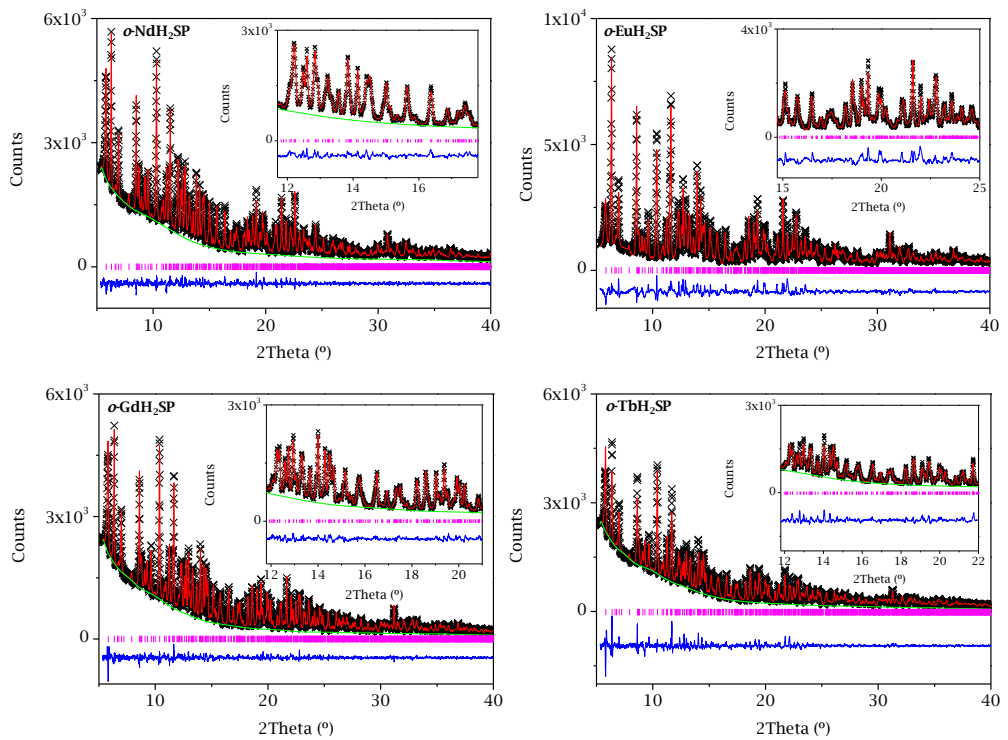


Figure AIII.5. Final Rietveld plots for $o\text{-LnH}_2\text{SP}$ (Ln= Nd, Eu, Gd and Tb).

APPENDIX III

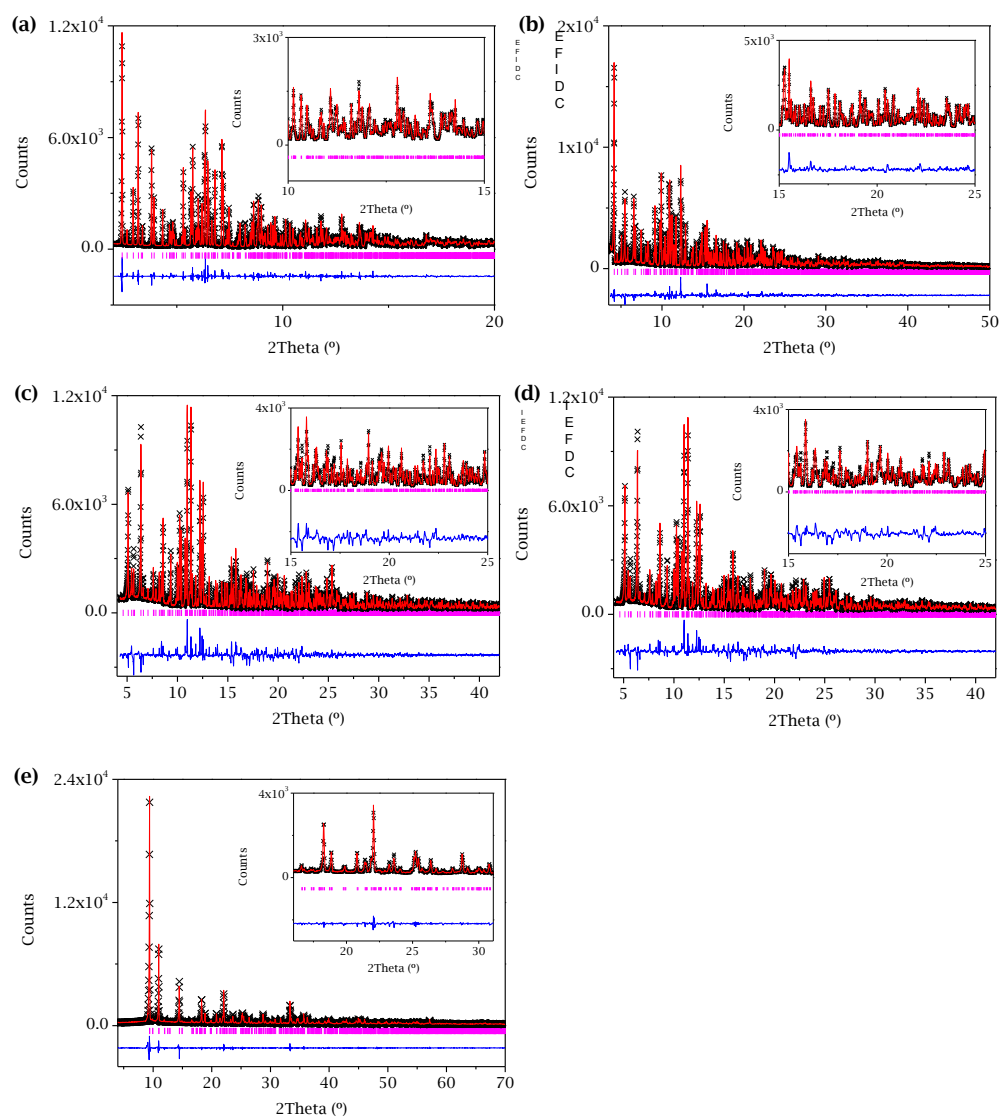


Figure AIII.6. Final Rietveld plots for (a) Eu-I, (b) Gd-I, (c) Er-I and (d) Yb-I and Le Bail fit for (e) Pr-I.

FINAL RIETVELD PLOTS

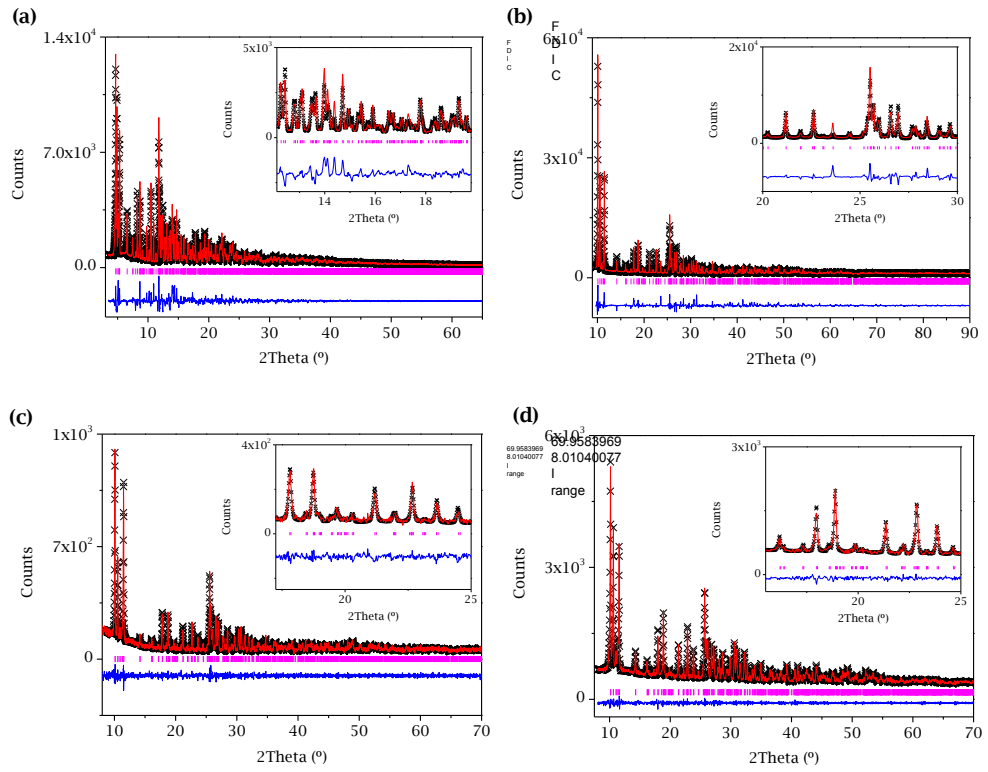


Figure AIII.7. Final Rietveld plots for (a) Pr-II and (b) Gd-II and Le Bail fits for (c) Nd-II and (d) Eu-II.

APPENDIX III

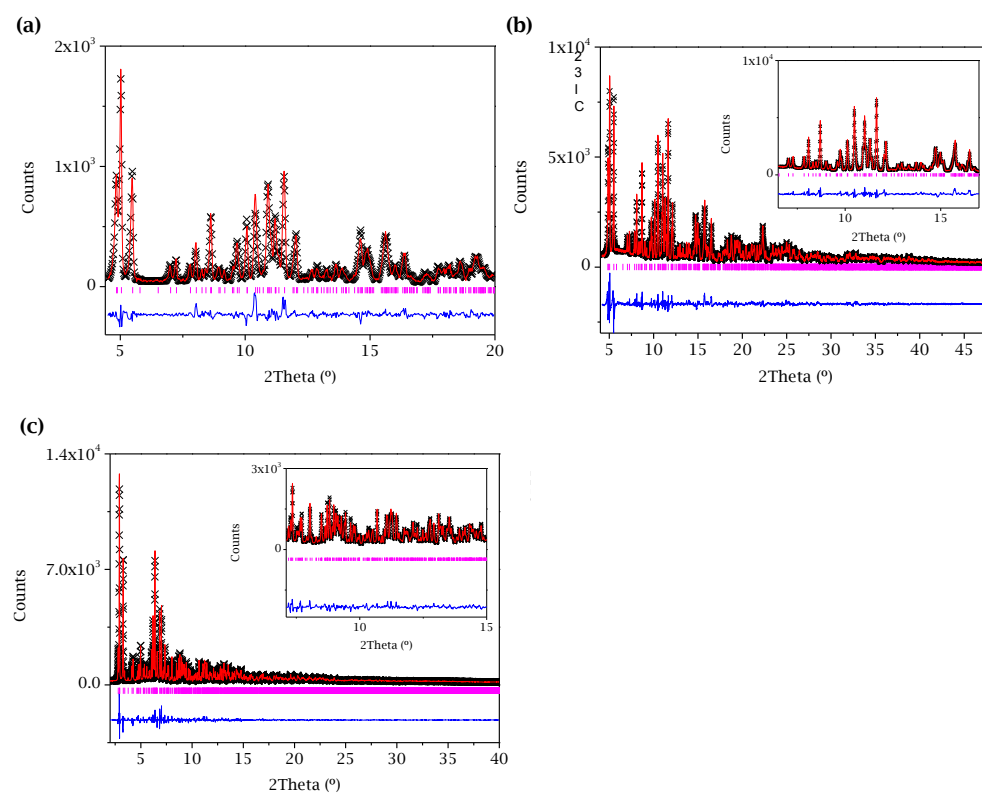


Figure AIII.8. Final Rietveld plots for (a) Eu-I-230, (b) Tb-I-230 and (c) SD-Tb-I.

Appendix IV

Nyquist Plots





UNIVERSIDAD
DE MÁLAGA

NYQUIST PLOTS

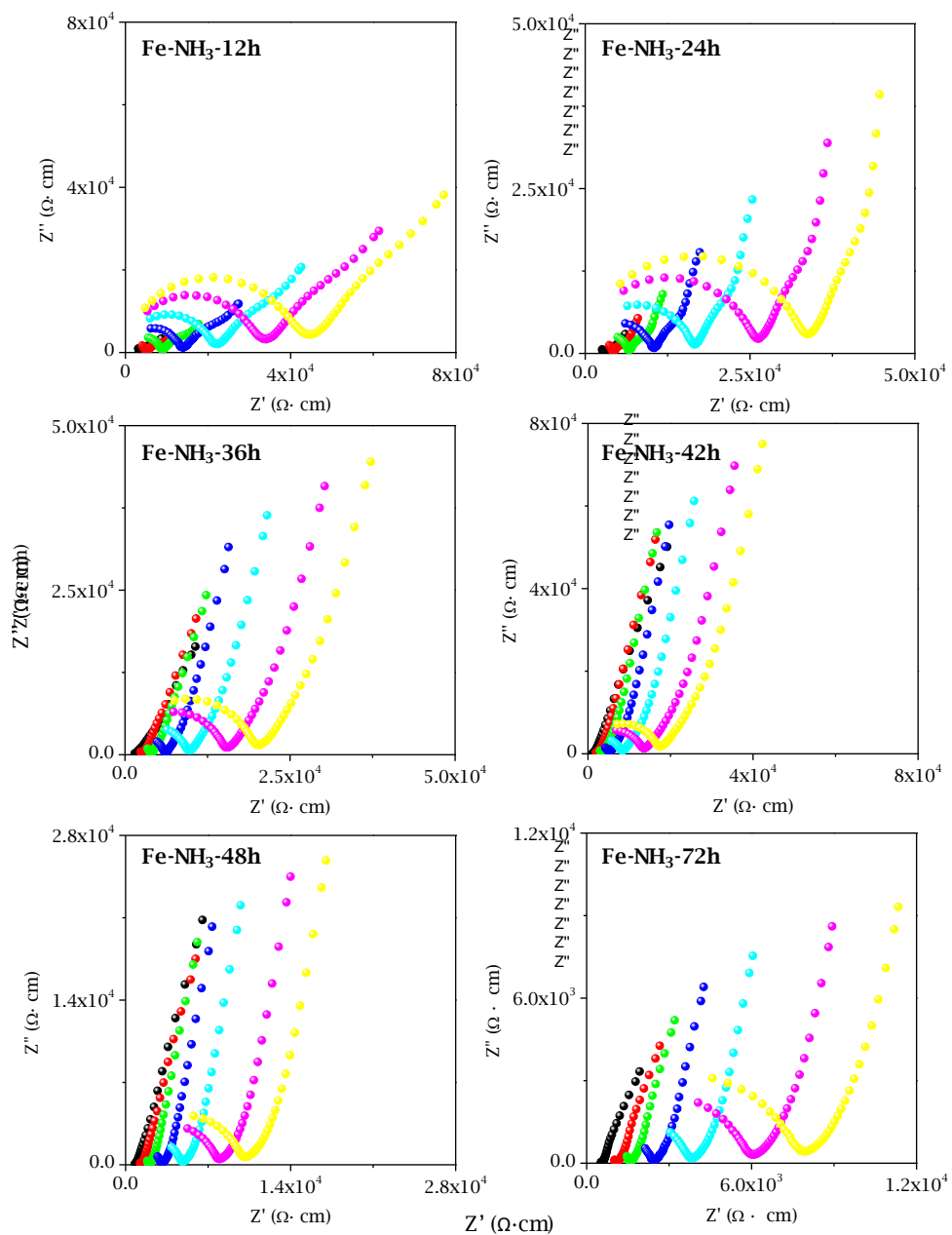


Figure AIV.1. Plots of the complex impedance plane for **Fe-NH₃-xh** derivatives at 95% RH and temperatures of: 80 (black), 70 (red), 60 (green), 50 (blue), 40 (cyan), 30 (magenta) and 25 °C (yellow).

APPENDIX IV

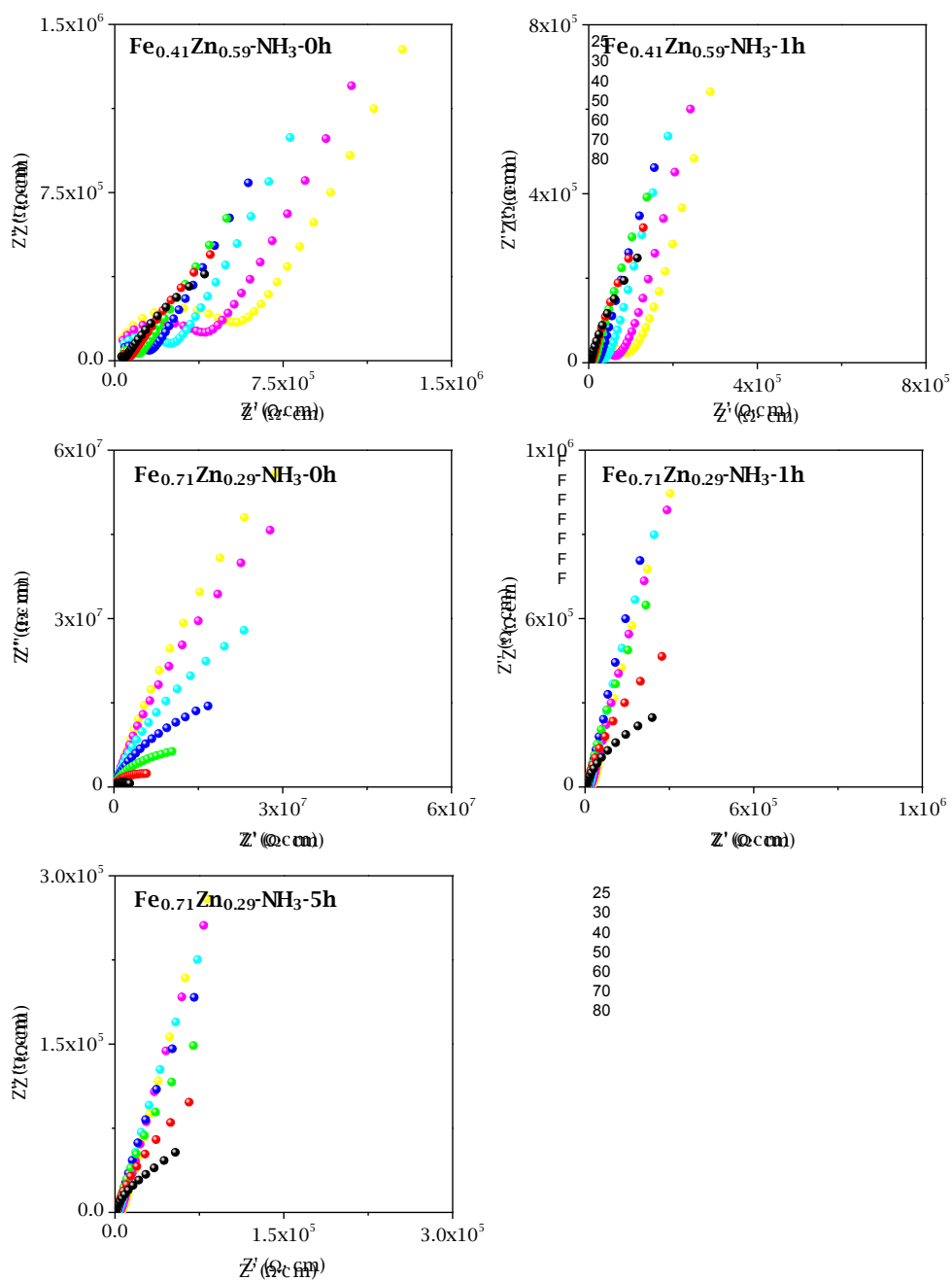


Figure AIV.2. Plots of the complex impedance plane for $\text{Fe}_x\text{Zn}_{1-x}\text{-NH}_3\text{-xh}$ derivatives at 95% RH and temperatures of: 80 (black), 70 (red), 60 (green), 50 (blue), 40 (cyan), 30 (magenta) and 25 °C (yellow).

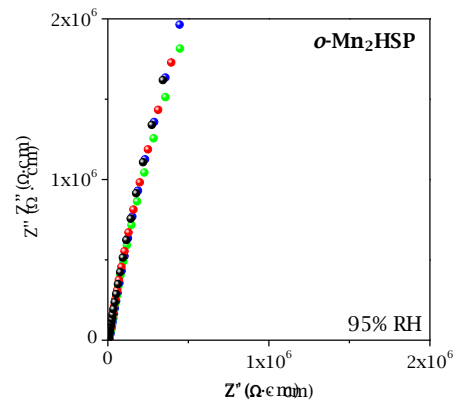


Figure AIV.3. Complex impedance plane plots for *o*-Mn₂HSP at different RH and temperatures: 80 (black), 70 (red), 60 (green), 50 (blue), 40 (cyan), 30 (magenta) and 25 °C (yellow).

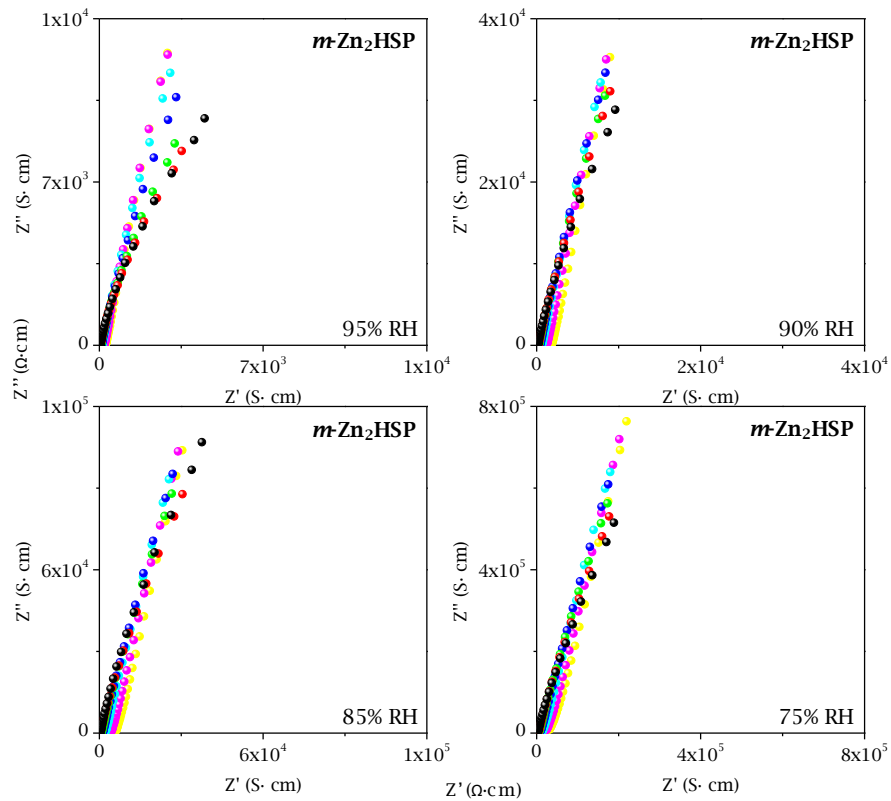


Figure AIV.4. Complex impedance plane plots for *m*-Zn₂HSP at different RH and temperatures: 80 (black), 70 (red), 60 (green), 50 (blue), 40 (cyan), 30 (magenta) and 25 °C (yellow).

APPENDIX IV

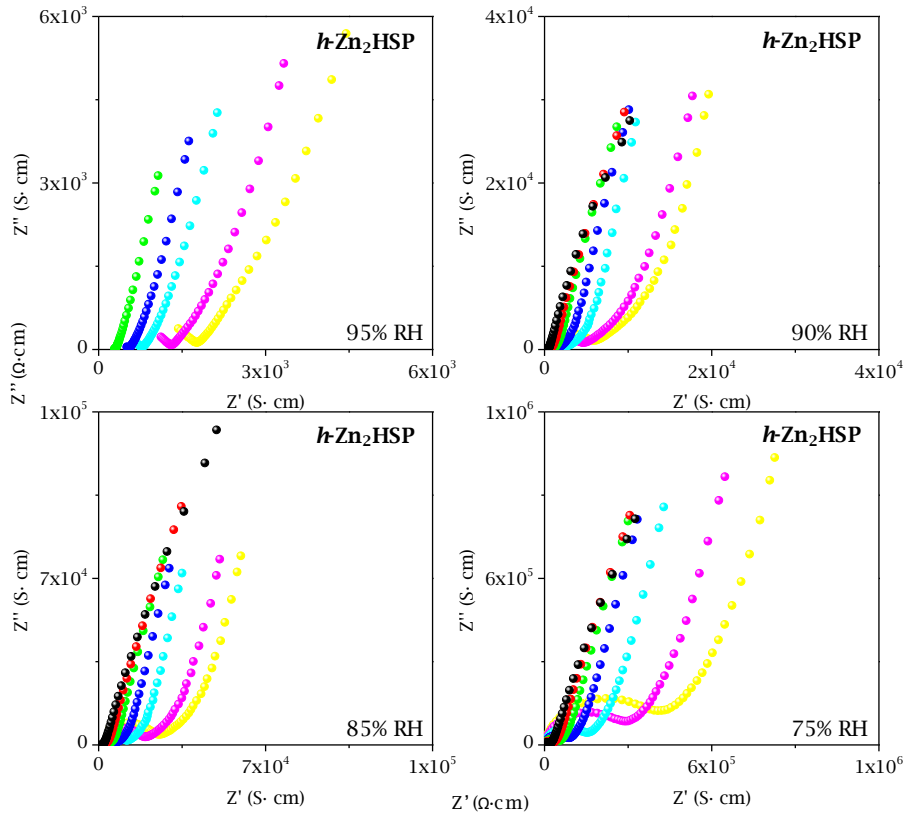


Figure AIV.5. Complex impedance plane plots for *h-Zn₂HSP* at different RH and temperatures: 80 (black), 70 (red), 60 (green), 50 (blue), 40 (cyan), 30 (magenta) and 25 °C (yellow).

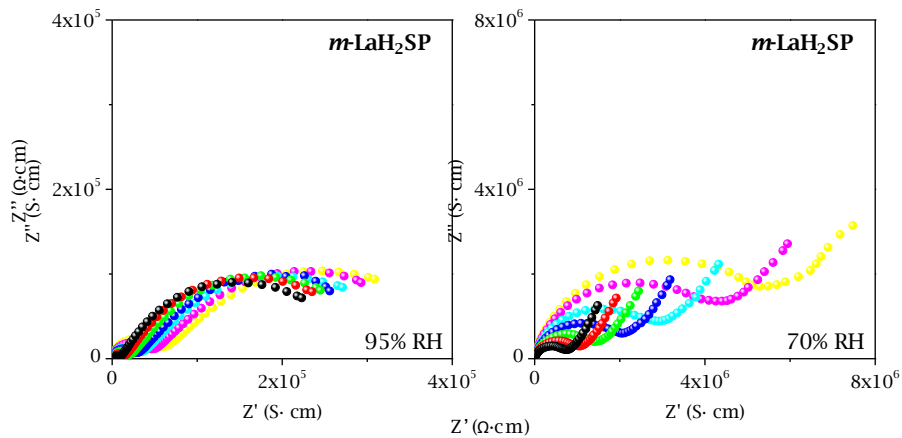


Figure AIV.6. Complex impedance plane plots for *m-LaH₂SP* at different RH and temperatures: 80 (black), 70 (red), 60 (green), 50 (blue), 40 (cyan), 30 (magenta) and 25 °C (yellow).

NYQUIST PLOTS

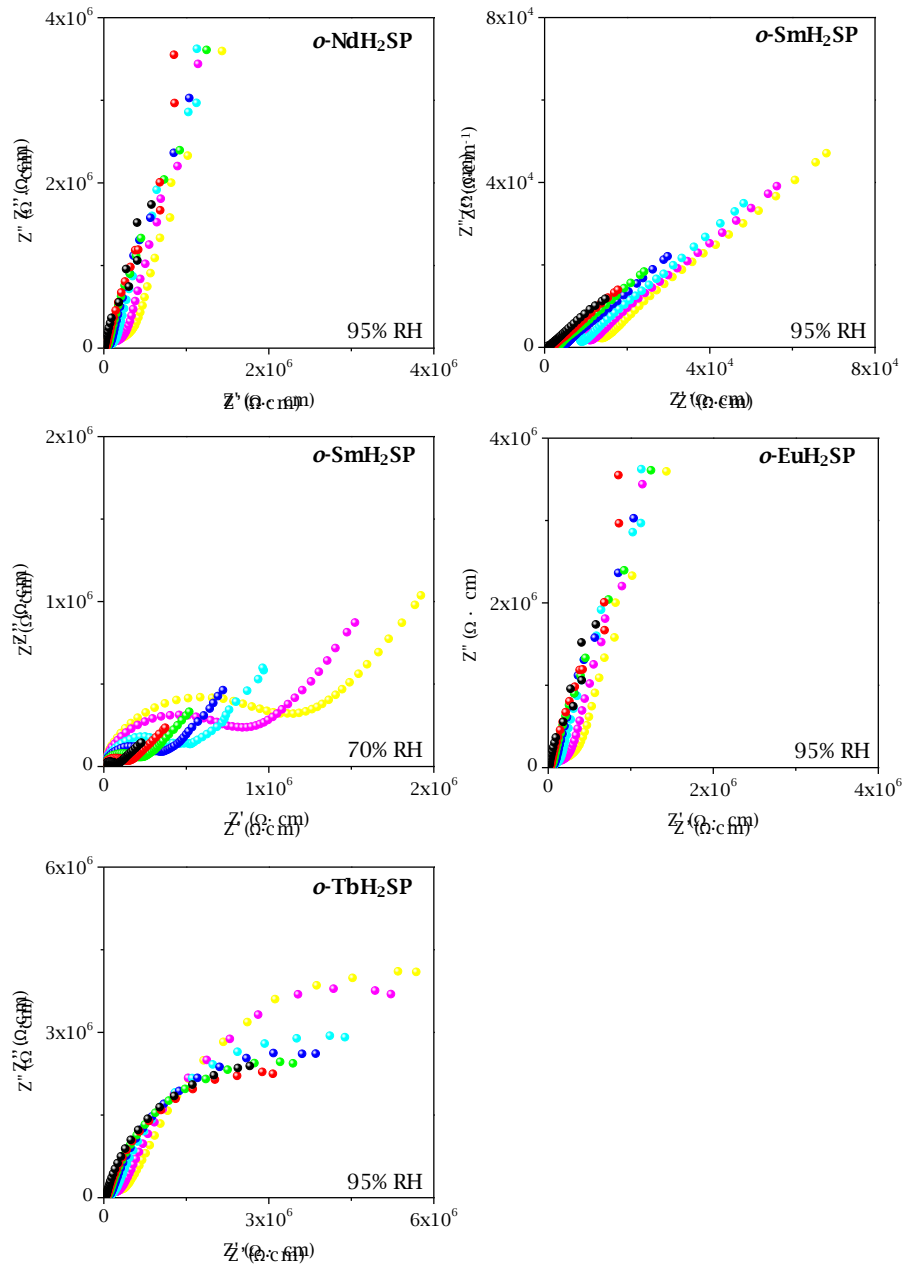


Figure AIV.7. Complex impedance plane plots for $\text{o-LnH}_2\text{SP}$ ($\text{Ln} = \text{Nd}, \text{Sm}, \text{Eu}, \text{and Tb}$) at different RH and temperatures: 80 (black), 70 (red), 60 (green), 50 (blue), 40 (cyan), 30 (magenta) and 25 °C (yellow).

APPENDIX IV

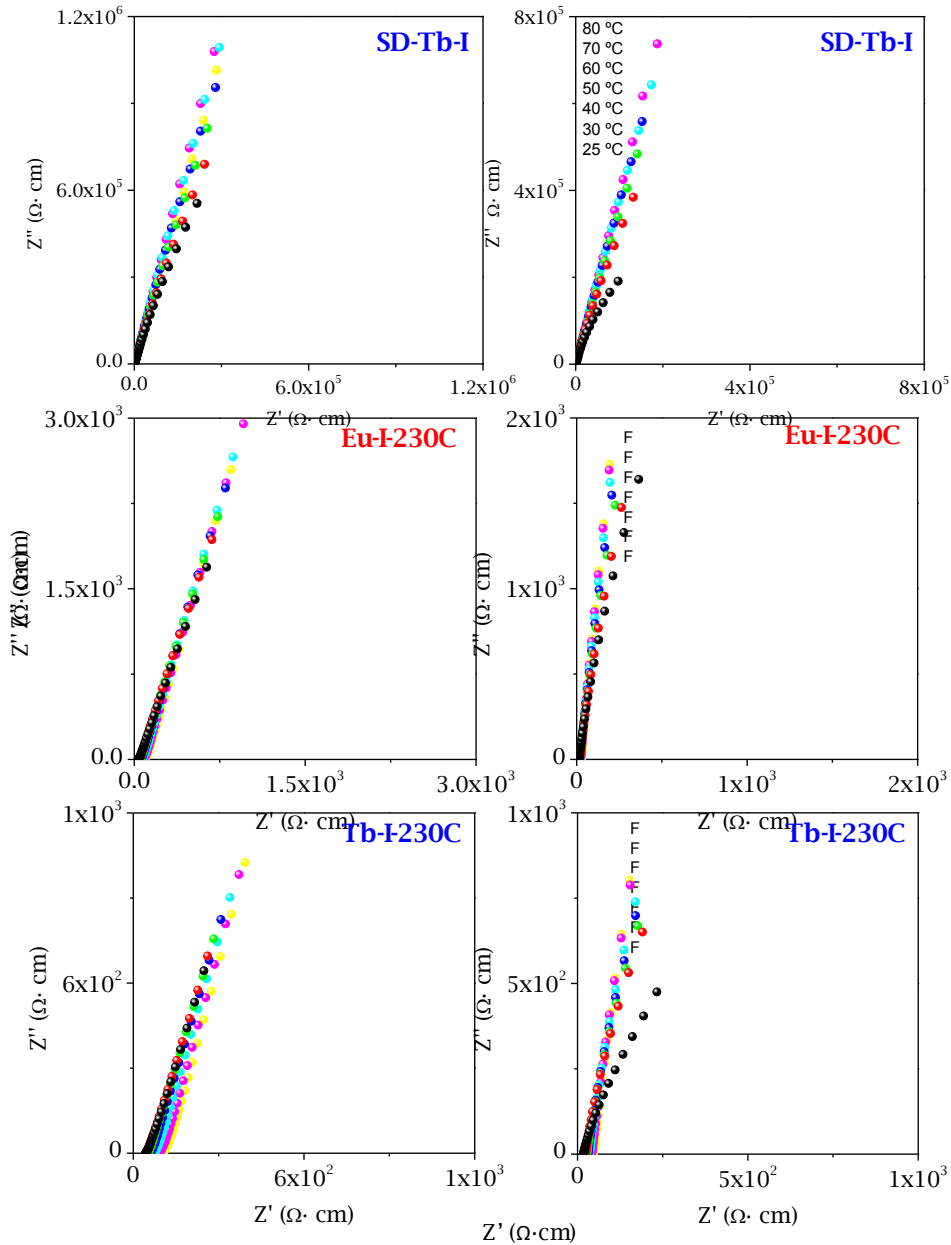


Figure AIV.8. Complex impedance plane plots for Tb-I-SD and Ln-I-230C derivatives at 75 (left) or 95% RH (right) and different temperatures: 80 (black), 70 (red), 60 (green), 50 (blue), 40 (cyan), 30 (magenta) and 25 °C (yellow).

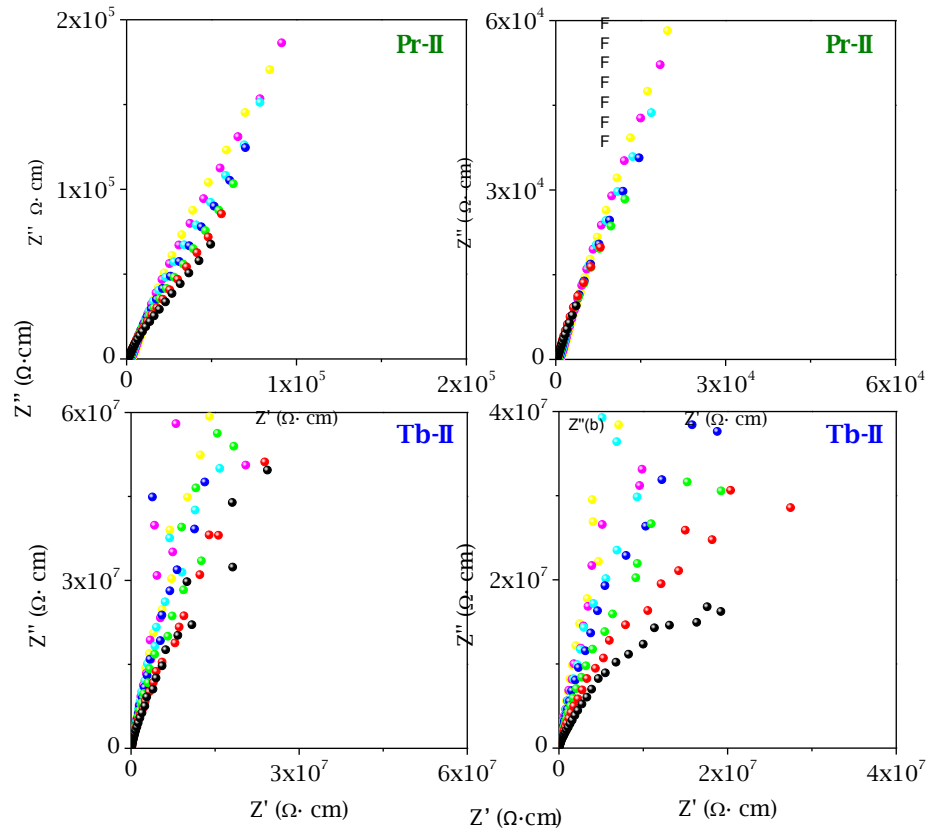


Figure AIV.9. Complex impedance plane plots for Ln-II derivatives at 75 (left) or 95% RH (right) and different temperatures: 80 (black), 70 (red), 60 (green), 50 (blue), 40 (cyan), 30 (magenta) and 25 °C (yellow).

APPENDIX IV

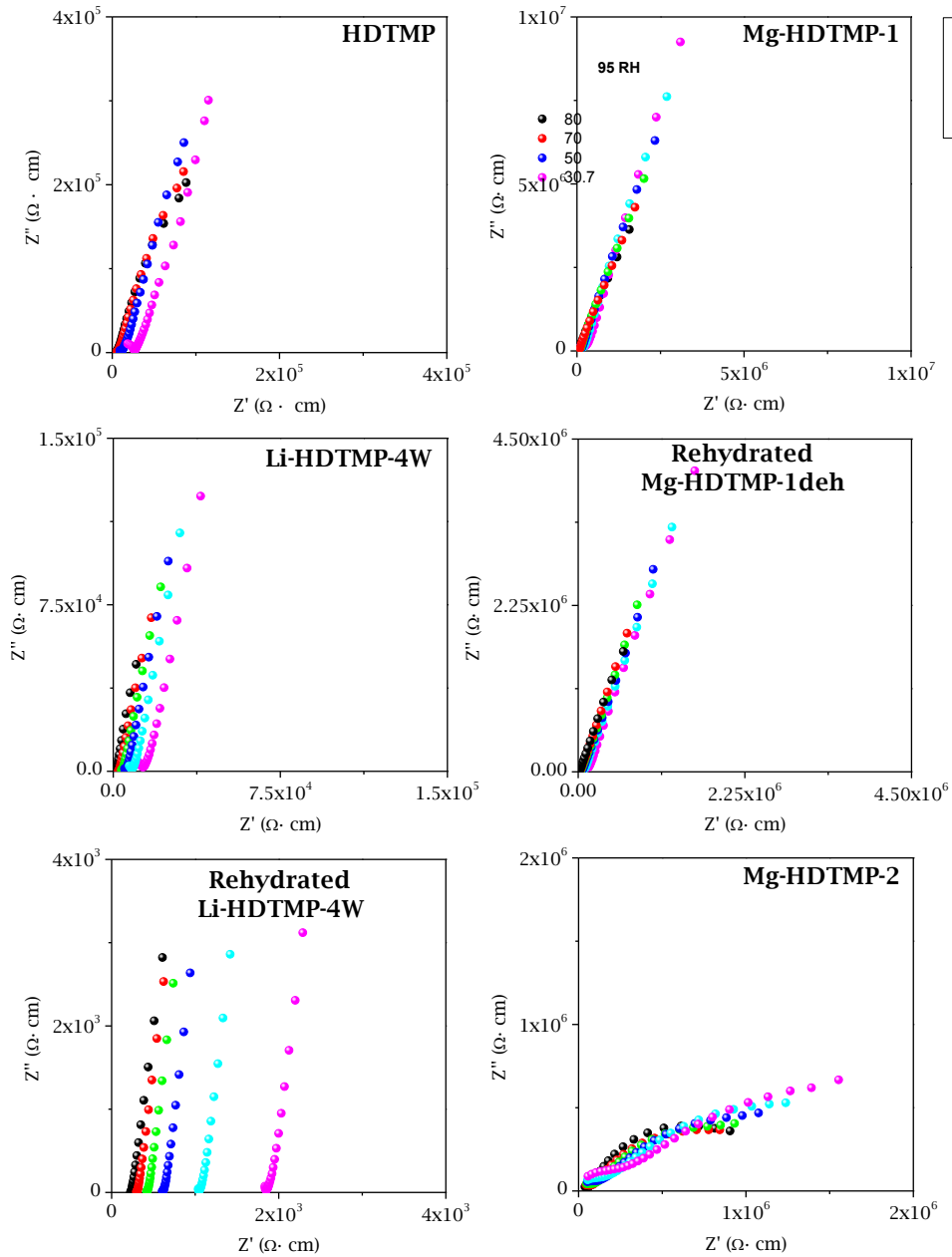


Figure AIV.10. Plots of the complex impedance plane for HDTMP, Li-HDTMP-4W, rehydrated Li-HDTMP, Mg-HDTMP-1, rehydrated Mg-HDTMP-1deh and Mg-HDTMP-2 at 95% RH and temperatures: 80 (black), 70 (red), 60 (green), 50 (blue), 40 (cyan) and 30 °C (magenta).

Appendix V

Articles



UNIVERSIDAD
DE MÁLAGA

Article #1
Salcedo et al., 2020

Salcedo, I. R.; Bazaga-García, M.; Cuesta, A.; Losilla, E. R.; Demadis, K. D.; Olivera-Pastor, P.; Colodrero, R. M. P.; Cabeza, A. $\text{NH}_3/\text{H}_2\text{O}$ -mediated proton conductivity and photocatalytic behaviour of Fe(II)-hydroxyphosphonoacetate and M(II)-substituted derivatives. *Dalton Trans.*, 2020, 49(13), 3981-3988.

APPENDIX V

Dalton Trans., 2020, 49(13), 3981–3988 - Reproduced by permission of The Royal Society of Chemistry. Copyright (2020).



Cite this: *Dalton Trans.*, 2020, 49, 3981

NH₃/H₂O-mediated proton conductivity and photocatalytic behaviour of Fe(II)-hydroxyphosphonoacetate and M(II)-substituted derivatives†

Inés R. Salcedo,^a Montse Bazaga-García,^a Ana Cuesta,^a Enrique R. Losilla,^b Konstantinos D. Demadis,^c Pascual Olivera-Pastor,^a Rosario M. P. Colodrero^{a,c} and Aurelio Cabeza^{a*}

Synthesis redesign and derivatisation of Fe(II)-hydroxyphosphonoacetate, incorporating different ammonia loads and M(II) isomorphous substitutions (M = Mn, Co and Zn), have been implemented. The NH₃ adsorption led to materials with enhanced proton conductivity, up to ~10⁻³ S cm⁻¹, although it caused a progressive amorphization. The Pair Distribution Function (PDF) analysis for this material confirmed the loss of crystallinity but the local order appeared to be maintained. The parent compound was shown to be an efficient photocatalyst for phenol, 4-chlorophenol and methylene blue even under mild conditions, with TOC removal of 75–90% at 50–150 min of reaction. The M(II)-substituted derivatives displayed similar behaviour in properties, and therefore their multifunctional character, as the parent compound, although with slightly reduced capabilities.

Received 30th October 2019,
Accepted 27th December 2019

DOI: 10.1039/c9dt04210e

rsc.li/dalton

Introduction

Among the multitude of organic ligands, (poly)phosphonic acids have received intense attention in the last 20 years.^{1,2} There are several reasons for this: (a) the double deprotonation capability can create the mono-, or the di-anion (depending on pH) species, each one possessing different metal coordination

behavior.³ (b) Phosphonates show high affinity for virtually all metal ions (from “small” monocations, such as Li⁺, to “large” trivalent lanthanides), with enhanced bridging capabilities.⁴ (c) The strong metal–oxygen and P–C bonds are resistant to thermal⁵ or oxidative/hydrolytic cleavage.⁶

In the rich phosphonate linker “toolbox”, one can single out phosphonates that contain one, two, three, four (or even more) phosphonate moieties,^{1,2,7} but also ligands that contain one (or more) phosphonate groups and additional functional moieties. These can be one or more amine,⁸ carboxylate,⁹ sulfonate,¹⁰ pyridine,¹¹ pyrazole,¹² imidazole,¹³ hydroxyl,¹⁴ etc. A recent review presents all these “mixed” phosphonate ligands and their coordination chemistry in the construction of metal-organic materials.¹⁵

The linker *R,S* 2-hydroxyphosphonoacetic acid (HPAA) has been explored as a multifunctional linker in the construction of structurally diverse compounds.^{16–19} Its important structural features include a bis-acidic phosphonic moiety, a mono-acidic carboxylic group and a hydroxyl group. In the compounds reported, HPAA has a preferred (but not exclusive) coordination chemistry, which involves formation of two chelating rings (a 5-membered one utilizing a carboxylate and the hydroxyl oxygens, and a 6-membered one from a phosphonate oxygen and a second carboxylate oxygen). This coordination mode of HPAA is shown in Fig. 1. Certain metal derivatives of HPAA have been investigated for potential applications as corrosion inhibitors,^{20–23} proton conductors^{24,25} and catalysts.²⁶ Since functionality is also provided by the specifically selected

^aDepartamento de Química Inorgánica, Universidad de Málaga, Campus Teatinos S/N, 29071-Málaga, Spain. E-mail: aurelio@uma.es; Tel: +34 952131874

^bCrystal Engineering, Growth and Design Laboratory, Department of Chemistry, University of Crete, Voutes Campus, Crete GR-71003, Greece

^cFaculty of Science & Engineering, University of Wolverhampton, Wulfruna Street, Wolverhampton WV1 1XZ, UK. E-mail: r.p.colodrero@wolverhampton.ac.uk

† Electronic supplementary information (ESI) available: Fig. S1: XRPD patterns for Fe-NH₂-rh, Fe_{0.41}Zn_{0.59}-NH₂-rh and Fe_{0.71}Zn_{0.29}-NH₂-rh derivatives; Fig. S2 and S3: Rietveld plots for M-HPAA and Fe_{0.71}Zn_{0.29}-HPAA; Fig. S4: XRD pattern of Fe-HPAA/Zn-HPAA mixture and Fe_{0.71}Zn_{0.29}-HPAA; Fig. S5: phase identification for Fe_{0.41}Zn_{0.59}-HPAA calcined at 1000 °C; Fig. S6: Rietveld plots for Fe-NH₂-rh; Fig. S7: X-ray PDF analysis; Fig. S8: TG and DTA curves for Fe-HPAA and Fe-NH₂-rh; Fig. S9: Rietveld plots for Fe_{0.41}P_{0.59}O, obtained by calculation of Fe-HPAA and Fe-NH₂-rh; Fig. S10 and S11: Nyquist plots for Fe-NH₂-rh and Fe_{0.41}Zn_{0.59}-NH₂-rh; Fig. S12: FTIR spectra for Fe-HPAA and Fe-NH₂-rh; Fig. S13–15: particle size distribution for Fe-NH₂-rh and Fe_{0.41}Zn_{0.59}-NH₂-rh; Fig. S16: time evolution of Fe, P and Zn leached for the photocatalytic reaction; Fig. S17: Mössbauer absorption spectra for Fe-HPAA solids; Fig. S18: time evolution of TOC removal in different cycles; Fig. S19: XRPD patterns for Fe-HPAA before and after photocatalytic test. Table S1: Elemental analysis and stoichiometries for Fe-NH₂-rh and Fe_{0.41}Zn_{0.59}-NH₂-rh compounds; Table S2: Crystallographic data for M-HPAA and Fe_{0.71}Zn_{0.29}-HPAA; Table S3: Chemical composition for Fe_{0.41}Zn_{0.59}-HPAA; Table S4: XPS Fe(2p)/Fe(s) atomic ratio. See DOI: 10.1039/c9dt04210e

APPENDIX V

Article #2
Bazaga-García et al., 2019

Bazaga-García, M.; Salcedo, I. R.; Colodrero, R. M. P.; Xanthopoulos, K.; Villemin, D.; Stock, N.; López-González, M.; del Río, C.; Losilla, E. R.; Cabeza, A.; Demadis, K. D.; Olivera-Pastor, P. Layered Lanthanide Sulfophosphonates and Their Proton Conduction Properties in Membrane Electrode Assemblies. *Chem. Mater.*, 2019, 31(23), 9625-9634.

APPENDIX V

Reprinted with permission from *Chem. Mater.*, 2019, 31(23), 9625-9634. Copyright (2019) American Chemical Society.

Layered Lanthanide Sulfophosphonates and Their Proton Conduction Properties in Membrane Electrode Assemblies

Montse Bazaga-García,[†] Inés R. Salcedo,[†] Rosario M. P. Colodrero,[‡] Konstantinos Xanthopoulos,[§] Didier Villemain,[¶] Norbert Stock,^{||} Mar López-González,[§] Carmen del Río,[§] Enrique R. Losilla,^{||} Aurelio Cabeza,^{||} Konstantinos D. Demadis,^{§,§} and Pascual Olivera-Pastor^{*,†}

[†]Departamento de Química Inorgánica, Universidad de Málaga, Campus Teatinos s/n, Málaga 29071, Spain

[‡]Faculty of Science & Engineering, University of Wolverhampton, Wulfruna Street, Wolverhampton WV1 1LY, U.K.

[§]Crystal Engineering, Growth and Design Laboratory, Department of Chemistry, University of Crete, Voutes Campus, Heraklion, Crete GR-71003, Greece

^{||}Institut für Anorganische Chemie, Christian-Albrechts-Universität zu Kiel, 24098 Kiel, Germany

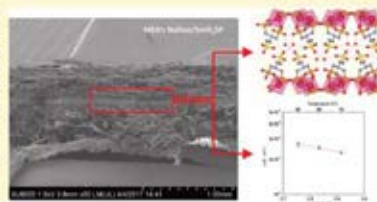
[¶]Laboratoire de Chimie Moléculaire et Thioorganique, ENSICAEN & Université de Caen, UMR CNRS 6507, INC3M, FR 3038 Caen, France

^{*}Instituto de Ciencia y Tecnología de Polímeros (ICTP-CSIC), Juan de la Cierva 3, 28006 Madrid, Spain

Supporting Information

Downloaded via UNIV DE MALAGA on December 10, 2019 at 10:45:31 (UTC).
See <https://pubs.acs.org/sharingguidelines> for options on how to legitimately share published articles.

ABSTRACT: Metal phosphonates containing acidic groups exhibit a wide range of proton conduction properties, which may enhance the performance of membrane electrode assemblies (MEAs). In this work, focus is placed on proton conduction properties of coordination polymers derived from the combination of lanthanide ions with a phosphonate derivative of taurine (2-[bis(phosphonomethyl)amino]ethanesulfonic acid, **H₂SP**). High-throughput hydrothermal screening (140 °C) was used to reach optimal synthesis conditions and access pure crystalline phases. Seven compounds with the composition $\text{Ln}[\text{H}(\text{O},\text{PCH}_2)_2\text{-NH}(\text{CH}_2)_2\text{-SO}_3] \cdot 2\text{H}_2\text{O}$ were isolated and characterized, which crystallize in two different structures, monoclinic *m*-**LaH₂SP** and orthorhombic *o*-**LnH₂SP** (Ln = Pr, Nd, Sm, Eu, Gd, and Tb), with unit cell volumes of ~1200 and ~2500 Å³, respectively. Their crystal structures, solved ab initio from X-ray powder diffraction data, correspond to different layered frameworks depending on the Ln³⁺ cation size. In the orthorhombic series, *o*-**LnH₂SP**, the sulfonate group is noncoordinated and points toward the interlayer space, while for *m*-**LaH₂SP**, both phosphonate and sulfonate groups coordinate to the Ln³⁺ centers. As a consequence, different H-bonding networks and proton transfer pathways are generated. Proton conductivity measurements have been carried out between 25 and 80 °C at 70–95% relative humidity. The Sm³⁺ derivative exhibits a conductivity of ~1 × 10⁻³ S cm⁻¹ and activation energy characteristic of a Grotthuss-type mechanism for proton transfer. Preliminary MEA assays indicate that these layered lanthanide sulfophosphonates assist in maintaining the proton conductivity of Nafion membranes at least up to 90 °C and perform satisfactorily in single proton-exchange membrane fuel cells.



INTRODUCTION

Recent interest in phosphonate-based coordination polymers (CPs) relies on chemical robustness and functional versatility of metal phosphonate materials, which make them attractive for a number of potential applications.^{1–5} Among the CP-based proton conductors, metal phosphonates hold a prominent position.^{6–8} Such materials are sought due to their attractive properties such as: (a) hydrolytic stability of the P–C and M–O bonds,^{9,10} (b) stability to higher temperatures,¹¹ (c) structures with well-defined proton conduction pathways,^{12–17} (d) acidic sites on the ligands,^{18–22} or (e) presence of lattice water molecules that commonly participate

in the proton conduction mechanism.^{23–26} Efforts have been put forth to enhance the proton conduction efficiency by introducing acidic moieties into the phosphonate ligand backbone^{25,28} or by replacing the phosphonate ligand altogether with another that possesses (more) acidic groups.^{29,30} One prominent example is the sulfonate group. Metal phosphonates containing sulfonate groups have been among the first such materials that were studied for proton

Received: July 19, 2019
Revised: November 6, 2019
Published: November 7, 2019

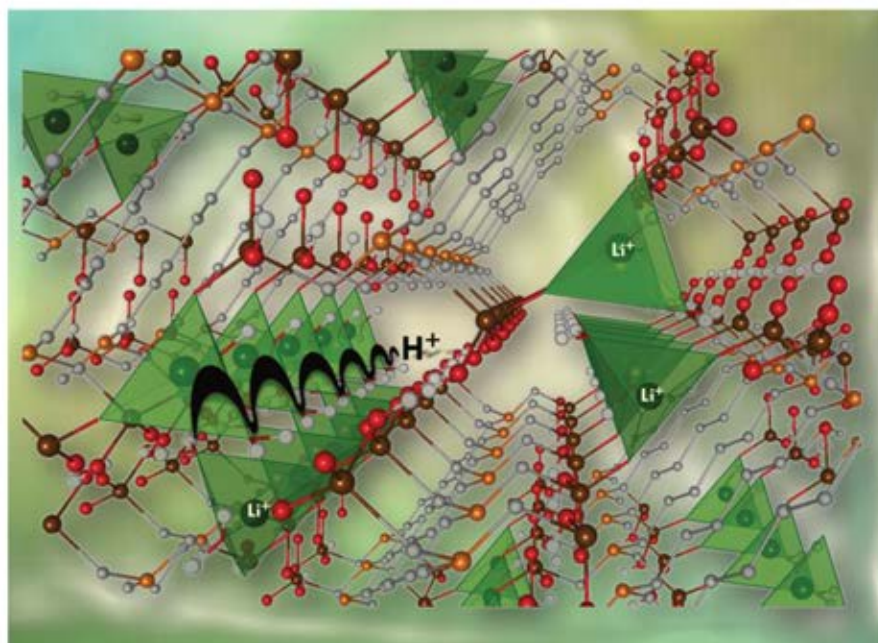
APPENDIX V

Article #3
Salcedo et al., 2018

Salcedo, I. R.; Colodrero, R. M. P.; Bazaga-García, M.; Vasileiou, A.; Papadaki, M.; Olivera-Pastor, P.; Infantes-Molina, A.; Losilla, E. R.; Mezei, G.; Cabeza, A.; Demadis, K. D. From light to heavy alkali metal tetrphosphonates (M= Li, Na, K, Rb, Cs): Cation size-induced structural diversity and water-facilitated proton conductivity. *Cryst. Eng. Comm.*, **2018**, 20(47), 7648-7658.

APPENDIX V

Cryst. Eng. Comm., 2018, 20(47), 7648-7658 - Reproduced by permission of The Royal Society of Chemistry. Copyright (2018).



Showcasing research by Inés R. Salcedo, Rosario M. P. Colodrero, Montse Bazaga-García, Pascual Olivera-Pastor, Antonia Infantes-Molina, Enrique R. Losilla and Aurelio Cabeza from the Departamento de Química Inorgánica (Universidad de Málaga, Spain); Antonia Vasileiou, Maria Papadaki and Konstantinos D. Demadis from the Department of Chemistry (University of Crete, Greece) and Gellert Mezei from the Department of Chemistry (Western Michigan University, USA).

From light to heavy alkali metal tetraphosphonates (M = Li, Na, K, Rb, Cs): cation size-induced structural diversity and water facilitated proton conductivity

Among the structural diversity of coordination polymers formed by the reaction of hexamethylenediamine-*N,N,N',N'*-tetrakis(methylenephosphonic acid) with alkali metal ions, a remarkable proton conductivity for that of the Li⁺ derivative, enhanced by reversible structural rearrangements upon dehydration/rehydration, is highlighted.

As featured in:



See Gellert Mezei, Aurelio Cabeza, Konstantinos D. Demadis et al., *CrystEngComm*, 2018, 20, 7642.



rsc.li/crystengcomm

Registered charity number: 207990

Cite this: *CrystEngComm*, 2018, 20, 7648

From light to heavy alkali metal tetraphosphonates (M = Li, Na, K, Rb, Cs): cation size-induced structural diversity and water-facilitated proton conductivity†

Inés R. Salcedo,^a Rosario M. P. Colodrero,^b Montse Bazaga-García,^b Antonia Vasileiou,^c Maria Papadaki,^c Pascual Olivera-Pastor,^a Antonia Infantes-Molina,^a Enrique R. Losilla,^a Gellert Mezei,^{a,d} Aurelio Cabeza^{e,f,g} and Konstantinos D. Demadis^{a,c}

A family of alkali metal-based frameworks containing the tetraphosphonate ligand hexamethylenediamine-*N,N,N',N'*-tetrakis(methylene phosphonic acid), HDTMP, is reported. A cation size-induced structural diversity, from monodimensional solids (Li⁺ and Na⁺) through layered (K⁺) to pillared-layered (Rb⁺ and Cs⁺) structures, was found. The proton conductivity properties of the Li compounds (hydrated and dehydrated) are reported and the influence of dehydration/rehydration processes in enhancing proton transfer processes is highlighted. Reversible changes in the dimensionality occurred upon full dehydration/rehydration with minor rearrangements in the framework, implying variations in the Li⁺-ligand connectivity but preserving the tetracoordination of the metal ion. The reversibly dehydrated-rehydrated sample displayed the highest proton conductivity ($5 \times 10^{-3} \text{ S cm}^{-1}$ at 80 °C and 95% RH), a behavior attributed to reversible formation/reformation of P–O(H)–Li bonds that, in turn, provoked changes in the acidity of acid groups and water mobility in the temperature range of impedance measurements.

Received 11th August 2018,
Accepted 16th September 2018

DOI: 10.1039/c8ce01353a

rsc.li/crystengcomm

1. Introduction

The field of metal phosphonate compounds has experienced constant growth during the last decades.¹ This is primarily due to the rich structural diversity of these hybrids and their potential applications,² including gas storage,^{3–5} photoluminescence,^{6,7} proton conductivity,^{8–14} corrosion control^{15–20} and metal ion absorption.^{21,22} Phosphonic acids and their water-soluble salts find extensive use in several industrial and pharmaceutical applications, such as mineral

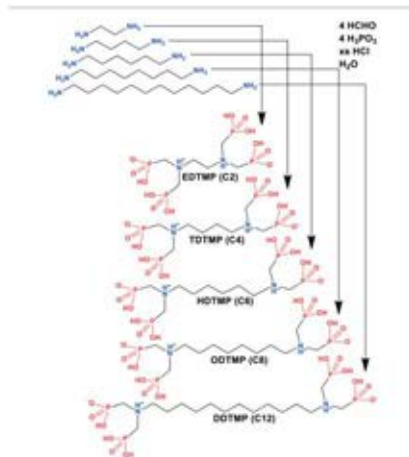
^a Departamento de Química Inorgánica, Universidad de Málaga, Campus Teatinos s/n, Málaga 29071, Spain. E-mail: aurelio@uma.es

^b Faculty of Science & Engineering, University of Wolverhampton, Wulfruna Street, Wolverhampton WV1 1LY, UK

^c Crystal Engineering, Growth and Design Laboratory, Department of Chemistry, University of Crete, Voutes Campus, Crete, GR-71003, Greece. E-mail: demadis@uoi.gr

^d Department of Chemistry, Western Michigan University, Kalamazoo, Michigan 49008-5413, USA. E-mail: gellert.mezei@wmich.edu

† Electronic supplementary information (ESI) available: CIF files for all M-HDTMP compounds (M = Li, Na, K, Rb, and Cs), Rietveld plot for Li-HDTMP-0W, powder XRD patterns, ATR IR spectra, additional TGA traces, graphs relating coordination numbers and M–O bond distances with cation size, and impedance results. CCDC 1584813–1584820. For ESI and crystallographic data in CIF or other electronic format see DOI: 10.1039/c8ce01353a



Scheme 1 Schematic structures of the tetraphosphonate family members in their zwitterionic form.

Article #4
Colodrero et al., 2018

Colodrero, R. M. P.; Salcedo, I. R.; Bazaga-García, M.; Barouda, E.; Papadaki, M.; Papathanasiou, K. E.; Hernández-Alonso, D.; Rius, J.; Aranda, M. A. G.; Losilla, E. R.; Olivera-Pastor, P.; Demadis, K. D.; Cabeza, A. High-Throughput Synthesis of Pillared-Layered Magnesium Tetrakisphosphate Coordination Polymers: Framework Interconversions and Proton Conductivity Studies. *Inorganics*, **2018**, 6(3), 96.

APPENDIX V



Article

High-Throughput Synthesis of Pillared-Layered Magnesium Tetrakisphosphate Coordination Polymers: Framework Interconversions and Proton Conductivity Studies

Rosario M.P. Colodrero ¹, Inés R. Salcedo ², Montse Bazaga-García ², Eleni Barouda ³, María Papadaki ³, Konstantinos E. Papathanasiou ³, Daniel Hernández-Alonso ², Jordi Rius ⁴, Miguel A.G. Aranda ⁵, Enrique R. Losilla ², Pascual Olivera-Pastor ², Konstantinos D. Demadis ^{3,*} and Aurelio Cabeza ^{2,*}

¹ Faculty of Science & Engineering, University of Wolverhampton, Wulfruna Street, Wolverhampton WV1 1LY, UK; r.perezcolodrero@wlv.ac.uk

² Departamento de Química Inorgánica, Universidad de Málaga, Campus Teatinos s/n, 29071 Málaga, Spain; iners@uma.es (I.R.S.); m.bazaga@uma.es (M.B.-G.); hernandez.alonso.d@gmail.com (D.H.-A.); r_losilla@uma.es (E.R.L.); poliverap@uma.es (P.O.-P.)

³ Crystal Engineering, Growth and Design Laboratory, Department of Chemistry, University of Crete, Voutes Campus, Crete GR-71003, Greece; leni_mpar@yahoo.gr (E.B.); magia@chemistry.uoc.gr (M.P.); kpatha@fiu.edu (K.E.P.)

⁴ Institut de Ciència de Materials de Barcelona (CSIC), 08193 Bellaterra, Catalunya, Spain; jordi.rius@icmab.es

⁵ ALBA Synchrotron, Ctra. BP1413 km 3.3, 08290 Cerdanyola del Vallès, Barcelona, Spain; g.aranda@cells.es
* Correspondence: demadis@uoc.gr (K.D.D.); aurelio@uma.es (A.C.); Tel: +30-2810-545051 (K.D.D.); +34-952-131-874 (A.C.)

Received: 8 August 2018; Accepted: 7 September 2018; Published: 11 September 2018



Abstract: Novel pillared-layered framework materials were synthesized by high-throughput or microwave-assisted methodology that contain Mg^{2+} and the zwitterionic linker HDTMP (hexamethylenediamine-*N,N,N',N'*-tetrakis(methylenephosphonic acid)). Three compounds were structurally characterized by X-ray powder diffraction. In the compound $[Mg\{(HO_2PCH_2)_2N(CH_2)_6N(CH_2PO_3H_2)_2\} \cdot (H_2O)]_n$ (**1**), obtained at 140 °C by hydrothermal or microwave-assisted reaction, the layers are built by isolated Mg^{2+} octahedra coordinated by oxygen atoms from six different zwitterionic HDTMP ligands. Each amino-*bis*(methylenephosphonate) moiety links three Mg^{2+} ions, bridging two of them through one phosphonate group and connecting the third polyhedron in a monodentate fashion. In Compound **2**, $[Mg\{(HO_2PCH_2)_2N(CH_2)_6N(CH_2PO_3H_2)_2\}]_n$, hydrothermally synthesized at 180 °C, the layers are composed of bidentate amino-*bis*(methylenephosphonate) moieties connected to three Mg^{2+} ions, with one of the phosphonate groups acting as a bridging ligand. Various subtle structural changes are noted for the other two compounds. Thermomodification of **1** reveals that a crystalline-to-crystalline phase transformation occurs concomitantly with its dehydration, leading to a new anhydrous phase, namely, $[Mg\{(HO_2PCH_2)_2N(CH_2)_6N(CH_2PO_3H_2)_2\}]_n$ (**1deh**). This process is fully reversible upon equilibrating the solid at room temperature. The reported compounds can adsorb ammonia and CO_2 . Compound **1** exhibits a moderate proton conductivity, $\sim 1.5 \times 10^{-5} S \cdot cm^{-1}$ at 80 °C and 95% RH, that increases a half order of magnitude after experiencing a complete dehydration/rehydration process, **1** → **1deh** → **1**.

Keywords: proton conductivity; coordination polymers; metal phosphonates; tetrakisphosphonates; gas adsorption; dehydration/rehydration



APPENDIX V

Appendix VI

Other Articles





UNIVERSIDAD
DE MÁLAGA

2016

Bazaga-García, M.; Angeli, G. K.; Papathanasiou, K. E.; [Salcedo, I. R.](#); Olivera-Pastor, P.; Losilla, E. R.; Choquesillo-Lazarte, D.; Hix, G. B.; Cabeza, A.; Demadis, K. D. Luminescent and Proton Conducting Lanthanide Coordination Networks Based on a Zwitterionic Tripodal Triphosphonate. *Inorg. Chem.*, **2016**, 55(15), 7414-7424.

2017

Colodrero, R. M.; [Salcedo, I. R.](#); Bazaga-García, M.; Milla-Pérez, D. F.; Durán-Martín, J. D.; Losilla, E. R.; Moreno-Real, L.; Rius, J.; Aranda, M. A. G.; Demadis, K. D.; Olivera-Pastor, P.; Cabeza, A. Structural variability in M²⁺ 2-hydroxyphosphonoacetate moderate proton conductors. *Pure Appl. Chem.*, **2017**, 89(1), 75-87.

Vallejo, J.; [Salcedo, I. R.](#); Colodrero, R. M.; Cabeza, A.; Świtlicka, A.; Cano, J.; Viciano-Chumillas, M. Zinc (ii), cobalt (ii) and manganese (ii) networks with phosphoserine ligand: synthesis, crystal structures and magnetic and proton conductivity properties. *Dalton Trans.*, **2017**, 46(47), 16570-16579.

2018

Armakola, E.; Colodrero, R. M.; Bazaga-García, M.; [Salcedo, I. R.](#); Choquesillo-Lazarte, D.; Cabeza, A.; Kirillova, M. V.; Kirillov, A. M.; Demadis, K. D. Three-Component Copper-Phosphonate-Auxiliary Ligand Systems: Proton Conductors and Efficient Catalysts in Mild Oxidative Functionalization of Cycloalkanes. *Inorg. Chem.*, **2018**, 57(17), 10656-10666.

2019

Armakola, E.; [Salcedo, I. R.](#); Bazaga-García, M.; Olivera-Pastor, P.; Mezei, G.; Cabeza, A.; Fernandes, T. A.; Kirillov, A. M.; Demadis, K. D. Phosphonate Decomposition-Induced Polyoxomolybdate Dumbbell-Type Cluster Formation: Structural Analysis, Proton Conduction, and Catalytic Sulfoxide Reduction. *Inorg. Chem.*, **2019**, 58(17), 11522-11533.

Shearan, S. J.; Stock, N.; Emmerling, F.; Demel, J.; Wright, P. A.; Demadis, K. D.; Vassaki, M.; Costantino, F.; Vivani, R.; Sallard, S.; [Salcedo, I. R.](#); Cabeza, A.; Taddei, M. New Directions in Metal Phosphonate and Phosphinate Chemistry. *Crystals*, **2019**, 9(5), 270.



UNIVERSIDAD
DE MÁLAGA

Appendix VII

Copyright Permission



UNIVERSIDAD
DE MÁLAGA

COPYRIGHT PERMISSION

Article #1

Salcedo, I. R.; Bazaga-García, M.; Cuesta, A.; Losilla, E. R.; Demadis, K. D.; Olivera-Pastor, P.; Colodrero, R. M. P.; Cabeza, A. NH₃/H₂O-mediated proton conductivity and photocatalytic behaviour of Fe(II)-hydroxyphosphonoacetate and M(II)-substituted derivatives. *Dalton Trans.*, 2020, 49(13), 3981-3988.

1. Dalton transactions		0,00 EUR	
ISSN Type of Use	1477-9234 Republ in a thesis/dissertation	Publisher Portion	ROYAL SOCIETY OF CHEMISTRY Chapter/article Publisher Terms and Conditions Special Terms Apply
Hide Details			
LICENSED CONTENT			
Publication Title	Dalton transactions	Country	United Kingdom of Great Britain and Northern Ireland
Author/Editor	Royal Society of Chemistry (Great Britain)	Rights holder	Royal Society of Chemistry
Date	01/01/2003	Publication Type	eJournal
Language	English		
REQUEST DETAILS			
Portion Type	Chapter/article	Rights Requested	Main product
Page range(s)	3981-3988	Distribution	Worldwide
Total number of pages	7	Translation	Original language of publication
Format (select all that apply)	Print, Electronic	Copies for the disabled?	No
Who will republish the content?	Academic institution	Minor editing privileges?	No
Duration of Use	Life of current edition	Incidental promotional use?	No
Lifetime Unit Quantity	Up to 499	Currency	EUR
NEW WORK DETAILS			
Title	Electrochemical and photochemical applications of multifunctional metal phosphonates	Institution name	Universidad de Málaga
Instructor name	Aurelio Cabeza	Expected presentation date	2020-05-29
ADDITIONAL DETAILS			
Order reference number	N/A	The requesting person / organization to appear on the license	Ima Ruiz Salcedo
REUSE CONTENT DETAILS			
Title, description or numeric reference of the portion(s)	Dalton Trans., 2020, 49, 3981-3988	Title of the article/chapter the portion is from	NH ₃ /H ₂ O-mediated proton conductivity and photocatalytic behaviour of Fe(II)-hydroxyphosphonoacetate and M(II)-substituted derivatives
Editor of portion(s)	N/A	Author of portion(s)	Salcedo, I. R.; Bazaga-García, M.; Cuesta, A.; Losilla, E. R.; Demadis, K. D.; Olivera-Pastor, P.; Colodrero, R. M. P.; Cabeza, A.
Volume of serial or monograph	N/A	Issue, if republishing an article from a serial	49
Page or page range of portion	3981-3988	Publication date of portion	2020-01-02
If changes are required, remove the item from your cart and visit Special Requests within Manage Account Remove			
Total Items: 1		Cart Total: 0,00 EUR	
		Apply Promotional Code	CHECKOUT

APPENDIX VII

Article #2

Bazaga-García, M.; Salcedo, I. R.; Colodrero, R. M. P.; Xanthopoulos, K.; Villemin, D.; Stock, N.; López-González, M.; del Río, C.; Losilla, E. R.; Cabeza, A.; Demadis, K. D.; Olivera-Pastor, P. Layered Lanthanide Sulfophosphonates and Their Proton Conduction Properties in Membrane Electrode Assemblies. *Chem. Mater.*, **2019**, 31(23), 9625-9634.

Layered Lanthanide Sulfophosphonates and Their Proton Conduction Properties in Membrane Electrode Assemblies

Author: Montse Bazaga-García, Inés R. Salcedo, Rosario M. P. Colodrero, et al

Publication: Chemistry of Materials

Publisher: American Chemical Society

Date: Dec 1, 2019

Copyright © 2019, American Chemical Society

PERMISSION/LICENSE IS GRANTED FOR YOUR ORDER AT NO CHARGE

This type of permission/license. Instead of the standard Terms & Conditions, is sent to you because no fee is being charged for your order. Please note the following:

- Permission is granted for your request in both print and electronic formats, and translations.
- If figures and/or tables were requested, they may be adapted or used in part.
- Please print this page for your records and send a copy of it to your publisher/graduate school.
- Appropriate credit for the requested material should be given as follows: "Reprinted (adapted) with permission from (COMPLETE REFERENCE CITATION). Copyright (YEAR) American Chemical Society." Insert appropriate information in place of the capitalized words.
- One-time permission is granted only for the use specified in your request. No additional uses are granted (such as derivative works or other editions). For any other uses, please submit a new request.

[BACK](#) [CLOSE WINDOW](#)

Article #3

Salcedo, I. R.; Colodrero, R. M. P.; Bazaga-García, M.; Vasileiou, A.; Papadaki, M.; Olivera-Pastor, P.; Infantes-Molina, A.; Losilla, E. R.; Mezei, G.; Cabeza, A.; Demadis, K. D. From light to heavy alkali metal tetrphosphonates (M= Li, Na, K, Rb, Cs): Cation size-induced structural diversity and water-facilitated proton conductivity. *Cryst. Eng. Comm.*, 2018, 20(47), 7648-7658.

CrystEngComm

GENERAL INFORMATION

Request ID	600014100	Request Date	19 May 2020
Request Status	Approved	Price	0.00 EUR  Special Terms

ALL DETAILS

ISSN:	1486-8033	Publisher:	ROYAL SOCIETY OF CHEMISTRY
Type of Use:	Republish in a thesis/dissertation	Portion:	Chapter/article

LICENSED CONTENT

Publication Title	CrystEngComm	Country	United Kingdom of Great Britain and N...
Author/Editor	Royal Society of Chemistry (Great Brice...	Rightholder	Royal Society of Chemistry
Date	01/01/1999	Publication Type	e-Journal
Language	English	URLs	http://www.rsc.org/Publishing/journals...

REQUEST DETAILS

Portion Type	Chapter/article	Rights Requested	Main product
Page range(s)	7648-7658	Distribution	Worldwide
Total number of pages	10	Translation	Original language of publication
Format (select all that apply)	Print, Electronic	Copies for the disabled?	No
Who will republish the content?	Academic Institution	Minor editing privileges?	No
Duration of Use	Life of current edition	Incidental promotional use?	No
Lifetime Unit Quantity	Up to 499	Currency	EUR

NEW WORK DETAILS

Title	Electrochemical and photochemical ad...	Institution name	Universidad de Málaga
Instructor name	Aurelio Cabeza	Expected presentation date	2020-05-28

ADDITIONAL DETAILS

The requesting person / organization to appear on the license	Inés Ruiz Salcedo
---	-------------------

REUSE CONTENT DETAILS

Title, description or numeric reference of the portion(s)	CrystEngComm, 2018, 20, 7648-7658	Title of the article/chapter the portion is from	From light to heavy alkali metal tetrap...
Editor of portion(s)	N/A	Author of portion(s)	Salcedo, I. R.; Colodrero, R. M. P.; Baz...
Volume of serial or monograph	N/A	Issue, if republishing an article from a serial	47
Page or page range of portion	7648-7658	Publication date of portion	1999-01-01

APPENDIX VII

Figure 1.4. HT investigation of the influence of temperature and pH value on product formation in the system $\text{CdCl}_2/\text{H}_3\text{L}/\text{NaOH}$. Reproduced from Ref. Bauer & Stock (2007) with permission from Wiley Online Library. Copyright (2007).



Implementation of a Temperature-Gradient Reactor System for High-Throughput Investigation of Phosphonate-Based Inorganic–Organic Hybrid Compounds

Author: Norbert Stock, Sebastian Bauer
 Publication: Angewandte Chemie International Edition
 Publisher: John Wiley and Sons
 Date: Sep 4, 2007

Copyright © 2007 WILEY-VCH Verlag GmbH & Co. KGaA, Weinheim

Order Completed

Thank you for your order.

This Agreement between Inés Ruiz Salcedo ("You") and John Wiley and Sons ("John Wiley and Sons") consists of your license details and the terms and conditions provided by John Wiley and Sons and Copyright Clearance Center.

Your confirmation email will contain your order number for future reference.

License Number: 4836620699934 [Printable Details](#)

License date: May 26, 2020

Licensed Content		Order Details	
Licensed Content Publisher	John Wiley and Sons	Type of use	Dissertation/Thesis
Licensed Content Publication	Angewandte Chemie International Edition	Requestor type	University/Academic
Licensed Content Title	Implementation of a Temperature-Gradient Reactor System for High-Throughput Investigation of Phosphonate-Based Inorganic–Organic Hybrid Compounds	Format	Print and electronic
Licensed Content Author	Norbert Stock, Sebastian Bauer	Portion	Figure/table
Licensed Content Date	Sep 4, 2007	Number of figures/tables	1
Licensed Content Volume	46	Will you be translating?	No
Licensed Content Issue	36		
Licensed Content Pages	4		

About Your Work		Additional Data	
Title	Electrochemical and Photochemical Applications of Multifunctional Metal Phosphonates	Portions	Figure from graphical abstract
Institution name	Universidad de Málaga		
Expected presentation date	May 2020		

Requestor Location	Tax Details
Inés Ruiz Salcedo Campus de Teatinos	Publisher Tax ID EU826007151
Requestor Location	
Málaga, Malaga 29071 Spain Attn:	
\$ Price	
Total	0.00 EUR

Would you like to purchase the full text of this article? If so, please continue on to the content ordering system located here: [Purchase PDF](#)
If you click on the buttons below or close this window, you will not be able to return to the content ordering system.

Total: 0.00 EUR

[CLOSE WINDOW](#) [ORDER MORE](#)

APPENDIX VII

Figure 1.5. Structure of solid (1), (2), (3) and (4). Adapted from Ref. Lin & Zhou (2020) with permission from Elsevier. Copyright (2020).

Synthesis, crystal structures, and characterizations of a series of divalent metal carbonate phosphonates
 Author: Jing-Ping Liu, Chao-Lin Zhou
 Publication: Journal of Solid State Chemistry
 Publication Date: 15 May 2020
 © 2020 Elsevier Inc. All rights reserved.

Order Completed

Thank you for your order.
This agreement includes the Full Article, Table of Contents, and the online version published by ScienceDirect.com.

Your confirmation order will contain your order number for future reference.

Order Number	4040158421	Printed Order
Order Date	May 05, 2020	

<p>Journal Details</p> <p>Journal Title: Journal of Solid State Chemistry</p> <p>Journal Volume: Synthesis, crystal structures, and characterizations of a series of divalent metal carbonate phosphonates</p> <p>Journal Issue: Jing-Ping Liu, Chao-Lin Zhou, et al., 2020</p> <p>Journal Article: 1-11</p> <p>Journal Type: JST</p>	<p>Order Details</p> <p>Type of Use: Access to the Full Article</p> <p>Number of Reproduction Rights: 7</p> <p>Number of Reproduction Rights: 7</p> <p>Are you the author of this document? No</p> <p>Are you the author of this document? No</p>
---	---

<p>Related User Works</p> <p>Title: Synthesis and Photocatalytic Applications of Multicomponent Metal-Organic Frameworks</p> <p>Author Name: Chao-Lin Zhou</p> <p>Publication Date: May 2020</p>	<p>Additional Data</p> <p>Address: Original address with order receipt</p>
--	--

<p>Regional Location</p> <p>Region: Asia Pacific</p> <p>Country: China</p> <p>City: Beijing</p>	<p>Tax Details</p> <p>Customer Tax ID: 9130101010101010101</p>
---	--

Total Price	2000.00 EUR	Total: 2000.00 EUR
--------------------	-------------	---------------------------

Cancel Order
Print Order

Figure 1.6. Schematic diagram of the reaction mechanism of H₂O₂ activation by MIL-88B-Fe. Reproduced from Ref. Gao et al. (2017a) with permission from Elsevier. Copyright (2017).

The image shows a screenshot of an Elsevier article page. At the top, there is a yellow banner with the article title: "Enhanced Fenton-like catalysis by iron-based metal-organic frameworks for degradation of organic pollutants". Below the banner, the article details are listed: "Journal of Catalysis", "Volume 352, December 2017", and "Pages 1-10". The main content area is titled "Order Completed" and contains a green message box: "Thank you for your order. This agreement between you and Elsevier on the terms and conditions is hereby acknowledged." Below this, there are several sections: "Order Details", "About Your Order", "Additional Data", and "Tax Details". The "Order Details" section includes fields for "Order Number" (4000000000), "Order Date" (May 24, 2017), "Order Status" (Paid), "Type of Use" (Paper in a non-commercial context), "Number of Signatures/Initials" (1), "Number" (1), "Are you the author of this material?" (No), and "Are you the copyright owner?" (No). The "About Your Order" section includes "Title" (Synthesis and Photocatalytic Application of MIL-88B-Fe), "Publication Name" (Journal of Catalysis), "Published on" (May 2017), "Author" (Jin-Rui Zhang, Li-Hua Tang, Liang-Liang Zhang, Liang-Liang Zhang, Liang-Liang Zhang), "Volume" (352), "Issue" (1), "Pages" (1-10), and "Journal Type" (JCAT). The "Additional Data" section includes "Authors" (Jin-Rui Zhang, Li-Hua Tang, Liang-Liang Zhang, Liang-Liang Zhang, Liang-Liang Zhang) and "Subject" (Applied Catalysis). The "Tax Details" section includes "Publication Year" (2017) and "Publication Date" (20 May 2017). At the bottom right, there is a "Total: 0.00 EUR" and a "Check Order" button.

APPENDIX VII

Figure 1.8. The 1D channels in $\{H[(N(CH_3)_4)_2][Gd_3(NIPA)_6]\} \cdot 3H_2O$ showing four different orientations. Reproduced from Ref. Xing et al. (2019) with permission from The Royal Society of Chemistry. Copyright (2019).

1. Chemical communications 0,00 EUR

Order license ID ISSN Type of Use	Pending 1364 548X Republish in a thesis/dissertation	Publisher Portion	ROYAL SOCIETY OF CHEMISTRY Image/photo/illustration
---	---	----------------------	---

[Hide Details](#)

LICENSED CONTENT

Publication Title	Chemical communications	Country	United Kingdom of Great Britain and Northern Ireland
Author/Editor	Royal Society of Chemistry (Great Britain)	Rights holder	Royal Society of Chemistry
Date	01/01/1996	Publication Type	e-Journal
Language	English		

REQUEST DETAILS

Portion Type	Image/photo/illustration	Distribution	Worldwide
Number of images / photos / illustrations	1	Translation	Original language of publication
Format (select all that apply)	Print, Electronic	Copies for the disabled?	No
Who will republish the content?	Academic institution	Minor editing privileges?	Yes
Duration of Use	Life of current edition	Incidental promotional use?	No
Lifetime Unit Quantity	Up to 499	Currency	EUR
Rights Requested	Main product		

NEW WORK DETAILS

Title	Electrochemical and Photochemical Applications of Multifunctional Metal Phosphonates	Institution name	Universidad de Málaga
Instructor name	Aurelio Cabeza	Expected presentation date	2020-05-29

ADDITIONAL DETAILS

Order reference number	N/A	The requesting person / organization to appear on the license	Inés Ruiz Salcedo
------------------------	-----	---	-------------------

REUSE CONTENT DETAILS

Title, description or numeric reference of the portion(s)	Fig. 1. (d)	Title of the article/chapter the portion is from	Chem. Commun., 2019,55, 1241-1244
Editor of portion(s)	N/A	Author of portion(s)	Royal Society of Chemistry (Great Britain)
Volume of serial or monograph	N/A	Issue, if republishing an article from a serial	5
Page or page range of portion	1242	Publication date of portion	2019-06-04


[Print License](#)

Total Items: 1 Total Due: 0,00 EUR

Accepted: All Publisher and CCC Terms and Conditions [Continue Shopping](#)

COPYRIGHT PERMISSION

Figure 1.10. Emission spectra in the presence of different volumes of 10^{-3}M (a) Fe^{3+} and (b) $\text{Cr}_2\text{O}_7^{2-}$ solutions: from 0 (black) to 500 μL (violet). Adapted from Ref. Hou et al. (2020) with permission from The Royal Society of Chemistry. Copyright (2020).

1. Dalton transactions  0,00 EUR

ISSN	1477-9234	Publisher	ROYAL SOCIETY OF CHEMISTRY
Type of Use	Republish in a thesis/dissertation	Portion	Image/photo/illustration

[Hide Details](#)

LICENSED CONTENT

Publication Title	Dalton transactions	Country	United Kingdom of Great Britain and Northern Ireland
Author/Editor	Royal Society of Chemistry (Great Britain)	Rightsholder	Royal Society of Chemistry
Date	01/01/2009	Publication Type	eJournal
Language	English		

REQUEST DETAILS

Portion Type	Image/photo/illustration	Distribution	Worldwide
Number of images / photos / illustrations	1	Translation	Original language of publication
Format (select all that apply)	Print, Electronic	Copies for the disabled?	No
Who will republish the content?	Academic institution	Minor editing privileges?	Yes
Duration of Use	Life of current edition	Incidental promotional use?	No
Lifetime Unit Quantity	Up to 499	Currency	EUR
Rights Requested	Main product		

NEW WORK DETAILS

Title	Electrochemical and Photochemical Applications of Multifunctional Metal Phosphonates	Institution name	Universidad de Málaga
Instructor name	Auralee Cabeza	Expected presentation date	2020-05-29

ADDITIONAL DETAILS

Order reference number	N/A	The requesting person / organization to appear on the license	Inés Ruiz Salcedo
------------------------	-----	---	-------------------

REUSE CONTENT DETAILS

Title, description or numeric reference of the portion(s)	Dalton Trans., 2020,49: 3809-3815	Title of the article/chapter the portion is from	Two-dimensional layered lanthanide di(phosphonates): synthesis, structures and sensing properties toward Fe^{3+} and $\text{Cr}_2\text{O}_7^{2-}$
Editor of portion(s)	N/A	Author of portion(s)	Royal Society of Chemistry (Great Britain)
Volume of serial or monograph	N/A	Issue, if republishing an article from a serial	-49
Page or page range of portion	6	Publication date of portion	2019-12-02

[Remove](#)

Total Items: 1 Cart Total: 0,00 EUR

Apply Promotional Code
CHECKOUT



UNIVERSIDAD
DE MÁLAGA



UNIVERSIDAD
DE MÁLAGA



UNIVERSIDAD
DE MÁLAGA